coatings

Special Issue Reprint

Toward Sustainability through Bio-Based Materials at the Interfaces with Living Systems

Edited by
Seungil Kim

mdpi.com/journal/coatings

MDPI

Toward Sustainability through Bio-Based Materials at the Interfaces with Living Systems

Toward Sustainability through Bio-Based Materials at the Interfaces with Living Systems

Editor

Seungil Kim

MDPI

Basel • Beijing • Wuhan • Barcelona • Belgrade • Novi Sad • Cluj • Manchester

Editor
Seungil Kim
Department of Surgery,
University of Pittsburgh
Pittsburgh, PA, USA

Editorial Office
MDPI
St. Alban-Anlage 66
4052 Basel, Switzerland

This is a reprint of articles from the Special Issue published online in the open access journal *Coatings* (ISSN 2079-6412) (available at: https://www.mdpi.com/journal/coatings/special_issues/biobased_materials_interfaces).

For citation purposes, cite each article independently as indicated on the article page online and as indicated below:

Lastname, A.A.; Lastname, B.B. Article Title. *Journal Name* **Year**, *Volume Number*, Page Range.

ISBN 978-3-0365-9338-8 (Hbk)
ISBN 978-3-0365-9339-5 (PDF)
doi.org/10.3390/books978-3-0365-9339-5

Contents

About the Editor

Seungil Kim

Dr. Seungil Kim serves as a Research Assistant Professor at the McGowan Institute for Regenerative Medicine, located at the University of Pittsburgh. His expertise lies at the intersection of polymer chemistry and biomedical engineering, where he dedicates his research efforts to the advancement of minimally invasive topical delivery systems. Dr. Kim achieves this by designing innovative polymeric biomaterials and medical devices.

One of his prominent contributions involves the development of biodegradable embolization systems. These systems are designed to deliver therapeutic peptides and stem cells, offering a permanent solution for the treatment of cerebral saccular aneurysms without leaving behind any foreign materials within the body.

coatings

MDPI

Review

Whether Carbon Nanotubes Are Capable, Promising, and Safe for Their Application in Nervous System Regeneration. Some Critical Remarks and Research Strategies

Andrzej Zieliński *and Beata Majkowska-Marzec

Department of Biomaterials Technology, Faculty of Mechanical Engineering and Ship Technology, Institute of Manufacturing and Materials Technology, Gdańsk University of Technology, Narutowicza 11/12, 80-233 Gdańsk, Poland

* Correspondence: andrzej.zielinski@pg.edu.pl

Abstract: Carbon nanotubes are applied in or considered for different fields of medicine. Among them is the regeneration or rebuilding of nervous system components, which still lack substantial progress; this field is supported by carbon nanotubes to a great extent as the principal material. The limited research on this issue has involved PU/silk/MWCNTs, PCL/silk/MWCNTs, PCL/PGS/CNTs, chitin/CNTs, PGF/CNTs, CNTs/PGFs/PLDLA, MWCNTs/chitosan, MWCNTs/PPy, PLA/MWCNTs, PU/PAA/MWCNts, GelMA/SACNTs, and CNTs alone, which have been subjected to different surface modifications and applied in the form of solid materials or scaffolds that are degradable or nondegradable. So far, these attempts have shown that the use of surface-modified MWCNTs is a promising way to improve the functions of nervous systems as a whole, even though some drawbacks, such as the potential cytotoxicity or the weak adhesion of CNTs to other components, may appear and be eliminated by their proper functionalization. The present review presents an idea of a nonbiodegradable scaffold structure composed of a chosen conductive polymer that is able to create a scaffold structure, a selected nanocarbon form (with MWCNTs as the first candidate), and a corrosion-resistant metal as a conductor. Other substances are also considered for their ability to increase the mechanical strength and adhesion of CNTs and their biological and electrical properties. The novelty of this approach is in the simultaneous use of nanocarbon and conductive metallic fibers in a polymer scaffold structure.

Keywords: nervous system failure and regeneration; carbon nanotubes and fibers; biodegradable and conductive polymers; nanometals; bioactive reinforcing ceramics

Citation: Zieliński, A.; Majkowska-Marzec, B. Whether Carbon Nanotubes Are Capable, Promising, and Safe for Their Application in Nervous System Regeneration. Some Critical Remarks and Research Strategies. *Coatings* **2022**, *12*, 1643. https://doi.org/10.3390/coatings12111643

Academic Editor: Doyoon Kim

Received: 29 September 2022
Accepted: 27 October 2022
Published: 30 October 2022

1. Failures of the Nervous System

The damages to the nervous system belong to the toughest failures of the human body, which frequently become irreversible. Some of them undergo difficult and risky surgeries, and others can only be the object of long-term rehabilitation, but many such accidents cannot be successfully treated. The reasons are due to the high entanglement of the nervous system [1]. That following, the repairing of harmed nerves and the recovery of their functions is still uncertain [2]. Neurological injuries appear to be the most recurrent and need rapid and effective interventions [3].

The nervous system has two components: (i) the peripheral nervous system (PNS) and (ii) the central nervous system (CNS). The PNS includes the cranial, spinal, and peripheral nerves and neuromuscular junctions, and the CNS is located in the brain and spinal cord. The PNS is more prone to impairment because it is not protected by, e.g., hard bone tissue or the blood-brain barrier [4]. On the other side, the recovery of the CNS is slower and less effective than for the PNS due to the deficit of the Schwann cells, which support the development, performance, and regeneration of nerves [5,6]. The mutual contact between bone and nerves is crucial for the correction of large bone defects as well as for the recon-

struction of peripheral nerves using the materials most suitable to ensure osteoconduction, osteoinduction, neuroconduction, neuroinduction, and neuroattraction [7].

Conventional surgery with the use of autografts, allografts, and xenografts is not an excellent medical solution for many reasons. In particular, for autografts, the implanted nerves come from other parts of the body, and it is often difficult to obtain the number of nerves necessary for a full recovery [6]. Moreover, allografts and xenografts create the risk of transmitting diseases that might be followed an implant rejection.

The current research strategies for the development of nerve implants focus on several problems, which include the physical form and structure and the composition of the used implant, its proper application, regeneration efficacy for the nervous system, and the anticipated toxicity of this to different organs. This paper shows some of the selected aspects of the strategy problems proposed based on the state-of-the-art in this field and several of our assumptions, with the most plausible approach for future research, in our opinion, keeping in mind that all these remarks and considerations are highly subjective.

2. Biomaterials for the Nervous Systems

As was suggested over 20 years ago, the tissue-engineered nerve construct should have four components: a scaffold construction for the proliferation of axons, Schwann or other support cells, growth factors, and an extracellular matrix [6]. According to another concept, such a conduit must be dissolvable in a biological environment, fast vascularized, and possess low antigenicity, porosity, and be resistant to long-term compressive stress [8]. An engineered "nerve guidance channel" (NGC) that is able to guide the regeneration of damaged nerves was also proposed [9]. Such an NGC is imagined as a tubular device with a single lumen creating the bridge for the reconstruction of the damaged peripheral nerves, which separates the regenerating axons and scar tissue and prevents compression by the surrounding tissue.

For implants, several material classes, like metals and alloys, solid and resorbable ceramics, bioglasses, polymers, carbon (and its organic derivatives), and many composite materials have been proposed [10], yet the nervous system needs specific materials. New synthetic and natural polymers are used most frequently to assemble the perfect scaffold enriched with some cells and growth factors, which can exactly mimic the extracellular matrix (ECM). Such a combination of biochemical, topographical, and electrical signals via various polymers, cells, and growth factors is considered the best solution for efficient regeneration [11,12]. The regarded strategies propose to develop a scaffold similar to the natural ECM that can provide an ideal environment for 3D cell cultures and is fully biocompatible and biodegradable [13]. However, the FDA approved until 2016 [3] only polyglycolic acid (PGA), PCL polycaprolactone, collagen, and polyvinyl alcohol (PVA). Other polymers have been investigated for neurosurgery aims and they include natural compounds such as hyaluronic acid (HA), the benzyl ester of hyaluronic acid (HYAFF), and synthetic polymers such as PLLA (polylactide of lactic acid), PLGA (poly(lactic-co-glycolic acid), polypyrrole (PPy), chitin, and chitosan, polyanhydride, polyhydroxyalkanoate, poly (propylene fumarate) and polyvinyl alcohol [6,9,13,14], (poly(3,4-ethylene dioxythiophene) (PEDOT) [15], and some others which are still under study. Such strategies look reasonable if the nerve conduit implant is designed to undergo a complete transformation. As polymers have several drawbacks, polymer-based composite materials have also been proposed for nerve tissue engineering, including recently bicomponent 3D scaffolds consisting of collagen and chondroitin sulfate [16] and antibacterial cellulose-based composites [17].

Other than only polymeric, materials are increasingly investigated for these considered branches of medicine, with nanotechnology and nano-based materials permanently important. Among them, diverse nanocarbon forms, random and aligned nanofibers, nanopatterning, and inorganic, organic, metallic, and biologically derived nanoparticles of the surface are the most preferred [18]. A need for new materials is especially distinct for long gaps in the nervous conduits [19]. In the past, various strategies have been proposed to provide a bridge between two detached nerve stumps and facilitate the regeneration

of axons [20]. Three generations of such materials include [1] (i) nondegradable materials like silicone conduit, an implant that acts as a tube and connection bridge but must be removed from the body; (ii) dissolvable conduits, like PLA, PVA, and PLGA-based conduits, which, however, act only as a tube and cannot promote nerve regeneration [21–24]; and (iii) conductive materials to form synthetic nerve conduits [25]. Conductive substrates can support cellular activity with or without electrical stimulation [26–28]. The intrinsically conductive and electroactive polymers with easy-to-tailor properties, such as polyaniline (PANI), PPy, polythiophene, polyphenylene sulfide, and oligomers for neural stimulation are among the most popular [29,30]. In addition, nanoparticles, such as gold nanoclusters, graphene nanosheets, and the here-described carbon nanotubes, were applied to increase the conductivity of polymer networks to the desired level of about 10^{-3} S/m [31,32].

Despite the materials used, electrical stimulation at various frequencies was shown to enhance the progress of axonal outgrowth in nerves. Moreover, peripheral nerve regeneration in extended gaps occurred effectively after electrical stimulation [33–35], but also pulsed magnetic field and ultrasound waves were utilized [36,37]. Among the different compounds called piezoelectric nano-biomaterials are barium titanate nanoparticles, boron nitride nanotubes, zinc oxide, polyvinylidene fluoride, and fluoride-trifluoroethylene, PLA, collagen, silk fibroin, and graphene oxide [38]. The electrospun conductive PVA)/PEDOT (poly(3,4-ethylene dioxythiophene) scaffolds seem to be one of the best for such a purpose among the composite materials [39].

The electrical stimulation occurs via microelectrodes. When considering the non-carbon materials used for coating, such electrodes are also used as polymers (such as PEDOT [40]) and as composites for nano bioglass/gelatin scaffolds implemented with antibacterial nanosilver and developed as a conduit for peripheral nerve regeneration [41]. The wide application of CNTs for biosensors (for glucose detection) and neurosensors is well-known [42], and they can also be used as biocatalysts, ion channel blockers, tools in cancer diagnosis and therapy, and nanovectors [43]. The electrochemical neurotransmitter sensors capable of detecting dopamine, serotonin, acetylcholine, glutamate, nitric oxide, and adenosine are widely based on carbon-nanostructure-modified electrodes, including carbon nanotubes, graphene and graphene oxide (GO), graphdiyne, and carbon nanofibers (CNFs) [44]. For example, CNTs were applied for flexible neuronal microelectrode devices [45–48], which were important because of their high surface-to-volume ratio. The carbon fiber microelectrodes were covered with a high-surface diamond film to improve neural stimulation [49]. The GO-PANI nanocomposite was shown to be promising as a coating of microelectrodes [50].

The biomaterials for the regeneration of the nervous system can be classified differently. They can be divided [2] into isotropic hydrogel fillers, which provide interluminal support for nerve regeneration; fibrous interluminal fillers, which offer intraluminal topographical guidance for neurites; and patterned interluminal scaffolds, which provide nerve growth with three dimensional (3D) structural support. On the other side, to talk about such biomaterials, it is plausible to consider them in their simplest form, based on either a physical shape or chemical composition, depending on a specific application. However, physical form, composition, and medical destination are interrelated so that the authors have decided (keeping in mind elementary carbon as an essential element of all the here-considered technical solutions) to divide all materials into nonporous (solid) materials and scaffolds, both either prone or resistant to biological degradation. As the title alludes to, we have focused on nanocarbon applications, mainly, but not exclusively, in the form of nanotubes. This is because, despite numerous investigations and proposals focusing on many biomaterials for repairing nervous systems, with a lot of reservations against carbon nanotubes, the last elementary nanocarbon form is still being investigated with growing interest. Therefore, this paper is exclusively limited to biomaterials and mainly to carbon nanotubes (CNTs) destined for the regeneration of the nervous system. Our aim is not only to demonstrate the state-of-the-art in this specific area but to propose a novel strategy for

the future research and development of CNT-based nervous implants, together with the existing hopes, justifications, and apprehensions.

3. Carbon Nanotubes

3.1. Forms and Characteristics of Elementary Bionanocarbon

Elementary carbon nanostructures are diverse. The three most popular ones used for the anticipated medical applications are single-walled carbon nanotubes (SWCNTs), multiwalled carbon nanotubes (MWCNTs), and carbon nanofibers (CNFs) [51–59]. Carbon nanotubes were created and described for the first time by Iijima in his well-known article [60]. They are intensively investigated and used for different purposes in medicine and engineering fields because of their significant mechanical, thermal, magnetic, optical, electrical, surface, and chemical properties, in particular, a very high Young's modulus and strength, increased electrical and thermal conductivity, and high chemical activity [61].

These unique properties make CNTs promising candidates for drug carriers in cancer treatment, and in regenerative medicine, bone implants, and nerve restoration [62,63]. Hopley et al. [64], in their nice review, have pointed out that the incorporation of CNTs into polymer scaffolds results in, among other things, increased scaffold strength and flexibility, improved biocompatibility, the retardation of cancer cell division, and the enhancement of angiogenesis. What seems to be the most important, tensile properties of the CNTs gives robust mechanics and dynamics, and their electrical and thermal features are plausible for neural, bone, and cardiac implants. On the other side, carbon fibers were also proposed to make organoids for studying brain-associated neurodegenerative diseases [65].

The CNTs are recommended as components of neural implants as they demonstrate outstanding biocompatibility, cell adhesion, viability, growth, and differentiation, and their high conductivity and mechanical behavior seem advantageous for neural tissue engineering [66–68]. Recently, a major focus has been aimed at MWCNTs applications for nerve regeneration [69]. In the first published paper in this field [70], embryonic rat-brain neurons were grown on MWCNTs, demonstrating that nanotubes, after their functionalization (coating with the bioactive molecule of 4-hydroxynonenal), allowed neurons to develop multiple neurites and enhanced their extensive branching. Afterward, a great amount of research confirmed the notable and subtle effects of CNTs which were attributed to starting axon growth, enhanced by electrical stimulation and contact guidance signals [25,71–86]. The CNTs placed in conductive polymers, e.g., polypyrrole (PPy) [87], polyaniline (PAn), poly (o-phenylenediamine) (PoPD), and polythiophene (PTh) [88], demonstrated remarkable electrical, magnetic, and electronic performance. Moreover, CNTs have also been considered as carriers for nano-drug delivery in chronic neurological disorders such as Alzheimer's and Parkinson's diseases [89].

Such applications become possible due to the CNTs having dimensions comparable to a single protein [90] and being chemically stable, biocompatible, having surface topography mimicking neural tissue, and allowing for the intracellular delivery of biomolecules [71]. Most crucially, neurons and neuronal cell lines can grow and differentiate on CNT substrates [70,80–82,91–95]. The fundamental purpose for such behavior is their high electrical conductivity, in particular, that of purified MWCNTs, which can enhance neuronal circuit network functioning [81,91,96,97]. Besides, functionalized MWCNTs do not alter neuronal morphology and viability [98–100].

Various carbon nanostructures, such as CNTs and CNFs, were synthesized and tested specifically for neural tissue engineering applications [68,82,101–105]. The CNTs remain the most popular form of nanocarbon in medicine, even if there are opinions that CNFs possessing similar properties are cheaper and can be more easily produced [106,107]. The chemical-vapor deposition (CVD) at an elevated temperature is a method commonly used to produce CNTs [95,104], despite some concerns related to the potentially allergic effect of nickel used in the technological process. More advanced free-standing nanostructured matrices were produced by another technology composed of conventional lithography and a layer-by-layer technique [101]. These modified SWCNT structures held up the

outgrowth of neuritis, cell-to-cell communication, and cell differentiation [8]. Patterned microfabricated substrates composed of CNT islands [108] appeared to be a perfectly organized neural network, in which the cells aggregated to the islands of the CNTs, and neuronal cells between neighboring islands grew by connecting axons. The resultant scaffold showed a cohesive structure and excellent mechanical flexibility. The graphitic structure generated by annealing rendered the carbon nanofibrous scaffold with superior electrical conductivity [35]. Fullerenes have also been considered for such a purpose [109].

Another physical form of CNTs, except for fibrous networks, is a mesh or a sponge composed of CNTs [110], able to integrate neuronal networks. For example, in a sponge-like structure, the 3D mesh was made from CNTs, creating the scaffold so as to efficiently regenerate the damaged neural tissue [111]. The carbon nanotubes guided the formation of the nerve fibers, creating a hybrid structure; without a scaffold form, nerve fibers regrew in all directions, weakly creating the bridge between the damaged sections.

CNT-based scaffolds can be obtained by different methods. Scaffolds made by electrospinning, either by the "sandwich" or dual deposition methods, were highly electrically conductive and cytocompatible and were proposed for several neural applications, such as spinal cord and peripheral nerve regeneration, and even as microfluidic models of the brain [35,112]. It is noteworthy that even if CNTs can be implanted to guide nerve regrowth, these conduits cannot help with the repair of long defects [113]. However, the opposite opinion [114] has also been presented, meaning further research seems necessary as it is a crucial point in neural system regeneration.

As previously mentioned, besides being in the nanoscale range, the most attractive feature of these materials relies on their ability to display metallic and superconducting electron transport properties. However, original CNTs do not have the necessary solubility for their direct application in Medicine. Therefore, it is obligatory to functionalize CNTs, not only to make them more soluble but to allow for their integration into many organic, inorganic, and biological systems and applications without any cytotoxic effects.

3.2. Functionalization of Carbon Nanotubes

Two of the main strategies applied to CNTs in physiological conditions include either covalent or noncovalent functionalization [115]. Besides, functionalization, such as topological patterning and electrical stimulation, can yield a significant improvement in nerve guidance conduits [97]. The functionalization of CNTs is important for the prevention of toxicity, and MWCNTs seem safer than SWCNTs [116].

Covalent surface modification can reduce the possible toxicity of CNTs. The noncovalent functionalization destroys the van der Waals bonds and prevents the aggregation of CNTs into bundles, improving water miscibility [51]. The chemical modification of CNTs changes their surface charge, improving the growth of neurons [89,117–119]. Specifically, the surface charges of MWCNTs can influence the length of neuritis, branching, and the number of growth cones, and the positively charged MWCNTs, in comparison to the negatively charged version, have a higher number of growth cones and neurite branches that promote neurite outgrowth [120–122]. A positively charged surface enhances the electrostatic interactions between the negatively charged plasma membranes of neural cells. Besides, amine groups promote the growth of neurons. In an integrated SWCNT–neuron system, electrical stimulation delivered by SWCNTs can induce neuronal signaling [94]. The growth of the neuronal circuit on a CNT substrate is accompanied by an increment in the network activity related to the electrical conductivity of nanotubes, providing a route for direct electric current transfer and distributing the charge along the surface, which results in a strengthening of the direct electrical bonding between neurons [81,123]. CNT concentration has a critical impact on neurite outgrowth and extension [79]. The incorporation of MWCNTs can result in abnormal neuronal growth and it is important when making surface modification to keep balanced cellular activity [124]. CNTs have a significant affinity for DNA and RNA, creating a complex with the polynucleotides that can be suitable for delivering genes into cells, and CNTs functionalized with PEG improve

blood circulation, reduce retention via the reticuloendothelial system, and stop the binding of proteins [125]. To achieve this goal, CNTs in scaffolds are conjugated with biologically active compounds or with differently charged molecules such as, e.g., 4-hydroxynonenal (4-HNE), a lipid peroxidation product, type IV collagen, and extracellular matrix proteins. Another approach is chemical functionalization via the covalent attachment of functional groups such as neurotrophin [71], polylysine, polyornithine, poly-m-aminobenzene sulfonic acid (PABS), and ethylenediamine [126]. The CNTs chemically functionalized with polyethyleneimine can enhance neural regeneration, in particular, neurite branching, outgrowth, and the attachment of growth cones [127]. MWCNTs can control and promote neurite outgrowth if they are bonded with neurotrophin [71]. For unmodified nanotubes, the neurons extend to only one or two neurites, and after receiving their coating with a bioactive substance, multiple neurites and extensive branching were observed [70].

3.3. Surface Films and Membranes

The search for new electrode materials is crucial for improving the long-term performance of neuroprosthetic devices. CNTs have been applied to the coating of electrode sites as CNT electrode sites and 3D CNT probes [128]. One such attempt [129], which involved electrochemically codeposited PPy/SWCNT films, saw the electrode-neural interface characterized by a substantially high charge, low electrode impedance, and reasonable stability, which resulted in cell adhesion and neurite outgrowth. In another neural application, vertically aligned CNFs were coated with PPy films to use them as electrodes [130], demonstrating the improved biocompatibility and electrical and mechanical properties of such a coating. The combination of a conductive polymer (PEDOT) and MWCNTs deposited on the electrode surface (and doped with dexamethasone) resulted in lower in vitro and in vivo impedance values, less neuronal damage, and a reduced inflammatory response [75]. In other research concerning the recording of electrodes [76], a polyimide-based neural interface electrode was coated with gold, showing extremely low impedance and a significant increase in the signal recording resolution. MWCNTs that were applied as coatings on tungsten and stainless steel wire electrodes improved both the recording and electrical stimulation of neural electrodes [131]. Finally, the glassy carbon electrodes modified with bamboo-like CNTs and dispersed into DNA, were shown to achieve highly sensitive and selective quantification of neurotransmitters [132].

The positioning of nanotubes on substrates has importance [133]. When producing horizontally aligned CNTs, the longest neurites on the CNTs tended to align with their direction, although the average neurite length was similar for both CNTs and glass surfaces. Their flexible mechanical properties depend on the length of the CNTs as well as their distance and diameter [134].

In order to avoid the mechanical failure of polymer/CNT composites, freestanding SWCNTs/polyelectrolyte membranes were prepared using a layer-by-layer technique [135]. The tensile strength of such membranes was said to be close to that of ceramics [82]. Besides, SWCNT/polymer films induced cell attachment and differentiation and controlled neurite outgrowth. Such films both maintained the electrophysiological properties of neurons and stimulated neuronal cells for repairing the injured nerves [136]. In other research [91], a similar film was shown to improve the differentiation of neural stem cells into neurons and aided neurite outgrowth.

Some other approaches and compounds were also reported. The layer-by-layer SWCNTs-poly(ethyleneimine), with the last being a polyelectrolyte, seeded with mouse embryonic neural stem cells successfully differentiated into neurons, astrocytes, and oligodendrocytes with the clear formation of neurites [91]. In other research, a poly(acrylic acid)-grafted CNT thin film, was fabricated exhibiting enhanced neuron differentiation and cell adhesion [137]. The structural polarization-controlled neuronal differentiation of human neuronal cells was developed on the CNT monolayer coating, promoting their selective growth [138]. CNTs in conductive polymers were applied to create biosensors for different (also not medical) applications [89]. Flexible 3D carbon nanotubes were proposed

as a peripheral nerve interface [139]. Carbon multielectrode arrays were the best peripheral nerve interface for neural recording and nerve stimulation [140].

3.4. Toxicity of Carbon Nanotubes

Cytotoxicity remains the limiting factor for the use of CNTs in biological systems [58]. All nanomaterials can promote cytotoxicity by mechanisms that depend on the type of nanomaterial. Despite the lower cell penetration of carbon nanomaterials, single CNTs can be detected inside cells, and they demonstrate high cytotoxic and genotoxic effects, presumably because of surface chemistry [141]. The bioactivity and cytotoxicity of CNTs are affected by their diameter, length, and functionalization in vitro and in vivo and also by the fabrication method, e.g., a metal impurity such as iron can induce undesirable effects. The genotoxic effect of CNTs via direct contact with DNA was shown to induce mutations in the DNA. The physicochemical properties could then make CNTs toxic to living organisms or the environment [142,143]. The toxicity manifests itself as membrane damage, DNA damage, the appearance of oxidative stress, and changes in the mitochondrial activity and intracellular metabolic routes. The nonbiodegradable nature of CNTs is then the strongest contradiction against their use in implants. CNTs are considered to have carcinogenicity and cause lung tumors, with the effect attenuated by decreasing tube length [144]. The available data provide initial information on the potential reproductive and developmental toxicity of CNTs. MWCNTs likely inhibit the neuronal differentiation of some cells [18]. An exposure of MWCNTs to DRG cultures disturbs regenerative axonogenesis [145,146].

Inhalation of MWCNTs significantly alters the balance between the sympathetic and parasympathetic nervous systems. Whether such transient alterations in autonomic nervous performance would alter cardiovascular function and raise the risk of cardiovascular events in people with pre-existing cardiovascular conditions warrants further study [147]. The toxicity of carbon can be expressed as cytotoxicity, pulmonary toxicity, genotoxicity, dermotoxicity, cardiovascular toxicity, genotoxicity, carcinogenic toxicity, and liver toxicity [146]. Truly, respiratory toxicity is the main concern when carbon nanomaterials are used [148–150]. Other works report nontoxic effects both in in vivo and in vitro [73,83]. MWCNTs are likely to be a more neural-friendly interface than SWCNTs since they allow for a wider external surface and effective functionalization [97].

Nanoparticles can damage and cause cell death due to their small size and large surface area by different mechanisms: creating forms of reactive oxygen species (ROS), rupturing cell membranes, and causing immune responses and chronic inflammation [64]. Four aspects of CNT toxicity have been proposed: (i) increased CNT contents, either in solution or in polymer scaffolds, create reduced cell growth and increased apoptosis, (ii) smaller CNTs show enhanced cell and protein adherence as they are more likely to interfere with cell membranes, but CNT rods that are longer than macrophages (20 μm) will not be phagocytosed and degraded, (iii) synthesis, postfabrication treatments and functionalization influence CNT purity and toxicity, and (iv) each case of cytotoxicity depend on the cell type.

The Fe impurities strapped inside the CNTs produced by CVD may be partially responsible for neurotoxicity generation as they can reduce cell viability and increase the cytoskeletal disruption of cells, diminishing the ability to form mature neurites [151]. CNTs can be manufactured by different methods (arc discharge, chemical vapor deposition, and laser ablation of graphite, among others), and they can have adverse effects due to several other heavy metal nanoparticles, like Fe, Co, Ni, and Y, being present during their synthesis [144–146].

To summarize, carbon nanomaterials may enhance toxicity for two reasons [142]. First, their small size induces permeability changes in cell membranes, enhancing cellular uptake. Second, a high surface area may evoke great chemical reactivity, leading to toxicological responses (positive or negative). But it seems certain that the proper functionalization of CNTs can prevent all forms of toxicity provided that they are not present in excessive

amounts. However, long-term in vivo studies of this grave problem should appear more often than they do currently.

Figure 1 shows the possible advantages and drawbacks of the application of CNTs in medicine. The positives seem to dominate over the negatives, and the last can be eliminated or at least minimized by proper functionalization.

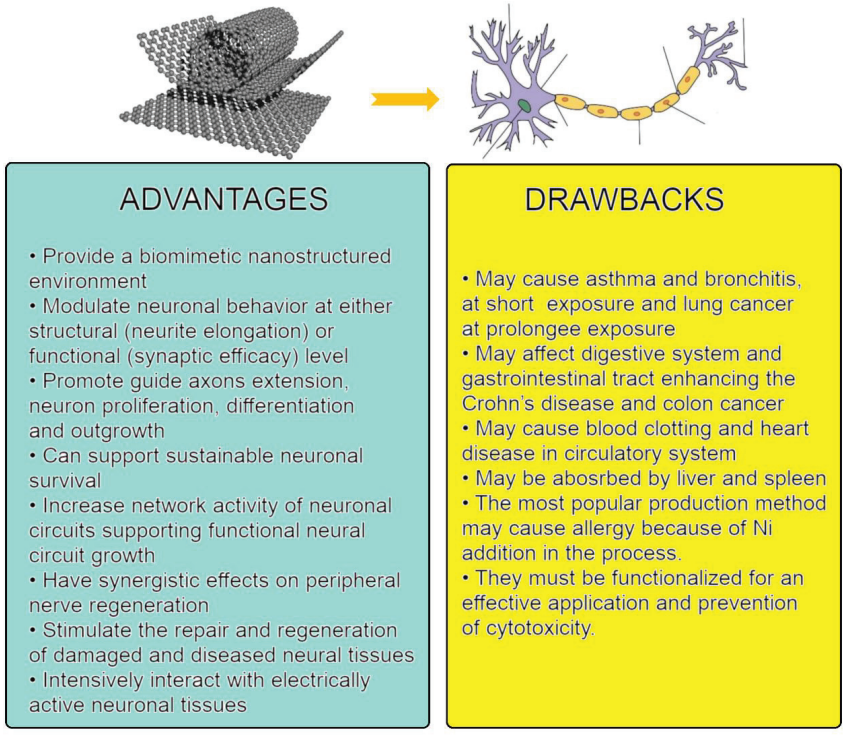

Figure 1. Scheme of anticipated interaction between carbon nanotubes and the nervous system: advantages and drawbacks. Figures on the top are from: (**left**) Michael Berger. Carbon nanotubes – what they are, how they are made, what they are used for. https://www.nanowerk.com/nanotechnology/introduction/introduction_to_nanotechnology_22.php (accessed on 28 September 2022); (**right**) Alex Bolano. Labeled Neuron Diagram. From: "Neuron" by US National Cancer Institute via WikiCommons CC BY-SA 3.0. https://sciencetrends.com/labeled-neuron-diagram/ (accessed on 28 September 2022).

4. CNT-Based Composite Materials

4.1. Nonbiodegradable Solid Nanocarbon-Based Composites

There are not many carbon-based composites that can be fully called nonporous and nonbiodegradable. As the first such example [77], an active neural implant was produced by immersing MWCNTs in silicone rubber, followed by etching the surface. Then, the rubber layer was reduced to 13 nm, which covered the CNTs. The fibroblasts and human neuroblastoma cell lines had adequate biocompatibility for the neural implant. In another approach [78], the MWCNTs were incorporated into a polydimethylsiloxane (PDMS) sheet via a printing method to promote the proliferation of the primary neuronal cells. Increased mechanical properties and roughness and superior electroconductivity were observed when compared to PDMS. The new composite material also saw increased adhesion and the proliferation of primary DRG (Dorsal Root Ganglion) cells, and SCs (human peripheral blood mononuclear single cells), referring to poly-l-lysine (PLL), were usually applied to increase cellular attach-

ment. The polymer networks based on polyurethane (PU)/crosslinked polyacrylic acid (PAA) and MWCNTs were also prepared [152]. Considering swelling, mechanical strength, tensile strength, and electrical conductivity, the most plausible content for the CNTs was 1–3 wt. pct. Additionally, the PU/PAA/MWCNT nanocomposites were considered a properly biocompatible material for artificial tendons. Finally, another approach saw the production of a graphene—MWCNTs hybrid material [62]. The hybrid material was not toxic to hESCs (human embryonic stem cells) and could be used for promoting and stimulating the adhesion, proliferation, and differentiation of SCs for neural tissue regenerative treatment. In another study [153], a conductive and nontoxic implant composed of agarose and carbon nanotube fibers allowed for orderly nerve growth, increased differentiation, and the proliferation of neural cells.

4.2. Nonbiodegradable Carbon-Based Scaffolds

Such materials are more common than solid neural implants. The reason for this is that scaffolds may make it possible to grow neural cells without any loss of electrical or mechanical properties.

Among the most applied polymers is polycaprolactone (PCL). The scaffolds composed of the MWCNTs and collagen/polycaprolactone (PCL) nanofibers were produced by electrospinning [83]. The composites supported SC adhesion and elongation in vitro. In the in vivo studies, MWCNT-enhanced collagen/PCL conduits were shown to effectively promote the nerve regeneration of sciatic nerve defects and prevent muscle atrophy without body rejection or grave inflammation. Another study [154] focused on aligned PCL/PGS (polyglycerol sebacate) fibers containing different amounts of MWCNTs, fabricated via electrospinning. The Young's modulus, ultimate tensile strength, wettability, and water uptake values increased for the observed scaffolds with rising MWCNTs content. A quite similar approach [105] demonstrated a fibrous composite based on PCL, and either CFs or SWCNTs. The PCL/SWCNTs nanocomposite was especially satisfactory in creating a suitable environment for endothelial cells. Additionally, in [137], PCL/graphene and PCL/CNTs were tested as conductive nerve guidance conduits in sciatic nerve repair. The PCL/graphene/CNTs composite exhibited a higher number of axons and nerve areas when compared to PCL scaffolds and either graphene or CNTs. Furthermore, the addition of graphene to the PCL/CNT composite facilitated the CNT dispersion within the PCL, and enhanced nerve regeneration. Two-dimensional thin film scaffolds composed of biocompatible polymer-grafted carbon nanotubes (CNTs) can selectively differentiate human embryonic stem cells into neuron cells while maintaining excellent cell viability.

Another highly interesting conducting polymer is the polyurethane (PU) used in [155], together with polypyrrole (PPy) for the formation of a self-electrical stimulated double-layered nerve guidance conduit (NGC), assembled from electrospun mats with an aligned oriented inward layer covered with a random oriented outer layer. The biomimetic NGC was achieved from chitosan-grafted PU with well-dispersed functionalized MWCNT nanofibrous mats after a uniform coating of PPy. The structural framework of the NGC exhibited a cellular biomaterial interface improving the electrical conductivity, mechanical strength, and cytocompatibility, in particular, the regrowth, proliferation, and migration of Schwann cells. Nanostructured fibrous scaffolds based on flexible thermoplastic PU and surface-functionalized MWCNTs were also produced by electrospinning [156]. A linear correlation between electrical conductivity and cell signaling, and neural gene expression was found, and an increase in both bulk and surface modulus was due to the presence of MWCNTs in the scaffolds. In similar research [157], fibrous scaffold PU-silk fibroin-functionalized MWCNTs showed the important electrical conductivity and absorption of extracellular matrices (ECM), and in the aligned scaffolds, the substantial growth and proliferation of SCs.

Chitosan is a natural polymer frequently considered for medical applications, even if its properties strongly depend on its deacetylation degree and are hardly

repeatable. Such composite scaffolds [85] were created by aligning MWCNTs in a chitosan scaffold fabricated by an electric-field-alignment technique. Not only were the mechanical properties greatly improved, with the incorporation of only 0.5 wt. pct. of the aligned MWCNTs, but also electrical conductivity increased 100,000 times along its direction. In [158], an MWCNT/chitosan scaffold (highest conductivity) and GNP (graphene platelets)/chitosan scaffold (lowest conductivity) were obtained. The hybrid scaffolds showed increased elastic modulus and ultimate tensile strength over the MWCNT/chitosan and GNP/chitosan scaffolds. Considering the potential cell adhesion, the MWCNT/chitosan composites were more effective than GNP/chitosan and both revealed cytocompatibility.

4.3. Biodegradable Solid Nanocarbon-Based Composites

Guidance conduits (to nerve cells) prepared as composites of MWCNTs and poly(2-hydroxyethyl methacrylate) (pHEMA) composites showed effective adhesion, activity, and viability to biological cells [159]. In another work, a composite of silk, fibronectin, and SWCNTs resulted in ideal bioactivity and a subsequent nerve guidance conduit [160]. Three-dimensional collagen–fibrin–MWCNT composite materials were also developed [161]. Investigating the PCL/nanocarbon/graphene composite, a two-fold increase in the number of myelinated axons was found for this prosthesis of the sciatic nerve together with muscle atrophy [162].

4.4. Biodegradable Nanocarbon-Based Scaffolds

Some totally or partially biodegradable porous or fibrous structures were used to construct an implant for the nervous system. They include some polyesters, mainly poly(glycolic acid (PGA), PLA, poly(lactic acid–glycolic acid) (PLGA), and only some polyurethanes. Additional nondegradable materials include natural fibrin, collagen, keratin, alginate, chitin and chitosan, and silk fibroin, as well as extracellular matrices [2]. The idea of these technical solutions is to combine two substances: the first, which forms a skeleton, and the second, which may degrade to allow the nerves to grow. Surprisingly, in this specific review, no nanocarbon forms have been mentioned, even if a lot of these composites have already been developed [54].

PLA and PLLA are likely the most often used biodegradable polymers. For the conductive conduit prosthesis (nine weeks after implantation), the tissue-engineered construct made of a rolled sheet of SWCNT/PLLA nanofibrous scaffolds, with some implemented cells, promoted the axonal outgrowth and regeneration of peripheral nerves [163]. A similar nanocomposite scaffold [74] was obtained by dispersing the MWCNTs in a PLA matrix to provide electrical signals and mimic neural topography. A more complex scaffold [164] for a neural guidance conduit was prepared from PLLA and modified MWCNTs and was filled with SCs and nanocurcumin-encapsulated chitosan nanoparticles. Controlled curcumin release decreased SC apoptosis, enhancing the regeneration of injured peripheral nerves. A significant increase in the number of axons in the damaged sciatic nerve and a compelling fall in the number of vessels in the fibrin groups were detected by histological testing. The fabrication of nerve guidance channels was also created using PLA/MWCNTs/gelatin nanofibrils coated with recombinant human erythropoietin-loaded chitosan nanoparticles [165]. In the work carried out by the authors of [84], laminated CNTs were chemically linked onto the surface of aligned phosphate glass microfibers (PGFs). The CNT-interfaced PGFs (CNT–PGFs) were successfully placed into 3D poly(L/D-lactic acid) (PLDLA) porous tubes by wrapping the CNTs-PGFs onto a PLDLA nanofiber mesh embedding them into a porous PLDLA tube afterward.

4.5. Carbon Nanotubes on Solid Substrates

CNT networks deposited on solid substrates were also used for the directed growth and differentiation of hMSCs, which could recognize the arrangement of individual CNTs in the network and grow in the direction of the CNT alignment [166]. In other research [28], a CNT rope substrate was developed and seeded with neural stem cells. After electrical stimulation, neurite elongation and increased differentiation of NSCs into neuronal cells appeared.

4.6. Hydrogels

The chitin/CNT composite hydrogels [73] demonstrated enhanced tensile strength and elongation and decreased swelling when compared to chitin only. They also exhibited good hemocompatibility, biodegradation in vitro, biocompatibility, and no cytotoxic effect. Besides, the promotion of adhesion in those implants enriched with calcium ions in the form of tubular hydrogels was obtained [72]. Other technical solutions [167] constituting methacrylated gelatin (GelMA) hydrogel and super-aligned carbon nanotube sheets (SACNTs) were used to form a material that showed good biocompatibility (GelMA) and conductivity for CNTs. In another work [79], SWCNTs were applied to control the electrical properties of a collagen-based composite hydrogel. Another hydrogel was produced via a multistage complex technique and was composed of reduced graphene oxide (rGO), CNTs, oligo(poly(ethylene glycol) fumarate) (OPF), and 2-(methacryloyloxy)ethyltrimethylammonium chloride (MTAC) [63]. In [168], a biomimetic core-shell scaffold based on aligned conductive nanofiber yarns (NFYs) within a hydrogel was developed. The aligned NFYs were composed of PCL, silk fibroin (SF), and CNTs. Such a 3D hierarchically aligned core-shell scaffold mimics the nerve fiber structure and positively affects the alignment and extension of neurites, with the hydrogel shell protecting nerve cell organization within a 3D environment/In the other research,, a highly stable and uniform dispersion of multiwall carbon nanotubes in an aqueous solution was applied to prepare [169] CNT/sericin hydrogel, in [170] multiwall carbon nanotube/gelatin–polyvinyl alcohol nanocomposites, with varying MWCNT content using solution casting, and in [171] gelatin-chitosan hydrogel. The desired effect of the addition of the MWCNTs on the mechanical, thermal, and swelling properties of the gelatin-chitosan composites was achieved. The covalent functionalization of MWCNTs facilitated the interfacial interaction between the natural polymer blend and the nanotubes, which further enhanced the dispersion within the matrix and, thus, ultimately enhanced the mechanical properties of the blends. The surface and interface structures of the composites were studied by SEM, and the intimate relationship between the structure and the overall performance of the composite was revealed. The thermal, swelling, and drug-releasing properties were also found to be superior compared with the gelatin-chitosan blend due to the addition of nanotubes. Besides the effectiveness of the drug release rate, the prepared MWCNTs/gelatin-chitosan nanocomposites have not shown any cytotoxicity, and it is believed that such nanocomposites can be employed as targeted drug delivery agents in nanomedicine, targeted thermal tumor ablation, and the magnetic field-targeting of tumors. The directional growth of hMSCs follows, as a rule, the alignment direction of the individual CNTs.

The different materials applied for the regeneration of the nervous system are shown in Figure 2, and their different physical forms are listed in Figure 3.

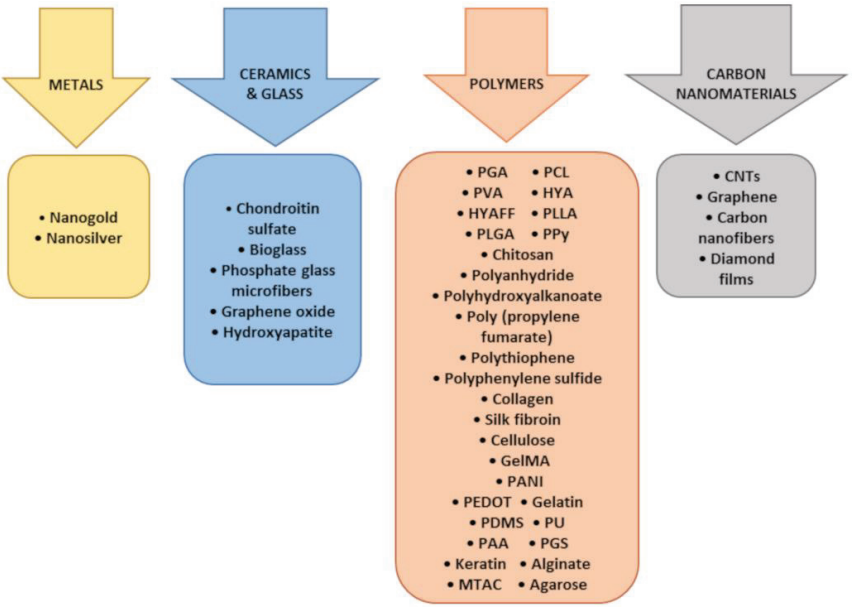

Figure 2. Materials used for applications in the regeneration of the nervous system.

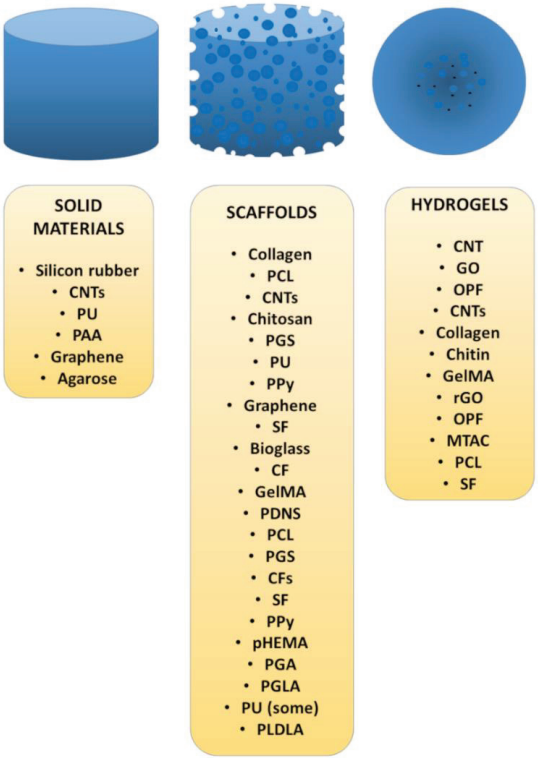

Figure 3. Different physical forms and chemical compositions of biomaterials for the regeneration of the nervous system.

5. Anticipated Research Strategy for Nervous Conduit Implants

For a start, let us consider what qualitative/quantitative indices should be the most plausible for the specific application of an artificial nervous conduit.

It should have sufficient conductivity, at least 3 S/cm. This condition needs the application of either carbon nanostructures or conductive polymers or some metallic structures. We propose to use the following materials: (i) MWCNTs functionalized with a chosen organic compound and carbon nanofibrils and/or graphene, (ii) polypyrrole (PPy) and/or poly(3,4-ethylenedioxythiophene), and poly(styrenesulfonate) (PEDOT: PSS); among the conducting polymers; (iii) gold, platinum, silver, and/or copper wires, as noble or seminoble metals. So far, another applied solution is the use of biodegradable scaffolds without any conductive components, besides the use of CNTs, whose electrical properties increase after biodegradation, followed by gradual angiogenesis and the growth of neural axons. A similar effect can be expected from stable scaffolds. The question remains whether each patient's body, possessing mechanical failures in the nervous system, will be capable of developing a novel nervous network in a reasonable time and whether a gradual decrease in scaffold mechanical strength will positively affect the delicate implant construction, which might destroy the body. We think that the conductive nervous implant based on permanent polymeric scaffolds is the best solution, at least for aged patients, or, better, for those whose regeneration systems can be insufficient to create the electrical circuits by the growth of new conduits. Therefore, the highly conductive implant seems a good alternative compared to biodegradable scaffolds or stable solid implants.

The implant should demonstrate no cytotoxicity. For all the above-mentioned conductors, and in particular, for CNTs, such fairs (justified or not as the experiments have given different results, and the results obtained in vivo on animals can be the same for human beings, also depending on individual patient's features) appear. Carbon nanotubes are often declared potentially carcinogenic. However, cancer cells appear in living bodies for different reasons and grow abnormally fast only in some conditions. The use of small quantities of CNTs, especially less toxic functionalized MWCNTs, seems reasonable. However, concerning the remaining CNTs, as important mechanical constructs, the electrical conductance can be, according to our strategy, enhanced by carbon nanofibers.

The application of some polymers is reasonable, but it seems reasonable to select only conducting polymers that have already proved their importance in forming scaffolds by electrodeposition or patterning, or even 3D printing, as being the most likely. We are going to look for other conducting polymers which fulfill four conditions: (i) are good conductors, (ii) can form scaffolds, (iii) are nonbiodegradable, and (iv) are nontoxic.

Finally, noble and seminoble metals can be supposedly safely used inside a living body to increase the conductivity of a nervous implant. It is true that all metals, which means over 90% of all elements, present in an elementary form (and not either in inorganic (bone tissue) or organic (blood with chelated iron) compounds) have upper limits, above which they might become toxic. However, in the expected applications, the corrosion dissolution is very low, even after many years. Besides, the proposed amounts of metals are also limited.

Passing over to the recapitulation and conclusions, it seems necessary or at least plausible to show all important quantitative indices from the references here emphasized. Table 1 illustrates this and the considered properties. It can be well-observed that there are still many specific points that have not been characterized yet. On the other hand, some data look discrepant, which can be certainly attributed to substrates and their characteristics, process parameters, applied methods, and several other factors.

Table 1. Mechanical and electrical properties of CNT-implemented coatings and scaffolds.

Components	Morphology	Ultimate Tensile Stress or Compression Strength ** Elastic Modulus at Tension * or Compression ** [MPa]	Electrical Conductivity S/m × 10^{-3}	Reference
Carbon rope with MWCNTs	Elevated and lowered ridgelike structures propagating through the surface of the CNT rope in a spiral direction; the bundles of CNTs of diameters of about 20 nm.	-	-	[28]
GO and PANI nanocomposite coatings on titanium	The presence of two phases derived from GO and PANI stacked on top of each other to form a laminate			[50]
CNT-GO-OPF hydrogel	Four types of hydrogel: neutral transparent, positively charged transparent; opaque with dark color from carbon; positively charged opaque (conductive)	0.56–58 0.60–0.80 **	0.31–5.75	[63]
Chitosan-CNT-HAp hydrogel	Semi-transparent, network morphology	0.50–0.57 * 0.72–0.78 *	-	[72]
CNT-polymer scaffold	Uniform coatings with nanofibrous morphology	-	-	[74]
SWCNT-collagen hydrogel	-	- No effect on bulk modulus		[79]
Collagen/PCL/MWCNTs scaffold	Fibrous meshes and porous conduits	4.5 * -	-	[83]
CNT-bioglass scaffold	Functional arrangement: the microfibers packed inside, the thin wrapping sheet, and the slightly thicker outermost layer	-	-	[84]
CNT-chitosan scaffold	Uniform black films, macroscale uniformity of aligned CNTs	50–75 * 1600–1650 *	0.84–5.25	[85]
PCL/PGS/MWCNT scaffold	Bead-free and uniform aligned fibers	0.7–1.1 * 0.29–0.41 *	-	[154]
MWCNT/PU/PPy/chitosan mat	Random and aligned fibrous mats	14 * -	-	[155]
PU-CNT scaffold	MWCNT particles oriented along the fibers' axis	13.17–20.57 * 3.94–10.01 *	9–31.5	[156]
PU-SF-MWCNT scaffold	MWCNT particles dispersed along the fibers' axis	16 * -	-	[157]
MWCNT-graphene-chitosan scaffold	Tubular morphology for MWCNTs, and GNPs appearing as wrinkled nanoplatelets in the chitosan matrix	80–90 * 2700–3200 *	0.005–0.019	[158]
MWCNT-pHEMA membrane	The MWCNTs were randomly distributed on the hydrogel surface; some of the nanotubes formed clumps and some were dispersed	1.25–2.0 * 0.32–0.41 *	-	[159]
SF/MWCNT/FN tubular nerve guide conduit	Aligned fibronectin containing nanofibers on freeze-dried silk fibroin/SWCNT substrates	-	2.1	[160]
CNT-GelMa scaffold	The ordered and parallel arrangement of the super-aligned carbon nanotubes with a diameter of 30–50 nm	-	-	[167]
CNT/sericin hydrogel	Interconnected porous microstructure	0.04–0.07 * 0.034–0.76 *	0.03–0.39	[169]
CNTs-Gelatin-PVA	MWCNTs are homogeneously distributed into the nanocomposites matrices and the increase in CNT loading progressively blackened the blend nanocomposites.	90 * 641 *	0.0085	[170]
CNT-PDMS (poly(dimethylsiloxane)	-	4.3 * 3.6 *		[172]
Hyaluronan/CNT hydrogel	Porous structure with a mean pore size decreasing in the presence of MWCNTs	0.017–0.067 ** in the low compression zone and 0.45–0.60 in ** the high compression zone	Conductivity is slightly lower than of hyaluronan alone	[173]

Table 1 illustrates that mechanical properties are sometimes highly different. The reason is that these material solutions appear as either scaffolds, coatings, membranes, or mats and ropes. Among the coatings, the mechanical properties are similar. For scaffolds, the differences are sometimes great, in particular, the Young's modulus is particularly high (i.e., the material is not deformed even at high loads) for the CNT-chitosan and MWCNT-graphene-chitosan scaffolds.

Table 2 shows the results of some of the biochemical tests. There are several differences and similarities between the tests.

Table 2. Biological properties of CNT-implemented coatings and scaffolds.

Components	WST-1 Test [%]	LDH Test [%]	MTT Test [%]	Live/Dead Assay [%]	Reference
Carbon rope with MWCNTs	103–105	About 100		> 90	[28]
GO and PANI nanocomposite coatings on titanium		The cytotoxic effect after 24 h observed for GO:PANI (1:1) weight ratio			[50]
CNT-GO-OPF hydrogel	100			80–102	[63]
Chitosan-CNT-HAp coating			97 to 112		[72]
Chitin/CNT hydrogel			100–115		[73]
CNT-polymer scaffold		About 100			[74]
CNT-bioglass scaffold	105–110				[84]
CNT-chitosan scaffold			85–145		[85]
MWCNT-PAA scaffold	About 100				[137]
PCL/PGS/MWCNT scaffold			120–220		[154]
MWCNT/PU/PPy/chitosan				140–220	[155]
PU-CNT scaffold			170–200		[156]
MWCNT-graphene-chitosan scaffold			65–140		[158]
MWCNT-pHEMA membrane			14–124		[159]
SF/MWCNT/FN tubular nerve guide conduit			105–110		[160]
CNT-GelMa scaffold	95–120			About 100	[167]
CNT/sericin hydrogel				About 100%	[169]
CNT-PDMS (poly(dimethylsiloxane)			No significant decrease in viability		[172]
Hyaluronan/CNT hydrogel			No significant effect		[173]

The WST-1 assay comprises the reduction of the tetrazolium salt WST-1 to formazan. It is applied for the measurement of cell mitochondria functionality. The CCK8 test is similar with some small modifications.

The LDH assay measures the value of the enzyme lactate dehydrogenase (LDH), which is released upon cell lysis. It is an index of necrosis.

The MTT assay assesses cell metabolic activity. Some cellular oxidoreductase enzymes reflect the number of viable cells and can reduce the tetrazolium dye MTT to insoluble formazan of a purple color. The assay is also similar to the WST and CCK tests, differing in some chemicals and procedures.

The Live/Dead assay is a cell staining procedure. Live cells are stained with calcein and demonstrate green fluorescence upon the excitation evolved by their cytoplasm. The dead cells are labeled with the ethidium homodimer dye (EthD) bond to their DNA and express the red fluorescence.

As can be seen, in almost every test, the viability of the tested cells has not demonstrated cytotoxic effects. However, the effects of different materials on adhesion, migration, and proliferation of cells have often been positive, yet they are shown here as being hardly comparable to each other.

Summarizing our considerations, the most fruitful and safe material strategy can or should (from our research planning) include MWCNTs and carbon nanofibers, with some

conductive polymers (at least one among those proposed so far and recommended for medical biodevices) and one of the four corrosion-resistant metals here mentioned. The future strategy will focus on the optimal composition of this conduction part of an implant, taking as criteria the conductivity, cytotoxicity, and mutual adhesion.

The shown research strategy defines, to some extent, the discrimination criteria and materials to be investigated. The main criteria in vitro for an assessment of the tested solutions are the following: (i) electrical conductivity, (ii) mechanical properties in long-term tests, (iii) cytotoxicity, and (iv) biocompatibility defined as in vitro wettability. In addition, we plan biological tests in vitro to monitor the growth of neural cells and the number of axons. Besides, for mechanical strength, only carbon nanotubes, carbon nanofibers, and possible graphene among the discussed nanocarbon-based conductive materials can likely be purposeful. On the other hand, all elementary carbon forms have poor adhesion to the rest of the composite, and cracks can be initiated at their interface. Therefore, CNTs are usually (and must be) surface-modified to enhance their adhesion and prevent cytotoxicity. Besides that, we plan to strengthen the composite materials by the addition of some ceramics, in particular, a nano form of reduced graphene oxide (rGO), other nano oxides, or nanohydroxyapatite.

The composite material for nervous conduits should demonstrate antibacterial properties. Such an effect can be obtained by implementing metals, but this hypothesis will be verified.

Finally, each strategy should focus not only on the optimization of material properties but also take into account the material and manufacturing costs. Therefore, each research piece and proposal for new materials will also calculate such costs.

6. Future Perspectives

Based on the presented literature review, it can be concluded that carbon nanotubes are a promising material candidate for applications in the regeneration of nerve tissues due to their unique electrical, thermal, and mechanical properties. They are chemically stable and biocompatible, and their topography mimics nervous tissue, which makes them an ideal substrate for neurons and neuronal cell lines. To avoid toxic effects and to better join the CNTs and polymeric scaffold, the MWCNTs subjected to obligatory chemical functionalization should be applied as the first component. Moreover, functionalized CNTs will change neither the morphology nor viability of neurons. The functionalization of CNTs is also important as it affects their surface charge, improving the growth of neurons. Making CNTs positively charged will promote neurite outgrowth and strengthen the direct bonds between neurons.

The anticipated optimized artificial neural conduit should include MWCNTs and carbon nanofibrils to elevate the electric conductance and strengthen the scaffold; one or two have already been recommended for medical biodevices and are not prone to degradation, with noble or seminoble metals used to increase the electric signals. The nerve conduit would be best produced by rolling polymer(s) film with nanocarbon forms and metallic wires set into the strong mechanical tube. The future strategy will focus on the optimal composition of this conduction part of an implant, taking as criteria the conductivity, cytotoxicity, and mutual adhesion, with focus on the development of the fabrication procedure of these small implants.

Various forms of CNTs, such as sponges, 3D meshes, and CNTs islands, might also be considered for making scaffolds for nerve substitutes. Additionally, CNTs are implanted to direct nerve regrowth. The SWCNT/polymer films have also been shown to improve the differentiation of neural stem cells into neurons and aid neurite outgrowth.

The main criteria for the optimization of the tested material solution should include electrical conductivity, mechanical properties (in long-term tests), cytotoxicity, and biocompatibility defined by wettability. Special biological tests should monitor the growth of neural cells in vitro and the number of axons. The other components of the scaffold, such as graphene oxide, an increase in mechanical strength, and the growth factors should also

be considered. These in vivo studies are necessary to accurately verify the achievement of a substantial improvement in nervous conductivity.

Each strategy should also take into account the material and manufacturing costs, which are usually the ignored aspects of research work.

Author Contributions: Both authors equally contributed to this paper. In particular: Conceptualization, A.Z. and B.M.-M.; methodology, A.Z. and B.M.-M.; resources, A.Z. and B.M.-M.; writing—original draft preparation, A.Z. and B.M.-M.; writing—review and editing, A.Z. and B.M.-M. All authors have read and agreed to the published version of the manuscript.

Funding: This research received no external funding.

Institutional Review Board Statement: Not applicable.

Informed Consent Statement: Not applicable.

Data Availability Statement: Not applicable.

Conflicts of Interest: The authors declare no conflict of interest.

Abbreviations

CNS—central nervous system; CNF(s)—carbon nanofibers; CNT(s): carbon nanotubes; FN: fibronectine; GelMA: Gelatin-methacryloyl; GO: graphene oxide; HA—hyaluronic acid; HAp: hydroxyapatite; hMCS—human mesenchymal stem cells; HYAFF—benzyl ester of hyaluronic acid; MWCNT)(s)—multiwall carbon nanotubes; NGC—nerve guidance channels; OPF—oligo(poly(ethylene glycol) fumarate); PAA—polyacrilic acid; PCL—polycaprolactone; PANI—polyaniline; PCL—polycaprolactone; PEDOT—poly(3,4-ethylene dioxythiophene); PGA—polyglycolic acid; PGS—poly glecerol sebacate; pHEMA—poly(2-hydroxyethyl methacrylate; PCL—polycaprolactone; PLGA—poly(lactic-co-glycolic) acid; PLA—polylactic acid; PLLA—polylactide of lactic acid; PNS—peripheral nervous system; PPy—polypyrrole; PU—polyurethane; PVA—polyvinyl alcohol; PU—polyurethane; PPy—polypyrrrole; pHEMA—poly(2-hydroxyethyl methacrylate; OPF—oligo(poly(ethylene glycol) fumarate); SF—silk fibroin; SWCNT—single-wall carbon nanotubes.

References

1. Gaudin, R.; Knipfer, C.; Henningsen, A.; Smeets, R.; Heiland, M.; Hadlock, T. Approaches to peripheral nerve repair: Generations of biomaterial conduits yielding to replacing autologous nerve grafts in craniomaxillofacial surgery. *BioMed Res. Int.* **2016**, *2016*. [CrossRef] [PubMed]
2. Gu, X. Biodegradable Materials and the Tissue Engineering of Nerves. *Engineering* **2021**, *7*, 1700–1703. [CrossRef]
3. López-Cebral, R.; Silva-Correia, J.; Reis, R.L.; Silva, T.H.; Oliveira, J.M. Peripheral Nerve Injury: Current Challenges, Conventional Treatment Approaches, and New Trends in Biomaterials-Based Regenerative Strategies. *ACS Biomater. Sci. Eng.* **2017**, *3*, 3098–3122. [CrossRef] [PubMed]
4. Rosso, G.; Liashkovich, I.; Gess, B.; Young, P.; Kun, A.; Shahin, V. Unravelling crucial biomechanical resilience of myelinated peripheral nerve fibres provided by the Schwann cell basal lamina and PMP22. *Sci. Rep.* **2014**, *4*, 4–11. [CrossRef] [PubMed]
5. Zhang, N.; Yan, H.; Wen, X. Tissue-engineering approaches for axonal guidance. *Brain Res. Rev.* **2005**, *49*, 48–64. [CrossRef] [PubMed]
6. Evans, G.R.D. Peripheral nerve injury: A review and approach to tissue engineered constructs. *Anat. Rec.* **2001**, *263*, 396–404. [CrossRef]
7. Wan, Q.Q.; Qin, W.P.; Shen, M.J.; Ma, Y.X.; Li, B.; Liu, S.Y.; Tay, F.R.; Jiao, K.; Niu, L. Simultaneous Regeneration of Bone and Nerves Through Materials and Architectural Design: Are We There Yet? *Adv. Funct. Mater.* **2020**, *30*, 2003542. [CrossRef]
8. Huang, Y.C.; Huang, Y.Y. Biomaterials and strategies for nerve regeneration. *Artif. Organs* **2006**, *30*, 514–522. [CrossRef]
9. Amani, H.; Kazerooni, H.; Hassanpoor, H.; Akbarzadeh, A.; Pazoki-Toroudi, H. Tailoring synthetic polymeric biomaterials towards nerve tissue engineering: A review. *Artif. Cells Nanomed. Biotechn.* **2019**, *47*, 3524–3539. [CrossRef]
10. Gautam, S.; Bhatnagar, D.; Bansal, D.; Batra, H.; Goyal, N. Recent advancements in nanomaterials for biomedical implants. *Biomed. Eng. Adv.* **2022**, *3*, 100029. [CrossRef]
11. Sensharma, P.; Madhumathi, G.; Jayant, R.D.; Jaiswal, A.K. Biomaterials and cells for neural tissue engineering: Current choices. *Mater. Sci. Eng. C* **2017**, *77*, 1302–1315. [CrossRef] [PubMed]
12. Dubey, N.; Kushwaha, C.S.; Shukla, S.L. A review on electrically conducting polymer bionanocomposites for biomedical and other applications. *Int. J. Polym. Mater. Polym. Biomater.* **2020**, *69*, 709–727. [CrossRef]

13. Ai, J.; Kiasat-Dolatabadi, A.; Ebrahimi-Barough, S.; Ai, A.; Lotfibakhshaiesh, N.; Norouzi-Javidan, A.; Saberi, H.; Arjmand, B.; Aghayan, H.R. Polymeric Scaffolds in Neural Tissue Engineering: A Review. *Arch. Neurosci.* **2013**, *1*, 15–20. [CrossRef]
14. Chen, G.Q.; Zhang, J. Microbial polyhydroxyalkanoates as medical implant biomaterials. *Artif. Cells Nanomed. Biotechnol.* **2018**, *46*, 1–18. [CrossRef] [PubMed]
15. Pires, F.; Ferreira, Q.; Rodrigues, C.A.V.; Morgado, J.; Ferreira, F.C. Neural stem cell differentiation by electrical stimulation using a cross-linked PEDOT substrate: Expanding the use of biocompatible conjugated conductive polymers for neural tissue engineering. *Biochim. Biophys. Acta—Gen. Subj.* **2015**, *1850*, 1158–1168. [CrossRef] [PubMed]
16. Pietrucha, K. Physicochemical properties of 3D collagen-CS scaffolds for potential use in neural tissue engineering. *Int. J. Biol. Macromol.* **2015**, *80*, 732–739. [CrossRef] [PubMed]
17. Jabbari, F.; Babaeipour, V.; Bakhtiari, S. Bacterial cellulose-based composites for nerve tissue engineering. *Int. J. Biol. Macromol.* **2022**, *217*, 120–130. [CrossRef]
18. Carvalho, C.R.; Silva-Correia, J.; Oliveira, J.M.; Reis, R.L. Nanotechnology in peripheral nerve repair and reconstruction. *Adv. Drug Deliv. Rev.* **2019**, *148*, 308–343. [CrossRef]
19. Palispis, W.A.; Gupta, R. Surgical repair in humans after traumatic nerve injury provides limited functional neural regeneration in adults. *Exp. Neurol.* **2017**, *290*, 106–114. [CrossRef]
20. Zarrintaj, P.; Zangene, E.; Manouchehri, S.; Amirabad, L.M.; Baheiraei, N.; Hadjighasem, M.R.; Farokhi, M.; Ganjali, M.R.; Walker, B.W.; Saeb, M.R.; et al. Conductive biomaterials as nerve conduits: Recent advances and future challenges. *Appl. Mater. Today* **2020**, *20*, 100784. [CrossRef]
21. Stocco, E.; Barbon, S.; Lora, L.; Grandi, F.; Sartore, L.; Tiengo, C.; Petrelli, L.; Dalzoppo, D.; Parnigotto, P.P.; MacChi, V.; et al. Partially oxidized polyvinyl alcohol conduitfor peripheral nerve regeneration. *Sci. Rep.* **2018**, *8*, 604. [CrossRef] [PubMed]
22. Bakhshandeh, B.; Zarrintaj, P.; Oftadeh, M.O.; Keramati, F.; Fouladiha, H.; Sohrabi-jahromi, S.; Ziraksaz, Z. Tissue engineering; strategies, tissues, and biomaterials. *Biotechnol. Genet. Eng. Rev.* **2017**, *33*, 144–172. [CrossRef]
23. Zarrintaj, P.; Manouchehri, S.; Ahmadi, Z.; Saeb, M.R.; Urbanska, A.M.; Kaplan, D.L.; Mozafari, M. Agarose-based biomaterials for tissue engineering. *Carbohydr. Polym.* **2018**, *187*, 66–84. [CrossRef] [PubMed]
24. Zarrintaj, P.; Ahmadi, Z.; Reza Saeb, M.; Mozafari, M. Poloxamer-based stimuli-responsive biomaterials. *Mater. Today Proc.* **2018**, *5*, 15516–15523. [CrossRef]
25. Zarrintaj, P.; Bakhshandeh, B.; Rezaeian, I.; Heshmatian, B.; Ganjali, M.R. A Novel Electroactive Agarose-Aniline Pentamer Platform as a Potential Candidate for Neural Tissue Engineering. *Sci. Rep.* **2017**, *7*, 1–13. [CrossRef] [PubMed]
26. Zarrintaj, P.; Urbanska, A.M.; Gholizadeh, S.S.; Goodarzi, V.; Saeb, M.R.; Mozafari, M. A facile route to the synthesis of anilinic electroactive colloidal hydrogels for neural tissue engineering applications. *J. Colloid Interface Sci.* **2018**, *516*, 57–66. [CrossRef] [PubMed]
27. Wong, J.Y.; Langert, R.; Ingberi, D.E. Electrically conducting polymers can noninvasively control the shape and growth of mammalian cells (polypyrrole/flbronectin/DNA snhe/tisue W/culture substra). *Appl. Biol. Sci.* **1994**, *91*, 3201–3204.
28. Huang, Y.J.; Wu, H.C.; Tai, N.H.; Wang, T.W. Carbon nanotube rope with electrical stimulation promotes the differentiation and maturity of neural stem cells. *Small* **2012**, *8*, 2869–2877. [CrossRef]
29. Guo, B.; Glavas, L.; Albertsson, A.C. Biodegradable and electrically conducting polymers for biomedical applications. *Prog. Polym. Sci.* **2013**, *38*, 1263–1286. [CrossRef]
30. Zarrintaj, P.; Ahmadi, Z.; Vahabi, H.; Ducos, F.; Reza Saeb, M.; Mozafari, M. Polyaniline in retrospect and prospect. *Mater. Today Proc.* **2018**, *5*, 15852–15860. [CrossRef]
31. Kaur, G.; Adhikari, R.; Cass, P.; Bown, M.; Gunatillake, P. Electrically conductive polymers and composites for biomedical applications. *RSC Adv.* **2015**, *5*, 37553–37567. [CrossRef]
32. Cunha, C.; Panseri, S.; Antonini, S. Emerging nanotechnology approaches in tissue engineering for peripheral nerve regeneration. *Nanomed. Nanotechnol. Biol. Med.* **2011**, *7*, 50–59. [CrossRef] [PubMed]
33. Jin, G.; Li, K. The electrically conductive scaffold as the skeleton of stem cell niche in regenerative medicine. *Mater. Sci. Eng. C* **2015**, *45*, 671–681. [CrossRef] [PubMed]
34. Xu, H.; Holzwarth, J.M.; Yan, Y.; Xu, P.; Zheng, H.; Yin, Y.; Li, S.; Ma, P.X. Conductive PPY/PDLLA conduit for peripheral nerve regeneration. *Biomaterials* **2014**, *35*, 225–235. [CrossRef]
35. Zhu, W.; Ye, T.; Lee, S.J.; Cui, H.; Miao, S.; Zhou, X.; Shuai, D.; Zhang, L.G. Enhanced neural stem cell functions in conductive annealed carbon nanofibrous scaffolds with electrical stimulation. *Nanomed. Nanotechn. Biol. Med.* **2018**, *14*, 2485–2494. [CrossRef]
36. Park, S.C.; Oh, S.H.; Seo, T.B.; Namgung, U.; Kim, J.M.; Lee, J.H. Ultrasound-stimulated peripheral nerve regeneration within asymmetrically porous PLGA/Pluronic F127 nerve guide conduit. *J. Biomed. Mater. Res.—Part B Appl. Biomater.* **2010**, *94*, 359–366. [CrossRef]
37. Beck-Broichsitter, B.E.; Lamia, A.; Geuna, S.; Fregnan, F.; Smeets, R.; Becker, S.T.; Sinis, N. Does Pulsed Magnetic Field Therapy Influence Nerve Regeneration in the Median Nerve Model of the Rat? *Biomed Res. Int.* **2014**, *2014*. [CrossRef]
38. De, I.; Sharma, P.; Singh, M. Emerging approaches of neural regeneration using physical stimulations solely or coupled with smart piezoelectric nano-biomaterials. *Eur. J. Pharm. Biopharm.* **2022**, *173*, 73–91. [CrossRef]
39. Babaie, A.; Bakhshandeh, B.; Abedi, A.; Mohammadnejad, J.; Shabani, I.; Ardeshirylajimi, A.; Reza Moosavi, S.; Amini, J.; Tayebi, L. Synergistic effects of conductive PVA/PEDOT electrospun scaffolds and electrical stimulation for more effective neural tissue engineering. *Eur. Polym. J.* **2020**, *140*, 110051. [CrossRef]

40. Chen, H.; Tian, G.; Yan, H.; Yang, S.; Kim, D.H. Fabrication of vertically aligned PEDOT nanotube arrays on microelectrodes to interface neurons. *Electrochim. Acta* **2022**, *404*, 139583. [CrossRef]
41. Koudehi, M.F.; Fooladi, A.A.I.; Aghozbeni, E.A.H.; Nourani, M.R. Nano bioglass/gelatin scaffold enhanced by nanosilver as an antibacterial conduit for peripheral nerve regeneration. *Mater. Techn.* **2019**, *34*, 776–784. [CrossRef]
42. Pulugu, P.; Ghosh, S.; Rokade, S.; Choudhury, K.; Arya1, N.; Kumar, P. A perspective on implantable biomedical materials and devices for diagnostic applications. *Curr. Opin. Biomed. Eng.* **2021**, *18*, 100287. [CrossRef]
43. Rauti, R.; Musto, M.; Bosi, S.; Prato, M.; Ballerini, L. Properties and behavior of carbon nanomaterials when interfacing neuronal cells: How far have we come? *Carbon* **2019**, *143*, 430–446. [CrossRef]
44. Song, H.; Liu, Y.; Fang, Y.; Zhang, D. Carbon-Based Electrochemical Sensors for In Vivo and In Vitro Neurotransmitter Detection. *Critic. Rev. Analyt. Chem.* **2021**. [CrossRef]
45. David-Pur, M.; Bareket-Keren, L.; Beit-Yaakov, G.; Raz-Prag, D.; Hanein, Y. All-carbon-nanotube flexible multi-electrode array for neuronal recording and stimulation. *Biomed. Microdevices* **2014**, *16*, 43–53. [CrossRef]
46. Giagka, V.; Serdijn, W.A. Realizing flexible bioelectronic medicines for accessing the peripheral nerves—Technology considerations. *Bioelectr. Med.* **2021**, *4*, 8. [CrossRef]
47. Wang, L.; Chen, K.; Fan, Y.; Yin, L. Novel implantable devices delivering electrical cues for tissue regeneration and functional restoration. *Med. Nov. Techn. Devices* **2022**, *16*, 100146. [CrossRef]
48. Wang, Y.; Zhu, H.; Yang, H.; Argall, A.D.; Luan, L.; Xie, C.; Guo, L. Nano functional neural interfaces. *Nano Res.* **2018**, *11*, 5065–5106. [CrossRef]
49. Hejazi, M.A.; Tong, W.; Stacey, A.; Soto-Breceda, A.; Ibbotson, M.R.; Yunzab, M.; Maturana, M.I.; Almasi, A.; Jung, Y.J.; Sun, S.; et al. Hybrid diamond/carbon fiber microelectrodes enable multimodal electrical/chemical neural interfacing. *Biomaterials* **2020**, *30*, 119648. [CrossRef]
50. Fraczek-Szczypta, A.; Jantas, D.; Ciepiela, F.; Grzonk, J. Graphene oxide-conductive polymer nanocomposite coatings obtained by the EPD method as substrates for neurite outgrowth. *Diamond. Relat. Mater.* **2020**, *102*, 107663. [CrossRef]
51. Fraczek-Szczypta, A. Carbon nanomaterials for nerve tissue stimulation and regeneration. *Mater. Sci. Eng. C* **2014**, *34*, 35–49. [CrossRef] [PubMed]
52. Yokoyama, A.; Sato, Y.; Nodasaka, Y.; Yamamoto, S.; Kawasaki, T.; Shindoh, M.; Kongo, T.; Akasaka, T.; Uo, M.; Watari, F.; et al. Biological behavior of hat-stacked carbon nanofibers in the subcutaneous tissue in rats. *Nano Lett.* **2005**, *5*, 157–161. [CrossRef] [PubMed]
53. Klein, K.L.; Melechko, A.V.; McKnight, T.E.; Retterer, S.T.; Rack, P.D.; Fowlkes, J.D.; Joy, D.C.; Simpson, M.L. Surface characterization and functionalization of carbon nanofibers. *J. Appl. Phys.* **2008**, *103*, 061301. [CrossRef]
54. Tran, P.A.; Zhang, L.; Webster, T.J. Carbon nanofibers and carbon nanotubes in regenerative medicine. *Adv. Drug Deliv. Rev.* **2009**, *61*, 1097–1114. [CrossRef] [PubMed]
55. Foldvari, M.; Bagonluri, M. Carbon nanotubes as functional excipients for nanomedicines: I. pharmaceutical properties. *Nanomed. Nanotechnol. Biol. Med.* **2008**, *4*, 173–182. [CrossRef] [PubMed]
56. Wei, W.; Sethuraman, A.; Jin, C.; Monteiro-Riviere, N.A.; Narayan, R.J. Biological properties of carbon nanotubes. *J. Nanosci. Nanotechnol.* **2007**, *7*, 1284–1297. [CrossRef]
57. Engel, E.; Michiardi, A.; Navarro, M.; Lacroix, D.; Planell, J.A. Nanotechnology in regenerative medicine: The materials side. *Trends Biotechnol.* **2008**, *26*, 39–47. [CrossRef]
58. Alshehri, R.; Ilyas, A.M.; Hasan, A.; Arnaout, A.; Ahmed, F.; Memic, A. Carbon Nanotubes in Biomedical Applications: Factors, Mechanisms, and Remedies of Toxicity. *J. Med. Chem.* **2016**, *59*, 8149–8167. [CrossRef]
59. Thostenson, E.T.; Ren, Z.; Chou, T.-W. Advances in the science and technology of carbon nanotubes and their composites: A review. *Compos. Sci. Technol.* **2001**, *61*, 1899–1912. [CrossRef]
60. Iijima, S. Synthesis of Carbon Nanotubes. *Nature* **1991**, *354*, 56–58. [CrossRef]
61. Yarlagadda, T.; Sharma, S.; Yarlagadda, P.D.K.V.; Sharma, J. Recent Developments in the Field of Nanotechnology for Development of Medical Implants. *Proceed. Manufact.* **2019**, *30*, 544–551. [CrossRef]
62. Sebaa, M.; Nguyen, T.Y.; Paul, R.K.; Mulchandani, A.; Liu, H. Graphene and carbon nanotube-graphene hybrid nanomaterials for human embryonic stem cell culture. *Mater. Lett.* **2013**, *92*, 122–125. [CrossRef]
63. Liu, X.; Miller, A.L.; Park, S.; Waletzki, B.E.; Zhou, Z.; Terzic, A.; Lu, L. Functionalized Carbon Nanotube and Graphene Oxide Embedded Electrically Conductive Hydrogel Synergistically Stimulates Nerve Cell Differentiation. *ACS Appl. Mater. Interfaces* **2017**, *9*, 14677–14690. [CrossRef] [PubMed]
64. Hopley, E.L.; Salmasi, S.; Kalaskar, D.M.; Seifalian, A.M. Carbon nanotubes leading the way forward in new generation 3D tissue engineering. *Biotechnol. Adv.* **2014**, *32*, 1000–1014. [CrossRef]
65. Tejchman, A.; Znój, A.; Chlebanowska, P.; Fraczek-Szczypta, A.; Majka, M. Carbon Fibers as a New Type of Scaffold for Midbrain Organoid Development. *Int. J. Mol. Sci.* **2020**, *21*, 5959. [CrossRef]
66. Cellot, G.; Cilia, E.; Cipollone, S.; Rancic, V.; Sucapane, A.; Giordani, S.; Gambazzi, L.; Markram, H.; Grandolfo, M.; Scaini, D.; et al. Carbon nanotubes might improve neuronal performance by favouring electrical shortcuts. *Nat. Nanotechnol.* **2009**, *4*, 126–133. [CrossRef]
67. Hummer, G.; Rasaiah, J.C.; Noworyta, J.P. Water conduction through the hydrophobic channel of a carbon nanotube. *Nature* **2001**, *414*, 188–190. [CrossRef]

68. Seidlits, S.K.; Lee, J.Y.; Schmidt, C.E. Nanostructured scaffolds for neural applications. *Nanomedicine* **2008**, *3*, 183–199. [CrossRef]
69. Oprych, K.M.; Whitby, R.L.D.; Mikhalovsky, S.V.; Tomlins, P.; Adu, J. Repairing Peripheral Nerves: Is there a Role for Carbon Nanotubes? *Adv. Healthc. Mater.* **2016**, *5*, 1253–1271. [CrossRef]
70. Mattson, M.P.; Haddon, R.C.; Rao, A.M. Molecular functionalization of carbon nanotubes and use as substrates for neuronal growth. *J. Mol. Neurosci.* **2000**, *14*, 175–182. [CrossRef]
71. Matsumoto, K.; Sato, C.; Naka, Y.; Kitazawa, A.; Whitby, R.L.D.; Shimizu, N. Neurite outgrowths of neurons with neurotrophin-coated carbon nanotubes. *J. Biosci. Bioeng.* **2007**, *103*, 216–220. [CrossRef] [PubMed]
72. Nawrotek, K.; Tylman, M.; Rudnicka, K.; Gatkowska, J.; Balcerzak, J. Tubular electrodeposition of chitosan-carbon nanotube implants enriched with calcium ions. *J. Mech. Behav. Biomed. Mater.* **2016**, *60*, 256–266. [CrossRef] [PubMed]
73. Wu, S.; Duan, B.; Lu, A.; Wang, Y.; Ye, Q.; Zhang, L. Biocompatible chitin/carbon nanotubes composite hydrogels as neuronal growth substrates. *Carbohydr. Polym.* **2017**, *174*, 830–840. [CrossRef] [PubMed]
74. Scapin, G.; Salice, P.; Tescari, S.; Menna, E.; De Filippis, V.; Filippini, F. Enhanced neuronal cell differentiation combining biomimetic peptides and a carbon nanotube-polymer scaffold. *Nanomed. Nanotechnol. Biol. Med.* **2015**, *11*, 621–632. [CrossRef]
75. Kolarcik, C.L.; Catt, K.; Rost, E.; Albrecht, I.N.; Bourbeau, D.; Du, Z.; Kozai, T.D.Y.; Luo, X.; Weber, D.J.; Cui, X.T. Evaluation of poly(3,4-ethylenedioxythiophene)/carbon nanotube neural electrode coatings for stimulation in the dorsal root ganglion. *J. Neural Eng.* **2015**, *12*, 016008. [CrossRef]
76. Xue, N.; Sun, T.; Tsang, W.M.; Delgado-Martinez, I.; Lee, S.H.; Sheshadri, S.; Xiang, Z.; Merugu, S.; Gu, Y.; Yen, S.C.; et al. Polymeric C-shaped cuff electrode for recording of peripheral nerve signal. *Sens. Actuators B Chem.* **2015**, *210*, 640–648. [CrossRef]
77. Tegtmeier, K.; Aliuos, P.; Lenarz, T.; Doll, T. Residual rubber shielded multi walled carbon nanotube electrodes for neural interfacing in active medical implants. *Phys. Med.* **2016**, *1*, 8–19. [CrossRef]
78. Kang, D.W.; Sun, F.; Choi, Y.J.; Zou, F.; Cho, W.H.; Choi, B.K.; Koh, K.; Lee, J.; Han, I.H. Enhancement of primary neuronal cell proliferation using printing-transferred carbon nanotube sheets. *J. Biomed. Mater. Res.—Part A* **2015**, *103*, 1746–1754. [CrossRef]
79. Koppes, A.N.; Keating, K.W.; McGregor, A.L.; Koppes, R.A.; Kearns, K.R.; Ziemba, A.M.; McKay, C.A.; Zuidema, J.M.; Rivet, C.J.; Gilbert, R.J.; et al. Robust Neurite Extension Following Exogenous Electrical Stimulation within Single Walled Carbon Nanotube-Composite Hydrogels. *Acta Biomater.* **2016**, *15*, 34–43. [CrossRef]
80. Galvan-Garcia, P.; Keefer, E.W.; Yang, F.; Zhang, M.; Fang, S.; Zakhidov, A.A.; Baughman, R.H.; Romero, M.I. Robust cell migration and neuronal growth on pristine carbon nanotube sheets and yarns. *J. Biomater. Sci. Polym. Ed.* **2007**, *18*, 1245–1261. [CrossRef]
81. Lovat, V.; Pantarotto, D.; Lagostena, L.; Cacciari, B.; Grandolfo, M.; Righi, M.; Spalluto, G.; Prato, M.; Ballerini, L. Carbon nanotube substrates boost neuronal electrical signaling. *Nano Lett.* **2005**, *5*, 1107–1110. [CrossRef] [PubMed]
82. Gheith, M.K.; Sinani, V.A.; Wicksted, J.P.; Matts, R.L.; Kotov, N.A. Single-walled carbon nanotube polyelectrolyte multilayers and freestanding films as a biocompatible platform for neuroprosthetic implants. *Adv. Mater.* **2005**, *17*, 2663–2670. [CrossRef]
83. Yu, W.; Jiang, X.; Cai, M.; Zhao, W.; Ye, D.; Zhou, Y.; Zhu, C.; Zhang, X.; Lu, X.; Zhang, Z. A novel electrospun nerve conduit enhanced by carbon nanotubes for peripheral nerve regeneration. *Nanotechnology* **2014**, *25*, 165102. [CrossRef] [PubMed]
84. Ahn, H.S.; Hwang, J.Y.; Kim, M.S.; Lee, J.Y.; Kim, J.W.; Kim, H.S.; Shin, U.S.; Knowles, J.C.; Kim, H.W.; Hyun, J.K. Carbon-nanotube-interfaced glass fiber scaffold for regeneration of transected sciatic nerve. *Acta Biomater.* **2015**, *13*, 324–334. [CrossRef] [PubMed]
85. Gupta, P.; Sharan, S.; Roy, P.; Lahiri, D. Aligned carbon nanotube reinforced polymeric scaffolds with electrical cues for neural tissue regeneration. *Carbon N. Y.* **2015**, *95*, 715–724. [CrossRef]
86. Roberts, M.J.; Leach, M.K.; Bedewy, M.; Meshot, E.R.; Copic, D.; Corey, J.M.; Hart, A.J. Growth of primary motor neurons on horizontally aligned carbon nanotube thin films and striped patterns. *J. Neural Eng.* **2014**, *11*, 036013. [CrossRef]
87. Stejskal, J.; Trchová, M. Conducting polypyrrole nanotubes: A review. *Chem. Pap.* **2018**, *72*, 1563–1595. [CrossRef]
88. Mostafa, M.H.; Ali, E.S.; Darwish, M.S.A. Recent Developments of Conductive Polymers/Carbon Nanotubes Nanocomposites for Sensor Applications. *Polym. Plast. Technol. Mater.* **2022**, *61*, 1456–1480. [CrossRef]
89. John, A.A.; Subramanian, A.P.; Vellayappan, M.V.; Balaji, A.; Mohandas, H.; Jaganathan, S.K. Carbon nanotubes and graphene as emerging candidates in neuroregeneration and neurodrug delivery. *Int. J. Nanomed.* **2015**, *10*, 4267–4277.
90. Dlugon, E.; Simka, W.; Fraczek-Szczypta, A.; Niemiec, W.; Markowski, J.; Szymanska, M.; Blazewicz, M. Carbon nanotube-based coatings on titanium. *Bull. Mater. Sci.* **2015**, *38*, 1339–1344. [CrossRef]
91. Jan, E.; Kotov, N.A. Successful differentiation of mouse neural stem cells on layer-by-layer assembled single-walled carbon nanotube composite. *Nano Lett.* **2007**, *7*, 1123–1128. [CrossRef] [PubMed]
92. Bardi, G.; Tognini, P.; Ciofani, G.; Raffa, V.; Costa, M.; Pizzorusso, T. Pluronic-coated carbon nanotubes do not induce degeneration of cortical neurons in vivo and in vitro. *Nanomed. Nanotechnol. Biol. Med.* **2009**, *5*, 96–104. [CrossRef] [PubMed]
93. Mazzatenta, A.; Giugliano, M.; Campidelli, S.; Gambazzi, L.; Businaro, L.; Markram, H.; Prato, M.; Ballerini, L. Interfacing neurons with carbon nanotubes: Electrical signal transfer and synaptic stimulation in cultured brain circuits. *J. Neurosci.* **2007**, *27*, 6931–6936. [CrossRef] [PubMed]
94. Xiang, C.; Zhang, Y.; Guo, W.; Liang, X.J. Biomimetic carbon nanotubes for neurological disease therapeutics as inherent medication. *Acta Pharm. Sin. B* **2020**, *10*, 239–248. [CrossRef] [PubMed]
95. Andrews, R.; Jacques, D.; Qian, D.; Dickey, E.C. Purification and structural annealing of multiwalled carbon nanotubes at graphitization temperatures. *Carbon N. Y.* **2001**, *39*, 1681–1687. [CrossRef]

96. Suh, W.H.; Suslick, K.S.; Stucky, G.D.; Suh, Y.-H. Nanotechnology, nanotoxicology, and neuroscience. *Prog. Neurobiol.* **2009**, *87*, 133–170. [CrossRef]
97. Tsang, W.M.; Stone, A.L.; Otten, D.; Aldworth, Z.N.; Daniel, T.L.; Hildebrand, J.G.; Levine, R.B.; Voldman, J. Insect-machine interface: A carbon nanotube-enhanced flexible neural probe. *J. Neurosci. Methods* **2012**, *204*, 355–365. [CrossRef]
98. Gaillard, C.; Cellot, G.; Li, S.; Toma, F.M.; Dumortier, H.; Spalluto, G.; Cacciari, B.; Prato, M.; Ballerini, L.; Bianco, A. Carbon nanotubes carrying cell-adhesion peptides do not interfere with neuronal functionality. *Adv. Mater.* **2009**, *21*, 2903–2908. [CrossRef]
99. Yan, Y.; Yao, R.; Zhao, J.; Chen, K.; Duan, L.; Wang, T.; Zhang, S.; Guan, J.; Zheng, Z.; Wang, X.; et al. Implantable nerve guidance conduits: Material combinations, multi-functional strategies and advanced engineering innovations. *Bioact. Mater.* **2022**, *11*, 57–76. [CrossRef]
100. Kunisaki, A.; Kodama, A.; Ishikawa, M.; Ueda, T.; Lima, M.D.; Kondo, T.; Adachi, N. Carbon-nanotube yarns induce axonal regeneration in peripheral nerve defect. *Sci. Rep.* **2021**, *11*, 19562. [CrossRef]
101. Firkowska, I.; Olek, M.; Pazos-Peréz, N.; Rojas-Chapana, J.; Giersig, M. Highly ordered MWNT-based matrixes: Topography at the nanoscale conceived for tissue engineering. *Langmuir* **2006**, *22*, 5427–5434. [CrossRef]
102. Kotov, N.A.; Winter, J.O.; Clements, I.P.; Jan, E.; Timko, B.P.; Campidelli, S.; Pathak, S.; Mazzatenta, A.; Lieber, C.M.; Prato, M.; et al. Nanomaterials for neural interfaces. *Adv. Mater.* **2009**, *21*, 3970–4004. [CrossRef]
103. Zhang, L.; Webster, T.J. Nanotechnology and nanomaterials: Promises for improved tissue regeneration. *Nano Today* **2009**, *4*, 66–80. [CrossRef]
104. Harrison, B.S.; Atala, A. Carbon nanotube applications for tissue engineering. *Biomaterials* **2007**, *28*, 344–353. [CrossRef] [PubMed]
105. Bianco, A.; Del Gaudio, C.; Baiguera, S.; Armentano, I.; Bertarelli, C.; Dottori, M.; Bultrini, G.; Lucotti, A.; Kenny, J.M.; Folin, M. Microstructure and cytocompatibility of electrospun nanocomposites based on poly(ε-caprolactone) and carbon nanostructures. *Int. J. Artif. Organs* **2010**, *33*, 271–282. [CrossRef]
106. Kim, C.; Jeong, Y., II; Ngoc, B.T.N.; Yang, K.S.; Kojima, M.; Kim, Y.A.; Endo, M.; Lee, J.W. Synthesis and characterization of porous carbon nanofibers with hollow cores through the thermal treatment of electrospun copolymeric nanofiber webs. *Small* **2007**, *3*, 91–95. [CrossRef]
107. Márquez-Lucero, A.; Gomez, J.A.; Caudillo, R.; Miki-Yoshida, M.; José-Yacaman, M. A method to evaluate the tensile strength and stress-strain relationship of carbon nanofibers, carbon nanotubes, and C-chains. *Small* **2005**, *1*, 640–644. [CrossRef]
108. Gabay, T.; Jakobs, E.; Ben-Jacob, E.; Hanein, Y. Engineered self-organization of neural networks using carbon nanotube clusters. *Phys. A Stat. Mech. Its Appl.* **2005**, *350*, 611–621. [CrossRef]
109. Baldrighi, M.; Trusel, M.; Tonini, R.; Giordani, S. Carbon Nanomaterials Interfacing with Neurons: An In vivo Perspective. *Front. Neurosci.* **2016**, *10*, 00250. [CrossRef]
110. Mezzasalma, S.A.; Grassi, L.; Grassi, M. Physical and chemical properties of carbon nanotubes in view of mechanistic neuroscience investigations. Some outlook from condensed matter, materials science and physical chemistry. *Mater. Sci. Eng. C* **2021**, *131*, 112480. [CrossRef]
111. Sealy, C. Carbon nanotube scaffold touches a nerve. *Nano Today* **2016**, *11*, 538–539.
112. Suh, T.C.; Twidd, J.; Mahmood, N.; Ali, K.M.; Lubna, M.M.; Bradford, P.D.; Daniele, M.A.; Gluck, J.M. Electrospun Carbon Nanotube-Based Scaffolds Exhibit High Conductivity and Cytocompatibility for Tissue Engineering Applications. *ACS Omega* **2022**, *7*, 20006–20019. [CrossRef] [PubMed]
113. Sealy, C. Carbon nanotubes show nerve in repair. *Mater. Today* **2015**, *18*, 127–128. [CrossRef]
114. Tavangarian, F.; Lie, Y. Carbon nanostructures as nerve scaffolds for repairing large gaps in severed nerves. *Ceram. Int.* **2012**, *38*, 6075–6090. [CrossRef]
115. Tasis, D.; Tagmatarchis, N.; Bianco, A.; Prato, M. Chemistry of carbon nanotubes. *Chem. Rev.* **2006**, *106*, 1105–1136. [CrossRef] [PubMed]
116. Ai, J.; Biazar, E.; Jafarpour, M.; Montazeri, M.; Majdi, A.; Aminifard, S.; Zafari, M.; Akbari, H.R.; Rad, H.G. Nanotoxicology and nanoparticle safety in biomedical designs. *Int. J. Nanomed.* **2011**, *6*, 1117–1127.
117. Bosi, S.; Fabbro, A.; Ballerini, L.; Prato, M. Carbon nanotubes: A promise for nerve tissue engineering? *Nanotechnol. Rev.* **2013**, *2*, 47–57. [CrossRef]
118. Saito, N.; Haniu, H.; Usui, Y.; Aoki, K.; Hara, K.; Takanashi, S.; Shimizu, M.; Narita, N.; Okamoto, M.; Kobayashi, S.; et al. Safe clinical use of carbon nanotubes as innovative biomaterials. *Chem. Rev.* **2014**, *114*, 6040–6079. [CrossRef]
119. Hwang, J.Y.; Shin, U.S.; Jang, W.C.; Hyun, J.K.; Wall, I.B.; Kim, H.W. Biofunctionalized carbon nanotubes in neural regeneration: A mini-review. *Nanoscale* **2013**, *5*, 487–497. [CrossRef]
120. Huang, B. Carbon nanotubes and their polymeric composites: The applications in tissue engineering. *Biomanufactur. Rev.* **2020**, 5. [CrossRef]
121. Redondo-Gomez, C.; Leandro-Mora, R.; Blanch-Bermudez, D.; Espinoza-Araya, C.; Hidalgo-Barrantes, D.; Vega-Baudrit, J. Recent Advances in Carbon Nanotubes for Nervous Tissue Regeneration. *Adv. Polym. Technol.* **2020**, *2020*. [CrossRef]
122. Fabbro, A.; Prato, M.; Ballerini, L. Carbon nanotubes in neuroregeneration and repair. *Adv. Drug Deliv. Rev.* **2013**, *65*, 2034–2044. [CrossRef] [PubMed]
123. Vigmond, E.J.; Perez Velazquez, J.L.; Valiante, T.A.; Bardakjian, B.L.; Carlen, P.L. Mechanisms of electrical coupling between pyramidal cells. *J. Neurophysiol.* **1997**, *78*, 3107–3116. [CrossRef] [PubMed]

124. Gladwin, K.M.; Whitby, R.L.D.; Mikhalovsky, S.V.; Tomlins, P.; Adu, J. In Vitro Biocompatibility of Multiwalled Carbon Nanotubes with Sensory Neurons. *Adv. Healthc. Mater.* **2013**, *2*, 728–735. [CrossRef] [PubMed]
125. Zhang, Y.; Bai, Y.; Yan, B. Functionalized carbon nanotubes for potential medicinal applications. *Drug Discov. Today* **2010**, *15*, 428–435. [CrossRef] [PubMed]
126. Hu, H.; Ni, Y.; Mandal, S.K.; Montana, V.; Zhao, B.; Haddon, R.C.; Parpura, V. Polyethyleneimine functionalized single-walled carbon nanotubes as a substrate for neuronal growth. *J. Phys. Chem. B* **2005**, *109*, 4285–4289. [CrossRef]
127. Hu, H.; Ni, Y.; Montana, V.; Haddon, R.C.; Parpura, V. Chemically Functionalized Carbon Nanotubes as Substrates for Neuronal Growth. *Nano Lett.* **2004**, *4*, 507–511. [CrossRef]
128. Patil, A.C.; Thakor, N.V. Implantable neurotechnologies: A review of micro and nanoelectrodes for neural recording. *Med. Biol. Eng. Comput.* **2016**, *54*, 23–44. [CrossRef]
129. Lu, Y.; Li, T.; Zhao, X.; Li, M.; Cao, Y.; Yang, H.; Duan, Y.Y. Electrodeposited polypyrrole/carbon nanotubes composite films electrodes for neural interfaces. *Biomaterials* **2010**, *31*, 5169–5181. [CrossRef]
130. Barbara Nguyen-Vu, T.D.; Chen, H.; Cassell, A.M.; Andrew, R.; Meyyappan, M.; Li, J. Vertically aligned carbon nanoflber arrays: An advance toward electrical-neural interfaces. *Small* **2006**, *2*, 89–94. [CrossRef]
131. Keefer, E.W.; Botterman, B.R.; Romero, M.I.; Rossi, A.F.; Gross, G.W. Carbon nanotube coating improves neuronal recordings. *Nat. Nanotechnol.* **2008**, *3*, 434–439. [CrossRef] [PubMed]
132. Gutiérrez, A.; Primo, E.N.; Eguílaz, M.; Parrado, C.; Rubianes, M.D.; Rivas, G.A. Quantification of neurotransmitters and metabolically related compounds at glassy carbon electrodes modified with bamboo-like carbon nanotubes dispersed in double stranded DNA. *Microchem. J.* **2017**, *130*, 40–46. [CrossRef]
133. Yildiz, K.A.; Shin, A.Y.; Kaufman, K.R. Interfaces with the peripheral nervous system for the control of a neuroprosthetic limb: A review. *J. NeuroEng. Rehab.* **2020**, *17*, 43. [CrossRef]
134. Schneider, J.V. Vertically Aligned Carbon Nanotubes as Platform for Biomimetically Inspired Mechanical Sensing, Bioactive Surfaces, and Electrical Cell Interfacing. *Adv. Biosyst.* **2017**, *1*, 1700101. [CrossRef] [PubMed]
135. Mamedov, A.A.; Kotov, N.A.; Prato, M.; Guldi, D.M.; Wicksted, J.P.; Hirsch, A. Molecular design of strong single-wall carbon nanotube/polyelectrolyte multilayer composites. *Nat. Mater.* **2002**, *1*, 190–194. [CrossRef] [PubMed]
136. Gheith, M.K.; Pappas, T.C.; Liopo, A.V.; Sinani, V.A.; Shim, B.S.; Motamedi, M.; Wicksted, J.P.; Kotov, N.A. Stimulation of neural cells by lateral currents in conductive layer-by-layer films of single-walled carbon nanotubes. *Adv. Mater.* **2006**, *18*, 2975–2979. [CrossRef]
137. Chao, T.I.; Xiang, S.; Chen, C.S.; Chin, W.C.; Nelson, A.J.; Wang, C.; Lu, J. Carbon nanotubes promote neuron differentiation from human embryonic stem cells. *Biochem. Biophys. Res. Commun.* **2009**, *384*, 426–430. [CrossRef]
138. Park, S.Y.; Choi, D.S.; Jin, H.J.; Park, J.; Byun, K.Y.; Lee, K.B.; Hing, S. Polarization-Controlled Differentiation of Human Neural Stem Cells Using Synergistic Cues from the Patterns of Carbon Nanotube Monolayer Coating. *ACS Nano* **2011**, *5*, 4704–4711. [CrossRef] [PubMed]
139. Tian, P.; Yi, W.; Chen, C.; Hu, J.; Qi, J.; Zhang, B.; Cheng, M.M.C. Flexible 3D carbon nanotubes cuff electrodes as a peripheral nerve interface. *Biomed. Microdevices* **2018**, *20*, 21. [CrossRef]
140. Zhang, X.; Chen, C.; Ni, G.; Hai, Y.; Chen, B.; Zhou, Y.; Zhang, B.; Chen, G.; Cheng, M.M.C. Carbon multi-electrode arrays as peripheral nerve interface for neural recording and nerve stimulation. *Med. Devices Sens.* **2019**, *2*, e10026. [CrossRef]
141. Rozhina, E.; Batasheva, S.; Miftakhova, R.; Yan, X.; Vikulina, A.; Volodkin, D.; Fakhrullin, R. Comparative cytotoxicity of kaolinite, halloysite, multiwalled carbon nanotubes and graphene oxide. *Appl. Clay Sci.* **2021**, *205*, 106041. [CrossRef]
142. Kong, H.; Wang, L.; Zhu, Y.; Huang, Q.; Fan, C. Culture medium-associated physicochemical insights on the cytotoxicity of carbon nanomaterials. *Chem. Res. Toxicol.* **2015**, *28*, 290–295. [CrossRef] [PubMed]
143. Hurt, R.H.; Monthioux, M.; Kane, A. Toxicology of carbon nanomaterials: Status, trends, and perspectives on the special issue. *Carbon N. Y.* **2006**, *44*, 1028–1033. [CrossRef]
144. Jain, N.; Tiwari, S. Biomedical application of carbon nanotubes (CNTs) in vulnerable parts of the body and its toxicity study: A state-of-the-art-review. *Mater. Today Proc.* **2021**, *46*, 7608–7617. [CrossRef]
145. Kobayashi, N.; Izumi, H.; Morimoto, Y. Review of toxicity studies of carbon nanotubes. *J. Occup. Health* **2017**, *59*, 394–407. [CrossRef]
146. Wu, D.; Pak, E.S.; Wingard, C.J.; Murashov, A.K. Multi-walled carbon nanotubes inhibit regenerative axon growth of dorsal root ganglia neurons of mice. *Bone* **2012**, *507*, 72–77. [CrossRef]
147. Zheng, W.; McKinney, W.; Kashon, M.; Salmen, R.; Castranova, V.; Kan, H. The influence of inhaled multi-walled carbon nanotubes on the autonomic nervous system. *Part. Fibre Toxicol.* **2016**, *13*, 8. [CrossRef]
148. Lam, C.W.; James, J.T.; McCluskey, R.; Hunter, R.L. Pulmonary toxicity of single-wall carbon nanotubes in mice 7 and 90 days after intractracheal instillation. *Toxicol. Sci.* **2004**, *77*, 126–134. [CrossRef]
149. Muller, J.; Huaux, F.; Moreau, N.; Misson, P.; Heilier, J.F.; Delos, M.; Arras, M.; Fonseca, A.; Nagy, J.B.; Lison, D. Respiratory toxicity of multi-wall carbon nanotubes. *Toxicol. Appl. Pharmacol.* **2005**, *207*, 221–231. [CrossRef]
150. Boczkowski, J.; Lanone, S. Respiratory toxicities of nanomaterials—A focus on carbon nanotubes. *Adv. Drug Deliv. Rev.* **2012**, *64*, 1694–1699. [CrossRef]

151. Meng, L.; Jiang, A.; Chen, R.; Li, C.; Wang, L.; Qu, Y.; Wang, P.; Zhao, Y.; Chen, C. Inhibitory effects of multiwall carbon nanotubes with high iron impurity on viability and neuronal differentiation in cultured PC12 cells. *Toxicology* **2013**, *313*, 49–58. [CrossRef] [PubMed]
152. Zenoozi, S.; Sadeghi, G.M.M.; Shahrousvand, M.; Rafiee, M. Preparation and optimization of polyurethane/crosslinked poly acrylic acid semi-IPNs containing multi wall carbon nanotube applicable for artificial tendon. *Colloids Surf. A Physicochem. Eng. Asp.* **2022**, *640*, 128415. [CrossRef]
153. Lewitus, D.Y.; Landers, J.; Branch, J.R.; Smith, K.L.; Callegari, G.; Kohn, J.; Neimark, A.V. Biohybrid carbon nanotube/agarose fibers for neural tissue engineering. *Adv. Funct. Mater.* **2011**, *21*, 2624–2632. [CrossRef]
154. Saudi, A.; Zebarjad, S.M.; Alipour, H.; Katoueizadeh, E.; Alizadeh, A.; Rafienia, M. A study on the role of multi-walled carbon nanotubes on the properties of electrospun Poly(Caprolactone)/Poly(Glycerol sebacate) scaffold for nerve tissue applications. *Mater. Chem. Phys.* **2022**, *282*, 125868. [CrossRef]
155. Shrestha, S.; Shrestha, B.K.; Kim, J.I.; Won Ko, S.; Park, C.H.; Kim, C.S. Electrodeless coating polypyrrole on chitosan grafted polyurethane with functionalized multiwall carbon nanotubes electrospun scaffold for nerve tissue engineering. *Carbon N. Y.* **2018**, *136*, 430–443. [CrossRef]
156. Pouladzadeh, F.; Katbab, A.A.; Haghighipour, N.; Kashi, E. Carbon nanotube loaded electrospun scaffolds based on thermoplastic urethane (TPU) with enhanced proliferation and neural differentiation of rat mesenchymal stem cells: The role of state of electrical conductivity. *Eur. Polym. J.* **2018**, *105*, 286–296. [CrossRef]
157. Shrestha, S.; Shrestha, B.K.; Lee, J.; Joong, O.K.; Kim, B.S.; Park, C.H.; Kim, C.S. A conducting neural interface of polyurethane/silk-functionalized multiwall carbon nanotubes with enhanced mechanical strength for neuroregeneration. *Mater. Sci. Eng. C* **2019**, *102*, 511–523. [CrossRef] [PubMed]
158. Gupta, P.; Agrawal, A.; Murali, K.; Varshney, R.; Beniwal, S.; Manhas, S.; Roy, P.; Lahiri, D. Differential neural cell adhesion and neurite outgrowth on carbon nanotube and graphene reinforced polymeric scaffolds. *Mater. Sci. Eng. C* **2019**, *97*, 539–551. [CrossRef]
159. Arslantunali, D.; Budak, G.; Hasirci, V. Multiwalled CNT-pHEMA composite conduit for peripheral nerve repair. *J. Biomed. Mater. Res.—Part A* **2014**, *102*, 828–841. [CrossRef]
160. Mottaghitalab, F.; Farokhi, M.; Zaminy, A.; Kokabi, M.; Soleimani, M.; Mirahmadi, F.; Shokrgozar, M.A.; Sadeghizadeh, M. A Biosynthetic Nerve Guide Conduit Based on Silk/SWNT/Fibronectin Nanocomposite for Peripheral Nerve Regeneration. *PLoS ONE* **2013**, *8*, 6–17. [CrossRef]
161. Voge, C.M.; Johns, J.; Raghavan, M.; Morris, M.D.; Stegemann, J.P. Wrapping and dispersion of multiwalled carbon nanotubes improves electrical conductivity of protein-nanotube composite biomaterials. *J. Biomed. Mater. Res.—Part A* **2013**, *101A*, 231–238. [CrossRef] [PubMed]
162. Assaf, K.; Leal, C.V.; Derami, M.S.; de Rezende Duek, E.A.; Ceragioli, H.J.; de Oliveira, A.L.R. Sciatic nerve repair using poly(ε-caprolactone) tubular prosthesis associated with nanoparticles of carbon and graphene. *Brain Behav.* **2017**, *7*, 1–12. [CrossRef] [PubMed]
163. Kabiri, M.; Oraee-Yazdani, S.; Shafiee, A.; Hanaee-Ahvaz, H.; Dodel, M.; Vaseei, M.; Soleimani, M. Neuroregenerative effects of olfactory ensheathing cells transplanted in a multi-layered conductive nanofibrous conduit in peripheral nerve repair in rats. *J. Biomed. Sci.* **2015**, *22*, 35. [CrossRef]
164. Jahromi, H.K.; Farzin, A.; Hasanzadeh, E.; Barough, S.E.; Mahmoodim, N.; Najafabadi, M.R.H.; Farahani, M.S.; Mansoori, K.; Shirian, S.; Ai, J. Enhanced sciatic nerve regeneration by poly-L-lactic acid/multi-wall carbon nanotube neural guidance conduit containing Schwann cells and curcumin encapsulated chitosan nanoparticles in rat. *Mater. Sci. Eng. C* **2020**, *109*, 110564. [CrossRef] [PubMed]
165. Salehi, M.; Naseri-Nosar, M.; Ebrahimi-Barough, S.; Nourani, M.; Khojasteh, A.; Hamidieh, A.A.; Amani, A.; Farzamfar, S.; Ai, J. Sciatic nerve regeneration by transplantation of Schwann cells via erythropoietin controlled-releasing polylactic acid/multiwalled carbon nanotubes/gelatin nanofibrils neural guidance conduit. *J. Biomed. Mater. Res.—Part B Appl. Biomater.* **2018**, *106*, 1463–1476. [CrossRef]
166. Namgung, S.; Baik, K.Y.; Park, J.; Hong, S. Controlling the growth and differentiation of human mesenchymal stem cells by the arrangement of individual carbon nanotubes. *ACS Nano* **2011**, *5*, 7383–7390. [CrossRef] [PubMed]
167. Hu, Y.; Chen, W.; Yin, H.; Chen, X.; Cai, J.; Guo, J.; Zhou, S.; Chai, R.; Tang, M. Super-aligned carbon nanotubes and GelMA hydrogel composite scaffolds promote spiral ganglion neuron growth and orientation. *Mater. Today Nano* **2022**, *18*, 100181. [CrossRef]
168. Wang, L.; Wu, Y.; Hu, T.; Ma, P.X.; Guo, B. Aligned conductive core-shell biomimetic scaffolds based on nanofiber yarns/hydrogel for enhanced 3D neurite outgrowth alignment and elongation. *Acta Biomater.* **2019**, *96*, 175–187. [CrossRef]
169. Li, X.; Yang, W.; Xie, H.; Wang, J.; Zhang, L.; Wang, Z.; Wang, L. CNT/Sericin Conductive Nerve Guidance Conduit Promotes Functional Recovery of Transected Peripheral Nerve Injury in a Rat Model. *ACS Appl. Mater. Interfaces* **2020**, *12*, 36860–36872. [CrossRef]
170. Salem, K.S.; Lubna, M.M.; Mustafir Rahman, A.F.M.; Nurnabil, M.; Islam, R.; Khan, M.A. The effect of multiwall carbon nanotube additions on the thermo-mechanical, electrical, and morphological properties of gelatin–polyvinyl alcohol blend nanocomposite. *J. Comp. Mater.* **2015**, *49*, 1379–1391. [CrossRef]

171. Sharmeene, S.; Mustafizur Rahman, A.F.M.; Lubna, M.M.; Salem, K.S.; Islam, R.; Khan, M.A. Polyethylene glycol functionalized carbon nanotubes/gelatin-chitosan nanocomposite: An approach for significant drug release. *Materials* **2018**, *3*, 236–244. [CrossRef] [PubMed]
172. Barshutina, M.N.; Kirichenko, S.O.; Wodolajsky, V.A.; Lopachev, A.V.; Barshutin, S.N.; Gorsky, O.V.; Deriabin, K.V.; Sufianov, A.A.; Bulgin, D.V.; Islamova, R.M.; et al. PDMS-CNT composite for soft bioelectronic neuronal implants. *Compos. B* **2022**, *247*, 110286. [CrossRef]
173. Ruiz, I.M.; Vilariño-Feltrer, G.; Mnatsakanyan, H.; Vallés-Lluch, A.; Pradas, M.M. Development and evaluation of hyaluronan nanocomposite conduits for neural tissue regeneration. *J. Biomater. Sci.* **2021**, *32*, 2227–2245. [CrossRef] [PubMed]

coatings

MDPI

Article

Permeability of Skin-Mimicking Cell Coatings by Polymers of Complex Architecture Based on Polyoxazolines

Gia Storti [1], Giulia Romano [1], Kristen Gilmore [1], Nicholas Sadowski [1], Andrii Tiiara [2], Igor Luzinov [2] and Alexander Sidorenko [1,*]

[1] Department of Chemistry and Biochemistry, Saint Joseph's University, Phildelphia, PA 19131, USA; gs20605058@sju.edu (G.S.)
[2] Department of Materials Science and Engineering, Clemson University, Clemson, SC 29634, USA
* Correspondence: asidorenko@sju.edu

Abstract: In the scope of drug delivery, the transdermal route is desirable because it provides attainable therapeutic concentrations and has minimal systemic side effects. To make the skin a feasible route for the delivery of therapeutic agents, the biggest challenge is overcoming its natural coating. In this paper, we investigate the effect of the architectures (homopolymer vs. block copolymer vs. hybrid block–graft copolymer) of several amphiphilic polymeric derivatives of poly(2-oxazoline) on skin permeability. The block copolymers are composed of a hydrophobic poly(2-oxazoline) block and a hydrophilic PEG block. The hybrid block–graft copolymers are obtained by grafting hydrophobic side chains of polycaprolactone to a poly(2-oxazoline) backbone. We used the commercially available EpiDerm™ by MatTek, composed of human epidermal cells, as a model of human skin. Two parameters of skin permeation are reported: penetration rate and lag time. We hypothesize that the skin permeation characteristics correlate with the critical micelle concentration and particle size of the studied polymers, while both parameters are a function of the complex architectures of the presented macromolecular constructs. While homopolymer poly(2-oxazolines) show the least permeation, the block copolymers demonstrate partial permeation. The hybrid block–graft copolymers exhibited full penetration through the model skin samples.

Keywords: hybrid block–graft copolymer; block copolymer; critical micelle concentration; poly(2-oxazolines)

Citation: Storti, G.; Romano, G.; Gilmore, K.; Sadowski, N.; Tiiara, A.; Luzinov, I.; Sidorenko, A. Permeability of Skin-Mimicking Cell Coatings by Polymers of Complex Architecture Based on Polyoxazolines. *Coatings* **2023**, *13*, 1007. https://doi.org/10.3390/coatings13061007

Academic Editor: Seungil Kim

Received: 29 April 2023
Revised: 22 May 2023
Accepted: 25 May 2023
Published: 29 May 2023

1. Introduction

The stratum corneum (SC), the outermost layer of the skin, comprises about twenty micrometers of dead corneocytes and squamous cells embedded in a lipid matrix. This layer controls absorption and acts as an effective barrier against infection and penetration of large therapeutics [1–3]. Methods such as microneedles and chemical enhancers are used to overcome the SC barrier. However, there are preservation issues and the potential for skin irritation when using such approaches [4–6]. Thus, a need for dynamic biocompatible vehicles capable of permeating the SC is of great importance.

The use of amphiphilic polymers for skin penetration has come to the forefront of drug delivery [7–10]. Micelle-forming nanocarriers have been shown to surpass the SC without damaging the tissue while efficiently delivering therapeutics [11,12]. We previously reported on the synthesis of a family of bio-benign amphiphilic poly(2-oxazoline)-based block copolymers (BCPs) and hybrid block–graft copolymers (HCPs) [13]. Poly(2-oxazolines) are a family of emerging innovative biomaterials that demonstrate notable results compared to other polymeric therapeutics [14–16]. Some of these polymers are readily modifiable, permitting amphiphilicity and solubility to be adjusted based on their functionality [17,18].

In this study, we hypothesize that poly(2-oxazoline)-based BCPs and HCPs will demonstrate amphiphilic properties and permeate the epidermis of human skin (Figure 1). HCPs

are macromolecular constructs constituted from a block copolymer (BCP) backbone with side chains grafted from one of the blocks. Poly(2-oxazoline)-based HCPs composed from both hydrophilic (polyethylene glycol, PEG) and hydrophobic (substituted poly(2-oxazoline)) components are of significant interest for skin permeability, as they are expected to be biodegradable and amphiphilic [19,20]. These qualities allow for low surface tension at the oil/water interface; thus, micelle formation may occur [21]. Self-assembly into micelles makes these amphiphilic hybrids useful in the delivery of medication, where the drug can be enclosed in the hydrophobic portion of the polymer matrix [22–24]. Interested readers are referred to a recent review on biodegradable polymeric micelles that summarizes findings on targeted and controlled drug delivery using PEG; polylactic, polyglycolic, and polyglutamic acids; poly(allyl glycidyl ether); poly(amido amine), etc. [25].

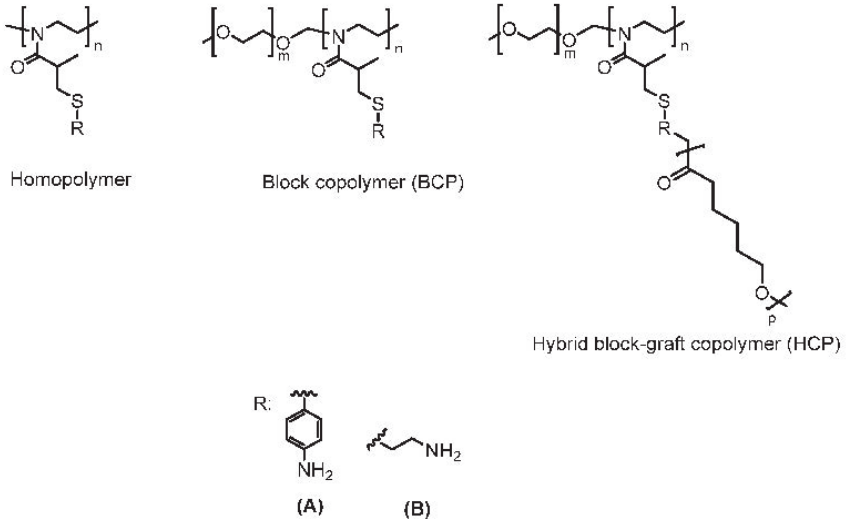

Figure 1. A generic structure for (A) aminothiophenol- and (B) cysteamine-functionalized homopolymer, block copolymer (BCP), and hybrid block–graft copolymer (HCP).

The most widely used biodegradable polymer for drug delivery is PEG. However, recent studies have highlighted the possibility of polymer buildup in tissues and an influx of anti-PEG antibodies in the immune system [26–28]. Previous work has shown that short sidechain poly(2-oxazolines) may be an improved PEG alternative due to better biocompatibility [29,30]. Thus, the family of bio-benign amphiphilic poly(2-oxazoline)-based BCPs and HCPs provide a promising substitution for PEG in drug delivery and transdermal applications.

The skin permeation experiments were performed on the EpiDerm™ Skin Model by MatTek. The EpiDerm™ tissues are cultured, normal, human-derived epidermal keratinocytes [31] that are commonly used for skin permeability studies [32,33]. Polymers functionalized with aminothiophenol (A) and cysteamine (B) were studied. The compositions of the polymers were established using ^{1}H NMR, Size-Exclusion Chromatography and fluorescence of FITC-labelled amino groups [13]; they are summarized in Table 1.

Table 1. Characteristics of the polymers tested in this study: weight-averaged molecular weight (Mw), kDa, polydispersity index (PDI), and fractions of hydrophilic (PEG) and hydrophobic (PCL) blocks.

	Mw, kDa	PDI	Fraction	
			PEG	PCL
Homopolymer A	3.9	1.18	-	-
BCP A	10.1	1.15	0.20	-
HCP A	17.1	1.21	0.12	0.41
Homopolymer B	10.2	1.11	-	-
BCP B	19.2	1.12	0.10	-
HCP B	24.4	1.11	0.08	0.21

1.1. Experimental Section

1.1.1. Materials

Fluorescein isothiocyanate isomer I (FITC, ≥90% (HPLC)), dimethyl sulfoxide (DMSO) (anhydrous, ≥99.9%), ethanol (anhydrous, 99%), diethyl ether (anhydrous, ACS reagent, ≥99%, contains BHT as inhibitor), and Pur-A-Lyzer™ Mega 6000 Da Dialysis Kit were purchased from Sigma-Aldrich and used without purification. EpiDerm™ EPI-200-X samples for skin permeability studies, EPI-100-LLMM-PRF (phenol red-free) media, and skin permeation devices were purchased from MatTek (Ashland, MA, USA) and used without purification.

1.1.2. Synthesis of the Hybrid Block–Graft Copolymer

This process is extensively described in our previous manuscript published elsewhere [13], shown in Scheme 1. The HCPs probed for skin permeation were synthesized using a three-step process. The first step was the functionalization of commercially available 2-isopropenyl-2-oxazoline with 4-aminothiophenol or 2-(Boc-amino) ethanethiol (common structure HS-R) via a thiol-ene click chemistry reaction. The second step consisted of ring-opening polymerization of the functionalized oxazoline monomers initiated by either methyl p-toluenesulfonate (leading to homopolymers A or B) or 2.0 kDa PEG methyl ether tosylate (macroinitiator). The latter resulted in BCP A and BCP B. (Note: homopolymer B and BCP B were Boc-deprotected by heating in a vacuum.) The last step was grafting polycaprolactone (PCL) side chains via ring-opening polymerization initiated by amino groups of (2-oxazoline) monomer units, yielding the amphiphilic biodegradable polyoxazoline-containing HCP A and HCP B.

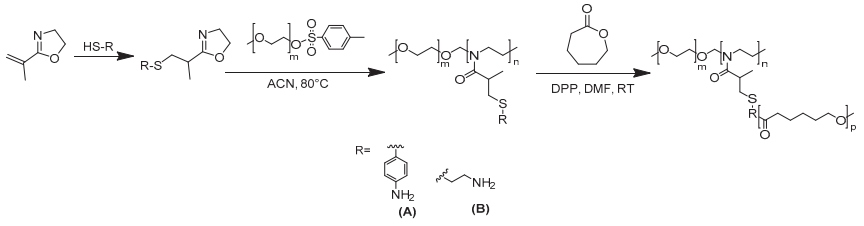

Scheme 1. The three-step synthetic scheme used for the synthesis of the HCPs. (A) aminothiophenol and (B) cysteamine.

1.1.3. NMR Spectroscopy

^{1}H NMR spectra were measured on a Bruker Avance III with a 400 MHz frequency using deuterated chloroform $CDCl_3$. All spectra were analyzed using TopSpin software.

1.1.4. Fluorescently Labeled Polymers

A solution of fluorescein isothiocyanate (FITC) was added dropwise to the homopolymers, BCPs, and HCPs in DMSO (1:10) overnight at room temperature, Scheme 2. The products were purified by precipitation in a 1:3 ethanol: diethyl ether solution and placed

in dialysis for three days. The polymers were dried under vacuum and analyzed using fluorescence.

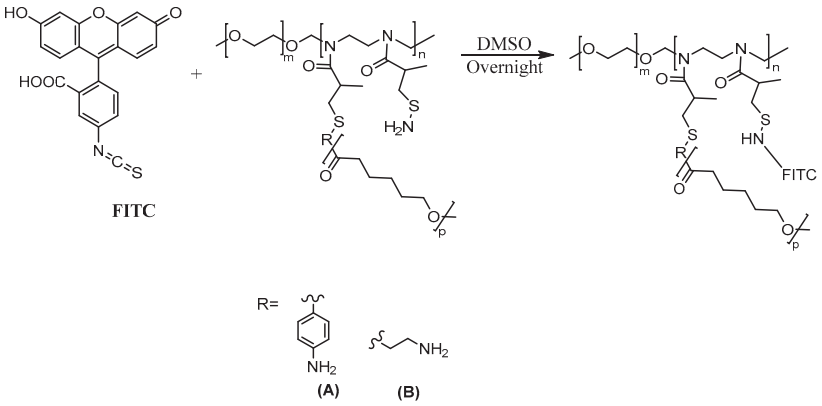

Scheme 2. Modification of hybrid block–graft copolymer with florescent fluorescein isothiocyanate. (A) aminothiophenol and (B) cysteamine.

1.1.5. Fluorescence Spectroscopy

A Cary Eclipse Fluorescence Spectrometer was used to collect the fluorescence spectra. The experiment was performed in emission mode. The PMT detector voltage of 750 V was used. The excitation wavelength used for the negative control, homopolymers, BCPs, and HCP was 490 nm, while the positive control wavelength was set to 260 nm.

1.2. Experimental Methods

1.2.1. Dynamic Light Scattering

Dispersions of HCP A and HCP B (0.1%) were prepared in water and prepared in a pH 6.86 buffer (0.01%). Each sample was filtered using a 0.45 µm filter then particle size was measured using a Malvern Zetasizer Nano ZS instrument at 30 °C; light source: He-Ne laser with 633 nm wavelength, cuvette cell type: glass cuvette PCS8501 made with quartz glass; the volume of the cuvette: 3.5 mL; light pathlength: 10 mm. Solvent: DI water, n = 1.330; viscosity, 0.7920 cP; polymers, n = 1.47; material absorption, 0.01.

1.2.2. Equilibration of EpiDerm™ Tissues

Under sterile conditions, the tissues were removed from the agarose packaging and placed in a 6-well plate with 0.9 mL of EPI-100-LLMM-X-PRF media. The samples were incubated overnight before use.

1.2.3. Skin Penetration Studies

The EpiDerm™ samples were removed from the incubator and placed inside the skin permeation devices provided by MatTek. Next, 0.4 mL of the fluorescently labeled polymer solutions (0.01%) was added to the receiver chamber of the devices (Figure 2). The media in the receiving chamber (5 mL) was collected after desired incubation time and substituted by new media. Fluorescence of the receiver solution was measured immediately after collection. The samples were taken and measured every 1–2 h for up to 24 h. Upon completion of the penetration experiments (24 h), the fluorescence of the donor solution was measured. The difference in fluorescence intensity of the donor solution before and after experimentation corresponded to the cumulative penetration of the polymers through the tissue film. The calculations for cumulative concentration and lag time were made in accordance with the recommendations given by MatTek [30].

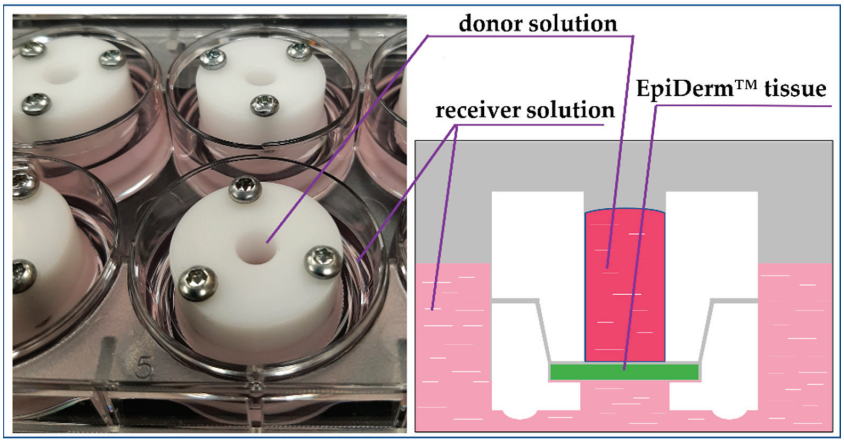

Figure 2. Skin penetration studies were performed in MatTek devices (cross-section is shown on the (**right**)) placed in 6-well plates (**left**). Donor solution was placed in the donor chamber on top of the EpiDerm tissue film. The receiver solution was collected for fluorescence measurement after desired incubation time.

1.2.4. Determination of Critical Micelle Concentration

The procedure was adapted from our previous work [13]. Aqueous stock solutions of HCPs (0.1%) were prepared. Aliquots of stock HCPs were made using serial dilutions by a factor of two. The absorbance of the HCP as a function of concentration was measured by UV/Vis (600 nm).

2. Results and Discussion

The structure of the polymers and HCPs was analyzed using ^{1}H NMR spectroscopy [13]. Homopolymer A is shown in green, and homopolymer B is shown in red (Figure 3). The long-chain polymer peaks are shown at 'e' and 'd'. The aromatic group of homopolymer A is shown at 6.6 ppm and 7.2 ppm. The Boc-protecting group of homopolymer B is shown at 1.4 ppm.

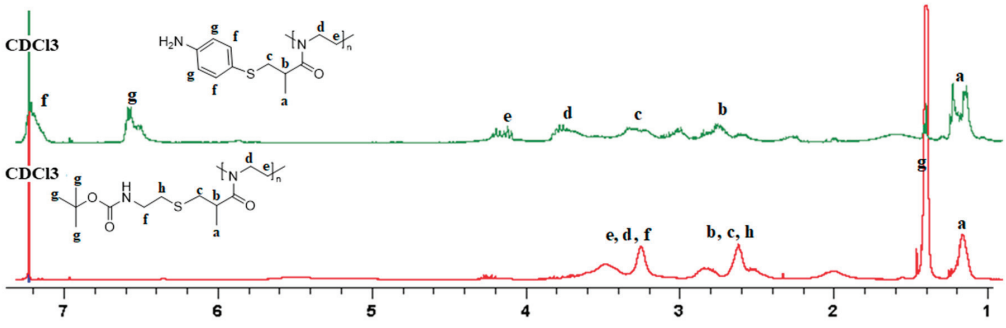

Figure 3. ^{1}H NMR spectra of the homopolymers probed for skin permeation: homopolymer A (green) and homopolymer B (red).

HCP A is shown in green, and HCP B is shown in red (Figure 4). The aromatic group on HCP A (green) remains unchanged and is visible at 6.6 ppm and 7.2 ppm. The PEG block is shown in both spectra at 3.6 ppm. The α-carbon on the PCL side chain is visible at 2.33 ppm. The long-chain carbons are shown at 1.67 ppm, 1.40 ppm, and 4.07 ppm.

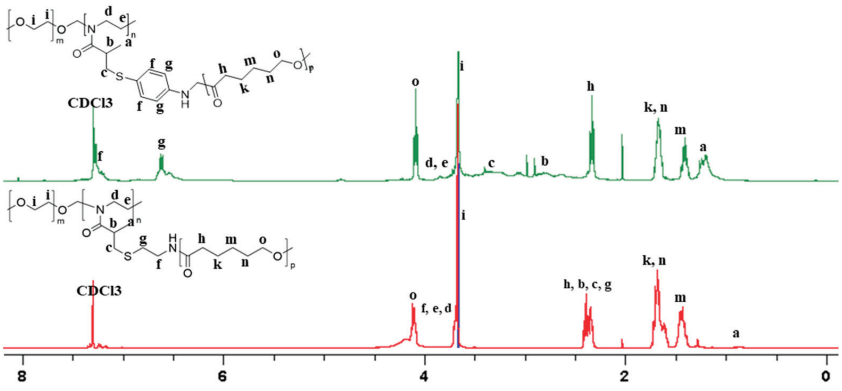

Figure 4. ^{1}H NMR spectra of the HCPs probed for skin permeation: HCP A (green), HCP B (red).

To study the size of the micelles formed by our HCPs, we performed DLS studies (Figures S1–S4) [34,35]. We studied two sets of solutions in DI water and a pH (6.86) buffer. The solutions in the buffer mimic the HCPs in the media when applied to the skin. The summary of our data is reported in Table 2.

Table 2. Summary of Micelle Size Collected from Dynamic Light Scattering.

	Micelle Size, nm	
	0.1% in DI Water	**0.01% in pH 6.86 Buffer**
HCP A	167.2.2 ± 71.6	275.5 ± 81.4
HCP B	227.9 ± 93.2	647.7 ± 119.2

Three parameters are considered to evaluate permeation efficiency: cumulative concentration, penetration rate, and lag time [36,37]. Cumulative concentration is the total amount of the polymer that penetrates through the sample. The penetration rate is the rate at which the polymer moves through the sample. The lag time is time required to polymer to appear in receiver solution.

The positive control was salicylic acid and the negative control was sodium fluorescein. Both controls were consistent throughout the experiment. Each experiment was performed in triplicate. The neat media solutions showed background fluorescence (intensity of 132 a.u. measured at 490 nm). The fluorescence intensity of the neat media was subtracted from the fluorescence intensity of the receiver media.

After two hours, the positive control fully penetrated the sample skin, and the negative control did not penetrate it, as expected. The fluorescence intensity of the donor solution, the donor solution after 24 h, and the analysis of the cumulative concentration are shown in the supplementary information (Figures S5 and S6).

Permeation of Aminothiophenol-Functionalized Polymers (A):

The stock solutions were diluted with media before applying them to the skin sample. The fluorescence intensity of the receiver media was taken every 1–2 h for 24 h. Each experiment was performed in triplicate. The fluorescence intensity of the neat media was subtracted from the fluorescence intensity of the receiver media. The fluorescence intensity of the donor solution, the donor solution after 24 h, and the cumulative concentration are shown in Figures 5 and 6.

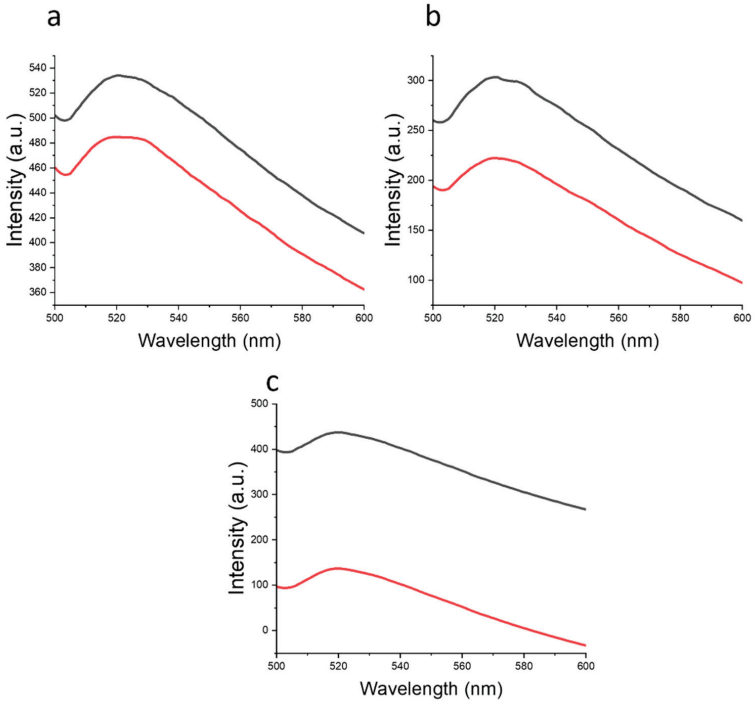

Figure 5. Emission spectra of (**a**) donor solution of homopolymer A before the experiment (black) and donor solution after the experiment (red), (**b**) donor solution of BCP A before the experiment (black) and donor solution after (red), and (**c**) donor solution of HCP A before the experiment (black) and donor solution after (red).

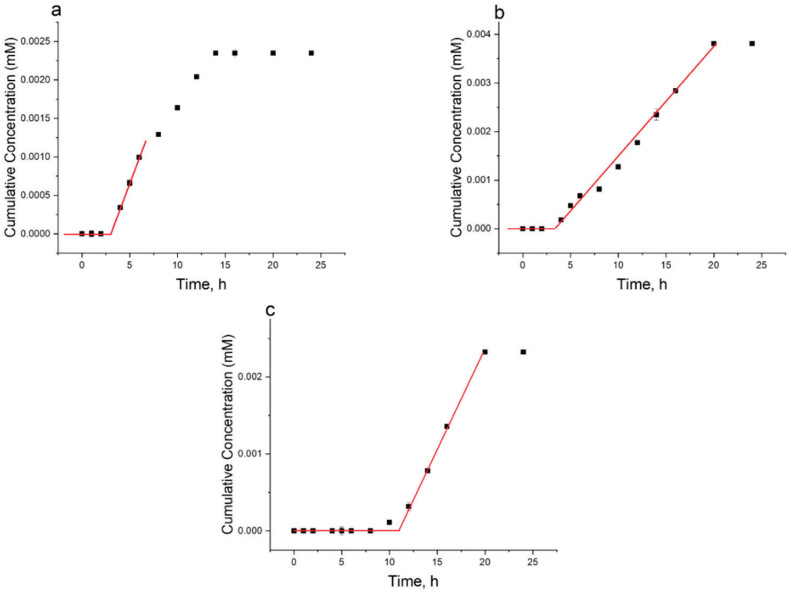

Figure 6. Cumulative concentration vs. time of (**a**) homopolymer A, (**b**) BCP A, and (**c**) HCP A.

The cumulative concentration plots show a change in the trend between 5 h and 10 h. We propose that this trend is due to the more rigid non-amphiphilic polymers becoming stuck in the skin sample.

Permeation of Cysteamine-Functionalized Polymers (B):

The stock solutions were diluted with media before applying them to the skin sample. The fluorescence intensity of the receiver media was taken every 1–2 h for 24 h. Each experiment was performed in triplicate. The fluorescence intensity of the neat media was subtracted from the fluorescence intensity of the receiver media. The fluorescence intensity and concentration of the donor solution, the donor solution after 24 h, and the cumulative concentration are shown in Figures 7 and 8.

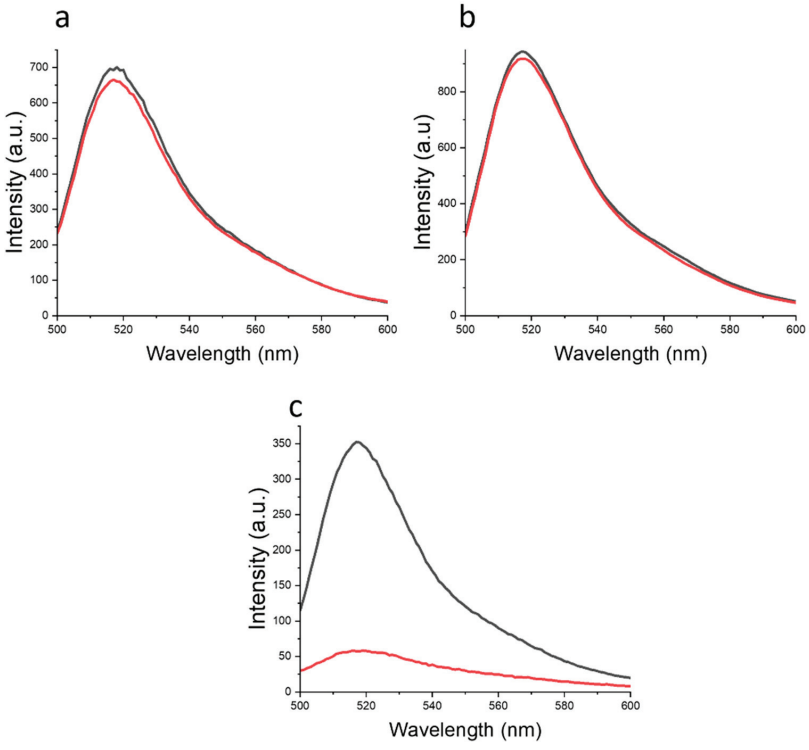

Figure 7. Emission spectra of (**a**) donor solution of homopolymer B before the experiment (black) and donor solution after the experiment (red), (**b**) donor solution of BCP B before the experiment (black) and donor solution after (red), (**c**) donor solution of HCP B before the experiment (black) and donor solution after (red).

The average penetration rate and lag time for all samples are shown in Figure 9. Homopolymer A slightly penetrated through the sample skin with a penetration percentage of 8.8%. The lag time of homopolymer A was the shortest of the aminothiophenol polymers. The penetration of homopolymer B was insignificant and could not be measured. BCP A partially penetrated through the sample, with a penetration percentage of 26.8%. The lag time of BCP A was between homopolymer A and HCP A. There was a significant discrepancy in the triplicate data collected for BCP B. We associate this discrepancy with the behavior of the BCP in the cells. Both HCPs fully penetrated through the sample of skin. We observed that the architecture of the HCP is more suitable for skin permeation than the architecture of the homopolymer and BCP. The lag time of HCP B ($\leq$30 min) is much

shorter than HCP A (9.38 h). This is in parallel with the DLS data, as well as previous data collected for their critical micelle concentration (CMC) values [13]. The CMC of HCP A is equal to 1.12×10^{-6} M $\pm$ 6.61×10^{-4} and HCP B is equal to 2.48×10^{-7} M $\pm$ 6.28×10^{-9} (Figure 10). The recorded micelle size of HCP A is smaller than the micelle size of HCP B (Table 2). We hypothesize that the penetration rate and lag time are not only related to micelle size but also may be related to CMC. The penetration characteristics, micelle size, and CMC depend on the hydrophilic/hydrophobic balance in the HCP.

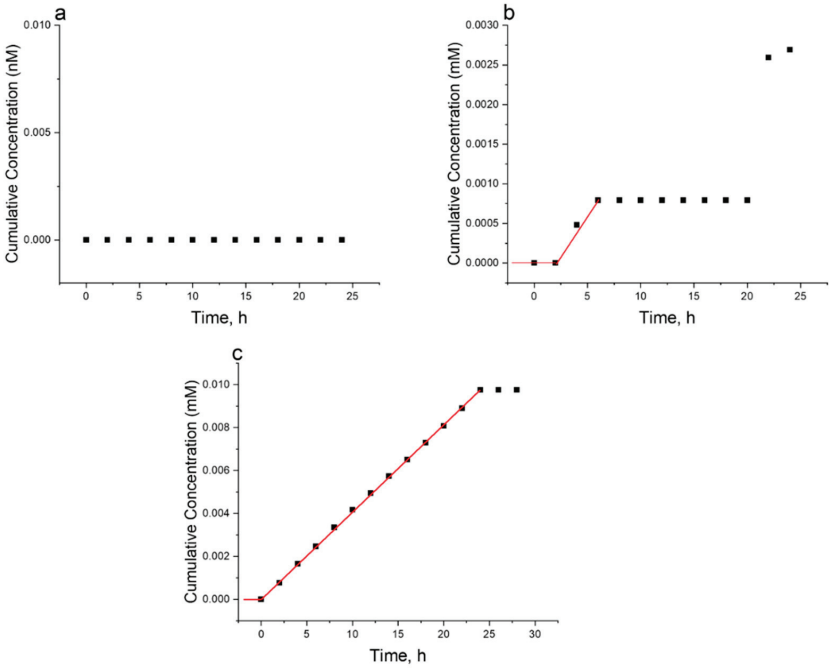

Figure 8. Cumulative concentration vs. time of (**a**) homopolymer B (**b**), BCP B, (**c**) HCP B.

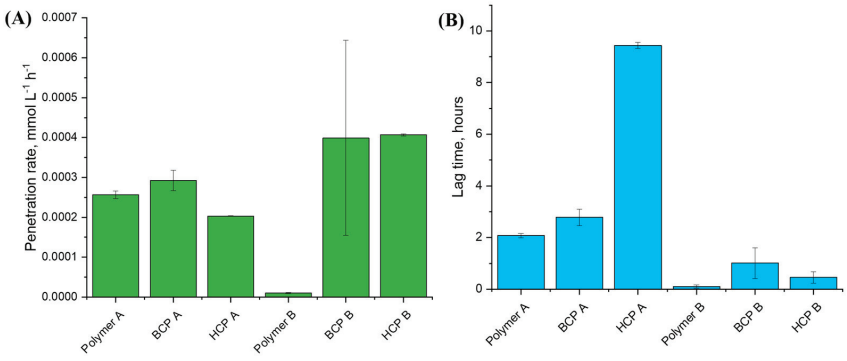

Figure 9. Bar graph of averaged (**A**) penetration rate and (**B**) lag time for all studied samples.

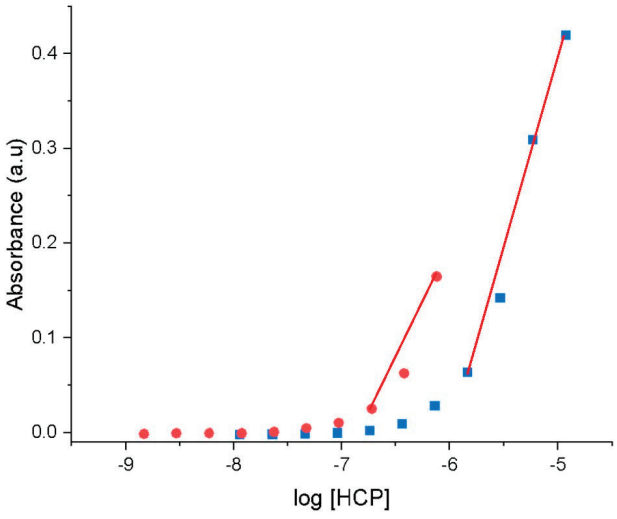

Figure 10. Critical micelle concentration of HCP A (blue) and HCP B (red).

3. Conclusions

The reported study shows that the hybrid block–graft copolymers based on a poly(2-oxazoline) backbone successfully penetrate the stratum corneum matrix, citing architecture and amphiphilicity as crucial characteristics for penetration efficiency. These hybrid polymers are good alternatives to PEG and can provide a simple and biocompatible vehicle for transdermal drug delivery. The skin permeation of the amino-containing oxazoline homopolymers, block copolymers, and hybrid block–graft copolymers was studied using the EpiDerm™ Skin Model. The homopolymers showed the lowest level of penetration. The block copolymer PEG-block-poly(4-aminothiophenol-2-oxazoline) partially penetrated the skin and had a lag time between that of the corresponding homopolymer and the hybrid polymer. The data collected for PEG-block-poly(cystamine-2-oxazoline) showed a significant discrepancy attributed to the micellar interaction with the cells. The hybrid copolymers showed the most efficient permeation, wherein cysteamine-modified hybrid B penetrated the tissue samples quicker than aminophenol-modified hybrid A. These observations correlate with the critical micelle concentration of the corresponding polymers. Interestingly, the size of the micelles is a less relevant characteristic for skin permeation. We hypothesize that a correct balance of hydrophobicity/hydrophilicity plays a primary role in permeability along with the architecture of the polymer (homopolymer vs. block vs. block–graft copolymer). More data are required to understand the mechanism of polymer permeation, and this is currently under investigation. In particular, more data on the correlation between hybrid polymer composition (fractions of hydrophobic polycaprolactone and hydrophilic PEG) and the length of each block may be of great importance, as well as toxicity studies of poly(2-oxazoline)-based constructs.

Supplementary Materials: The following supporting information can be downloaded at: https://www.mdpi.com/article/10.3390/coatings13061007/s1, Figures S1–S4: DLS data for 0.01% HCP A in buffer pH 6.86, 0.1% HCP A in water, 0.01% HCP B in buffer pH 6.86, 0.1% HCP B in water. Figure S5: Emission spectra of (a) donor solution of positive control before experiment (black) and donor solution after the experiment (red) (b) donor solution of negative control before experiment (black) and donor solution after experiment (red). Figure S6: Cumulative concentration vs. time of (a) positive control (b) negative control. Figure S7. Calibration curve of (a) positive control salicylic acid (b) negative control fluorescein sodium. Figure S8. Calibration curve of FITC-aminothiophenol-functionalized (a) homopolymers (b) BCPs (c) HCPs. Figure S9. Calibration curve of FITC-cysteamine-functionalized (a) homopolymers (b) BCPs (c) HCPs.

Author Contributions: Conceptualization, A.S. and G.S.; methodology, N.S.; formal analysis, A.T., and I.L.; investigation, G.S., G.R., K.G. and N.S.; data curation, G.R.; writing—original draft preparation, G.S.; writing—review and editing, A.S. and I.L.; supervision, A.S. All authors have read and agreed to the published version of the manuscript.

Funding: This research received no external funding.

Institutional Review Board Statement: Not applicable.

Informed Consent Statement: Not applicable.

Data Availability Statement: All data generated or analyzed during this study are included in this published article.

Conflicts of Interest: The authors declare no conflict of interest.

References

1. Prausnitz, M.R.; Langer, R. Transdermal Drug Delivery. *Nat. Biotechnol.* **2008**, *26*, 1261–1268. [CrossRef] [PubMed]
2. Chen, Z.; Lv, Y.; Qi, J.; Zhu, Q.; Lu, Y.; Wu, W. Overcoming or Circumventing the Stratum Corneum Barrier for Efficient Transcutaneous Immunization. *Drug. Discov. Today* **2018**, *23*, 181–186. [CrossRef] [PubMed]
3. Kapse, A.; Anup, N.; Patel, V.; Saraogi, G.K.; Mishra, D.K.; Tekade, R.K. Polymeric Micelles: A Ray of Hope Among New Drug Delivery Systems. In *Drug Delivery Systems*; Elsevier: Amsterdam, The Netherlands, 2020; pp. 235–289. [CrossRef]
4. Arora, A.; Prausnitz, M.R.; Mitragotri, S. Micro-Scale Devices for Transdermal Drug Delivery. *Int. J. Pharm.* **2008**, *364*, 227–236. [CrossRef] [PubMed]
5. Valenta, C.; Auner, B.G. The Use of Polymers for Dermal and Transdermal Delivery. *Eur. J. Pharm. Biopharm.* **2004**, *58*, 279–289. [CrossRef] [PubMed]
6. Kim, B.; Cho, H.-E.; Moon, S.H.; Ahn, H.-J.; Bae, S.; Cho, H.-D.; An, S. Transdermal Delivery Systems in Cosmetics. *Biomed. Dermatol.* **2020**, *4*, 10. [CrossRef]
7. Badri, W.; Eddabra, R.; Fessi, H.; Elaissari, A. Biodegradable Polymer Based Nanoparticles: Dermal and Transdermal Drug Delivery. *J. Colloid. Sci. Biotechnol.* **2014**, *3*, 141–149. [CrossRef]
8. Tiwari, N.; Osorio-Blanco, E.R.; Sonzogni, A.; Esporrín-Ubieto, D.; Wang, H.; Calderón, M. Nanocarriers for Skin Applications: Where Do We Stand? *Angew. Chem.-Int. Ed.* **2022**, *61*, e202107960. [CrossRef] [PubMed]
9. Raghavachari, N.; Fahl, W.E. Targeted Gene Delivery to Skin Cells in Vivo: A Comparative Study of Liposomes and Polymers as Delivery Vehicles. *J. Pharm. Sci.* **2002**, *91*, 615–622. [CrossRef]
10. Liechty, W.B.; Kryscio, D.R.; Slaughter, B.V.; Peppas, N.A. Polymers for Drug Delivery Systems. *Annu. Rev. Chem. Biomol. Eng.* **2010**, *24*, 12. [CrossRef]
11. Rancan, F.; Volkmann, H.; Giulbudagian, M.; Schumacher, F.; Stanko, J.I.; Kleuser, B.; Blume-Peytavi, U.; Calderón, M.; Vogt, A. Dermal Delivery of the High-Molecular-Weight Drug Tacrolimus by Means of Polyglycerol-Based Nanogels. *Pharmaceutics* **2019**, *11*, 394. [CrossRef]
12. Rancan, F.; Asadian-Birjand, M.; Dogan, S.; Graf, C.; Cuellar, L.; Lommatzsch, S.; Blume-Peytavi, U.; Calderón, M.; Vogt, A. Effects of Thermoresponsivity and Softness on Skin Penetration and Cellular Uptake of Polyglycerol-Based Nanogels. *J. Control. Release* **2016**, *228*, 159–169. [CrossRef] [PubMed]
13. Storti, G.; Jauhola-Straight, R.; Hannigan, J.R.; Sidorenko, A. Design of Amphiphilic, Biodegradable Functionalized Polyoxazoline Hybrid-Block Graft Copolymers Using Click Reactions. *Macromolecules* **2023**, *56*, 3538–3549. [CrossRef]
14. Nemati Mahand, S.; Aliakbarzadeh, S.; Moghaddam, A.; Salehi Moghaddam, A.; Kruppke, B.; Nasrollahzadeh, M.; Khonakdar, H.A. Polyoxazoline: A Review Article from Polymerization to Smart Behaviors and Biomedical Applications. *Eur. Polym. J.* **2022**, *178*, 111484. [CrossRef]
15. Luxenhofer, R.; Han, Y.; Schulz, A.; Tong, J.; He, Z.; Kabanov, A.V.; Jordan, R. Poly(2-Oxazoline)s as Polymer Therapeutics. *Macromol. Rapid. Commun.* **2012**, *33*, 1613–1631. [CrossRef] [PubMed]
16. Salgarella, A.R.; Zahoranová, A.; Šrámková, P.; Majerčíková, M.; Pavlova, E.; Luxenhofer, R.; Kronek, J.; Lacík, I.; Ricotti, L. Investigation of Drug Release Modulation from Poly(2-Oxazoline) Micelle through Ultrasound. *Sci. Rep.* **2018**, *8*, 9893. [CrossRef] [PubMed]
17. Cortez, M.A.; Grayson, S.M. Thiol-Ene Click Functionalization and Subsequent Polymerization of 2-Oxazoline Monomers. *Macromolecules* **2010**, *43*, 4081–4090. [CrossRef]
18. Zakharchenko, A.; Xue, Y.; Keeney, S.; Rock, C.A.; Alferiev, I.S.; Stachelek, S.J.; Takano, H.; Thomas, T.; Nagaswami, C.; Krieger, A.M.; et al. Poly-2-Methyl-2-Oxazoline–Modified Bioprosthetic Heart Valve Leaflets Have Enhanced Biocompatibility and Resist Structural Degeneration. *Proc. Natl. Acad. Sci. USA* **2022**, *119*, e2120694119. [CrossRef]
19. Zhou, C.; Wang, F.; Chen, H.; Li, M.; Qiao, F.; Liu, Z.; Hou, Y.; Wu, C.; Fan, Y.; Liu, L.; et al. Selective Antimicrobial Activities and Action Mechanism of Micelles Self-Assembled by Cationic Oligomeric Surfactants. *ACS Appl. Mater. Interfaces* **2016**, *8*, 4242–4249. [CrossRef]

20. Paulovičová, E.; Kroneková, Z.; Paulovičová, L.; Majerčíková, M.; Kronek, J. Cell-Mediated Immunoreactivity of Poly(2-Isopropenyl-2-Oxazoline) as Promising Formulation for Immunomodulation. *Materials* **2021**, *14*, 1371. [CrossRef]
21. Miyata, K.; Christie, R.J.; Kataoka, K. Polymeric Micelles for Nano-Scale Drug Delivery. *React. Funct. Polym.* **2011**, *71*, 227–234. [CrossRef]
22. Adams, N.; Schubert, U.S. Poly(2-Oxazolines) in Biological and Biomedical Application Contexts. *Adv. Drug. Deliv. Rev.* **2007**, *59*, 1504–1520. [CrossRef]
23. Vlassi, E.; Papagiannopoulos, A.; Pispas, S. Amphiphilic Poly(2-Oxazoline) Copolymers as Self-Assembled Carriers for Drug Delivery Applications. *Eur. Polym. J.* **2017**, *88*, 516–523. [CrossRef]
24. Simon, L.; Vincent, M.; Le Saux, S.; Lapinte, V.; Marcotte, N.; Morille, M.; Dorandeu, C.; Devoisselle, J.M.; Bégu, S. Polyoxazolines Based Mixed Micelles as PEG Free Formulations for an Effective Quercetin Antioxidant Topical Delivery. *Int. J. Pharm.* **2019**, *570*, 118516. [CrossRef] [PubMed]
25. Deng, C.; Jiang, Y.; Cheng, R.; Meng, F.; Zhong, Z. Biodegradable Polymeric Micelles for Targeted and Controlled Anticancer Drug Delivery: Promises, Progress and Prospects. *Nano. Today* **2012**, *7*, 467–480. [CrossRef]
26. Rudmann, D.G.; Alston, J.T.; Hanson, J.C.; Heidel, S. High Molecular Weight Polyethylene Glycol Cellular Distribution and PEG-Associated Cytoplasmic Vacuolation Is Molecular Weight Dependent and Does Not Require Conjugation to Proteins. *Toxicol. Pathw.* **2013**, *41*, 970–983. [CrossRef] [PubMed]
27. Ishida, T.; Kiwada, H. Accelerated Blood Clearance (ABC) Phenomenon upon Repeated Injection of PEGylated Liposomes. *Int. J. Pharm.* **2008**, *354*, 56–62. [CrossRef]
28. Verhoef, J.J.F.; Anchordoquy, T.J. Questioning the Use of PEGylation for Drug Delivery. *Drug. Deliv. Transl. Res.* **2013**, *3*, 499–503. [CrossRef]
29. Einzmann, M.; Binder, W.H. Novel Functional Initiators for Oxazoline Polymerization. *Polym. Chem.* **2001**, *29*, 2821–2831. [CrossRef]
30. Kobayashi, S.; Tokuzawa, T.; Saegusa, T. Cationic Ring-Opening Isomerization Polymerization of 2-[p-(Substituted)Phenyl]-2-Oxazolines. Effects of the Substituent on the Reactivities. *MTP Int. Rev. Sci. Phys. Chem. Ser.* **1982**, *15*, 495.
31. Mattek Company. *The EpiDermTM Skin Model*; BiCo Group: Gothenburg, Sweden, 2016. Available online: https://www.mattek.com/mattekproduct/epiderm/ (accessed on 20 April 2023).
32. Schäfer-Korting, M.; Bock, U.; Diembeck, W.; Düsing, H.J.; Gamer, A.; Haltner-Ukomadu, E.; Hoffmann, C.; Kaca, M.; Kamp, H.; Kersen, S.; et al. The Use of Reconstructed Human Epidermis for Skin Absorption Testing: Results of the Validation Study. *ATLA Altern. Lab. Anim.* **2008**, *36*, 161–187. [CrossRef]
33. Lombardi Borgia, S.; Schlupp, P.; Mehnert, W.; Schäfer-Korting, M. In Vitro Skin Absorption and Drug Release—A Comparison of Six Commercial Prednicarbate Preparations for Topical Use. *Eur. J. Pharm. Biopharm.* **2008**, *68*, 380–389. [CrossRef] [PubMed]
34. Topel, Ö.; Çakir, B.A.; Budama, L.; Hoda, N. Determination of Critical Micelle Concentration of Polybutadiene-Block-Poly(Ethyleneoxide) Diblock Copolymer by Fluorescence Spectroscopy and Dynamic Light Scattering. *J. Mol. Liq.* **2013**, *177*, 40–43. [CrossRef]
35. Sutherland, E.M.; Mercer, S.; Everist, M.G.; Leaist, D. Diffusion in Solutions of Micelles. What Does Dynamic Light Scattering Measure? *J. Chem. Amp. Eng. Data* **2008**, *54*, 272–278. [CrossRef]
36. Okamoto, H.; Taguchi, H.; Iida, K.; Danjo, K. Development of Polymer Film Dosage Forms of Lidocaine for Buccal Administration: I. Penetration Rate and Release Rate. *J. Control. Release* **2001**, *77*, 253–260. [CrossRef]
37. Perinelli, D.R.; Cespi, M.; Lorusso, N.; Palmieri, G.F.; Bonacucina, G.; Blasi, P. Surfactant Self-Assembling and Critical Micelle Concentration: One Approach Fits All? *Langmuir* **2020**, *36*, 5745–5753. [CrossRef]

coatings

MDPI

Article

Assessing the Bioreceptivity of Biobased Cladding Materials

Karen Butina Ogorelec [1,2,*], Ana Gubenšek [1,2], Faksawat Poohphajai [1,2,3] and Anna Sandak [1,2,4,*]

[1] InnoRenew CoE, Livade 6a, 6310 Izola, Slovenia; ana.gubensek@innorenew.eu (A.G.); faksawat.poohphajai@innorenew.eu (F.P.)
[2] Andrej Marušič Institute, University of Primorska, Muzejski trg 2, 6000 Koper, Slovenia
[3] Department of Bioproducts and Biosystems, Aalto University School of Chemical Engineering, 00076 Aalto, Finland
[4] Faculty of Mathematics, Natural Sciences and Information Technologies, University of Primorska, Glagoljaška 8, 6000 Koper, Slovenia
* Correspondence: karen.butina@innorenew.eu (K.B.O.); anna.sandak@innorenew.eu (A.S.)

Abstract: Materials exposed to the outdoors are prone to various deterioration processes. Architectural coatings are designed to protect surfaces against environmental and biotic degradation and to provide a decorative layer. The objective of this work was to examine the early colonisers on a diverse set of coated and non-coated biobased façade materials. A set of 33 wood-based cladding materials were exposed to four cardinal directions and monitored in outdoor conditions. The surfaces were sampled using a wet swab and plated on DG-18 agar, which prevents the growth of bacteria and limits the growth of fast-growing fungi. Pure cultures were then isolated and identified through PCR amplification and Sanger sequencing of specific DNA regions/genes. The response of cladding materials to weathering and fungal infestation was assessed. The proposed techniques enabled the identification of features that promote/inhibit fungal colonisation and revealed the preference of certain fungi for specific materials. Both the material type and the climate condition at the exposure site influence fungal colonisation. This study is a starting point for more exhaustive assays that aim to develop a novel coating system based on controlled and optimized fungal biofilm formation, and is proposed as a nature-inspired alternative for the protection of architectonic surfaces.

Keywords: coating; materials performance; bioreceptivity; natural weathering; fungal infestation; early fungal colonisers

Citation: Butina Ogorelec, K.; Gubenšek, A.; Poohphajai, F.; Sandak, A. Assessing the Bioreceptivity of Biobased Cladding Materials. *Coatings* **2023**, *13*, 1413. https://doi.org/10.3390/coatings13081413

Academic Editor: Seungil Kim

Received: 13 July 2023
Revised: 4 August 2023
Accepted: 8 August 2023
Published: 11 August 2023

1. Introduction

Wooden cladding materials are susceptible to biotic attack by moulds and decay fungi. The latter causes structural weakening of the wooden material, while the former leads to surface discolouration and affects the aesthetic appeal. The occurrence of either type depends on the environmental conditions, wood moisture content, and durability of the cladding material [1]. Together with other microorganisms and insects, fungi contribute to the biodeterioration of wood that occurs in parallel with abiotic deterioration caused by wind, rain, temperature, and UV radiation.

While their aesthetic appeal, availability, affordability, and environmental friendliness contribute to the popularity of wooden cladding materials, their maintenance remains challenging due to the reasons stated above [2]. Coatings are often applied for wood protection but have historically contained substantial amounts of VOCs. With growing environmental concerns, the use of high-VOC paints has been highly restricted according to European Directive 2004/42/CE. Low-emission coatings are, however, still niche products since 70% of the raw materials are based on petroleum (mineral oil) [3]. Nevertheless, there is a shift from solvent-based to water-based architectural coatings. Water-based coatings unfortunately do not always match the performance of solvent-based ones [4], posing a significant challenge to the coating industry. The water-based formulation leads to quick

evaporation of water resulting in tacky, more viscous paint [5]. Architectural coatings manufacturers are, therefore, focusing on developing formulations that offer longer open times for paint users, defined as the "time after application beyond which further reworking of the paint film results in visible surface defects" [6]. Moreover, aqueous raw materials used in the formulation of paints and coatings create a beneficial environment for the growth of bacteria, fungi, and yeast [7]. To prevent the growth of microorganisms, various biocides can be employed. Copper-rich systems are commonly used; however, there are concerns regarding damage to aquatic systems as well as the disposal of treated wood [8]. Due to the stringent EU legislation as well as awareness of health and environmental issues, there is a need to develop non-toxic biobased wood coatings with satisfactory performance [9].

Bioreceptivity is defined as the ability of a material to be colonised by one or several groups of living organisms without necessarily undergoing any biodeterioration [10]. However, it is often desirable to remove any kind of colonisation from building surfaces for preventive conservation but also to maintain cleanliness and order [11]. Nevertheless, in line with the bioreceptivity concept, an innovative approach to wood protection has been described, where the growth of a yeast-like fungus, *Aureobasidium pullulans* (*A. pullulans*), on wood impregnated with linseed oil has exhibited protection of the wood rather than its degradation [12]. This was made possible by understanding the interaction between the wood and the fungus and creating circumstances where the fungus exhibited a protective effect. We consider this an important milestone in the development of alternative coating systems, demonstrating that fungi are not necessarily only harmful but can be beneficial as well. An understanding of fungal colonisation on façade materials is indispensable to further such efforts and develop novel concepts for material protection. An example of such an alternative coating system based on a controlled and optimised fungal biofilm is currently under development within the frame of the ARCHI-SKIN project [13].

In most studies where fungal growth on wooden materials was investigated, the earliest time point for fungal infestation evaluation is 3 months after sample exposure [14–16] or more [17,18]. We would like to argue that earlier time points deserve more attention as they can provide information about the initial steps of fungal attachment and growth on surfaces [19], which is relevant both for their prevention and promotion.

In the literature, samples are often exposed in a single cardinal direction [15–18], yet Podgorski et al., who exposed samples in all four cardinal directions, found they did differ [14]. In real life, cladding materials are exposed in all cardinal directions (on buildings) and the information about their respective performance is of relevance. Moreover, the architectonic design and specific 3D geometry of buildings create specific zones that might be more or less exposed to the weathering process. Consequently, environmental exposure (dose) is closely related to material response [20].

The objective of this work was to examine the early colonisers on a diverse set of façade materials including commercial materials that are coated and non-coated. The effect of the exposure site on the microbial burden and the presence of dominant species on various materials were investigated. Simultaneously, the response of cladding materials to weathering and fungal infestation was assessed to determine whether fungal presence is necessarily connected with material deterioration. The experiment is ongoing with the aim of identifying fungal species that simultaneously possess the potential to uniformly cover the surface and not cause material deterioration.

2. Materials and Methods

2.1. Experimental Materials and Natural Weathering

Experimental samples were obtained from 30 industrial partners from 17 countries that provided experimental material for the BIO4 ever project [21] and included specimens representing natural wood, thermally, chemically, and surface-treated wood, impregnated wood, biobased composites, and hybrid modification merging more than one of the above categories. The size of each individual sample was ~150 L × ~75 W × ~20 T mm^3. Before

weathering, samples were scanned with an office scanner HP Scanjet 2710 (300 dpi, 24 bit) and saved as TIF files (Figure 1a). All information available about the samples can be found in Table 1. The 33 different cladding materials analysed in this work were a subset of 93 different cladding materials that were placed on the roof of the InnoRenew CoE building, situated in the coastal town of Izola, Slovenia (45.5350, 13.6577). For each cladding material, 2 duplicate samples (left, right) were exposed in each cardinal direction. Samples were mounted on a vertical stand on 13–14 October 2022 and exposed to natural weathering. The results related to microbial growth reported in this work are from observations conducted after the first month of exposure, unless when explicitly stated otherwise. The meteorological data were obtained from the Historical Weather API (https://open-meteo.com/, accessed on 14 June 2023) (Figure 1b). The data are based on reanalyses of datasets and employ a combination of radar, satellite, aircraft, buoy, and weather station observations. Mathematical models are used to fill in gaps in the data. Reference (=unweathered) samples were stored indoors at ambient conditions (~50% RH, ~21 °C).

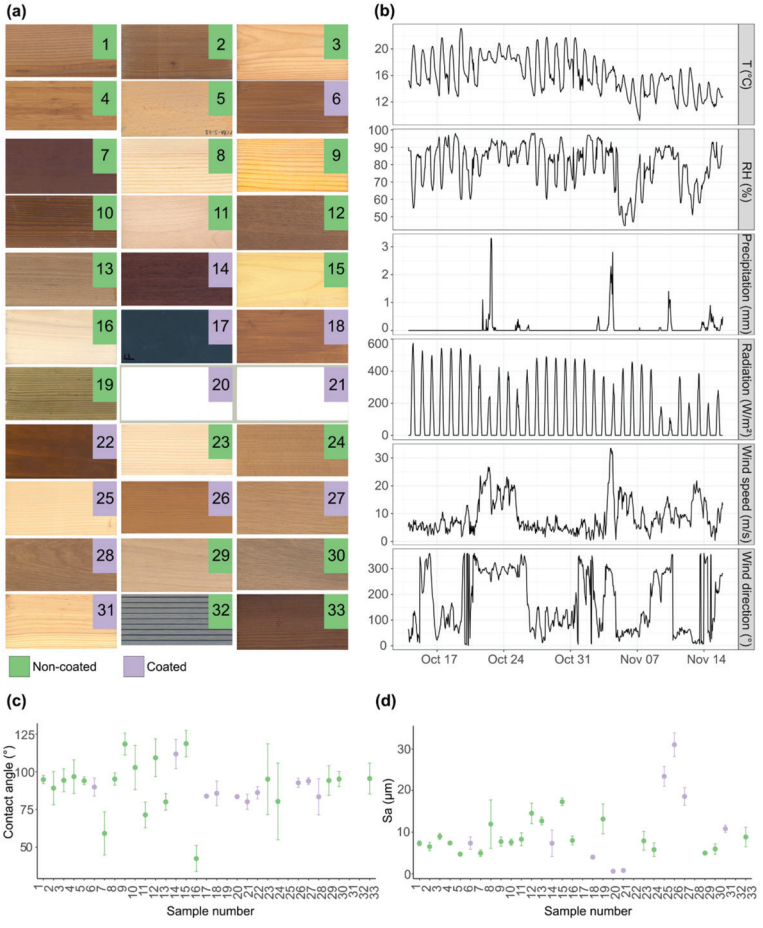

Figure 1. (**a**) Scans of samples included in the study. The sample number (see Table 1) in the purple square represents coated samples while those in the green square are not coated. (**b**) Weather data for one month of exposure (14 October 2022–15 November 2022). Hourly data for temperature (T), relative humidity (RH), precipitation, shortwave radiation (radiation), wind speed, and wind direction are displayed. (**c**,**d**) Contact angle (**c**) and Sa (**d**) of reference samples. Mean ± SD of technical replicates is shown. Colours are the same as in (**a**).

Table 1. List of cladding materials.

Sample nr.	Group [1]	Sample Information	Coating	Species
1	therm	Treated in 212 °C	no	spruce
2	hybr	Treated in 212 °C with addition of $FeSO_4$	no	spruce
3	natr	Heartwood kiln dried 50–70 °C	no	pine
4	surf	Oiled stick-glued bamboo façade profiles	no	bamboo
5	impr	Wood impregnated with silicone and silicate	no	beech
6	hybr	Thermally treated and coated (industrially) Semi-transparent coating	yes	spruce
7	chem	Furfurylated (industrially)	no	pine
8	impr	Impregnated with TO_2 nanoparticles	no	pine
9	hybr	Impregnated with TO_2 nanoparticles and linseed oil	no	pine
10	hybr	Thermally treated and impregnated with copper oxide, boric acid, and tebuconazole	no	pine
11	natr	Air dried	no	beech
12	therm	Hydro-thermally treated (industrially)	no	frake
13	chem	Acetylated (industrially)	no	beech
14	hybr	Thermally treated and coated (industrially) Semi-transparent coating	yes	frake
15	impr	Soaked with concentrated fluorosilane	no	poplar
16	impr	Melamine treated	no	poplar
17	comp	Coated acetylated MDF (industrially) Opaque petroleum grey coating	yes	composite
18	surf	Coated with solvent-based product (industrially) Semi-transparent coating	yes	pine
19	impr	Treated with copper ethanolamine	no	spruce
20	comp	Coated acetylated MDF (industrially) Opaque white coating	yes	composite
21	hybr	Acetylated and coated (industrially) Opaque white coating	yes	pine
22	hybr	Acetylated and coated (industrially) Semi-transparent coating	yes	pine
23	natr	Natural fir (kiln dried)	no	fir
24	therm	Thermally treated fir (vacuum)	no	fir
25	surf	Coated (industrially)Transparent coating	yes	fir
26	hybr	Coated thermally treated fir (industrially) Transparent coating	yes	fir
27	surf	Coated natural oak (industrially) Transparent coating	yes	oak
28	hybr	Coated thermally treated oak (industrially) Transparent coating	yes	oak
29	natr	Natural oak (kiln dried)	no	oak

Table 1. *Cont.*

Sample nr.	Group [1]	Sample Information	Coating	Species
30	therm	Thermally treated oak (vacuum)	no	oak
31	surf	Nanoparticle transparent coating, 3 layers (DIY application)	yes	pine
32	comp	Wood–plastic composite	no	composite
33	therm	Over-thermally treated spruce	no	spruce

[1] Group: therm = thermally treated; hybr = hybrid; natr = natural; impr = impregnated; chem = chemically treated; comp = composite; surf = surface treated.

2.2. Surface Wettability and Topography Measurements

The contact angle and topography measurements of reference samples were obtained with an Attension Theta Flex Auto 4 optical tensiometer equipped with a 3D topography module (Biolin Scientific, Gothenburg, Sweden). On each sample, five contact angle measurements with distilled water were performed. The drop volume was 4 µL, and the contact angle was evaluated at the 20 s timepoint. Image processing was performed with OneAttension v 4.0.5 software, and the Young–Laplace equation was employed to determine the contact angle. The contact angle could not be measured on samples 19, 25, 31, and 32. The last had a grooved surface, 19 and 25 were too hydrophilic and the contact angle could not be measured for 20 s during all five measurements, while 31 was too hydrophobic and the droplet did not attach to the surface. Three topography measurements, each covering an area of 3.2 mm × 2.8 mm were performed. The Sa parameter was evaluated. Measurements were performed on all reference samples except 17 and 22, which were too reflective, 28, where the signal-to-noise ratio was not acceptable, and 32, due to its particular topography. The contact angle and topography were also measured on a subset of wooden samples dismounted from the roof at the 2.5-month timepoint. The measurements were performed after climatising materials to the equilibrium moisture content (~50% RH, ~21 °C). The procedure was similar to the one described above; however, contact angle measurements were performed in triplicates and not quintuplicates.

2.3. Evaluation of Microbial Growth

Dichloran glycerol agar (DG-18, REF: 40587, NutriSelect® Plus, Merck Millipore, Merck KGaA, Darmstadt, Germany), potato dextrose agar (PDA, REF: 4019352, Biolife, Milan, Italy), and malt extract agar (MEA, REF: 4016552, Biolife, Milan, Italy) were prepared according to the manufacturers' instructions and poured into 90 mm diameter plastic Petri dishes. The plates were left to solidify at ambient conditions and stored at 4 °C until use. Nylon swabs (REF: 2123-1003, Citotest, Haimen, Jiangsu, China), wetted in sterilised distilled water, were used for sampling. An area of approx. 2.5 cm × 2.5 cm in the upper left corner of each sample was swabbed and directly spread on DG-18. Plates were incubated under ambient conditions for 1 week before evaluation. Colony forming units (CFU) were counted if possible—100 was defined as the upper limit and all plates containing counts >100 were assigned a CFU count of 100. From DG-18 plates with at least 10 CFU, where at least 90% of the colonies appeared to be of the same morphology (by visual evaluation), a representative colony of the prevalent morphology was isolated to a pure culture on PDA plates. Cultures were deposited in the Microbial Culture Collection Ex (Department of Biology, Biotechnical Faculty, University of Ljubljana, Ljubljana, Slovenia).

2.4. Visualisation and Identification of Fungal Macro- and Micromorphological Features

Selected cultures were retrieved from the Microbial Culture Collection Ex and grown on MEA at ambient conditions for 7–9 days. The macromorphology of pure cultures was visualised and imaged using the colonyQuant automated colony counter (Schuett, Göttingen, Germany). For *A. pullulans*, *A. melanogenum*, and *Penicillium* sp., a small portion of each respective pure culture was placed directly in a drop of 0.9% *w*/*v* sodium chloride

solution on a microscope slide, covered with a cover glass and sealed with nail polish. From pure cultures of *Alternaria alternata* and *Cladosporium* sp., two slide cultures were prepared using MEA agar cubes, as described previously [22]. Briefly, the agar cubes were placed on microscope slides, inoculated with each of the selected pure cultures, and covered with a cover glass. The slide cultures were incubated at 25 °C for 3 days. Subsequently, the cover glass was removed, placed on a drop of 0.9% *w*/*v* sodium chloride solution on a microscope slide, and sealed with nail polish. Transmitted light microscopy was performed with an EVOS™ M7000 Imaging System (Thermo Fisher Scientific, Waltham, MA, USA) using a 60× objective.

A subset of wooden samples was dismounted from the roof at the 2.5-month timepoint and imaging was performed after climatising materials to the equilibrium moisture content (~50% RH, ~21 °C). The samples were imaged with a Keyence VHX-6000 digital microscope (Keyence, Osaka, Japan). Colour images were acquired at 500× magnification.

2.5. Molecular Identification of Selected Isolates

Prior to DNA isolation, selected isolates were grown on PDA plates for one week. Genomic DNA was extracted after mechanical lysis in CTAB buffer as described previously [23]. Identification was based on PCR amplification and Sanger sequencing of certain DNA regions/genes. These included internal transcribed spacers 1 and 2 including the 5.8S rDNA (ITS) with primer set ITS5 [5′-GGA AGT AAA AGT CGT AAC AAG G-3′] and ITS4 [5′-TCC TCC GCT TAT TGA TAT GC-3′] [24] for a majority of isolates, partial sequences of genes encoding for actin (act) for genera *Alternaria* and *Cladosporium* with primers ACT-512F [5′-ATG TGC AAG GCC GGT TTC GC-3′] and ACT-738R [5′-TAC GAG TCC TTC TGG CCC AT-3′] [25], and β-tubulin (benA) for genus *Penicillium* with Ben2f [5′-TCC AGA CTG GTC AGT GTG TAA-3′] [26] and Bt2b [5′-ACC CTC AGT GTA GTG ACC CTT GGC-3′] [27]. After obtaining sequences of isolates from Microsynth (Austria), the most similar sequences of type strains and other important taxonomical reference strains were retrieved from the GenBank nucleotide database with the blast algorithm [28]. All sequences were aligned and phylogenetically analysed using the maximum likelihood method as implemented in program Mega11 [29]. All DNA sequences from the representative isolates from this study were deposited in the GenBank database: OR054020-OR054066.

For two samples where a majority of pink yeast (presumably *Aureobasidium* sp.) was observed, we were not able to obtain the species identity (29 west, left panel and 18 east, left panel).

2.6. Data Analysis

The R programming language [30] was used for data analysis. R and Inkscape were used for data visualisation. *p*-values were adjusted using the Bonferroni multiple testing correction method. The size of all tests was 0.05.

3. Results and Discussion

3.1. Experimental Setup

The investigated sample set consisted of a wide range of coated and non-coated commercial cladding materials (Table 1, Figure 1a). Since most of the samples were obtained from commercial entities, the exact chemical composition of certain coatings and treatments could not be obtained. Nonetheless, we considered these materials relevant for investigation since these are the materials that are used as façade elements in "real life." Just over a third of the investigated materials were coated, half of those were hybrid materials, one-third were surface-treated, and the rest were composites. Among non-coated samples, thermally treated and impregnated were the most represented, followed by natural, hybrid, chemically treated, surface-treated and composites. Eight different species were represented among non-coated samples, five among coated. The materials were exposed in all cardinal directions, with duplicate samples for each material in each direction—all together this amounted to eight samples for each material.

The roughness and wettability of investigated materials were evaluated (Figure 1c,d). We considered these parameters important as it has previously been shown that they influence fungal spore adhesion to surfaces [31,32]. There was no overall difference in the wettability and roughness between the coated and non-coated materials, both categories containing samples that spanned a wide range. Interestingly, certain non-coated samples (7, 10, 12, 23, 24) exhibited a rather wide scatter of the measured contact angles but not of Sa. This might be due to biological nature and intrinsic heterogeneity of investigated materials (e.g., differences between early and late wood, presence of wood defects).

The samples were exposed to natural weathering between mid-October and mid-November (Figure 1b). This was early autumn in a coastal region, with consistently high relative humidity and temperatures between 10 °C and 25 °C. These conditions were favourable for microbial growth [33] and the results presented in this work would most likely be different if another time period would be chosen for weathering and sampling.

3.2. Microbial Burden across Cardinal Directions

It has previously been reported that the cardinal direction of exposure affects the colour and chemical changes in the wood due to weathering [19,34–36]. Few reports are available on the effects of cardinal direction on fungal growth and/or associated surface discolouration [14,36]. To investigate this, samples exposed in all directions were swabbed and colony forming units (CFUs) were counted (Figure 2). The placement of sample materials on the stand (Figure 2a) and a visual representation of averaged counts of duplicate samples exposed in all cardinal directions are represented (Figure 2b–e).

It is important to mention that despite the physical contact between the samples, the fungal counts of neighbouring samples can differ profoundly. This means that the fungi did not spread uncontrollably between materials, indicating that their growth was governed by specific material properties.

Differences between the cardinal directions are summarised in a boxplot shown in Figure 2f. For all directions, we have materials that range between 0 and 100 colonies (upper limit); however, the central tendencies (represented by median and mean) between the cardinal directions differ. The distributions of the CFU counts on samples exposed in the four directions were found to differ significantly. The least growth was observed in the south, which might be due to the longer exposure to UV radiation leading to faster changes in surface moisture [19]. The highest fungal burden was observed in the east and west, which can partly be explained by the predominant wind direction in autumn in Izola (Figure 1b). The wind-driven rain is the largest moisture source that influences the hygrothermal performance of building envelopes [37], causing more pronounced mould growth.

Wet swabbing and direct re-plating on agar is a relatively fast method that made it possible to swab the 264 samples exposed on the roof in a single day, but there are shortcomings that need to be taken into account. Since only a limited area of the sample was swabbed, the results might not always be representative of the whole surface. Moreover, the swabbing technique in itself is problematic for the enumeration of CFUs since spores can produce more colonies on agar compared to the same biomass consisting of hyphae, and the choice of culturing media can affect the growth of fungi [38]. We did not perform dilution plating, which resulted in some plates being overgrown and the CFUs could not be enumerated but were assigned the arbitrary number of 100 CFU. Nonetheless, the approach taken was robust and enabled comparisons between samples, since the same errors were introduced for all samples. However, the interpretation of any absolute values should be performed with caution.

These results demonstrate that the cardinal direction of exposure influences fungal colonisation of materials and is in line with previously published reports [39]. The doses of UV, wind, and wind-driven rain all strongly depend on the exposure direction and influence material weathering, which might directly and indirectly influence fungal growth.

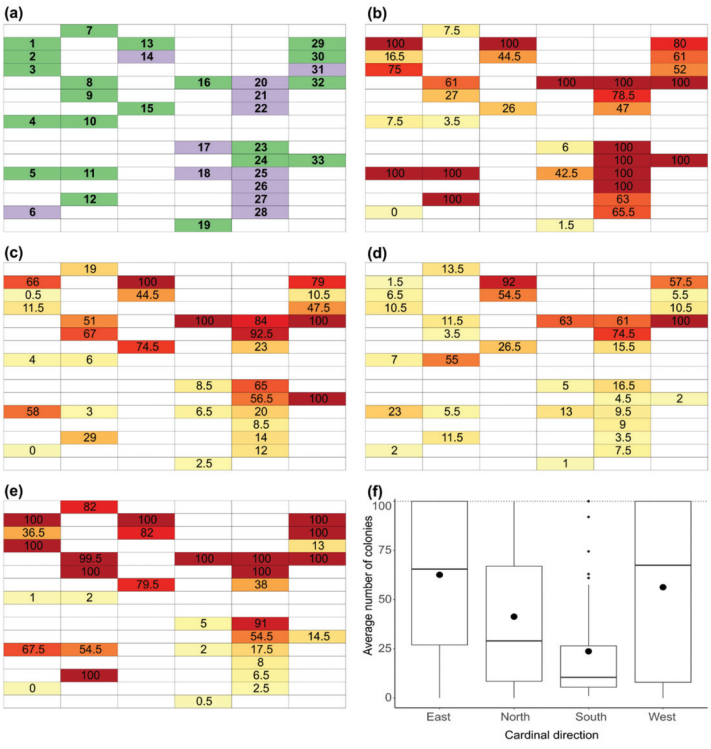

Figure 2. (**a**) Placement of material samples on the stands. The sample number (see Table 1) in the purple square represents coated samples while those in the green square are not coated. (**b**–**e**) Average number of colonies from duplicate samples exposed to the (**b**) east, (**c**) north, (**d**) south, and (**e**) west. (**f**) Average number of colonies at different cardinal directions. Black points represent mean values. The four groups do not have equal distributions (Friedman test, $p < 0.05$). There are significant differences between east and north, east and south, north and south, west and south (Wilcoxon signed-rank test, $p < 0.05$). Note: The colour gradient (bright yellow to dark red) corresponds to the average number of colonies (0 to 100, respectively).

3.3. Materials Resistant to Fungal Growth

Due to the biodegradation and discolouration associated with fungal colonisation and growth on wooden materials, great efforts are being invested in prevention. Most of the materials used in this study are commercial and several were treated to provide antifungal properties (Table 2).

To determine which samples were not susceptible to fungal colonisation and growth in our test, we identified those that had less than 10 CFUs from the swabbed regions of at least seven out of eight exposed samples (Figure 3a). Two of these samples were coated (samples nr. 6, 17) and two were not (samples nr. 4, 19). Two and a half months after the samples were exposed (that is 6 weeks after the first sampling), several samples (all N-L) were dismounted, conditioned, and examined under the microscope for the visual presence of fungi. Interestingly, samples 4 (Figure 3b) and 6 (Figure 3c) were still devoid of any visible fungal growth. This was in stark contrast with several other samples, where abundant growth was observed. As an example, sample 13 is shown in Figure 3d.

Table 2. Cladding materials with putative antifungal properties.

Sample	Antifungal Treatment/ Property	Mode of Action
2, thermally treated and impregnated	Iron(II) sulphate	Excess iron leads to disturbed iron homeostasis [40,41]
5, impregnated	Silicone and silicate	Acts as a water repellent and reduces moisture uptake of wood [42,43].
8, impregnated 9, impregnated	Titanium dioxide nanoparticles	Generation of free radicals (hydroxyl and superoxide anion) and hydrogen peroxide causing microbial growth reductions [44]
10, thermally treated and impregnated	Copper oxide, boric acid, and tebuconazole [45]	Copper can cause membrane damage [46] and protein denaturation [47]. Tebuconazole leads to ergosterol degradation [48,49].
15, impregnated	Fluorosilane	Acts as a water repellent and reduces moisture uptake of wood [50].
19, impregnated	Copper ethanolamine	Copper can cause membrane damage [46] and protein denaturation [47].

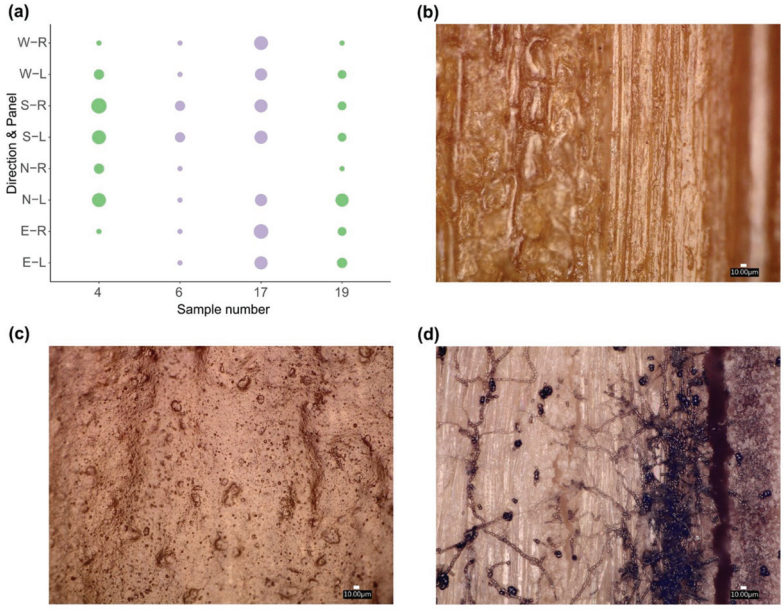

Figure 3. (**a**) Samples resistant to fungal growth. The abbreviations on Y-axis represent cardinal direction and panel (e.g., E-L = east left, N-R = north right). Colours represent coated (purple) and non-coated (green) samples. Symbol size corresponds to the number of CFUs (<10). (**b**–**d**) Microscope images of samples (**b**) 4, (**c**) 6, and (**d**) 13 at 500×. Scale bar represents 10 µm.

Sample 4 contains bamboo cladding and its resistance to fungi is surprising, given the breadth of the literature reporting its susceptibility to mould and decay [51]. However, the material used in this experiment (stick-glued bamboo façade profiles) provided by the industrial partner was additionally protected by oil, which might explain its high resistance. The second non-coated sample (19) was treated with copper ethanolamine, which is known to prevent fungal growth. For the two coated samples, 6 and 17, provided by industrial partners, the exact composition of the coating is unknown, and it is, therefore, difficult to interpret these results. It must be mentioned that only sample 19 from Table 1 demonstrated antifungal properties in practice, while we would expect similar performance from at least sample 10. However, the treatment of sample 10 was conducted under laboratory conditions

contrary to sample 19, which was prepared by an industrial partner. This might be the reason for the lower effectiveness of the treatment in this particular case.

3.4. Dominant Species

In long-term experiments, *Aureobasidium* sp., a polyextremotolerant fungus [52], has consistently been shown to be the prevalent species on wood-based materials [14,17,36]. Podgorski et al., who performed sampling every 3 months, reported that the diversity of fungal species decreases over time and that it is after 9 months that *Aureobasidium* sp. predominates [14]. To investigate the occurrence of dominant species in more detail and in a more quantitative manner, at the 1-month timepoint we identified samples where $\geq$ 90% of the CFUs appeared to have the same morphology. Pure cultures were obtained and selected DNA regions (internal transcribed spacers 1 and 2 including the 5.8S rDNA (ITS) and/or actin and/or β-tubulin) were sequenced to allow for identification. Dominant species were identified on at least one sample (out of 8) for 16 of the 33 tested materials (Figure 4a). Most of them were "heavily" colonised, having a CFU count of 100. On the vast majority of these materials, *Aureobasidium* sp. was the dominant genus, implying that *Aureobasidium* can establish dominance already during the early phases of colonisation. We found that *Aureobasidium melanogenum* (*A. melanogenum*) is the predominant species, with only a few occurrences of *A. pullulans*. However, it was only in 2014 that *A. melanogenum* was defined as a species [53]. Before this, it was a variety of *Aureobasidium pullulans* (*Aureobasidium pullulans* var. *melanogenum*), which explains why *A. pullulans* is the species commonly mentioned in publications. It has been shown that *A. melanogenum* is the predominant *Aureobasidium* species on oil-treated wood [54], but no other studies have, to our knowledge, compared the species composition on commercial cladding materials since *A. melanogenum* acquired the status of a species. *A. melanogenum* is considered an opportunistic pathogen as it can grow at 37 °C, which is a unique trait in the genus [53]. This might make it more competitive against *A. pullulans* when growing on surfaces exposed to warm weather. Another possible advantage of *A. melanogenum* could be its higher melanin content [55], which could provide efficient UV protection. Importantly, there might also be several other reasons contributing to the prevalence of *A. melanogenum*—such as its higher presence in the local environment, better attachment, faster growth, biofilm formation etc.

Only one material representing a wood–plastic composite (32) had a dominant species on all replicates. Different species of *Cladosporium*, as well as *Alternaria alternata* and *Penicillium* sp., were found on the surface of this material. The spores of all three species are commonly present in the outdoor air [56–59]. It must be mentioned that this wood–plastic composite had a specific topography (grooved surface), which might have influenced the retention of certain types of spores and/or led to non-homogenous growth over the material.

Representative macro- and micromorphologies of all species isolated from the materials are shown in Figure 4b,c, respectively. *A. melanogenum* is smooth, matt, and pinkish with areas of dark brown, indicating melanisation. On the microscopic picture, partly melanised vegetative hyphae and conidia can be observed. *A. pullulans* colonies are smooth, matt, and pinkish. Hyaline vegetative hyphae and conidia are visible. The colonies of *Cladosporium* sp. are powdery and olivaceous green, septate hyphae with conidiophores and conidia can be discerned from the microscopic image. *Alternaria alternata* appears woolly, olive-brown, and covered with short aerial hyphae. Dark, septate hyphae and ellipsoidal conidia, some in chains, are present. *Penicillium* sp. colonies appear powdery and greenish-blueish. Typical conidiophores with phialides forming basipetal conidia can be observed.

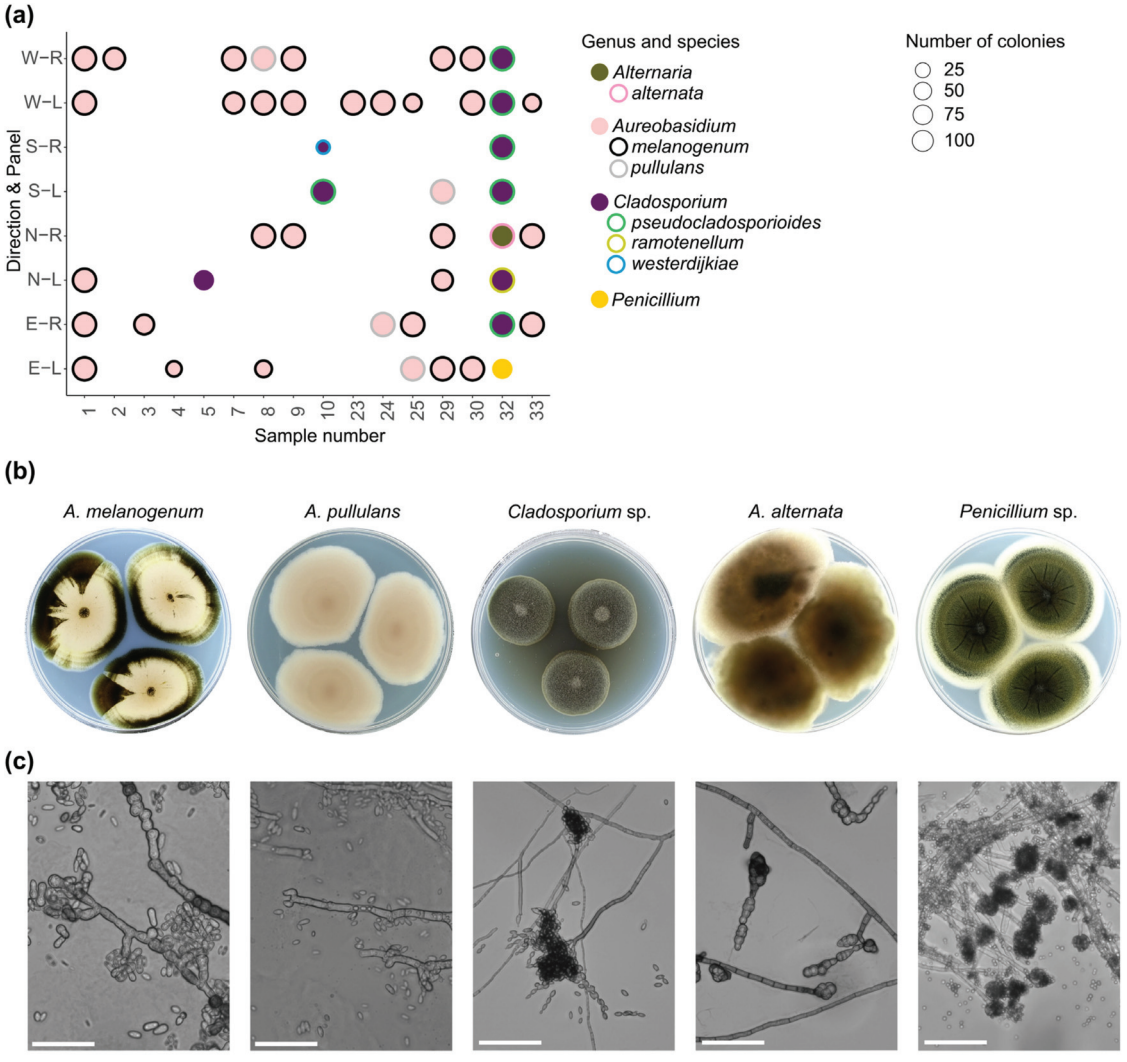

Figure 4. (**a**) Samples with dominant species. The abbreviations on Y-axis represent cardinal direction and panel. Colours represent fungal identity; inner symbol size corresponds to the number of CFU. (**b**) Images of pure cultures. (**c**) Microscopic images of pure cultures obtained with a 60× objective. Scale bar represents 50 µm.

3.5. Materials Characterisation

Roughness and wettability measurements for selected samples exposed to the north were conducted before and after 2.5 months of exposure. Samples were dismounted from the stand and stored in a controlled environment to reach equilibrium moisture content before measurements. The highest increase in surface roughness was evident for natural cladding materials (e.g., samples 29, 23, or 11). The arithmetical mean surface height (Sa) is the basic irregularity quantifier corresponding to the arithmetical mean height of the roughness profile (Ra), traditionally determined from the two-dimensional surface roughness profiles. ΔSa for the averaged measurements of samples 29, 23, and 11 was 8.9, 5.9, and 5.2 µm, respectively. An increase in surface roughness during weathering is associated with general erosion of the wood surface, removal of the single fibres, and the

leaching of photodegraded components [60]. Changes in the surface roughness during the weathering process are also linked to increased susceptibility to dirt accumulation, moisture, and pollutants as well as enhanced spore attachment and germination [61]. On the contrary, samples protected with a coating (e.g., 6) did not exhibit a change in the Sa parameter. Similar observations can be made while interpreting wettability results. Low contact angle values indicate that the liquid easily spreads over the assessed surface. Conversely, a high contact angle implies poor spreading and physical affinity. Unprotected samples already exhibited lower contact angle measurements after 2.5 months of the natural weathering process. The surfaces were easily wetted, and the sessile drops disappeared after a few seconds of the test. Contact angle parameters remained stable for coated samples (e.g., 6) where the difference was negligible. The contact angle measurement implies wettability by water (or other liquids) of the exposed material surface. The extent to which the contact angle changes is an important indicator of the progression of weathering [62]. Evaluation of investigated biobased cladding materials confirms that the most common material characteristics for improving bioreceptivity are high surface roughness, high open porosity, high capillary water content, and high wettability [63].

4. Conclusions

The goal of this work was to examine the early fungal colonisers on a diverse set of façade materials including commercial, coated, and non-coated materials. A set of 33 wood-based cladding materials were exposed to four cardinal directions and monitored in outdoor conditions. The response of these cladding materials to weathering and fungal infestation was assessed to verify if fungal presence is necessarily connected with material deterioration. The surfaces were sampled with a wet swab and plated on DG-18 agar. Pure cultures were then isolated and identified through PCR amplification and Sanger sequencing of specific DNA regions/genes.

- On most of the investigated materials where a dominant morphology was present, *Aureobasidium* sp. was the dominant genus, implying that *Aureobasidium* can establish dominance already during the early phases of colonisation.
- Both the material type and the climate condition at the exposure site influenced fungal colonisation. Samples exposed in another climate zone or at a different time of the year might exhibit different infestation patterns. Therefore, the current findings can only be interpreted within the experimental setting used.
- Coated materials were generally less susceptible to fungal infestation. The distributions of the CFU counts on samples exposed in four directions differed significantly. The least growth was observed in the south, while the highest fungal burden was observed in the east and west.
- Based on described results, *Aureobasidium* sp. is considered a candidate for a living component of a new nature-inspired coating system designed to effectively protect architectonic surfaces. We assume that due to its polyextremotolerance, *Aureobasidium* sp. would be a good candidate for living coatings to be used in different climate zones. Nonetheless, further research in diverse climatic regions might identify alternative species and/or even polymicrobial communities as candidates for living coatings.

Author Contributions: Conceptualisation, K.B.O., A.G., F.P. and A.S.; methodology, K.B.O., A.G., F.P. and A.S.; software, K.B.O. and A.G.; validation, K.B.O., A.G., F.P. and A.S.; formal analysis, K.B.O., A.G., F.P. and A.S.; investigation, K.B.O., A.G., F.P. and A.S.; resources, A.S.; data curation, K.B.O.; writing—original draft preparation, K.B.O.; writing—review and editing, K.B.O., A.G., F.P. and A.S.; visualisation, K.B.O.; supervision, A.S.; project administration, A.S.; funding acquisition, A.S. All authors have read and agreed to the published version of the manuscript.

Funding: Part of this work was conducted during the project WoodLCC (#773324), which is supported under the umbrella of ERA-NET Cofund ForestValue by the Ministry of Education, Science and Sport (MIZS)—Slovenia. The authors gratefully acknowledge the European Commission for funding the InnoRenew project (Grant Agreement #739574) under the Horizon2020 Widespread-Teaming

program, and the Republic of Slovenia (investment funding from the Republic of Slovenia and the European Union's European Regional Development Fund). This research was co-funded by the European Union (ERC, ARCHI-SKIN, #101044468). Views and opinions expressed are, however, those of the author(s) only and do not necessarily reflect those of the European Union or the European Research Council. Neither the European Union nor the granting authority can be held responsible for them.

Institutional Review Board Statement: Not applicable.

Informed Consent Statement: Not applicable.

Data Availability Statement: The dataset used for analysis in this study is available at the Zenodo.org Open Access Repository [64]. Created with BioRender.com, accessed on 4 August 2023.

Acknowledgments: The authors would like to acknowledge Nina Gunde-Cimerman for enabling access to the equipment and providing materials necessary for isolating DNA and performing PCR reactions, Mojca Matul for her help with depositing and retrieving the strains from the Microbial Culture Collection Ex, and Polona Zalar for her advice.

Conflicts of Interest: The authors declare no conflict of interest. The funders had no role in the design of the study; in the collection, analyses, or interpretation of data; in the writing of the manuscript; or in the decision to publish the results.

References

1. Schmidt, O. *Wood and Tree Fungi: Biology, Damage, Protection, and Use*, 1st ed.; Springer: Berlin/Heidelberg, Germany, 2006.
2. Hill, C.; Kymäläinen, M.; Rautkari, L. Review of the Use of Solid Wood as an External Cladding Material in the Built Environment. *J. Mater. Sci.* **2022**, *57*, 9031–9076. [CrossRef]
3. Kougoulis, J.S.; Kaps, R.; Walsh, B.; Bojczuk, K.; Crichton, T. *Revision of EU European Ecolabel and Development of EU Green Public Procurement Criteria for Indoor and Outdoor Paints and Varnishes*; EC Joint Research Center: Brussels, Belgium, 2012.
4. Gibbons, M.J.; Nikafshar, S.; Saravi, T.; Ohno, K.; Chandra, S.; Nejad, M. Analysis of a Wide Range of Commercial Exterior Wood Coatings. *Coatings* **2020**, *10*, 1013. [CrossRef]
5. Löfflath, F.; Gebhard, M. Rheological Changes during the Drying of a Waterborne Latex Coating. *J. Coat. Technol.* **1997**, *69*, 55–66. [CrossRef]
6. Van Der Kooij, H.M.; Fokkink, R.; Van Der Gucht, J.; Sprakel, J. Quantitative Imaging of Heterogeneous Dynamics in Drying and Aging Paints. *Sci. Rep.* **2016**, *6*, srep34383. [CrossRef] [PubMed]
7. Samyn, P.; Bosmans, J.; Cosemans, P. Current Alternatives for In-Can Preservation of Aqueous Paints: A Review. *Mater. Proc.* **2021**, *7*, 18.
8. Schultz, T.P.; Nicholas, D.D.; Preston, A.F. A Brief Review of the Past, Present and Future of Wood Preservation. *Pest Manag. Sci.* **2007**, *63*, 784–788. [CrossRef]
9. Broda, M. Natural Compounds for Wood Protection against Fungi—A Review. *Molecules* **2020**, *25*, 3538. [CrossRef]
10. Guillitte, O. Bioreceptivity: A New Concept for Building Ecology Studies. *Sci. Total Environ.* **1995**, *167*, 215–220. [CrossRef]
11. Sanmartín, P.; Miller, A.Z.; Prieto, B.; Viles, H.A. Revisiting and Reanalysing the Concept of Bioreceptivity 25 Years On. *Sci. Total Environ.* **2021**, *770*, 145314. [CrossRef]
12. Sailer, M.F.; van Nieuwenhuijzen, E.J.; Knol, W. Forming of a Functional Biofilm on Wood Surfaces. *Ecol. Eng.* **2010**, *36*, 163–167. [CrossRef]
13. Sandak, A. Engineered Living Materials for Sustainable and Resilient Architecture. *Nat. Rev. Mater.* **2023**, *8*, 357–359. [CrossRef]
14. Podgorski, L.; Reynaud, C.; Montibus, M. Fungal Growth on Coated Wood Exposed Outdoors: Influence of Coating Pigmentation, Cardinal Direction, and Inclination of Wood Surfaces. *Coatings* **2019**, *9*, 27. [CrossRef]
15. Poohphajai, F.; Sandak, J.; Sailer, M.; Rautkari, L.; Belt, T.; Sandak, A. Bioinspired Living Coating System in Service: Evaluation of the Wood Protected with Biofinish during One-Year Natural Weathering. *Coatings* **2021**, *11*, 701. [CrossRef]
16. Pfeffer, A.; Hoegger, P.J.; Kües, U.; Militz, H. Fungal Colonisation of Outside Weathered Modified Wood. *Wood Sci. Technol.* **2012**, *46*, 63–72. [CrossRef]
17. Gobakken, L.R.; Westin, M. Surface Mould Growth on Five Modified Wood Substrates Coated with Three Different Coating Systems When Exposed Outdoors. *Int. Biodeterior. Biodegrad.* **2008**, *62*, 397–402. [CrossRef]
18. Sjökvist, T.; Blom, Å. The Influence of Coating Color, Heartwood and Sapwood, on Moisture Content and Growth of Microorganisms on the Surface during Outdoor Exposure of Norway Spruce Boards. *J. Coat. Technol. Res.* **2019**, *16*, 819–826. [CrossRef]
19. Sandak, A.; Sandak, J.; Noël, M.; Dimitriou, A. A Method for Accelerated Natural Weathering of Wood Subsurface and Its Multilevel Characterization. *Coatings* **2021**, *11*, 126. [CrossRef]

20. Niklewski, J.; Sandak, J.; Bester Van Niekerk, P.; Brischke, C.; Acquah, R.; Sandak, A. Simplified Environmental Analysis of the Long-Term Performance of Wood Cladding and Decking. In Proceedings of the World Conference on Timber Engineering (WCTE 2023), Oslo, Norway, 19 June 2023; pp. 548–557.
21. Sandak, A.; Sandak, J.; Brzezicki, M.; Kutnar, A. *Bio-Based Building Skin*; Springer Nature: Singapore, 2019.
22. Riddell, R.W. Permanent Stained Mycological Preparations Obtained by Slide Culture. *Mycologia* **1950**, *42*, 265–270. [CrossRef]
23. Gerrits Van Den Ende, A.H.G.G.; De Hoog, G.S. Variability and Molecular Diagnostics of the Neurotropic Species Cladophialophora Bantiana. *Stud. Mycol.* **1999**, *1999*, 151–162.
24. White, T.J.; Bruns, T.; Lee, S.; Taylor, J. Amplification and Direct Sequencing of Fungal Ribosomal RNA Genes for Phylogenetics. In *PCR Protocols: A Guide to Methods and Applications*; Innis, M.A., Gelfand, D.H., Sninsky, J.J., White, T.J., Eds.; Academic Press: Cambridge, MA, USA, 1990; pp. 315–322.
25. Carbone, I.; Kohn, L.M. A Method for Designing Primer Sets for Speciation Studies in Filamentous Ascomycetes. *Mycologia* **1999**, *91*, 553–556. [CrossRef]
26. Hubka, V.; Kolarik, M. β-Tubulin Paralogue TubC Is Frequently Misidentified as the BenA Gene in Aspergillus Section Nigri Taxonomy: Primer Specificity Testing and Taxonomic Consequences. *Persoonia Mol. Phylogeny Evol. Fungi* **2012**, *29*, 1–10. [CrossRef]
27. Glass, N.L.; Donaldson, G.C. Development of Primer Sets Designed for Use with the PCR to Amplify Conserved Genes from Filamentous Ascomycetes. *Appl. Environ. Microbiol.* **1995**, *61*, 1323–1330. [CrossRef]
28. Altschul, S.F.; Gish, W.; Miller, W.; Myers, E.W.; Lipman, D.J. Basic Local Alignment Search Tool. *J. Mol. Biol.* **1990**, *215*, 403–410. [CrossRef] [PubMed]
29. Tamura, K.; Stecher, G.; Kumar, S. MEGA11: Molecular Evolutionary Genetics Analysis Version 11. *Mol. Biol. Evol.* **2021**, *38*, 3022–3027. [CrossRef] [PubMed]
30. R Core Team. *R: A Language and Environment for Statistical Computing*; R Foundation for Statistical Computing: Vienna, Austria, 2022.
31. Liauw, C.M.; Slate, A.J.; Butler, J.A.; Wilson-Nieuwenhuis, J.S.T.; Deisenroth, T.; Preuss, A.; Verran, J.; Whitehead, K.A. The Effect of Surface Hydrophobicity on the Attachment of Fungal Conidia to Substrates of Polyvinyl Acetate and Polyvinyl Alcohol. *J. Polym. Environ.* **2020**, *28*, 1450–1464. [CrossRef]
32. Whitehead, K.A.; Liauw, C.M.; Lynch, S.; El Mohtadi, M.; Amin, M.; Preuss, A.; Deisenroth, T.; Verran, J. Diverse Surface Properties Reveal That Substratum Roughness Affects Fungal Spore Binding. *iScience* **2021**, *24*, 102333. [CrossRef]
33. Poohphajai, F.; Myronycheva, O.; Karlsson, O.; Belt, T.; Rautkari, L.; Sandak, J.; Gubenšek, A.; Zalar, P.; Gunde-Cimerman, N.; Sandak, A. Fungal Colonisation on Wood Surfaces Weathered at Diverse Climatic Conditions. *Heliyon* **2023**, *9*, e17355. [CrossRef] [PubMed]
34. Sandak, J.; Sandak, A.; Riggio, M. Characterization and Monitoring of Surface Weathering on Exposed Timber Structures with a Multi-Sensor Approach. *Int. J. Archit. Herit.* **2015**, *9*, 674–688. [CrossRef]
35. Kržišnik, D.; Lesar, B.; Thaler, N.; Humar, M. Influence of Natural and Artificial Weathering on the Colour Change of Different Wood and Wood-Based Materials. *Forests* **2018**, *9*, 488. [CrossRef]
36. Rüther, P.; Jelle, B.P. Color Changes of Wood and Wood-Based Materials Due to Natural and Artificial Weathering. *Wood Mater. Sci. Eng.* **2013**, *8*, 13–25. [CrossRef]
37. Zhou, X.; Kubilay, A.; Derome, D.; Carmeliet, J. Comparison of Wind-Driven Rain Load on Building Facades in the Urban Environment and Open Field: A Case Study on Two Buildings in Zurich, Switzerland. *Build. Environ.* **2023**, *233*, 110038. [CrossRef]
38. Pitt, J.I.; Hocking, A.D. *Fungi and Food Spoilage*; Springer: New York, NY, USA, 2009; Volume 519.
39. Gobakken, L.R.; Bardage, S.L.; Long, C.J., II. Succession of Staining Fungi on Acetylated Wood and the Effect of Selected Influencing Factors. In Proceedings of the 7th Meeting of the Nordic-Baltic Network in Wood Material Science & Engineering (WSE), Oslo, Norway, 27–28 October 2011; pp. 13–18.
40. Robinson, J.R.; Isikhuemhen, O.S.; Anike, F.N. Fungal–Metal Interactions: A Review of Toxicity and Homeostasis. *J. Fungi* **2021**, *7*, 225. [CrossRef]
41. Fleurat-Lessard, P.; Dédaldéchamp, F.; Thibault, F.; Béré, E.; Roblin, G. Antifungal Effects of Iron Sulfate on Grapevine Fungal Pathogens. *Sci. Hortic.* **2011**, *130*, 517–523. [CrossRef]
42. Sèbe, G.; Brook, M.A. Hydrophobization of Wood Surfaces: Covalent Grafting of Silicone Polymers. *Wood Sci. Technol.* **2001**, *35*, 269–282. [CrossRef]
43. Mai, C.; Militz, H. Modification of Wood with Silicon Compounds. Treatment Systems Based on Organic Silicon Compounds-A Review. *Wood Sci. Technol.* **2004**, *37*, 453–461. [CrossRef]
44. De Filpo, G.; Palermo, A.M.; Rachiele, F.; Nicoletta, F.P. Preventing Fungal Growth in Wood by Titanium Dioxide Nanoparticles. *Int. Biodeterior. Biodegrad.* **2013**, *85*, 217–222. [CrossRef]
45. Mazela, B. Changes of Copper and Chromium Content in Wood Impregnated with the Ccb and Cb Preservatives after Leaching. *Folia For.* **2000**, *B*, 53–68.
46. Quaranta, D.; Krans, T.; Santo, C.E.; Elowsky, C.G.; Domaille, D.W.; Chang, C.J.; Grass, G. Mechanisms of Contact-Mediated Killing of Yeast Cells on Dry Metallic Copper Surfaces. *Appl. Environ. Microbiol.* **2011**, *77*, 416–426. [CrossRef]

47. *U.S. Environmental Protection Agency, Office of Prevention, Pesticides and Toxic Substances, Office of Pesticide Programs. Reregistration Eligibility Decision (RED) for Coppers*; U.S. Environmental Protection Agency: Washington, DC, USA, 2009.
48. Baudy, P.; Konschak, M.; Sakpal, H.; Baschien, C.; Schulz, R.; Bundschuh, M.; Zubrod, J.P. The Fungicide Tebuconazole Confounds Concentrations of Molecular Biomarkers Estimating Fungal Biomass. *Bull. Environ. Contam. Toxicol.* **2020**, *105*, 620–625. [CrossRef]
49. Peyton, L.R.; Gallagher, S.; Hashemzadeh, M. Triazole Antifungals: A Review. *Drugs Today* **2015**, *51*, 705–718. [CrossRef]
50. Adamopoulos, F.G.; Vouvoudi, E.C.; Achilias, D.S.; Karapanagiotis, I. Fluorosilane Water-Repellent Coating for the Protection of Marble, Wood and Other Materials. *Heritage* **2021**, *4*, 2668–2675. [CrossRef]
51. Schmidt, O.; Wei, D.S.; Tang, T.K.H.; Liese, W. Bamboo and Fungi. *J. Bamboo Ratt.* **2013**, *12*, 1–14.
52. Gostinčar, C.; Grube, M.; De Hoog, S.; Zalar, P.; Gunde-Cimerman, N. Extremotolerance in Fungi: Evolution on the Edge. *FEMS Microbiol. Ecol.* **2010**, *71*, 2–11. [CrossRef]
53. Gostinčar, C.; Ohm, R.A.; Kogej, T.; Sonjak, S.; Turk, M.; Zajc, J.; Zalar, P.; Grube, M.; Sun, H.; Han, J.; et al. Genome Sequencing of Four Aureobasidium Pullulans Varieties: Biotechnological Potential, Stress Tolerance, and Description of New Species. *BMC Genom.* **2014**, *15*, 549. [CrossRef]
54. van Nieuwenhuijzen, E.J.; Houbraken, J.A.M.P.; Meijer, M.; Adan, O.C.G.; Samson, R.A. Aureobasidium Melanogenum: A Native of Dark Biofinishes on Oil Treated Wood. *Antonie Leeuwenhoek* **2016**, *109*, 661–683. [CrossRef]
55. Zalar, P.; Gostinčar, C.; de Hoog, G.S.; Uršič, V.; Sudhadham, M.; Gunde-Cimerman, N. Redefinition of Aureobasidium Pullulans and Its Varieties. *Stud. Mycol.* **2008**, *61*, 21–38. [CrossRef]
56. Yates, M.V.; Nakatsu, C.H.; Miller, R.V.; Pillai, S.D. *Manual of Environmental Microbiology*; ASM Press: New York, NY, USA, 2016.
57. Patel, T.Y.; Buttner, M.; Rivas, D.; Cross, C.; Bazylinski, D.A.; Seggev, J. Variation in Airborne Fungal Spore Concentrations among Five Monitoring Locations in a Desert Urban Environment. *Environ. Monit. Assess.* **2018**, *190*, 1–10. [CrossRef] [PubMed]
58. Skjøth, C.A.; Damialis, A.; Belmonte, J.; De Linares, C.; Fernández-Rodríguez, S.; Grinn-Gofroń, A.; Jędryczka, M.; Kasprzyk, I.; Magyar, D.; Myszkowska, D.; et al. Alternaria Spores in the Air across Europe: Abundance, Seasonality and Relationships with Climate, Meteorology and Local Environment. *Aerobiologia* **2016**, *32*, 3–22. [CrossRef]
59. Bensch, K.; Braun, U.; Groenewald, J.Z.; Crous, P.W. The Genus Cladosporium. *Stud. Mycol.* **2012**, *72*, 1–401. [CrossRef] [PubMed]
60. Sandak, A.; Földvári-Nagy, E.; Poohphajai, F.; Diaz, R.H.; Gordobil, O.; Sajinčič, N.; Ponnuchamy, V.; Sandak, J. Hybrid Approach for Wood Modification: Characterization and Evaluation of Weathering Resistance of Coatings on Acetylated Wood. *Coatings* **2021**, *11*, 658. [CrossRef]
61. Gobakken, L.R.; Vestøl, G.I. Surface Mould and Blue Stain Fungi on Coated Norway Spruce Cladding. *Int. Biodeterior. Biodegrad.* **2012**, *75*, 181–186. [CrossRef]
62. Žlahtič, M.; Humar, M. Influence of Artificial and Natural Weathering on the Hydrophobicity and Surface Properties of Wood. *Bioresources* **2016**, *11*, 4964–4989. [CrossRef]
63. Veeger, M.; Ottelé, M.; Prieto, A. Making Bioreceptive Concrete: Formulation and Testing of Bioreceptive Concrete Mixtures. *J. Build. Eng.* **2021**, *44*, 102545. [CrossRef]
64. Butina Ogorelec, K.; Gubenšek, A.; Poohphajai, F.; Sandak, A. Assessing the bioreceptivity of biobased cladding materials. *Zenodo* **2023**, *9*, 8137772. [CrossRef]

coatings

MDPI

Article

Influence of Cu Substitution on the Properties of Hydroxyapatite Targets and Deposited Coatings

Konstantin Prosolov [1,*], Vladimir Lastovka [1], Margarita Khimich [1], Ivan Glukhov [1], Alexander Kashin [1], Nikita Luginin [1] and Yurii Sharkeev [1,2,*]

[1] Laboratory of Physics of Nanostructured Biocomposites, Institute of Strength Physics and Materials Science, Siberian Branch of Russian Academy of Sciences, 634055 Tomsk, Russia
[2] Research School of High-Energy Physics, National Research Tomsk Polytechnic University, 634050 Tomsk, Russia
* Correspondence: konstprosolov@gmail.com (K.P.); sharkeev@ispms.ru (Y.S.)

Abstract: In addressing the issue of optimizing the mechanical and electrochemical properties of hydroxyapatite (CaP) materials for biomedical applications, this research explored the incorporation of copper (Cu) into the material and scrutinized its impact through various processing stages, from powders to ceramics and finally to coatings. Our investigation indicated that the integration of CuO into CaP significantly changed the lattice parameters of hydroxyapatite from manufactured powders to sintered targets, indicating a structural evolution. Simultaneously, the change in the elemental composition and Ca/P ratio was also followed by each step from manufactured powders to deposited coatings. Mechanical testing revealed an impressive increase in the hardness of coatings to a high of 37 GPa for the 0.2CuO-CaP sample, a substantial improvement when compared to 13 GPa for pure Ti. The corrosion resistance of the coatings also improved, evidenced by the decrease in corrosion current density (Icorr) from 60.2 ± 5.2 nA/cm^2 for pure Ti to a lower 3.9 ± 0.5 nA/cm^2 for the CaP coating. Our study has revealed that the structural, mechanical, and electrochemical properties of CaP materials can be finely adjusted through the addition of Cu, promising advances in the realm of biomedical applications. Moreover, these results hint at the potential to tune the electrophysical characteristics of CaP coatings, an avenue for future exploration.

Keywords: substituted hydroxyapatite; thin films; bioactivity; magnetron sputtering; ceramic materials

Citation: Prosolov, K.; Lastovka, V.; Khimich, M.; Glukhov, I.; Kashin, A.; Luginin, N.; Sharkeev, Y. Influence of Cu Substitution on the Properties of Hydroxyapatite Targets and Deposited Coatings. *Coatings* **2023**, *13*, 1410. https://doi.org/10.3390/coatings13081410

Academic Editor: Seungil Kim

Received: 30 June 2023
Revised: 1 August 2023
Accepted: 8 August 2023
Published: 11 August 2023

1. Introduction

Recent advancements in the field of medical materials science have set the stage for a new era in the treatment of diseases related to the musculoskeletal system. This innovative approach harnesses the potential of regenerative medicine. It employs the use of varied implant types. Many of these implants are specifically modified to address various clinical scenarios [1,2].

The lifespan and effectiveness of these implants are largely influenced by their surface characteristics. This highlights the crucial role played by the choice of material and any subsequent modifications [3]. Notably, the material selection for these implants is not arbitrary; it is dictated by the need for mechanical compatibility with bone tissue. Therefore, materials with similar mechanical properties to bone tissue, such as metals and their alloys—including stainless steel, cobalt, titanium, zirconium, and tantalum—have been the choice of preference [4–6].

These selected alloys, known for their high strength and fatigue resistance, have found extensive use in the medical field. They have become integral in the fabrication of various medical devices, particularly those required for treating pathologies of the maxillofacial region and the musculoskeletal system. Titanium and its alloys have emerged as the most suitable materials for implants. Their ideal combination of mechanical and biomedical properties make them optimal for use in fields such as orthopedics, dentistry,

and maxillofacial surgery [7–10]. As we move forward in this era of personalized medicine, patient-specific implants, tailor-made through the comprehensive understanding of implant materials, their surface properties and modification techniques, will likely lead to improved clinical outcomes and quicker recovery periods [11].

A significant challenge for modern healthcare is the effective prevention of bacterial infections that accompany implant surgeries. One potential method for reducing the risk of postoperative complications due to bacterial infections is to modify implant surfaces with antibacterial coatings [12–15]. Forming antibacterial coatings on implants, which would possess high strength and adequate adhesion for operation under mechanical loads, is a pertinent issue in medical materials science. Importantly, these coatings should be biocompatible and bioactive, supporting bone growth and accelerated healing. Calcium phosphate (CaP) biocoatings meet these requirements [16–19].

Hydroxyapatite (HA)-based CaP biomaterials are widely used in implantology due to their elemental composition, being close to the mineral constituent of bone tissue [20]. The production and application of HA-based CaP biocoatings with the partial replacement of Ca^{2+} ions in the structure by cations of other metals are of considerable interest, as substitutions in the HA structure significantly change their physicochemical and biological properties, including improved biocompatibility [21–23]. Various metal ions can be used for synthesizing substituted HA, with Zn and Cu being particularly noteworthy. It has been found that ions of these metals contribute to the osteogenesis processes when used in certain concentrations. They are also interesting for their antibacterial properties, which could be useful for preventing peri-implantitis—inflammation of the tissues around a previously placed implant. By replacing Ca^{2+} ions with Zn^{2+} and Cu^{2+} in the HA lattice through manipulating deposition parameters, it is possible to tailor coating properties such as its biological activity and antibacterial effect [19,24].

RF magnetron sputtering serves as a commonly adopted approach for depositing calcium phosphate (CaP) coatings onto implant surfaces [25,26]. This technique enables the achievement of impressive adhesion between the coating and substrate while also offering control over the properties and morphology of CaP coatings. This control is crucial given the significant mechanical strain experienced by the surfaces of implant materials during the process of implantation [18,27,28]. Regarding the formation of CaP coatings via RF magnetron sputtering, targets play a pivotal role. The configuration and dimensions of these targets are dependent on the nature of the sputtering system and can be adjusted as per the technical requirements. it is essential to note that CaPs are typically brittle; therefore, the target must boast substantial microhardness and density for its secure attachment to the cathode [29]. The creation of a target involves two primary steps: forming the target from the relevant powdered material and subsequently sintering it. The initial target formation process comprises the manufacture of a press powder (a humid mass that includes a plasticizer and the original powder of a defined chemical composition). This press powder is then subjected to hot or cold pressure in molds [30,31]. Sintering is a densification procedure where the particles of the powder interconnect under high temperatures, resulting in material hardening [32]. It is widely accepted that the key properties of single-phase ceramics are strongly associated with material densification, which considerably reduces the level of porosity [33]. However, the choice of sintering regimes for HA ceramics is constrained due to the potential for hydroxyl group loss and material degradation at high temperatures [34]. During sintering in a vacuum, HAs can decompose into calcium oxide (CaO), tricalcium phosphate (TCP), tetracalcium phosphate (TTCP), and potentially result in the formation of phosphorus oxide P_2O_5 [35]. Thus, the production of HA targets for RF magnetron sputtering is a complex process requiring careful control over every step. Balancing the need for high-density, defect-free ceramics with the brittle nature of CaP materials, as well as the challenges posed by sintering, means that careful material and process selection is vital. With appropriate strategies in place, however, this method could provide an efficient way to create high-quality antibacterial coatings for implants.

The synthesis of CaP powder, the prior step to target sintering, plays a vital role in the success of the desired outcome. Over the past few decades, the mechanochemical method has emerged as a popular choice for synthesizing various compounds, including HA [36–38]. The appeal of this method lies in its simplicity and environmental benefits, as it can perform solid-phase reactions in a solvent-free environment, reducing the likelihood of undesirable side reactions. This procedure eliminates the need for high temperatures, executing processes at room temperature and pressure. In the mechanochemical synthesis, energy is liberated from the collisions of balls in a specialized planetary mill, instigating chemical reactions. This energy release is contingent on the mill's technical characteristics, specifically the kinetic energy of the balls, determined by the flask's rotation speed. Consequently, HA synthesis, occurring directly within the grinding flasks, is solely possible in ball mills operating at high rotation velocities. A higher rotation speed of the flask correlates to a shorter HA synthesis duration [38].

Furthermore, the mechanochemical method enables the creation of novel HA forms and facilitates HA synthesis with different doping ions, thus expanding the scope of potential applications. It also provides avenues for fabricating more complex, multi-component systems, underscoring its versatility in the realm of materials science. As it has already been said, the main focus nowadays in the field of materials science is to prevent complications related to infections. Therefore, many studies have already been performed in terms of antibacterial Cu containing coating deposition and materials manufacturing. In a study by Y. Huang et al., novel antibacterial Zn-Cu-HA coatings were synthesized using an electrodeposition method [39]. Similarly, this electrodeposition method was used to manufacture nanostructured Fe/Cu-coatings [40]. However, still a very limited number of papers have dealt with the RF magnetron deposition of Cu containing CaP coatings; some of the results could be found in two comprehensive review papers [41,42]. Therefore, there is a need for further research that could facilitate a deeper understanding of and reveal properties of Cu-containing CaP deposited by RF magnetron sputtering.

In our previous research [17,18,24], we used Cu-substituted powder manufactured by mechanochemistry when Cu content was introduced at small, doping concentrations in order to ensure manufacturing of a single-phase product. It is dictated by the fact that the CuO phase that might occur during synthesis, or that RF magnetron sputtering has drastically different bioactivity when compared to Cu [43]. In the present work, we aim to explore the difference in Cu addition to the HA structure up to the formation of CuO second phase and its influence on the deposition rate and properties of formed targets and resulting coatings in terms of structural, mechanical, and electrochemical properties of CaP materials, for each stage of preparation from powders to deposited RF magnetron coatings.

2. Materials and Methods

The preliminary materials for HA-based and Cu-HA-based targets were produced from powders, and manufactured via mechanochemical synthesis (MC), with the help of researchers from the Institute of Solid State Chemistry and Mechanochemistry's Laboratory of Intercalation and Mechanochemical Reactions, of the Siberian Branch of the RAS, Novosibirsk. Mechanochemical synthesis initiates chemical reactions using the energy discharged during the ball collisions in a unique planetary ball mill, facilitated by frictional forces. A planetary ball mill equipped with three steel drums, each having a 2000 mL capacity, was employed to manufacture the powders of stoichiometric HA and Cu-containing HA. The process took approximately 25–30 min to complete. The reactions that occurred during the synthesis are outlined below, including the denotations for the samples researched in the study:

$$6CaHPO_4 + 4CaO \rightarrow Ca_{10}(PO_4)_6(OH)_2 \cdot 2H_2O; \text{ (CaP)}$$

$$6CaHPO_4 + 3.8CaO + 0.2CuO \rightarrow Ca_{9.8}Cu_{0.2}(PO_4)_6(OH)_2 \cdot 2H_2O; \text{ (0.2CuO-CaP)}$$

$$6CaHPO_4 + 3.75CaO + 5CuO \rightarrow Ca_{9.75}Cu_{0.25}(PO_4)_6(OH)_2 \cdot 2H_2O + 4.75CuO \text{ (5CuO-CaP)}$$

The targets were synthesized from the resulting powders via uniaxial compression in steel molds using a hydraulic press model MIS-6000.4K (manufactured by IMASH LLC, Armavir, Russia). A maximum pressure of 80 MPa was applied during the last stage of a four-stage pressing regimen. The targets were sintered in an ITM 12.1200 electric furnace (ITM LLC, Tomsk, Russia) under ambient air conditions. The peak sintering temperature reached 1100 °C, with a heating cycle extending to this maximum over four hours, and a cooling cycle lasting beyond 30 h. The ceramic targets produced, namely, CaP, 0.2-CuO-CaP, and 5CuO-CaP; each had a diameter of 110 mm. Post-sintering, the targets were installed on a magnetron sputtering apparatus.

The substrates used for deposition were titanium (Ti) specimens, sourced from Russia (VSMPO-AVISMA, Verkhnyaya Salda, Russia), having dimensions of 10 × 10 × 1 mm.

Prior to sputtering, each Ti sample was mechanically processed using grinding papers of grades P400, P600, and P1000 (GOST 6456-82). The samples were then polished using diamond pastes with abrasive qualities of 14/10 and 5/3 (GOST 25593-83). After the polishing phase, the surfaces of the Ti disks were cleaned ultrasonically with the aid of acetone, soapy water, and alcohol. The samples were subsequently allowed to air-dry at room temperature. In every deposition process, a silicon wafer (Si) of dimensions 10 × 10 mm (100) was also coated for later ellipsometry studies. The current study employed an RF (13.56 MHz) magnetron system to deposit CaP coatings. This installation is equipped with a 2.5 kW RF power supply (COMDEL CX-2500S, Gloucester, MA, USA) and an automatic matching network (COMDEL Match pro CPMX-2500, Gloucester, MA, USA). The deposition of CaP coatings was conducted within a vacuum chamber where the operational gas, Ar, was maintained at a constant pressure with the help of a gas flow meter. This was configured to 20 sccm, leading to a deposition pressure of 0.1 Pa. The arrangement of the substrate ensured a throw distance of 70 mm. The substrate holder, operating under a floating potential, was positioned beneath the magnetron target during the deposition process. A stationary mode was chosen for sample deposition. To assess the kinetics of coating growth, the deposition process was set for a duration of 120 min, with an RF power range from 50 to 350 W. The target in use was pre-sputtered before each deposition cycle by gradually escalating the supplied RF power at a rate of 50 W every 5 min.

The thickness of the coatings was determined via ellipsometry, using monocrystalline Si samples. These measurements were conducted on an ELLIPS-1891 SAG spectral ellipsometric complex (SPC "Nanotechnology center", Novosibirsk, Russia). To ensure reliability, at least six samples from six different deposition runs, all operating under the same sputtering conditions per sputtering target, were evaluated. The results are presented as the mean ± standard deviation. The structural analysis of the resultant HA powders, post-sintering targets, and RF magnetron coatings was conducted via the X-ray diffraction (XRD) method. The structural phase state of the powder material and sputtering targets was determined using a DRON-8H diffractometer (Bourevestnik, St. Petersburg, Russia). This instrument operated in the range of angles 2θ = 10–100°, with a scanning step of 0.02° in Cu-Kα radiation. The full-profile Rietveld method was employed to determine lattice parameters and the size of coherent scattering regions (CSRs). In every case, the Rexp2-factor was no less than 0.94. Calculations of the lattice parameters and phase relations were performed using the Powder Cell 2.4 full-profile analysis program (Federal Institute for Materials Research and Testing, Berlin, Germany). The XRD study was conducted in standard Bragg–Brentano geometry. Standard ICDD PDF 4+ cards (International Centre for Diffraction Data, Newtown Square, PA, USA) were utilized for phase analysis, which included HA (00-009-0432), $Ca_3(PO_4)_2$ (00-032-0176), Ti (00-044-1294), and CuO (00-041-0254). A scanning electron microscope (SEM, LEO EVO 50, Carl Zeiss, Oberkochen, Stuttgart, Germany) equipped with an electron dispersive X-ray spectroscopy (EDX) INCA system (Oxford Instruments, High Wycombe, UK) was used to evaluate the surface morphology

and elemental composition of CaP powders, sintered targets and deposited coatings. EDX analysis was performed from the area under investigation that is visible in SEM image. To examine the microstructure of the synthesized CaP powders, a transmission electron microscope (TEM), specifically the JEOL JEM-2100 model (JEOL, Akishima, Japan), was employed. A minute quantity of CaP powder was dispersed in an alcohol solution via sonication, and subsequently transferred to a copper mesh for the TEM analysis. In order to assess the mechanical parameters of the deposited coatings, nano-indentation was performed on an MTS Nano Indenter G200 machine at loads of 10, 25, and 50 mN, with 6 imprints on each sample. The chosen load values for indentation are used to control the mechanical characteristics of the coating and to determine the optimal indentation parameters to eliminate the influence of substrates. The indenter is a Berkovich pyramid with a 65.3° apex angle, and a tip rounding radius of 20 nm. This analysis was performed using the National Research Tomsk Polytechnic University (TPU) instrumental base. Finally, the coatings' corrosion properties were examined using the electrochemical corrosion method. The measurements were carried out with a P-40X potentiostat-galvanostat coupled with an FRA-24 frequency analyzer module (Electrochemical instruments, Chernogolovka, Russia). All experiments were conducted in an E-7SF three-electrode cell (Electrochemical instruments, Chernogolovka, Russia) at room temperature. The electrolyte used consisted of 0.9 wt. % NaCl in distilled water, with a graphite counter electrode and a 4.2 M silver chloride reference electrode. The cell featured a fixed sample window, providing a constant area of 1 cm^2 for electrolyte–sample interaction. A gold-plated textolite served as a current collector. Potentiodynamic curves were drawn at a sweep of 2 mV/s across a range of ±300 mV of the open circuit potential (OCP) for each sample. Prior to the commencement of the experiment, each sample was kept in the cell for 60 min to ensure stabilization of all processes at the electrolyte–material interface. To determine the corrosion characteristics, Tafel lines were plotted with a correlation coefficient of at least 0.998 (±0.05 V from the E_{corr} value), with an allowable potential error of no more than 1 mV, in the accompanying ES8 software (Electrochemical instruments, Chernogolovka, Russia). The polarization resistance (*Rp*) was computed using the Stern–Giri Formula (1):

$$R_p = \frac{(\beta_a \cdot \beta_k)}{2.3 j_{corr} \cdot (\beta_a + \beta_k)} \quad (1)$$

Impedance spectroscopy was carried out in a potentiostatic mode at an open circuit potential with a sweep amplitude of 50 mV in a frequency range from 10^5 to 10^{-2} Hz. Approximation of the results of impedance measurements was carried out using the ZView software, followed by the modeling of equivalent circuits.

3. Results and Discussion

3.1. Characterization of Sintered Powders

X-ray diffraction (XRD) analysis was conducted on HA powders synthesized with varying concentrations of CuO (Figure 1), and results of calculated structural characteristics are summarized in Table 1. The nomenclature used for the samples throughout the study—CaP, 0.2CuO-CaP, and 5CuO-CaP—reflects the amount of CuO used in the synthesis process. XRD results revealed the presence of both HA and CuO phases in samples where a high concentration of CuO was used. Specifically, the crystal structure was determined to consist of 64% HA and 36% CuO. There could be a small quantity of CuO in the 0.2CuO-CaP sample (denoted by an asterisk); however, these reflections seem to overlap with those arising from the HA lattice.

Notably, the coherent scattering region of HA appeared to diminish with the addition of CuO. For the pure CaP, the coherent scattering region was found to be 94 ± 21 nm. However, for the 0.2CuO-CaP and 5CuO-CaP samples, the coherent scattering regions were 74 ± 13 nm and 18 ± 6 nm, respectively. This observation indicates that the CuO phase could be hindering the growth of HA crystals, leading to smaller crystal sizes with an increased concentration of CuO.

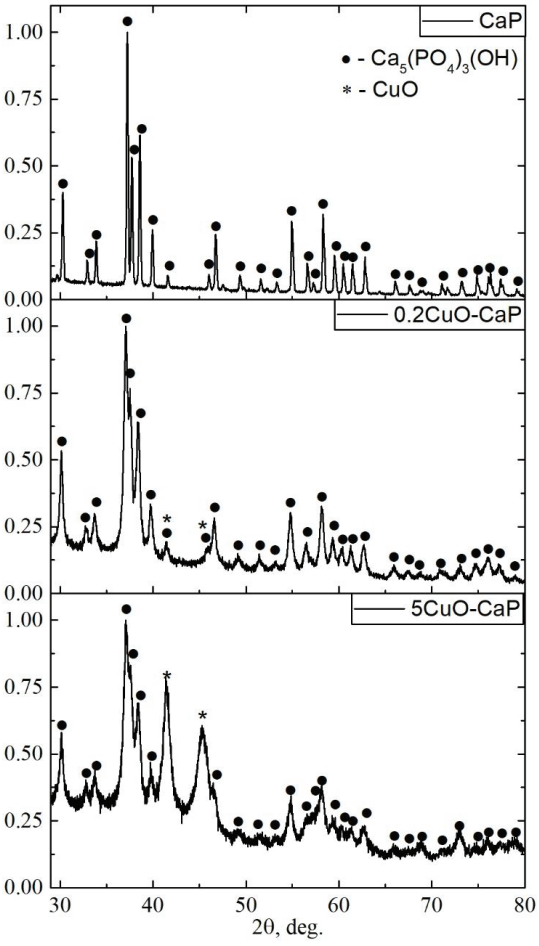

Figure 1. XRD of synthesized powders.

Table 1. Results of X-ray diffraction analysis of powders after mechanochemical synthesis.

Powder	*Phase Concentration, Mas.%*	*a* = *b*, Å	*c*, Å	CSR, nm
CaP	100 HA	9.4163 ± 0.0031	6.8763 ± 0.006	94 ± 20
0.2CuO-CaP	100 HA	9.4209 ± 0.0142	6.7664 ± 0.186	74 ± 14
5CuO-CaP	64 HA/36 CuO	9.4348 ± 0.0164	6.8858 ± 0.425	18 ± 5
ICDD	100 HA	9.422	6.881	

The alteration in the lattice parameter 'a' further corroborates this hypothesis. A gradual increase in the lattice parameter was observed as the CuO concentration increased. The 'a' parameter for CaP, 0.2CuO-CaP, and 5CuO-CaP was 9.4169 ± 0.0031 Å, 9.4211 ± 0.0042 Å, and 9.4344 ± 0.0086 Å, respectively. These results signify a potential distortion of the HA lattice structure due to the incorporation of Cu and interference of the CuO phase, as similarly reported in [44,45].

Considering these findings, it can be inferred that the addition of CuO not only interferes with the crystal growth of HA but may also result in the deformation of its crystal structure.

The introduction of Cu appears to significantly alter the microstructural and compositional properties of the powder, which is evident from SEM measurements (Figure 2). A noticeable trend was observed in the shape transition from more angular to rounder forms for 0.2CuO-CaP and 5CuO-CaP. There were also changes in the median particle size when CuO was incorporated. The median size for HA was 1.3 μm, while for 0.2CuO-CaP and 5CuO-CaP, the sizes were 4.1 μm and 2 μm, respectively. This shift may be attributed to the effect of Cu on the crystal growth of HA. With a greater Cu concentration, the HA crystals might experience inhibited growth, leading to smaller and more irregularly shaped particles. Turning to the EDX results, the Ca to P ratio, which is critical for calcium phosphates, showed a decrease as the Cu concentration increased. This might be due to the substitution of Ca ions by Cu ions in the HA lattice structure.

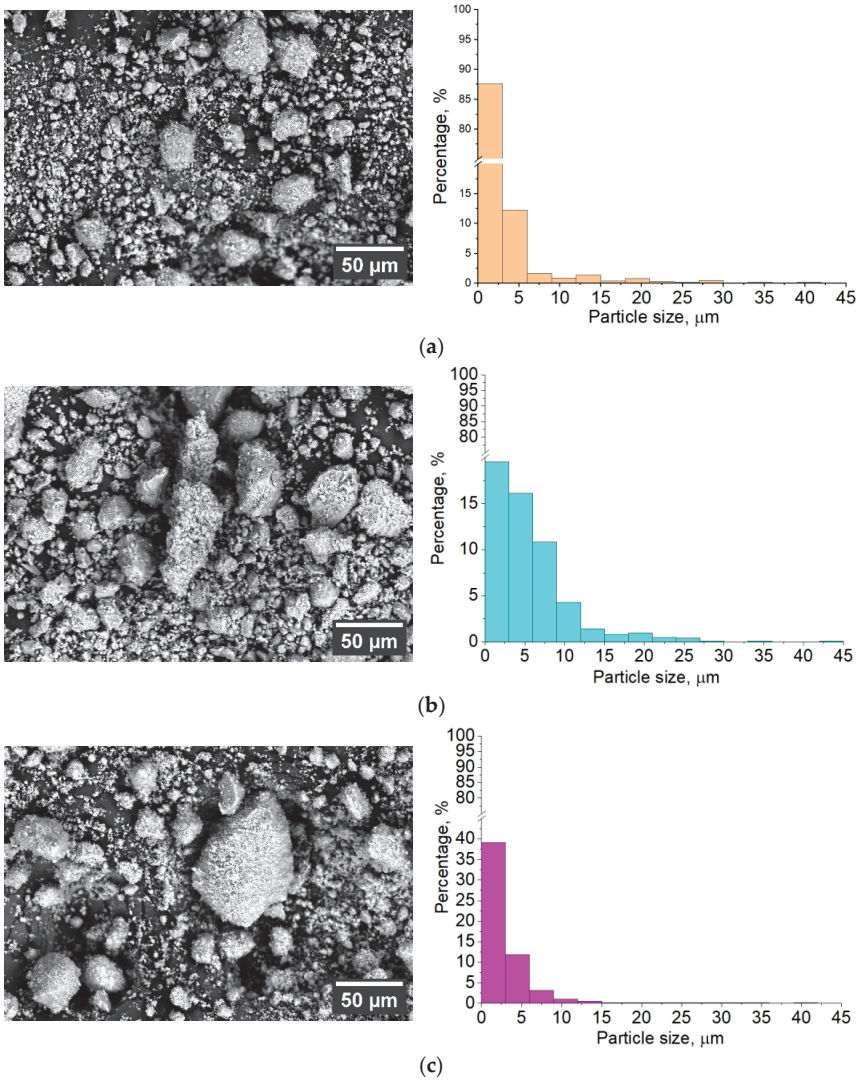

Figure 2. Scanning electron microscopy (SEM) images showing the morphological comparison of CaP (**a**), 0.2CuO-CaP (**b**), and 5CuO-CaP (**c**) synthesized powders with corresponding grain size distribution.

For the 5CuO-CaP sample, the Ca/P ratio was 1.61 ± 0.2 with 11.7 ± 2.6 at.% Cu, whereas for the 0.2CuO-CaP sample, the Ca/P ratio was 1.65 ± 0.2 with 0.48 ± 0.18 at.% Cu. The CaP sample showed a Ca/P ratio of 1.87 ± 0.45.

It is notable that the decrease in the Ca/P ratio did not exactly correspond to the increase in the Cu content. This discrepancy could be due to various factors, such as changes in the crystal structure, the formation of secondary phases, or the incomplete substitution of Ca ions by Cu ions.

In the TEM analysis, a marked difference in the morphology of CaP- and Cu-containing powders can be observed (Figure 3). The CaP powder comprises of nanometer-sized grain-like crystallites, characterized by well-defined, high-contrast boundaries. The crystallite size and strong contrast borders are indicative of a well-defined crystalline phase. The addition of CuO results in a deviation of crystallites, as is evident from the TEM results. This is consistent with the XRD results, which revealed a primarily HA phase for the CaP powder. The role of CuO during the mechanochemical process could be crucial to this behavior. Acting as a binder for the HA particles, the CuO could facilitate the formation of aggregates. The deviation in aggregate size governed by CuO content may also suggest an influence on the crystal growth process, with CuO possibly altering the growth kinetics or acting as a catalyst.

The detection of the CuO phase in the 5CuO-CaP powder via selected area electron diffraction (SAED) further substantiates this hypothesis. SAED patterns provide crystallographic information about the material, in this case revealing the presence of CuO in addition to the HA phase. This is further reinforced by the dark-field TEM image, which highlights the existence of Cu-containing species. For the 0.2CuO-CaP sample, the presence of the CuO phase was not prominent and could be found only in a few agglomerates, as depicted in Figure 3b, and which was confirmed by SAED. A crystallite that contains a significant concentration of Cu is revealed also by a notable change in contrast at the middle of an agglomerate. Otherwise, the sample is represented by an HA phase with distorted lattice parameters in relation to the ICDD database. However, it is worth noting that microscopy-based techniques, such as SEM and TEM, provide a very localized analysis. Therefore, to precisely monitor size deviation, alternative methods for particle size calculation should be employed. This, however, was not the primary focus of this research.

In conclusion of this subsection, it can be said that the combination of TEM, SAED, and dark-field imaging offers a detailed structural analysis of the synthesized powders, and, coupled with the SEM and XRD results, provides a comprehensive understanding of how CuO addition influences the crystal growth, aggregation, and phase composition of the HA powders.

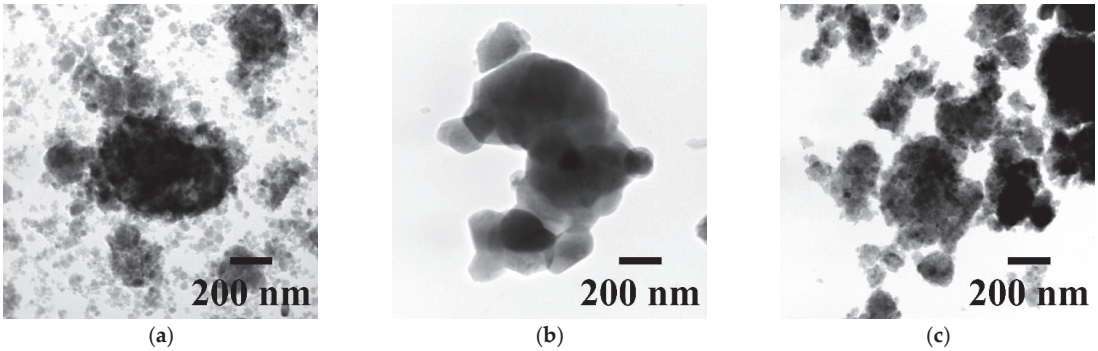

(**a**) (**b**) (**c**)

Figure 3. *Cont*.

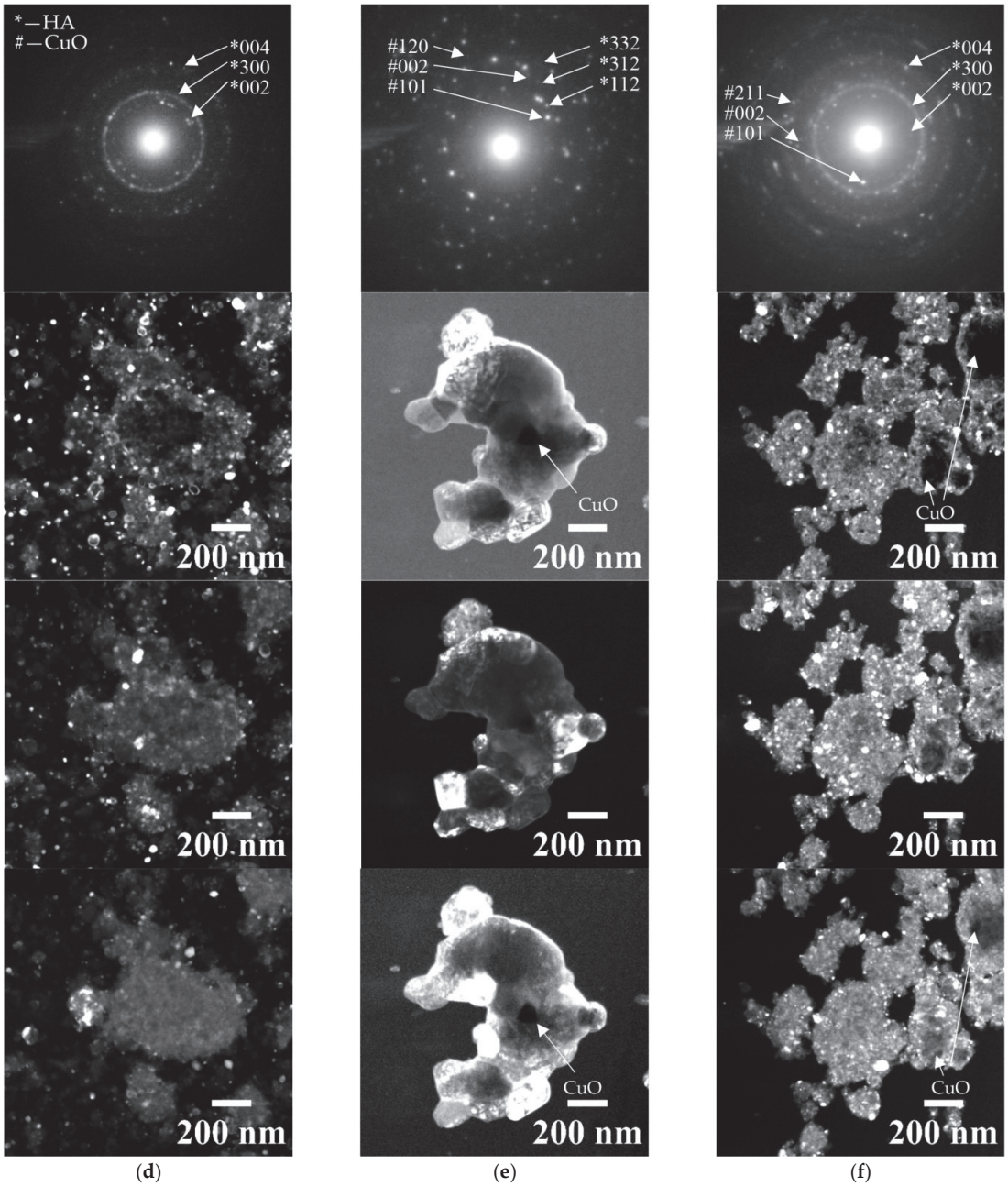

Figure 3. TEM image of CaP (**a**), 0.2CuO−CaP (**b**) and 5CuO−CaP (**c**) synthesized powders in bright-field mode with corresponding SAED obtained from the powder agglomerates and dark−field images (**d**–**f**).

3.2. Sintered Targets for an RF Magnetron Sputtering

In Figure 4, we have presented optical images of sintered targets derived from CaP, 0.2CuO-CaP, and 5CuO-CaP powders. A striking observation from these images is the

significant color shift from the pure white hue observed in the CaP target to the reddish and brownish shades seen in the 0.2CuO-CaP and 5CuO-CaP targets, respectively.

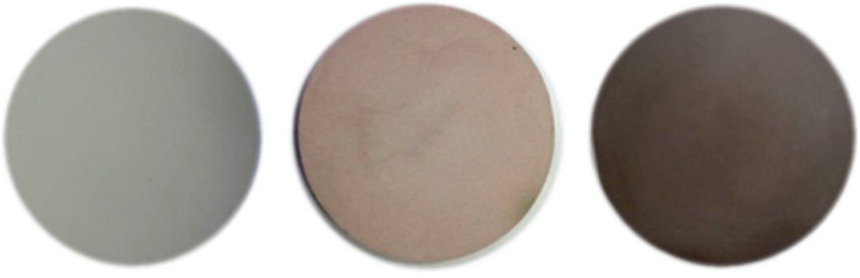

(**a**) (**b**) (**c**)

Figure 4. Optical images showing the appearance of the sintered targets composed of CaP (**a**), 0.2CuO-CaP (**b**), and 5CuO-CaP (**c**). The images display the color changes in the targets with the varying concentrations of CuO.

This alteration in color can be primarily attributed to the integration of Cu ions into the HA matrix. Cu, in its various oxidation states, brings about distinct colorations to the compounds it forms. In our case, the observable shift to reddish-brown is indicative of the presence of Cu(II) ions in the HA samples, similarly to what was previously reported for 3D sintering of Cu-containing HA [46], likely a consequence of Cu's d-orbital electron transitions when exposed to specific light wavelengths.

This color transformation also suggests changes in the band structure of the material, due to the different energy levels available for electronic transitions. As the concentration of CuO increases, it becomes evident that Cu ions are integrated more prominently into the crystal structure and possibly a CuO phase was formed, resulting in the observed color shifts. In addition to providing a visual indication of successful Cu integration, these color changes also offer valuable insights into the local crystal environment.

In Figure 5, we have presented the SEM images of the sintered targets prepared from the CaP (a), 0.2CuO-CaP (b), and 5CuO-CaP powders. The corresponding EDX analysis reveals the following Ca/P ratios and Cu percentages: for the 5CuO-CaP sample, Ca/P is 1.61 ± 0.1 and Cu is 12.1 ± 0.18 at.%; for the 0.2CuO-CaP sample, Ca/P is 1.69 ± 0.1 and Cu is 0.51 ± 0.08 at.%; for the CaP sample, Ca/P is 1.78 ± 0.2.

The SEM images highlight discernible differences in the surface morphology of the sintered targets, contingent on the Cu content. The CaP target exhibits modest porosity, with the particle coalescence suggesting the impact of the 1100 °C annealing process. However, as we increment the Cu content slightly, it appears that Cu might act as a fluxing agent, yielding a considerably smoother surface for the 0.2CuO-CaP target. The visible grooves likely arose from the grinding step.

Interestingly, the second phase is not detectable in the 0.2CuO-CaP target. When the Cu content is boosted further to 5CuO-CaP, it becomes apparent that the surface of the target consists of two distinct phases. The bright spots are believed to be linked to the CuO phase; nevertheless, EDX mapping did not provide definitive confirmation. Considering the bulk target's homogeneous Cu content, the EDX signal likely originates from not only the surface layer but also the lower layers. As a result, EDX mapping can only serve as an indicative tool in this context.

XRD analysis was conducted on sintered targets with varying concentrations of CuO (Figure 6), and the results of the calculated structural characteristics are summarized in Table 2. Based on the X-ray diffraction analysis of sintered targets, it is evident that the sintering process significantly impacted the crystal structure and phase composition of the samples, particularly those with CuO.

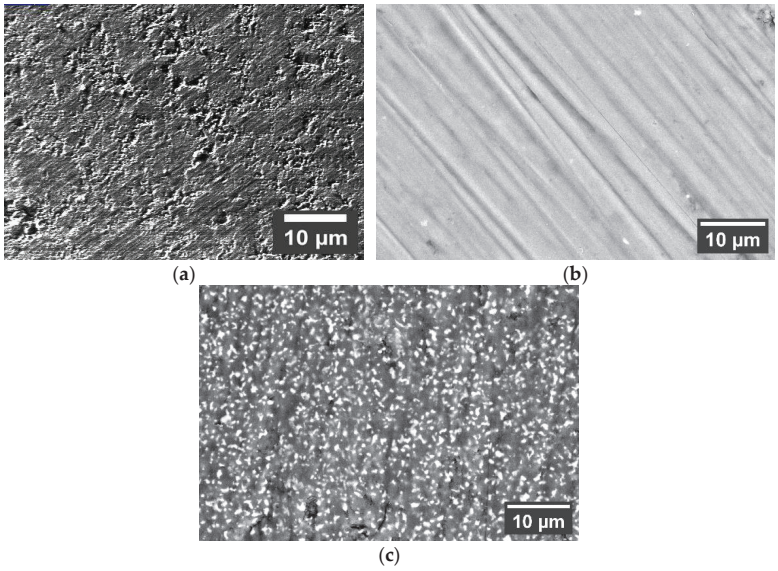

Figure 5. SEM images of sintered targets made of CaP (**a**), 0.2CuO-CaP (**b**) and 5CuO-CaP (**c**).

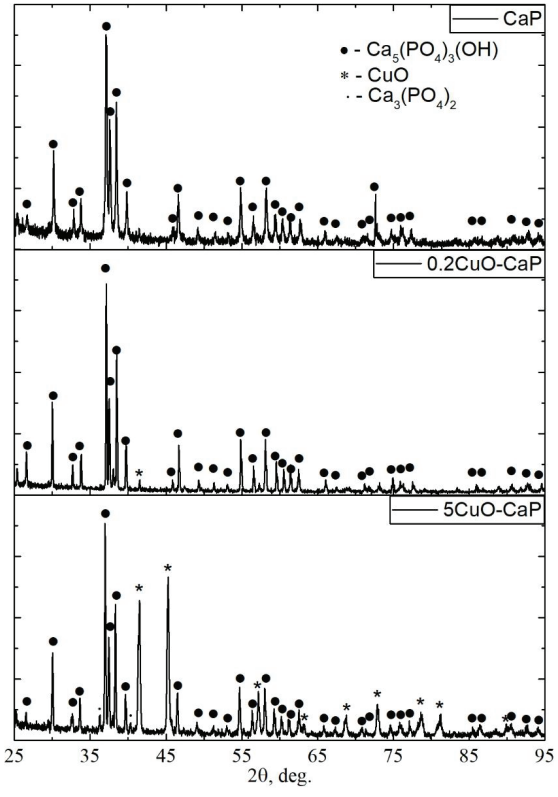

Figure 6. XRD of synthesized targets.

Table 2. Results of X-ray diffraction analysis of targets after synthesis.

Powder	*Phase Concentration, Mas.%*	*a = b*, Å	*c*, Å	CSR, nm
CaP	100 HA	9.4181 ± 0.0028	6.8765 ± 0.0027	93 ± 19
0.2CuO-CaP	100 HA	9.4158 ± 0.0013	6.8792 ± 0.0113	74 ± 15
5CuO-CaP	57 HA/42 CuO	9.4232 ± 0.0041	6.9038 ± 0.0036	57 ± 18
ICDD	100 HA	9.422	6.881	

For the CaP and 0.2CuO-CaP samples, the HA phase is dominant and is indicated by the sharp and high-intensity peaks in their diffractograms. The lattice parameters for these samples are close to the standard values for HA according to the ICDD database, signifying that the HA structure is maintained during sintering. It is interesting to note that the 'a' lattice parameter for the 0.2CuO-CaP sample slightly decreased compared to the powdered form, which might suggest a slight rearrangement or more ordered packing of atoms within the HA structure during sintering. The crystallite size, represented by the coherent scattering region (CSR), was slightly decreased for 0.2CuO-CaP, which could be due to the effect of sintering conditions on crystal growth. On the other hand, for the 5CuO-CaP sample, the presence of CuO had a more pronounced effect. Here, the phase composition consists of HA (54%), CuO (42%) and TCP (3%), indicating that a significant portion of the CuO is present after sintering. This CuO phase might have acted as a binding agent during sintering, which promoted densification and possibly inhibited the growth of HA crystals. Moreover, due to the high temperature influence, a small portion of TCP appeared. The 'a' lattice parameter in this sample slightly increased compared to the powdered form, suggesting some lattice distortion or expansion, likely due to the incorporation of Cu ions into the HA structure. The CSR also decreased compared to the powdered form, indicating that the crystal size became smaller, potentially due to the hindrance of crystal growth by the CuO phase.

These results indicate that the sintering process, in conjunction with the CuO concentration, plays a critical role in the phase composition, crystal structure, and crystallinity.

In conclusion to this subsection, it could be said that the inclusion of CuO significantly influenced the structural properties of HA in sintered targets. Lower CuO concentrations maintained the HA crystal structure, while high CuO concentrations revealed a HA-CuO mixed-phase composition. Distinct variations in structural parameters suggested potential lattice distortion and crystal size variation due to the CuO concentration and sintering effects. The CuO content also affected the target's visual appearance, leading to color change, and resulted in a smoother surface. These observations highlight the profound effect of CuO and sintering on the HA structure, paving the way for the improved design of HA-based materials. Further investigations will extend these findings, exploring the suitability of the sintered targets for RF magnetron sputtering.

3.3. Analysis of Deposited Coatings

The deposition rate is an essential characteristic that should be researched as it allows one to precisely control the coating thickness. In Figure 7, the deposition rate from all targets is reported. As observed from the SEM analysis of the sintered 5CuO-CaP target, there is clear phase segregation, resulting in two distinct phases. The presence of two distinct phases suggests a differential sputtering yield for the HA (CaP) and CuO phases. Given the inherent material properties, it is reasonable to propose that the CuO phase may have a higher sputtering yield compared to the CaP phase.

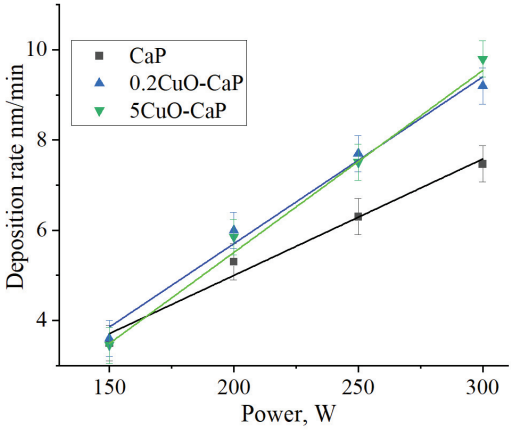

Figure 7. Deposition rate determination for sintered targets. Sputtering duration was 120 min in all cases.

The sputtering yield is influenced by several factors, including the mass and binding energy of the target material. CuO, being a metal oxide, likely has a lower binding energy compared to the complex HA structure, making it easier to sputter. Thus, areas of the target with a higher concentration of the CuO phase, due to phase segregation, would exhibit higher sputtering yields, leading to higher deposition rates.

Comparatively, the 0.2CuO-CaP target, with a lower Cu content, shows a more uniform and smooth surface under SEM. This implies a more homogeneous distribution of the CuO phase within the CaP matrix. This homogeneity would moderate the differences in sputtering yield across the target, resulting in a lower deposition rate than the 5CuO-CaP target, but higher than the pure CaP target. Lastly, the pure CaP target, without the presence of CuO, would likely exhibit the lowest sputtering yield among the three due to its higher binding energy and complex crystalline structure. Therefore, this results in the lowest deposition rate among the three targets.

Based on the SEM analysis (Figure 8), it was observed that all deposited coatings mimicked the surface structure of the ground Ti substrate, resulting in visibly marked grooves and ridges. Notably, the smoothest surface was evidenced in the case of the 5CuO-CaP sample, an outcome that might be attributable to an incremental increase in the deposition rate. The measured Ca/P ratios for each sample revealed distinct variations in stoichiometry. For the CaP sample, the Ca/P ratio was found to be 1.91 ± 0.2, deviating from the stoichiometric ratio of 1.67 for pure HA. An even higher deviation was observed for the 0.2CuO-CaP sample, with a Ca/P ratio of 2.22 ± 0.3, while maintaining a minimal Cu content of 0.4 at.%.

Contrastingly, the 5CuO-CaP sample exhibited a Ca/P ratio of 1.62 ± 0.1, which was closest to the stoichiometric ratio for HA, while simultaneously maintaining a significant Cu content of 12.6 ± 0.5 at.%. This observation indicates that the increase in Cu content led to the Ca/P ratio being closest to HA, while also introducing substantial amounts of Cu. It is a well-known fact that the Ca/P ratio is altered by the sputtering yield and re-sputtering of growing film. Interestingly, a high content of Cu could improve the stoichiometry of deposited using RF magnetron sputtering coatings.

A detailed analysis of the deposited coatings was conducted using X-ray diffraction (XRD) in order to assess the potential presence of CuO in the coatings and to study the structure of the deposited layers (Figure 9). From the XRD data, it is clear that only the peak corresponding to the Ti substrate could be distinctly identified in the area of interest. Concurrently, a halo arising from the amorphous calcium phosphate was observed for all the deposited coatings.

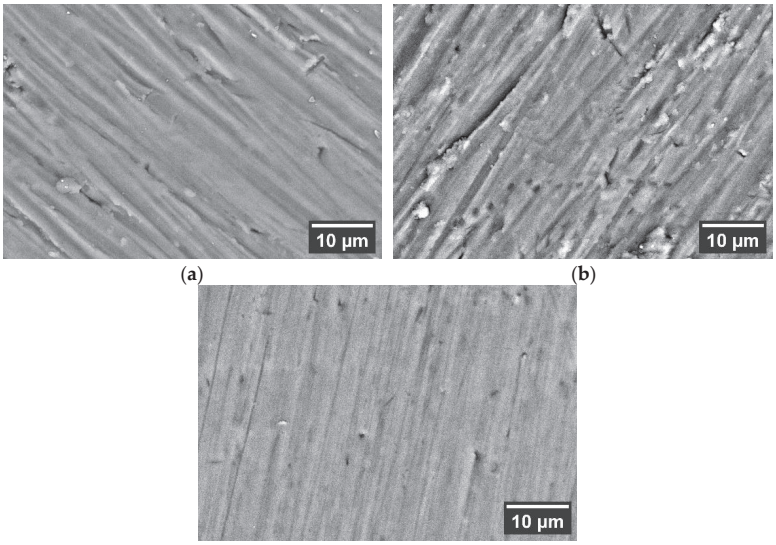

Figure 8. SEM images of coatings deposited using CaP (**a**), 0.2CuO-CaP (**b**) and 5CuO-CaP (**c**) targets.

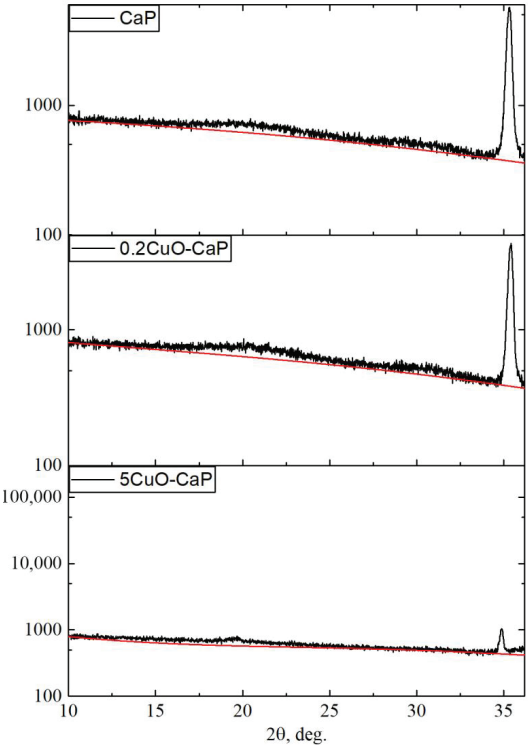

Figure 9. XRD of deposited coatings from corresponding targets. The deposition parameters for all cases were as follows: duration was set to 120 min, power was 250 W and throw distance was 70 mm.

Interestingly, the short-range order, evidenced by the halo intensity, appears to be affected by the presence of Cu, suggesting that the local structure of the amorphous calcium

phosphate may be modulated by CuO incorporation. Despite the high-sensitivity and comprehensive data provided by XRD, their efficacy for the analysis of thin solid films and low dopant concentrations can be limited.

For a more nuanced understanding of the structure and short-range order of the deposited layers, a cross-section TEM analysis is recommended. This technique will offer a more in-depth analysis and potentially reveal structural intricacies that could be pivotal in understanding the effect of CuO incorporation on the physical and chemical properties of the coatings.

Load–unload curves (Figure 10) for the 0.2CuO-CaP and 5CuO-CaP were analyzed under loads of 10, 25, and 50 mN in relation to the unmodified Ti substrate. A reduction in the surface indentation depth was observed, indicating an increased hardness of the coating relative to the Ti substrate. By examining the area under the load and unload curves, it is clear that the recovery behavior of the coatings exhibits an elastic–plastic nature (smaller area under the curve), while the recovery of Ti shows predominantly plastic behavior (larger area under the curve).

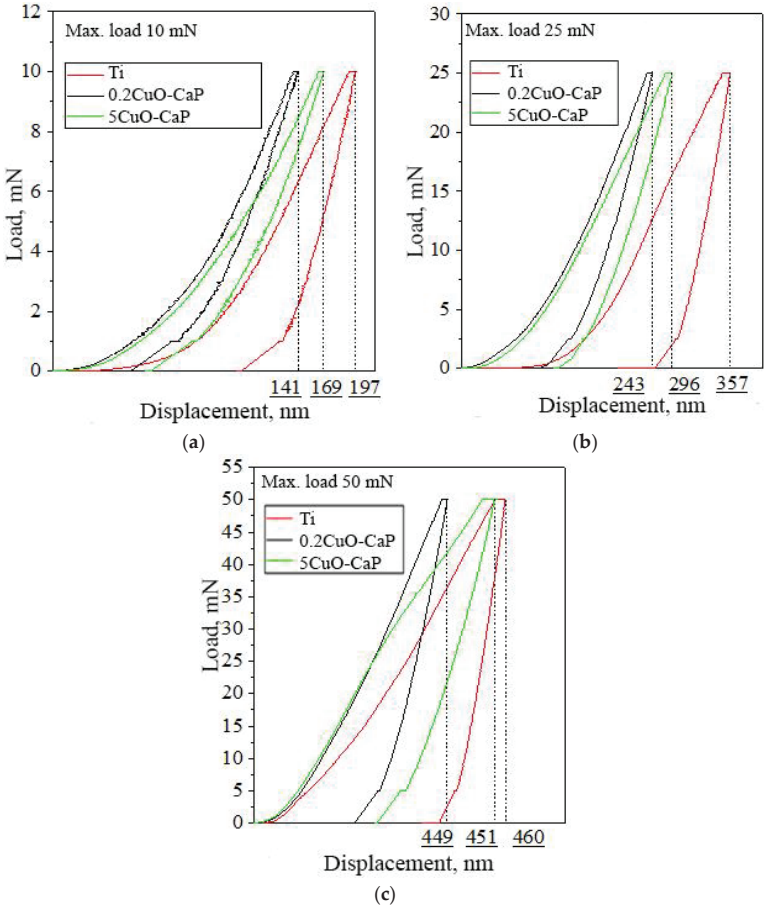

Figure 10. Load–unload curves for the polished Ti substrate and Cu-containing CaP coatings (0.2CuO-CaP and 5CuO-CaP) obtained at max. load of 10 mN (**a**), 25 mN (**b**) and 50 mN (**c**). The graph illustrates the differences in the mechanical responses of the materials under applied and removed load.

Further, the mechanical properties (hardness, modulus of elasticity, and plasticity (δ)) of the sample surfaces were assessed. The indentation depth (h) in the coatings was less

than in Ti, a distinction attributable to the variance in the mechanical properties (hardness and modulus of elasticity) of the coating and the Ti substrate. It is a well-known fact that ceramics exhibit a higher level of hardness; however, even amorphous thin CaP films also reflect the high values of hardness. The plasticity of the coating was almost half that of the Ti samples (under loads of 10 and 25 mN), suggesting a predominance of elastic properties in the coatings, while the polished titanium specimens exhibited a more plastic-deformation behavior.

As the indentation depth increased, the influence of the Ti substrate became more significant, causing the hardness and modulus of elasticity of the coatings (0.2CuO-CaP: H = 16 GPa, E = 272 GPa; 5CuO-CaP: H = 17 GPa, E = 211 GPa) to decrease to values close to those of titanium (H = 13 GPa, E = 360 GPa) (Figure 11). The mechanical properties of the coatings were analyzed using data obtained at a 10 mN load because the indentation depth was minimal and the substrate influence was minimized, as evidenced by the measured values of the hardness and modulus of elasticity (0.2CuO-CaP: H = 37 GPa, E = 503 GPa; 5CuO-CaP: H = 30 GPa, E = 304 GPa).

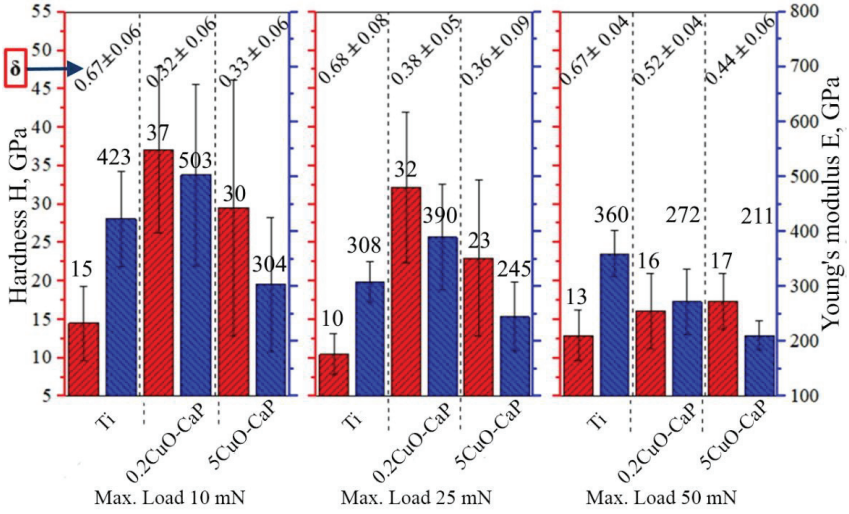

Figure 11. Mechanical characteristics of tested surfaces at different indentation loads.

It is noteworthy that the coating with a lower Cu content exhibited a higher hardness and modulus of elasticity than the coating with a higher Cu content. The observed mechanical properties of the coatings, particularly the hardness and modulus of elasticity, are largely attributed to their amorphous nature and the specific influence of the incorporated Cu. These mechanical enhancements, coupled with the already-known biocompatible nature of these coatings, highlight their potential utility in various orthopedic and dental applications.

The higher hardness and modulus of elasticity in the coating with the lower Cu content could be related to the reduced phase segregation. This may be due to the fact that with increasing Cu content, there is an increase in the proportion of the softer CuO phase, which would affect the overall hardness and modulus of elasticity of the coating. It is also possible that the introduction of a larger amount of CuO could lead to structural defects, further reducing these mechanical properties. However, it has not been reliably proven by XRD analysis. On the other hand, the lower Cu content may have facilitated a more homogenous distribution of the elements, leading to more-uniform mechanical properties.

Additionally, as the indentation depth increased, the influence of the Ti substrate became more prominent, causing the hardness and modulus of elasticity of the coatings to decrease towards the values for Ti. This is indicative of the effect of the substrate material properties at a larger indentation depth.

Finally, the electrochemical parameters of the deposited coatings were studied and Tafel slopes are presented in Figure 12. The corrosion characteristics of the material samples were presented in Table 3. The Open Circuit Potential (E_{ocp}) for pure Ti was found to be -0.03 ± 0.03 V while the corrosion potential (E_{corr}) was at -0.32 ± 0.03 V, with a corrosion current density (J_{corr}) of 60.2 ± 5.2 nA/cm^2. The corrosion rate was significantly higher in the case of the unmodified Ti sample compared to the coated samples, indicating their improved corrosion resistance due to the coating. The CaP-coated sample demonstrated a considerably lower corrosion current density (3.9 ± 0.5 nA/cm^2), which corresponds to a higher polarization resistance (R_p) of 16.0 MOhm/cm^2, indicating a lower rate of corrosion compared to the uncoated Ti sample.

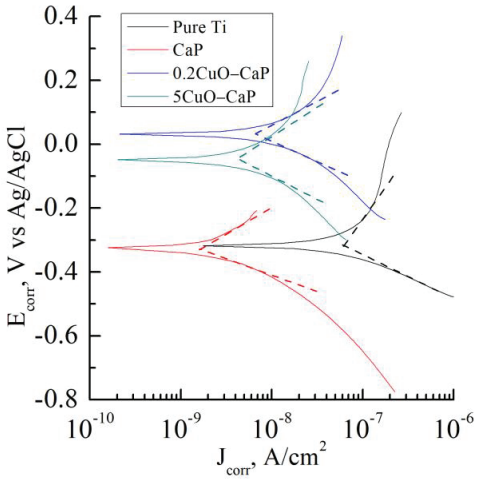

Figure 12. Potentiodynamic curves for pure Ti and coatings in 0.9 wt. % NaCl solution. (The dashed lines represent Tafel's slopes).

Table 3. Corrosion characteristics of material samples.

Sample	E_{ocp}, V	E_{corr}, V	J_{corr}, nA/cm^2	β_a, V/dec	β_k, V/dec	Rp, MΩ/cm^2	$\|Z\|_{f\to 0.01}$ Hz, MΩ × cm^2
Pure Ti	-0.03 ± 0.03	-0.32 ± 0.03	60.2 ± 5.2	0.13	0.40	0.7	0.2 ± 0.1
CaP	-0.32 ± 0.03	-0.32 ± 0.03	3.9 ± 0.5	0.21	0.47	16.0	0.2 ± 0.1
0.2CuO-CaP	0.22 ± 0.03	-0.01 ± 0.03	16.3 ± 1.6	0.26	0.44	4.4	9.2 ± 0.8
5CuO-CaP	0.07 ± 0.03	-0.04 ± 0.03	6.4 ± 1.1	0.23	0.34	9.4	5.1 ± 0.3

Adding a small amount of Cu in the CaP coating (0.2CuO-CaP) resulted in an increase in the corrosion current density (16.3 ± 1.6 nA/cm^2) compared to the CaP coated sample, but still much lower than the uncoated Ti sample. The corresponding polarization resistance was 4.4 MOhm/cm^2. When a higher amount of Cu was added (5CuO-CaP), the corrosion current density decreased to 6.4 ± 1.1 nA/cm^2, indicating improved corrosion resistance compared to the 0.2CuO-CaP sample. The polarization resistance increased to 9.4 MOhm/cm^2.

From these results, it is evident that the addition of Cu to the CaP coating affects the corrosion characteristics of the coated Ti samples. This is especially true in the case of the 5CuO-CaP sample, which demonstrated superior corrosion resistance characteristics compared to the other samples. The data of the corrosion characteristics suggest an intriguing relationship between the doping concentration and the conductivity of the CaP coatings. The addition of a small amount of Cu (0.2CuO-CaP) appears to significantly enhance the conductivity of the CaP. This increase could be attributed to a shift from ion conductivity to electron conductivity, a transition that has been observed in other metal-doped ceramic systems as Cu-doping results in an increase in the charge carrier concentration [47]. However, increasing the Cu concentration further (5CuO-CaP) seems to

reduce the conductivity. This trend may be attributed to the presence of CuO clusters in the coating, originating from the CuO in the target material used for deposition. CuO is known to behave as a dielectric, which might hinder its electron movement, thus decreasing its overall conductivity. An increase in insulating properties upon the increase in CuO content has been reported elsewhere [48].

Furthermore, impedance spectroscopy was performed for the deposited coatings, and Bode and Nyquist plots are presented in Figure 13a,b. Using these results, an equivalent circuit was modeled (Figure 13c–f). An equivalent circuit for a pure Ti sample is shown below (Figure 13c), consistent with the findings of other researchers [49]. This equivalent circuit, generally speaking, comprises three components: the active resistance of pure Ti (Rs), the TiO_2 oxide layer (CPE1, R1), and the interface between the electrolyte and oxide layer (CPE2, R2). The constant phase element (CPE) involves the charge transfer process related to the dispersion of a capacitance around a mean value, and can be modeled by two parameters, CPE-T and CPE-P. CPE was used here since it is more suitable to describe the non-ideal behavior of the coating. This circuit was characteristic of all metallic samples with a dielectric coating; in this case, the coating was the TiO_2 oxide layer. The values for simulated elements are presented in Table 4.

Table 4. Calculated values of the simulated circuit elements.

Sample	Pure Ti	CaP	0.2CuO−CaP	5CuO−CaP
Rs, $\Omega \times cm^2$	140	20	80	100
CPE1−T, $F \times cm^{-2}$	4.04×10^{-5}	1.40×10^{-6}	1.74×10^{-7}	7.63×10^{-8}
CPE1−P	0.89	0.57	0.76	0.81
R1, $\Omega \times cm^2$	2.65×10^{5}	1.63×10^{3}	2.53×10^{5}	1.88×10^{6}
CPE2−T, $F \times cm^{-2}$	2.39×10^{-4}	2.91×10^{-5}	7.73×10^{-8}	5.05×10^{-7}
CPE2−P	1.44	0.58	0.66	0.53
R2, $\Omega \times cm^2$	1.36×10^{5}	-	2.72×10^{6}	5.09×10^{6}
CPE4−T, $F \times cm^{-2}$	-	-	2.72×10^{-7}	-
CPE4−P	-	-	0.35	-
χ^2 (KK)	0.091	0.001	0.001	0.002

Since impedance measurements were performed at low frequencies (0.01–1 Hz) in this study, it was necessary to confirm whether these system data are stationary. For this, a Kramers–Kronig transformation (KK) was performed for each of the impedance spectra with the subsequent calculation of χ^2 as a parameter to assess the accuracy of the approximation. These values are provided in Table 3. All spectra demonstrated high convergence ($\chi^2 < 0.1$) after the transformation, which allowed us to assert the correctness of the selection of equivalent circuits at low-frequency intervals. In the case of the Pure Ti sample, the χ^2 value was slightly inflated compared to other samples due to the active resistance Rs, a more precise value of which could not be calculated.

It should be noted that as the proportion of copper oxide in the coating structure increases, the capacitance of the CPE1-P element decreases. This may suggest a higher conductivity of the TiO_2 surface layer in the case of the 5CuO-CaP sample. In the case of active resistances (R1, R2), their value increases, which indicates an increase in the proportion of active resistance when alloying the coating with copper.

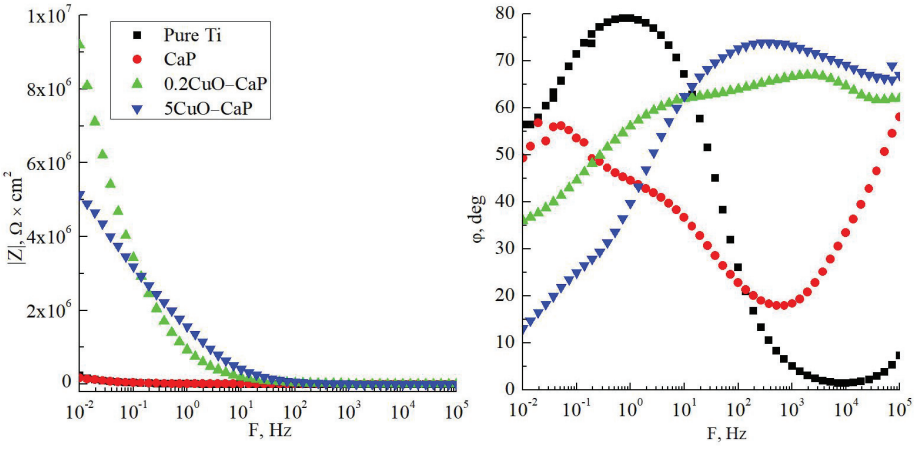

(**a**)

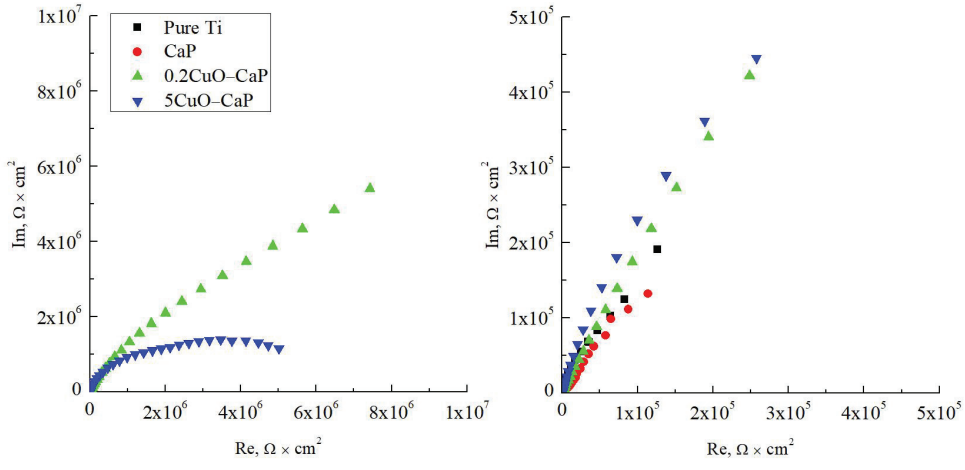

(**b**)

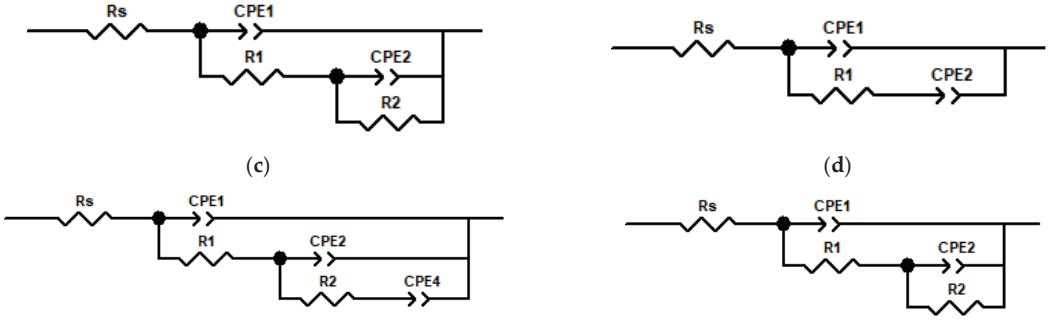

(**c**) (**d**)

(**e**) (**f**)

Figure 13. Bode plot (**a**), Nyquist plot (**b**) and equivalent circuit for pure titanium (**c**), CaP (**d**), 0.2CuO−CaP (**e**) and 5CuO−CaP (**f**).

The deposition of a coating (Figure 13d) modifies the nature of the third component, increasing the influence of the reactive resistance; therefore, R2 is excluded from the equivalent circuit. This behavior is associated with the dielectric conductivity of the transition layer CaP-electrolyte, which at low frequencies possesses a quasi-infinite active resistance. The addition of a small amount of Cu to the CaP coating (Figure 13e) adds another component to the equivalent circuit (CPE4) and leads to a limit in the active resistance of the third component. The fourth component characterizes the interface between the Cu-electrolyte, since small amounts of Cu do not form a uniform matrix, and the element is evenly distributed throughout the CaP layer as separate species in the amorphous matrix of CaP.

Adding more Cu content to the CaP coating (Figure 13f) leads to the exclusion of the fourth component due to the fact that Cu particles begin to form a uniform matrix within the CaP layer. Hence, the surface layer now comprises a unified structure in the form of a CuO-CaP composite, characterized only by the third component, similar to the case of pure Ti with a TiO_2 oxide layer. This suggests that the addition of higher concentrations of Cu change the electrochemical properties of the CaP layer.

These observations suggest the potential of tuning the electrical properties of CaP coatings by careful control over the dopant concentration. Given the growing interest in the electro-physical properties of biomedical coatings due to their potential use in implantable detectors, transducers, and actuators, this finding may have significant implications for future research. In particular, the enhancement of electrical properties of CaP coatings may pave the way for more advanced and functional biomedical implant coatings.

4. Conclusions

The transition of CuO-doped CaP materials from powders to ceramics to coatings demonstrated a significant evolution in their structural and elemental parameters. With lattice parameters for ceramics (a = 9.420 Å and c = 6.884 Å) notably higher than for the raw powders (a = 9.413 Å and c = 6.875 Å), we confirmed successful CuO incorporation into the HA lattice. The Ca/P ratio underwent an interesting transition from powders to ceramics and coatings. For example, the Ca/P ratio decreased from 2.22 $\pm$ 0.3 in 0.2CuO-CaP powder to 1.62 $\pm$ 0.1 in 5CuO-CaP coating. Simultaneously, the Cu content ascended from less than 0.4 at.% in the initial powder to an impressive 12.6 $\pm$ 0.5 at.% in the final coating, denoting the material's adaptability. Mechanical tests showed the hardness and Young's modulus of the coatings to be much higher than those of the Ti substrate, with the 0.2CuO-CaP coating exhibiting the highest hardness (H = 37 GPa) and modulus (E = 503 Gpa). In terms of electrochemical performance, the 0.2CuO-CaP coating exhibited an appreciable decrease in corrosion current density (16.3 $\pm$ 1.6 nA/cm^2) compared to pure Ti (60.2 $\pm$ 5.2 nA/cm^2), along with an increase in polarization resistance (4.4 Mohm/cm^2). The TEM study highlighted the need for in-depth layer analysis for thin solid films and low dopant concentrations, revealing a short-range order modification induced by the presence of Cu. It is important to note that comprehensive, long-term testing under physiological conditions, including evaluations of structural, mechanical, and electrochemical behavior, is essential to substantiate our findings. Our forthcoming research will be dedicated to assessing the cytotoxicity, immunological activity, and antibacterial effect of such coatings with an increased Cu content. With enhanced mechanical strength and electrochemical resilience, these coatings possess considerable potential for biomedical applications, such as implantable sensors and actuators. In conclusion, our study demonstrates the remarkable adaptability and tunability of CuO-doped CaP materials across various phases, underscoring their potential in materials science and biomedical applications. The structural, mechanical, and electrochemical enhancements realized through controlled Cu doping highlight the promise of this material for future research and practical applications.

Author Contributions: Conceptualization, K.P.; methodology, K.P. and V.L.; software, K.P. and N.L.; validation, K.P., M.K. and A.K.; formal analysis, K.P., V.L. and I.G.; investigation, K.P., N.L., A.K., M.K. and I.G.; resources, Y.S.; data curation, K.P. and Y.S.; writing—original draft preparation, K.P.; writing—review and editing, K.P.; visualization, K.P., M.K. and A.K.; supervision, K.P.; project administration, Y.S.; funding acquisition, Y.S. All authors have read and agreed to the published version of the manuscript.

Funding: The work was performed according to the Government research assignment for ISPMS SB RAS, project FWRW-2021-0007.

Institutional Review Board Statement: Not applicable.

Informed Consent Statement: Not applicable.

Data Availability Statement: Data is available after reasonable request.

Acknowledgments: The authors express their appreciation for the valuable contributions of A.I. Tolmachev from Institute of Strength Physics and Materials Science SB RAS (Tomsk, Russia) for their assistance in the preparation of the experimental materials. The investigations were carried out using the equipment of Share Use Centre "Nanotech" of the ISPMS SB RAS and Tomsk Materials Research Multiple Access Center of TSU, as well as the instrumental base of TPU. The authors also thank M.V. Chaikina and N.V. Bulina's team from the Institute of Mechanochemistry, Novosibirsk, Russia for synthesizing the HA powder.

Conflicts of Interest: The authors declare no conflict of interest.

References

1. Germaini, M.-M.; Belhabib, S.; Guessasma, S.; Deterre, R.; Corre, P.; Weiss, P. Additive Manufacturing of Biomaterials for Bone Tissue Engineering—A Critical Review of the State of the Art and New Concepts. *Prog. Mater. Sci.* **2022**, *130*, 100963. [CrossRef]
2. Basu, B.; Gowtham, N.H.; Xiao, Y.; Kalidindi, S.R.; Leong, K.W. Biomaterialomics: Data Science-Driven Pathways to Develop Fourth-Generation Biomaterials. *Acta Biomater.* **2022**, *143*, 1–25. [CrossRef]
3. Rial, R.; Liu, Z.; Messina, P.; Ruso, J.M. Role of Nanostructured Materials in Hard Tissue Engineering. *Adv. Colloid Interface Sci.* **2022**, *304*, 102682. [CrossRef] [PubMed]
4. Wickramasinghe, M.L.; Dias, G.J.; Premadasa, K.M.G.P. A Novel Classification of Bone Graft Materials. *J. Biomed. Mater. Res.* **2022**, *110*, 1724–1749. [CrossRef] [PubMed]
5. Jain, S.; Parashar, V. Analytical Review on the Biocompatibility of Surface-Treated Ti-Alloys for Joint Replacement Applications. *Expert Rev. Med. Devices* **2022**, *19*, 699–719. [CrossRef] [PubMed]
6. Khimich, M.A.; Prosolov, K.A.; Mishurova, T.; Evsevleev, S.; Monforte, X.; Teuschl, A.H.; Slezak, P.; Ibragimov, E.A.; Saprykin, A.A.; Kovalevskaya, Z.G.; et al. Advances in Laser Additive Manufacturing of Ti-Nb Alloys: From Nanostructured Powders to Bulk Objects. *Nanomaterials* **2021**, *11*, 1159. [CrossRef] [PubMed]
7. Vishwakarma, V.; Kaliaraj, G.S.; Amirtharaj Mosas, K.K. Multifunctional Coatings on Implant Materials—A Systematic Review of the Current Scenario. *Coatings* **2022**, *13*, 69. [CrossRef]
8. Kroczek, K.; Turek, P.; Mazur, D.; Szczygielski, J.; Filip, D.; Brodowski, R.; Balawender, K.; Przeszłowski, Ł.; Lewandowski, B.; Orkisz, S.; et al. Characterisation of Selected Materials in Medical Applications. *Polymers* **2022**, *14*, 1526. [CrossRef]
9. Wang, R.; Ni, S.; Ma, L.; Li, M. Porous Construction and Surface Modification of Titanium-Based Materials for Osteogenesis: A Review. *Front. Bioeng. Biotechnol.* **2022**, *10*, 973297. [CrossRef]
10. El-Saies, M.M.; Hassan, I.; El-Shazly, A.H.; El-Wakad, M.T. Titanium Foam for Dental Implant Applications: A Review. *SVU-Int. J. Eng. Sci. Appl.* **2023**, *4*, 107–112. [CrossRef]
11. Ho, D.; Quake, S.R.; McCabe, E.R.B.; Chng, W.J.; Chow, E.K.; Ding, X.; Gelb, B.D.; Ginsburg, G.S.; Hassenstab, J.; Ho, C.-M.; et al. Enabling Technologies for Personalized and Precision Medicine. *Trends Biotechnol.* **2020**, *38*, 497–518. [CrossRef] [PubMed]
12. Shen, J.; Gao, P.; Han, S.; Kao, R.Y.T.; Wu, S.; Liu, X.; Qian, S.; Chu, P.K.; Cheung, K.M.C.; Yeung, K.W.K. A Tailored Positively-Charged Hydrophobic Surface Reduces the Risk of Implant Associated Infections. *Acta Biomater.* **2020**, *114*, 421–430. [CrossRef] [PubMed]
13. Lisoń, J.; Taratuta, A.; Paszenda, Z.; Szindler, M.; Basiaga, M. Perspectives in Prevention of Biofilm for Medical Applications. *Coatings* **2022**, *12*, 197. [CrossRef]
14. Nouri, A.; Rohani Shirvan, A.; Li, Y.; Wen, C. Surface Modification of Additively Manufactured Metallic Biomaterials with Active Antipathogenic Properties. *Smart Mater. Manuf.* **2023**, *1*, 100001. [CrossRef]
15. Perrault, D.P.; Sharma, A.; Kim, J.F.; Gurtner, G.C.; Wan, D.C. Surgical Applications of Materials Engineered with Antimicrobial Properties. *Bioengineering* **2022**, *9*, 138. [CrossRef]

16. Prosolov, K.A.; Mitrichenko, D.V.; Prosolov, A.B.; Nikolaeva, O.O.; Lastovka, V.V.; Belyavskaya, O.A.; Chebodaeva, V.A.; Glukhov, I.A.; Litvinova, L.S.; Shupletsova, V.V.; et al. Zn-Doped CaP-Based Coatings on Ti–6Al–4V and Ti–6Al–7Nb Alloys Prepared by Magnetron Sputtering: Controllable Biodegradation, Bacteriostatic, and Osteogenic Activities. *Coatings* **2021**, *11*, 809. [CrossRef]
17. Prosolov, K.A.; Lastovka, V.V.; Belyavskaya, O.A.; Lychagin, D.V.; Schmidt, J.; Sharkeev, Y.P. Tailoring the Surface Morphology and the Crystallinity State of Cu- and Zn-Substituted Hydroxyapatites on Ti and Mg-Based Alloys. *Materials* **2020**, *13*, 4449. [CrossRef]
18. Prosolov, K.A.; Lastovka, V.V.; Khimich, M.A.; Chebodaeva, V.V.; Khlusov, I.A.; Sharkeev, Y.P. RF Magnetron Sputtering of Substituted Hydroxyapatite for Deposition of Biocoatings. *Materials* **2022**, *15*, 6828. [CrossRef]
19. Sedelnikova, M.B.; Komarova, E.G.; Sharkeev, Y.P.; Ugodchikova, A.V.; Mushtovatova, L.S.; Karpova, M.R.; Sheikin, V.V.; Litvinova, L.S.; Khlusov, I.A. Zn-, Cu- or Ag-Incorporated Micro-Arc Coatings on Titanium Alloys: Properties and Behavior in Synthetic Biological Media. *Surf. Coat. Technol.* **2019**, *369*, 52–68. [CrossRef]
20. Ielo, I.; Calabrese, G.; De Luca, G.; Conoci, S. Recent Advances in Hydroxyapatite-Based Biocomposites for Bone Tissue Regeneration in Orthopedics. *Int. J. Mol. Sci.* **2022**, *23*, 9721. [CrossRef]
21. Bulina, N.V.; Vinokurova, O.B.; Eremina, N.V.; Prosanov, I.Y.; Khusnutdinov, V.R.; Chaikina, M.V. Features of Solid-Phase Mechanochemical Synthesis of Hydroxyapatite Doped by Copper and Zinc Ions. *J. Solid State Chem.* **2021**, *296*, 121973. [CrossRef]
22. Chaikina, M.V.; Bulina, N.V.; Prosanov, I.Y.; Vinokurova, O.B.; Ishchenko, A.V. Structure Formation of Zinc-Substituted Hydroxyapatite during Mechanochemical Synthesis. *Inorg. Mater.* **2020**, *56*, 402–408. [CrossRef]
23. Khvostov, M.V.; Borisova, M.S.; Bulina, N.V.; Makarova, S.V.; Dumchenko, N.B.; Tolstikova, T.G.; Lyakhov, N.Z. The Influence of Zinc and Silicate Ions on Biological Properties of Hydroxyapatite Synthesized by a Mechanochemical Method. *Ceram. Int.* **2021**, *47*, 9495–9503. [CrossRef]
24. Prosolov, K.A.; Luginin, N.A.; Litvinova, L.S.; Fedorov, M.A.; Anisenya, I.I.; Mushtovatova, L.S.; Snetkov, A.A.; Bukharov, A.V.; Khlusov, I.A.; Sharkeev, Y.P. Antibacterial and Biocompatible Zn and Cu Containing CaP Magnetron Coatings for MgCa Alloy Functionalization. *J. Mater. Res. Technol.* **2023**, *25*, 2177–2203. [CrossRef]
25. Akhtar, M.; Uzair, S.A.; Rizwan, M.; Ur Rehman, M.A. The Improvement in Surface Properties of Metallic Implant via Magnetron Sputtering: Recent Progress and Remaining Challenges. *Front. Mater.* **2022**, *8*, 747169. [CrossRef]
26. Montazerian, M.; Hosseinzadeh, F.; Migneco, C.; Fook, M.V.L.; Baino, F. Bioceramic Coatings on Metallic Implants: An Overview. *Ceram. Int.* **2022**, *48*, 8987–9005. [CrossRef]
27. Ueda, K.; Narushima, T. Amorphous Calcium Phosphate Coatings. In *Phosphate and Borate Bioactive Glasses*; Obata, A., Brauer, D.S., Kasuga, T., Eds.; The Royal Society of Chemistry: London, UK, 2022; pp. 114–133, ISBN 978-1-83916-164-3.
28. Drevet, R.; Fauré, J.; Benhayoune, H. Bioactive Calcium Phosphate Coatings for Bone Implant Applications: A Review. *Coatings* **2023**, *13*, 1091. [CrossRef]
29. Ferreiro Balbuena, O.B.; Santos Paiva, L.F.; Ribeiro, A.A.; Monteiro, M.M.; Varella De Oliveira, M.; Pereira, L.C. Sintering Parameters Study of a Biphasic Calcium Phosphate Bioceramic Synthesized by Alcoholic Sol-Gel Technique. *Ceram. Int.* **2021**, *47*, 32979–32987. [CrossRef]
30. Ayode Otitoju, T.; Ugochukwu Okoye, P.; Chen, G.; Li, Y.; Onyeka Okoye, M.; Li, S. Advanced Ceramic Components: Materials, Fabrication, and Applications. *J. Ind. Eng. Chem.* **2020**, *85*, 34–65. [CrossRef]
31. Dobrzański, L.A.; Dobrzański, L.B.; Dobrzańska-Danikiewicz, A.D. Overview of Conventional Technologiesusing the Powders of Metals, Their Alloysand Ceramics in Industry 4.0 Stage. *J. Achiev. Mater. Manuf. Eng.* **2020**, *2*, 56–85. [CrossRef]
32. Upadhyaya, A.; Upadhyaya, G.S. Sintering of Copper-Alumina Composites through Blending and Mechanical Alloying Powder Metallurgy Routes. *Mater. Des.* **1995**, *16*, 41–45. [CrossRef]
33. Rahaman, M.N. Ceramic Processing and Sintering. In *Materials Engineering*, 2nd ed.; M. Dekker: New York, NY, USA, 2003; ISBN 978-0-8247-0988-4.
34. Que, W.; Khor, K.A.; Xu, J.L.; Yu, L.G. Hydroxyapatite/Titania Nanocomposites Derived by Combining High-Energy Ball Milling with Spark Plasma Sintering Processes. *J. Eur. Ceram. Soc.* **2008**, *28*, 3083–3090. [CrossRef]
35. Gross, K.A.; Berndt, C.C. Thermal Processing of Hydroxyapatite for Coating Production. *J. Biomed. Mater. Res.* **1998**, *39*, 580–587. [CrossRef]
36. Bulina, N.V.; Chaikina, M.V.; Prosanov, I.Y.; Dudina, D.V. Strontium and Silicate Co-Substituted Hydroxyapatite: Mechanochemical Synthesis and Structural Characterization. *Mater. Sci. Eng. B* **2020**, *262*, 114719. [CrossRef]
37. Chaikina, M.V.; Bulina, N.V.; Vinokurova, O.B.; Gerasimov, K.B.; Prosanov, I.Y.; Kompankov, N.B.; Lapina, O.B.; Papulovskiy, E.S.; Ishchenko, A.V.; Makarova, S.V. Possibilities of Mechanochemical Synthesis of Apatites with Different Ca/P Ratios. *Ceramics* **2022**, *5*, 404–422. [CrossRef]
38. Chaikina, M.V.; Bulina, N.V.; Vinokurova, O.B.; Prosanov, I.Y.; Dudina, D.V. Interaction of Calcium Phosphates with Calcium Oxide or Calcium Hydroxide during the "Soft" Mechanochemical Synthesis of Hydroxyapatite. *Ceram. Int.* **2019**, *45*, 16927–16933. [CrossRef]
39. Huang, Y.; Zhang, X.; Mao, H.; Li, T.; Zhao, R.; Yan, Y.; Pang, X. Osteoblastic Cell Responses and Antibacterial Efficacy of Cu/Zn Co-Substituted Hydroxyapatite Coatings on Pure Titanium Using Electrodeposition Method. *RSC Adv.* **2015**, *5*, 17076–17086. [CrossRef]

40. Karthika, A. Biocompatible Iron and Copper Incorporated Nanohydroxyapatite Coating for Biomedical Implant Applications. *Mater. Today Proc.* **2022**, *51*, 1754–1759. [CrossRef]
41. Safavi, M.S.; Surmeneva, M.A.; Surmenev, R.A.; Khalil-Allafi, J. RF-Magnetron Sputter Deposited Hydroxyapatite-Based Composite & Multilayer Coatings: A Systematic Review from Mechanical, Corrosion, and Biological Points of View. *Ceram. Int.* **2021**, *47*, 3031–3053. [CrossRef]
42. Arcos, D.; Vallet-Regí, M. Substituted Hydroxyapatite Coatings of Bone Implants. *J. Mater. Chem. B* **2020**, *8*, 1781–1800. [CrossRef]
43. Wu, F.; Harper, B.J.; Crandon, L.E.; Harper, S.L. Assessment of Cu and CuO Nanoparticle Ecological Responses Using Laboratory Small-Scale Microcosms. *Environ. Sci. Nano* **2020**, *7*, 105–115. [CrossRef]
44. Chatterjee, T.; Chatterjee, P.; Chakraborty, A.K.; Pradhan, S.K.; Meikap, A.K. Template-Free Growth of Copper-Doped Hydroxyapatite Nanowhiskers and Their Use as Uric Acid Electrochemical Sensor. *Mater. Today Commun.* **2022**, *33*, 104870. [CrossRef]
45. Bulina, N.V.; Eremina, N.V.; Vinokurova, O.B.; Ishchenko, A.V.; Chaikina, M.V. Diffusion of Copper Ions in the Lattice of Substituted Hydroxyapatite during Heat Treatment. *Materials* **2022**, *15*, 5759. [CrossRef]
46. Rouzé l'Alzit, F.; Bazin, T.; Cardinal, T.; Chung, U.-C.; Catros, S.; Bertrand, C.; Gaudon, M.; Vignoles, G. Powder Bed Laser Sintering of Copper-Doped Hydroxyapatite: Numerical and Experimental Parametric Analysis. *Addit. Manuf.* **2021**, *46*, 102044. [CrossRef]
47. Khamaru, N.; Das, A.; Das, D.; Karmakar, A.; Chatterjee, S. Effect of Cu-Doping on the Dielectric Properties of MnV_2O_6 Compound. *J. Magn. Magn. Mater.* **2020**, *512*, 167044. [CrossRef]
48. Liu, L.; Liu, T.; Liu, P.; Huang, Q.; Gui, H.; Lu, A. Crystallization, Spectroscopic and Dielectric Properties of CuO-Added Magnesium Aluminosilicate-Based Glasses. *Ceram. Int.* **2021**, *47*, 32666–32674. [CrossRef]
49. Pan, J.; Thierry, D.; Leygraf, C. Electrochemical Impedance Spectroscopy Study of the Passive Oxide Film on Titanium for Implant Application. *Electrochim. Acta* **1996**, *41*, 1143–1153. [CrossRef]

coatings

MDPI

Article

Mechanisms of Premature Fracture in Modular Neck Stems Made of CoCrMo/Ti6Al4V and Ti6Al4V/Ti6Al4V Alloy

Drago Dolinar [1,2,3,4], Miro Gorenšek [1,3], Klemen Avsec [2,4], Barbara Šetina Batič [5], Matej Hočevar [5], Matjaž Godec [5], Borut Žužek [5], Mojca Debeljak [6], Monika Jenko [1,3,5,*], John T. Grant [7] and Boštjan Kocjančič [2,4]

1 MD-RI Institute for Materials Research in Medicine, Bohoričeva 5, 1000 Ljubljana, Slovenia; dolinardrago@gmail.com (D.D.)
2 Department for Orthopaedic Surgery, UMC Ljubljana, Zaloška 9, 1000 Ljubljana, Slovenia; kavsec@gmail.com (K.A.); kocjancicb@gmail.com (B.K.)
3 MD-Medicina, Bohoričeva 5 a, 1000 Ljubljana, Slovenia
4 Chair of Orthopedics, Faculty of Medicine, University of Ljubljana, Vrazov Trg 2, 1000 Ljubljana, Slovenia
5 Institute of Metals and Technology, Lepi pot 11, 1000 Ljubljana, Slovenia; barbara.setina@imt.si (B.Š.B.); matej.hocevar@imt.si (M.H.); matjaz.godec@imt.si (M.G.); borut.zuzek@imt.si (B.Ž.)
6 University Rehabilitation Institute Republic of Slovenia Soča, Linhartova 51, 1000 Ljubljana, Slovenia; mojca.debeljak@ir-rs.si
7 Research Institute, University of Dayton, Dayton, OH 45469, USA; john.grant@surfaceanalysis.org
* Correspondence: monica.jenko@gmail.com; Tel.: +386-31-311-076

Abstract: In this paper, we present the mechanisms of premature fracture of modular neck stems in two case studies: (I) when the neck and stem are both made of the same Ti6Al4V alloy, and (II) when the neck and stem are made from two different alloys, CoCrMo and Ti6Al4V alloy. Our study integrates two orthopedic patients who have undergone primary uncemented THA for usual indications in two orthopedic centers (Community Health Centre and University Medical Centre). Both centers are part of the national public health care system. Both surgeries were performed by two skilled orthopedic surgeons with more than 10 years of experience in THA. The survivorship of the modular neck of cast CoCrMo alloy was 24 months. The survivorship of the modular neck from Ti6Al4V alloy was 84 months. Multivariate analyses were performed to assess the differences in the fretting, corrosion, and fatigue of the two prematurely failed modular neck stems: stereo light microscopy (SLM), scanning electron microscopy (SEM), X-ray energy-dispersive spectroscopy (EDS), and electron backscatter diffraction (EBSD). Patient demographic information, including sex, age, body mass index, survivorship of implants, and reason for the revision, was collected from medical records. We found that fretting and fatigue occurred on both neck-stem retrievals due to additional galvanic corrosion, but the CoCrMo/Ti6Al4V alloy system suffered more corrosion due to additional galvanic corrosion and fractured earlier than the Ti6Al4V/Ti6Al4V metal alloy system. Both metallic alloy systems used in this application are known to be highly corrosion-resistant, but the bio-tribo-corrosion processes need to be understood in detail and characterized so that appropriate improvements in design and materials can be made.

Keywords: total hip arthroplasty; modular neck; Ti6Al4V alloy; CoCrMo alloy; corrosion

Citation: Dolinar, D.; Gorenšek, M.; Avsec, K.; Šetina Batič, B.; Hočevar, M.; Godec, M.; Žužek, B.; Debeljak, M.; Jenko, M.; Grant, J.T.; et al. Mechanisms of Premature Fracture in Modular Neck Stems Made of CoCrMo/Ti6Al4V and Ti6Al4V/Ti6Al4V Alloy. *Coatings* **2023**, *13*, 1255. https://doi.org/10.3390/coatings13071255

Academic Editors: Filippo Berto and Michał Kulka

Received: 31 May 2023
Revised: 10 July 2023
Accepted: 14 July 2023
Published: 16 July 2023

1. Introduction

Modular neck stems were introduced to hip endoprosthesis with the expected benefits of reducing pain and improving the range of motion and leg length [1–3]. Besides classic stems (Figure 1a,c), Wright Medical Technology/Microport, Stryker, Depuy, Lima Corporate, Zimmer, Adler Ortho, Cremasoli, and others are recognized worldwide manufacturers of modular neck stems (Figure 1b). The stem and the neck are available in different sizes and different neck angles, as seen in Figure 1b, to tailor the implant to the individual patient. Increased implant modularity with modular necks made from Ti6Al4V and stems from the

same alloy has generated interest in recent years because the various neck sizes, offsets, lengths, and design configurations allow the surgeon to optimize the range of motion and the patient's leg length. However, there have been concerns due to early in vivo fractures as well as adverse tissue reactions related to corrosion at the neck–stem interface [2–11].

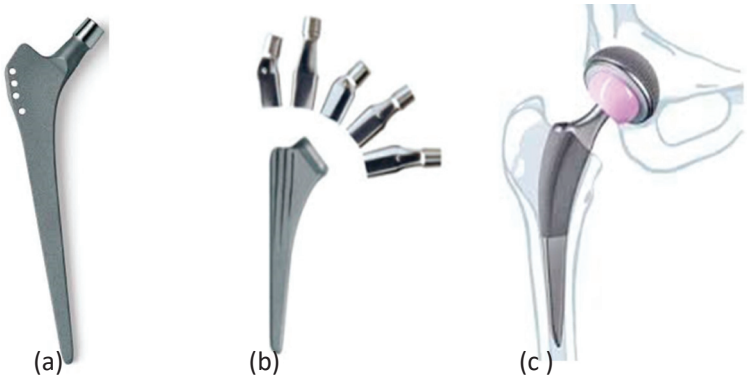

Figure 1. (**a**) Classic Ti6Al4V femoral cementless ZM stem; (**b**) modular stem with 5 different modular necks; the stem and the neck are in different sizes with different neck angles to tailor the implant to the individual; (**c**) total hip endoprostheses, classic stem with an acetabular composed of a ceramic head, highly cross-linked PE cup, and a trabecular metal cup.

The presence of the neck–stem interface using titanium alloys makes the neck junction vulnerable to fretting, corrosion, and fatigue fracture. Several authors reported an early fracture of long modular necks made of Ti6Al4V alloy [5–11].

Many of the femoral modular stems suffer from premature fractures after total hip arthroplasty (THA) of the titanium alloy neck. Due to the results of in vitro investigations which presented better wear and mechanical properties, as seen in Table 1, a cobalt–chromium–molybdenum neck was introduced [9–13].

CoCrMo neck fractures have also been reported after only a few months of implantation [12,14]. Some reports have shown cases of fractured necks that could not be detracted from the stem pocket, requiring the replacement of the otherwise well-fixed femoral stems [2,4,7,11].

Table 1. Physical and mechanical properties of CoCrMo cast alloy [15] and Ti6Al4V alloy [16].

Material	Density (kg/m^3)	Elastic Modulus (GPa)	Poisson's Ratio	Thermal Conductivity (W/mK)	Specific Heat (J/kgK)	Thermal Expansion Coefficient (10^{-6}/K)	Melting Point (K)
CoCrMo	8768	283	0.29	14.8	452	12	1663
Ti6Al4V	4430	109	0.34	6.8	611	9.0	1878

The main aim of our work was to investigate mechanisms of premature failure of two case studies due to the fracture of the long neck in two different metallic alloy systems: the same alloy (neck and stem are both made from the same Ti6Al4V alloy with a survivorship of 84 months) and different alloys (neck made from CoCrMo alloy with better mechanical properties and a stem body made from Ti6Al4V alloy, with a survivorship of only 24 months) [12–14].

The research was a joint effort of orthopedic surgery clinicians and material scientists.

2. Materials and Methods

2.1. Patient Characteristics

The present study examines the outcomes of two orthopedic patients who underwent primary uncemented total hip arthroplasty (THA) for typical indications at two reputable orthopedic centers: the Community Health Centre and the University Medical Centre. Both centers are part of the national public health care system.

2.2. Surgery Characteristics

Both surgeries were performed by two skilled orthopedic surgeons with more than 10 years of experience in THA, performing at least 200 THAs yearly. A standard anterolateral approach was used in both cases. Preoperative planning was performed using analog templates on standard calibrated 110 cm AP pelvic X-rays. Both surgeries were performed according to the patient's preoperative planning and anatomical features to restore hip anatomy, preventing hip instability and minimal postoperative leg length discrepancy. Patients received routine follow-ups at institutional outpatient clinics at 3 months, 6 months, and 1 year postoperatively, and thereafter upon request of the patient and/or their family physician. The X-rays of the patients with failed implants are shown in Figure 2.

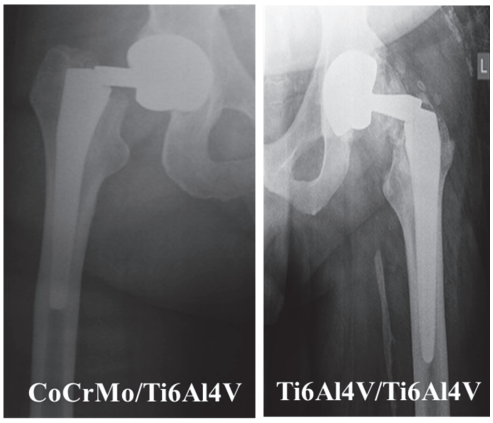

Figure 2. (**left** panel) Standard calibrated 110 cm AP pelvic X-rays of a fractured CoCrMo/Ti6Al4V modular neck of a 51-year-old male, survivorship 24 months. (**right** panel) X-ray of a fractured Ti6Al4V/Ti6Al4V modular neck of a 42-year-old male, lifetime 84 months.

The fractured surfaces of the CoCrMo modular neck of the different-metal system CoCrMo/Ti6Al4V with a survivorship of 24 months and the Ti6Al4V modular neck of the same-metal system Ti6Al4V/Ti6Al4V with a survivorship of 84 months are shown in Figure 3.

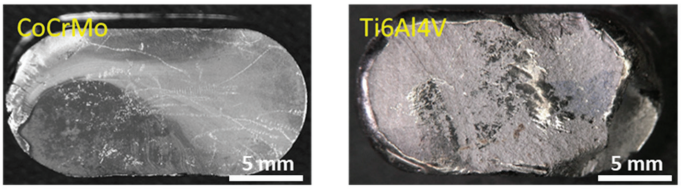

Figure 3. (**Left** panel) Fractured surface of CoCrMo modular neck of a 51-year-old male, survivorship 24 months. (**Right** panel) Fractured surface of Ti6Al4V modular neck of a 42-year-old male, survivorship 84 months. Stereo light microscope Tagarno FHD trend was used for the visualization of fractured surfaces of the CoCr Mo modular neck and Ti6Al4V modular neck.

2.3. Implant Characteristics

2.3.1. Modular Neck Stem Made of CoCrMo (Neck) and Ti6Al4V (Stem) Alloy

The fractured modular neck of cast CoCrMo alloy, manufactured by Wright Medical Technology/Microport, Profemur Plus Modular Neck size /°8 with reference PHAC 1254 (CoCr Mo alloy), was retrieved and provided by a community hospital. The femoral stem of forged Ti6Al4V alloy, manufactured by Wright Medical Technology Microport, was retrieved, with a stem size of 5 and length of 125 mm (Ti6Al4V alloy). The modular neck stem (CoCrMo/Ti6Al4V) is the femoral component of the hip endoprosthesis and Biolox Delta femoral head, size 32 mm PHA0410—the alumina matrix composite is a modern press-fit acetabulum acetabular component. The fractured sample was provided by the community hospital. The survivorship of the hip endoprosthesis was 24 months (2 years). The fracture surface of the retrieved implant is presented in Figure 3, left panel.

The chemical composition of CoCrMo cast alloy is presented in Table 2, and that of Ti6Al4V is presented in Table 3. The physical and mechanical properties of CoCrMo and Ti6Al4V are presented in Table 1.

Table 2. Chemical composition of CoCrMo (Mass%) cast alloy, ICP measurements at IMT.

Material	Cr	Mo	Ni	Fe	C	Si	Mn	P	S	Ti	Co
CoCrMo	29.5	6.6	0.25	0.07	0.35	0.7	0.5	0.2	0.1	0.1	balance

ICP—inductively coupled plasma spectroscopy, IMT—Institute of Metals and Technology, Ljubljana, Slovenia.

Table 3. Chemical composition of Ti6Al4V (Mass%), ICP measured at IMT.

Material	Al	V	Fe	O	C	N	H	Ti
Ti6Al4V	6.40	4.30	0.04	0.08	0.05	0.01	0.001	balance

ICP—inductively coupled plasma spectroscopy, IMT—Institute of Metals and Technology, Ljubljana, Slovenia.

The microstructure of CoCrMo alloys consists of face-centered cubic (fcc) and hexagonal close-packed (hcp) crystalline structures. Typically, the (fcc) phase is predominant at room temperature but the (fcc) $\rightarrow$ (hcp) transformation could be isothermally or strain-induced, as reported in detail in our previous paper [13].

The microstructure of Ti6Al4V alloy consists of a dual-phase microstructure, where the matrix is the Ti-α phase and the V-rich phase is the Ti-β phase, as reported in our previous paper [13].

2.3.2. Modular Neck Stem Made of the Same Ti6Al4V (Neck) and Ti6Al4V (Stem) Alloy

The fractured modular neck of forged Ti6Al4V alloy manufactured by Wright Medical Technology/Microport was retrieved, fractured, Profemur Plus Modular Neck size /°8 with reference PHAC 1254 (Ti6Al4V alloy). The femoral stem of forged Ti6Al4V alloy manufactured by Wright Medical Technology/Microport was retrieved, with a stem size of 8 and length of 140 mm (Ti6Al4V alloy). The modular neck stem (Ti6Al4V/Ti6Al4V) is the femoral component of the hip endoprosthesis and the Biolox Delta femoral head, size 32 mm PHA0410—the alumina matrix composite is a modern press-fit acetabulum component. The failed endoprosthesis was provided by the University Medical Center. The survivorship of hip endoprosthesis with a modular neck stem of the same alloy (Ti6Al4V neck and Ti6Al4V stem) was 84 months (7 years). The fracture surface of the retrieved implant is presented in Figure 3, right panel.

2.4. Sample Preparation

The retrieved Ti6Al4V stems and long modular necks of CoCrMo and Ti6Al4V alloys were cut using a Struers's saw for the preparation of metallographic samples and the samples for other investigations. For the microstructure analyses and surface chemistry measurements, the samples were ground with SiC 220 grinding paper (1 min), polished

with MD Largo 9 m blue lubricant (5 min), and oxide-polished with MDCHEM OP-S (STRUERS GmbH, Zweigniederlassung, Austria) and H_2O_2 (10 min). The samples for the bulk microstructure analyses were additionally etched with Kroll's reagent.

2.5. Methods

2.5.1. Stereo Light Microscopy (SLM)

A stereo light microscope, Tagarno FHD trend, was used for the visualization of the fractured surfaces of the Ti6Al4V modular neck and the Co-Cr-Mo modular neck.

2.5.2. Scanning Electron Microscopy (SEM, SEM/EDS, SEM/EBSD) Analysis

The morphology and microstructure of the fracture surfaces were analyzed using a scanning electron microscope, JEOL JSM 6500-F (JEOL Ltd., Japan). The SEM images were acquired using an accelerating voltage of 15 kV, with a current of about 500 pA and a working distance of 10 mm. Secondary electron and backscattered electron images were acquired. The elemental compositions of the samples were analyzed using Oxford INCA EDS analysis. The EDS spectra were acquired using a 15 kV and 1 nA beam, with an acquisition time of 60 s for each spectrum. The EDS spectra were analyzed using INCA Energy software to determine the elemental composition and distribution in the sample. Electron backscatter diffraction (EBSD) was also used to determine the type of carbides present in the microstructure. A Nordlys EBSD detector (HKL) and a Channel 5 data analysis suite were used. The EBSD patterns were acquired at 15 kV accelerating voltage and 2 nA current.

3. Results

3.1. Modular Neck Stem Made of CoCrMo (Neck) and /Ti6Al4V (Stem) Alloys

The patient with the implanted hip endoprostheses with a modular neck stem manufactured from two different alloys (long modular neck of CoCrMo and stem of Ti6Al4V alloy) was an active 51-year-old male with a normal BMI; he maintained his physical condition by light cycling. He slipped on the stairs at home, suddenly had terrible pains, and panicked because he was motionless. X-rays confirmed a fractured stem neck and required urgent revision surgery (Figure 2, left panel). The survivorship of the modular neck stem was 24 months (2 years).

Figure 4 represents in the inner panel the SLM image of the fractured surface of the CoCrMo modular neck in the inner panel with the marked Zones A, B1, B2, C, and D.

Details of the first part of the fracture, marked as Zone A, are shown in Figure 4. Deposits of biological material were observed on the surface, as well as cracked carbide particles. The crack initiated on the surface of the CoCrMo modular neck stem (pink arrow in Figure 4) due to several different factors, but the dominant mechanisms were fretting and crevice corrosion. The CoCrMo femoral neck was dynamically loaded, exposed to a corrosive medium in the human liquids, and surrounded by a Ti6Al4V alloy with different electrochemical potentials. Constant micromotions caused repeated breakage of the passive oxide films and an unstable electrochemical environment within the crevice for both the cobalt alloy and Ti alloy passive films, as reported in the literature [17–20]. AES and XPS analyses of the thin oxide (passive film), described in detail in our previous studies [12,13], show that the oxide film on CoCrMo consists of Cr_2O_3 and traces of CoO_3 oxides with an estimated thickness of 2 nm. The oxide film on Ti6Al4V alloy consists of TiO_2 and traces of Al_2O_3 with an estimated thickness of 7 nm. Thermodynamic data of passive oxide formation as well as electrochemical studies on CoCrMo and Ti6Al4V alloy confirm that the re-passivation is much faster on Ti [21–26].

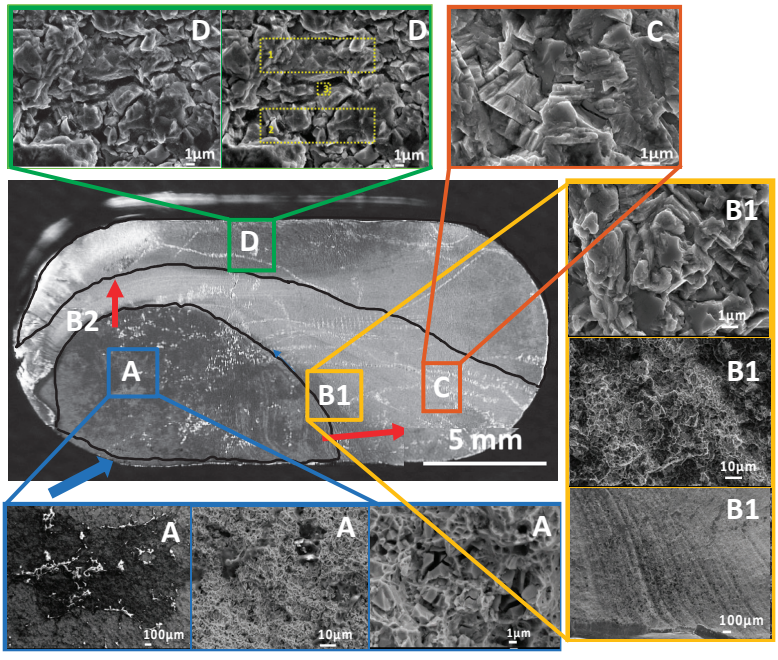

Figure 4. SLM of the fractured surface of CoCrMo neck on the main inside image represents the mechanism of CoCrMo alloy modular neck fracture. The blue arrow indicates the crack initiation; Zone A, the corroded fractured surface with deposited biological material, is shown in three SE images in three blue-marked panels: the **left** panel (**A**) at lower magnification, the detail of fatigue fracture and cracked carbides at higher magnification, panel (**A**) in the **middle**, and cracked carbide at highest magnification in the **right** panel (**A**). The red arrows show the direction of fatigue crack propagation in location (**B1**) and location (**B2**). The fatigue striations were observed in SE images in areas marked in yellow, and the microstructure details are shown in the **middle** and **upper** panels. In Zone (**C**), the fracture surface is very rough and angular. The fracture surface shows several secondary cracks that are perfectly straight and short. Next to these flat cracks, larger secondary cracks can be seen, which are branched and longer than the flat ones. The lower SEI shows the crack propagation and the **middle** and **upper** SEI shows the details at higher magnifications. The SE image of Zone (**D**), marked in green, shows a sudden fracture. Zone (**D**) in the **right** panel shows areas of EDS analysis of the fracture surface (yellow squares marked in the **right** panel).

In the zones marked B1 and B2, in Figure 4 (main inside panel), gradual fatigue crack progression is visible, and the main direction of crack progression is also marked with red arrows. Traces of the gradual progression of the crack at slightly higher magnifications using a scanning electron microscope are shown in panel B1, marked in yellow. Smaller secondary cracks are also present on the fracture surface, which were formed during the gradual progression of the main crack. The topography of the fracture is rounded, which is an indication that the crack was present for a long time and that during use, there was regular mutual contact between the two parts of the implant, which led to wear and, as a result, a smooth fracture surface [14].

In Zone C, the fracture surface is very rough and angular. The fracture surface shows several secondary cracks that are perfectly straight and short. Next to these flat cracks, larger secondary cracks can be seen, which are branched and longer than the flat ones. Based on the microstructure of the CoCrMo alloy, it can be concluded that the straight and short cracks originated at the twin boundaries (deformation twins in the microstructure)

and ended at the crystal grain boundaries. Longer and branched cracks, however, run along the crystal boundaries and the boundaries between the carbides and the matrix [14].

Due to crack propagation, the loads on the diminishing cross-section of the modular neck increased. When the remaining nonfractured area was too small, the rest of the material suddenly fractured. The fracture surface is shown in Figure 4, Zone D, marked in green. The marked yellow rectangles represent areas of EDS analysis. EDS analysis of the fracture surface showed that there was indeed some transfer of Ti from the Ti6Al4V part of the prosthesis to the CoCrMo part. The results of the EDS analysis are given in Table 4. EDS analysis confirms the dissolution of Co into the soft tissue, which is evident from the low content of cobalt on the fracture surface. The same observation is reported in the literature where cobalt is present in the serum, erythrocytes, and urine of patients caused by MoM (metal-on-metal) joints [26].

Table 4. EDS elemental analysis of spectra from the areas marked in Figure 4 (mass %).

Spectrum	C	O	Si	Ti	V	Cr	Mn	Fe	Co	Mo
1	3.9	5.5	0.8	4.7	0.0	26.7	0.0	0.9	50.9	6.2
2	4.5	7.4	0.5	6.3	0.0	26.7	0.0	0.0	48.4	6.2
3	1.3	6.7	0.0	28.0	1.9	27.3	0.0	0.0	34.7	

The upper half of Figure 5 shows the SE image of the CoCrMo microstructure, which was found under the fracture surface. For this purpose, a sample 15 mm below the fracture surface was cut and the metallographic sample was prepared by classic metallographic preparation methods, as described in Section 2.4. The brittle $Cr_{23}C_6$ carbides are embedded in the tough CoCrMo matrix. The fracture surface exhibits the cracked carbide $Cr_{23}C_6$, determined using EBSD–Kikuchi lines, as seen in the lower half of Figure 5. In addition to fretting and crevice corrosion, modular neck stems made of different alloys also suffered galvanic corrosion [23,26]. Our previous studies determined that the CoCrMo passive layer is thinner than the passive layer of the Ti6Al4V alloy and that CoCrMo is vulnerable to crevice corrosion on the surface due to the carbide formation and depletion of Cr [13].

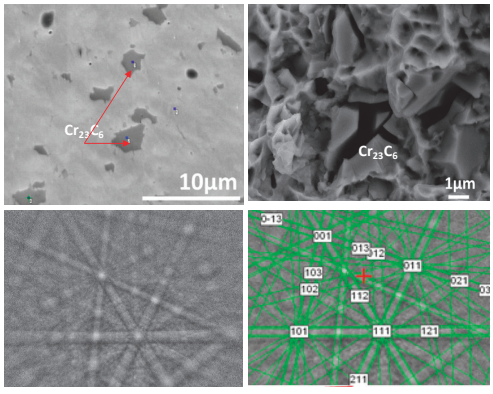

Figure 5. SE image of CoCrMo microstructure. The sample was cut 15 mm under the fractured surface. Matrix hcp structure is light gray, and brittle $Cr_{23}C_6$ carbide is dark gray. The fractured surface exhibits the cracked carbide $Cr_{23}C_6$ determined by the EBSD method by Kikuchi lines.

EDS results show the transfer of Ti ions from the stem to the CoCrMo neck, where Spectrum 3 shows an unexpectedly high titanium content (28.0 mass%) and, vice versa, a very low content of Co (34.7 mass%). According to Gilbert [26], the preferential dissolution of Co and the formation of intermetallic-phase Ti-CrMo occurred.

3.2. Modular Neck Stem Made of the Same Alloy: Ti6Al4V (Neck) and Ti6Al4V (Stem)

The patient with the implanted hip endoprostheses with a long modular neck stem manufactured from the same alloy (both the long modular neck and the stem were made of forged Ti6Al4V alloy) was an active 42-year-old male with a normal BMI. He felt a sudden pain in the hip and heard a crack from that region, and afterward, he was unable to stand. X-rays confirmed a fractured Ti6Al4V neck and required urgent revision surgery (Figure 2, right panel). The survivorship of the modular stem neck was 84 months (7 years).

The fracture surface of the Ti6Al4V neck is shown in Figure 6. The crack initiation site is marked by a green arrow, and the red arrows represent the direction of fatigue crack propagation.

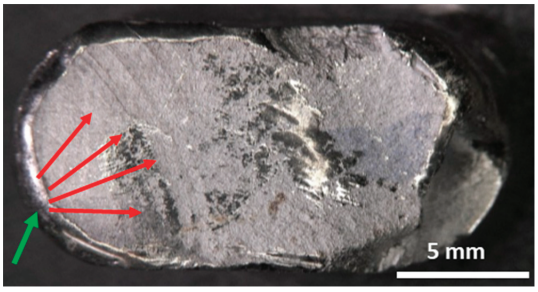

Figure 6. SLM image of the fractured modular neck made from Ti6Al4V alloy, taken from a 42-year-old male, lifetime 84 months. See the text for a description of the arrows.

With the increased stresses on the modular neck stem interface, passive oxide layers of Ti6Al4V are interrupted and re-passivation of the metal surface is prevented due to poor oxygen supply, which causes the release of chloride ions within the joint, and the consequence is a lower local pH. An anaerobic and acidic environment is created, and further abrasive wear and corrosion increase the risk of modular neck fracture over time [12,13,21,24–26].

The combined effects of corrosion, long modular necks, metal-on-metal components, patient obesity, as well as metallic, ceramic, corundum, and polyethylene wear particles and activity levels may create a local microenvironment that can initiate crack formation. During the loading of the same Ti6Al4V neck/Ti6Al4V stem metal system, the crack site of the long modular neck slowly and gradually advanced. Micro-motions at the interface induce fretting and crevice corrosion, contributing to micro-crack creation within the zone of corrosion and increasing the risk of dynamic fatigue fracture.

The part of the fractured surface was covered with organic material of ultra-high-molecular-weight polyethylene (UHMWPE) nanoparticles. The load on the rest of the cracked modular neck increased and traces of gradual crack progression appeared. When the remaining nonfractured area was too small, the rest of the material suddenly fractured.

Figure 7 shows the fractured surfaces on the Ti6Al4V long modular neck (a), where two different regions are found on the fractured surface; the first one is marked with a yellow square (b), and the second is marked with a green square (c). The first region shows signs of mechanical deformation due to walking, and in that region, signs of gradual crack propagation are visible at higher magnification where fatigue striations are seen in the range of 50–100 nm steps (d and e). The second region (a–c) shows the surface of the sudden fracture where a rough and uneven ductile fractured surface is seen with visible ridges and dimples, indicating tearing and deformation of material before the final fracture.

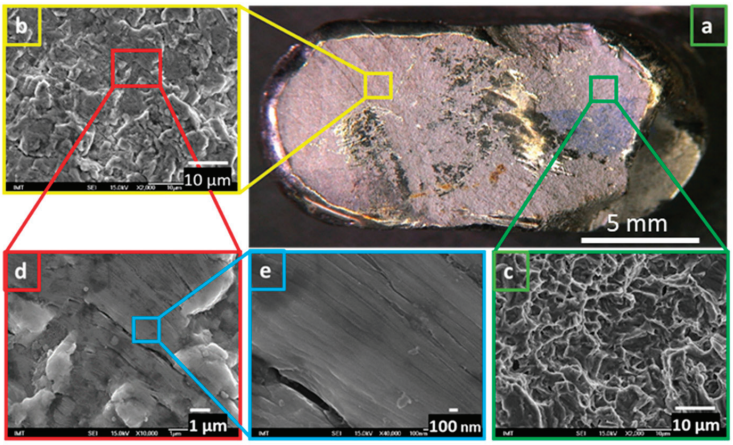

Figure 7. (**a**) Image of different fractured surface regions of fractured Ti6Al4V modular neck; (**a–b**) yellow-marked region and yellow-framed SE image of fatigue failure and with higher magnifications (**b**,**d**,**e**); (**a**,**c**) green-marked region and green-framed SE image with sudden ductile fracture. Organic deposits on fractured Ti6Al4V surface due to PE nanoparticle migration were found and visible as blue color (**a**).

4. Discussion

The use of modular femoral stems in total hip arthroplasty has increased in popularity over the past three decades. Although it offers several distinct advantages intraoperatively, long-term success has not yet been established. The potential complication of increasing modularity is modular neck fracture [3–11,14,17–20].

The results of our studies on the mechanisms of premature modular neck fracture of different and same alloys showed that fretting, corrosion, and fatigue occurred on both neck–stem retrievals of the same Ti6Al4V neck/Ti6Al4V stem alloy, as well as different CoCrMo neck/Ti6Al4V stem alloys where galvanic corrosion was also involved, which is in good agreement with literature data [21–27].

Our findings are in good agreement with Ref. [24], where Virtanen reports that for orthopedic implants, fretting corrosion (or generally, wear-assisted corrosion/tribo-corrosion) is often discussed as the dominant failure mode, especially in the case of high-corrosion-resistance passive alloys, for which the tribological load leads to local mechanical destruction of the passive film. Even though a subsequent spontaneous re-passivation reaction takes place in many cases, continuous activation/re-passivation cycles lead to an increased material loss. Virtanen reported that the fretting corrosion behavior and restoration ability were studied under various combinations of load, frequency, and number of fretting cycles and that the thickness and the nature of oxide–passive layers on Ti strongly influence the mechanism and the intensity of tribo-corrosion. The degradation of biomaterials in the biological environment is a complex process that depends on all material parameters (e.g., chemical composition, microstructure), environmental parameters (e.g., chemistry, temperature), as well as construction (e.g., presence of crevices). For materials in biomedical applications, the situation is more complex than in classical engineering applications because the biological environment of the host is a highly dynamic system [24].

In the case of a stem and neck composed of different alloys, Ti6Al4V and CoCrMo, the hip endoprosthesis designers ignore the fact that Ti6Al4V and CoCrMo have different electrochemical potentials which, after implantation, are immersed in a corrosive electrolyte, human liquids. Besides fretting, fatigue and corrosion occurred. The corrosion is usually crevice corrosion, but galvanic corrosion also occurred. This caused the formation of corrosion damage on the surface, and everyday normal activity due to dynamic loading leads to the formation of microcracks on the surface which then gradually propagate. No

excessive mechanical loadings were needed since crack tips are usually very sharp and stress concentrations are consequently high enough to cause the crack to propagate. Once the remaining cross-section of the implant is diminished, it can no longer support the loads, leading to a catastrophic break [21–24]. This statement is in good agreement with the survivorship of the modular neck stem of different alloys, which was only 24 months in our case study.

The main aim of our studies was to emphasize the importance of the optimal choice of materials for the modular neck stem of hip endoprostheses. To emphasize the importance of the materials, two cases of failed modular neck stems, which we received from two hospitals (a university clinical center and a community hospital), were studied.

Both metal systems of different alloys, CoCrMo/Ti6Al4V, and the same alloy, Ti6Al4V/Ti6Al4V, were immersed after implantation into a corrosive electrolyte, human liquids, and exposed to constant micromotion, leading to fretting and corrosion, but the system of different alloys suffered more corrosion due to additional galvanic corrosion due to different electrochemical potentials [26].

The neck and stem composed of the same material, Ti6Al4V, have the same electrochemical potential and the prosthesis is still immersed in body liquids and electrolytes. In this case, the initial crack formation can be slower and is not the consequence of corrosion damage, but occurs due to fretting and wear corrosion [19,20,22,24,26,27]. Again, the crack propagates by everyday normal activity, where each step represents the dynamic cycle of loading and causes the crack to slowly propagate. When the nominal cross-section of the implant is diminished to such an extent that the remaining cross-section can no longer support the load, catastrophic failure occurs. This statement is in good agreement with the survivorship of the modular neck stem of the same Ti6Al4V/Ti6Al4V alloy, which was 84 months in our case study.

The recent literature data on survivorship of the modular neck stem THA system confirm a lower yield than the similar mono-block stem THA system in a comparable clinical environment with long-term follow-up [28–33].

5. Conclusions

We found that fretting, corrosion, and fatigue occurred on both neck–stem retrievals of the same (Ti6Al4V neck/Ti6Al4V stem) and different (CoCrMo neck/Ti6Al4V stem) metal systems.

The cracked femoral neck made of CoCrMo alloy was dynamically loaded, exposed to a corrosive medium, and surrounded by a Ti6Al4V alloy with a different electrochemical potential. Due to the constant dynamic load and a combination of different materials in a corrosive medium, galvanic corrosion on the surface of the modular neck occurred.

The different-metal system made of CoCrMo/Ti6Al4V suffered more corrosion than the same-metal system made of Ti6Al4V/Ti6Al4V alloy due to additional galvanic corrosion.

The nature of the in vivo mechanisms causing the formation of the bio-tribo-corrosion processes needs to be understood and characterized so that appropriate changes in design and materials can be implemented.

Investigations of retrieved modular hip implants have revealed that significant corrosion can occur in vivo over the long term and may be a significant contributor to adverse biological effects and clinical failure seen in some patients (third body wear, remote trace metal accumulation, aseptic loosening, etc.), bringing into question the concept of modularity.

Author Contributions: Conceptualization, D.D., M.G. (Miro Gorenšek), M.J., B.K. and B.Ž.; methodology, M.J., J.T.G., M.G. and B.K., formal analysis, B.Ž., B.Š.B., M.J., M.H. and M.G. (Matjaž Godec); investigation, M.J., M.G., D.D. and K.A.; writing—original draft preparation, M.J., M.G. (Miro Gorenšek), D.D., B.K., M.D. and K.A., writing—review and editing, M.J., D.D. and B.Š.B. supervision, M.J. and D.D., project administration, M.D. and K.A., funding acquisition, M.J., M.G. (Miro Gorenšek) and D.D. All authors have read and agreed to the published version of the manuscript.

Funding: This research was funded by the Slovenian Research Agency ARRS (L3-2621 project and P2-0132—Research Program Institute of Metals and Technology) and Tertiary Projects of the Department of Orthopaedic Surgery of University Medical Centre Ljubljana (UMCLJ 20210029 and UMCLJ 201900684).

Institutional Review Board Statement: Not applicable for studies not involving humans or animals.

Informed Consent Statement: Not applicable for studies not involving humans or animals.

Data Availability Statement: Not applicable.

Conflicts of Interest: The authors declare no conflict of interest.

References

1. Azar, F.M.; Canale, S.T.; Beaty, J.H. Arthroplasty of the hip. In *Campbell's Operative Orthopaedics, E Book*, 13th ed.; Elsevier: Amsterdam, The Netherlands, 2017; pp. 166–337, ISBN 9780323392570.
2. Baleani, M.; Toni, A.; Ancarani, C.; Stea, S.; Bordini, B. Long-term survivorship of an exchangeable-neck hip prosthesis with a Ti-alloy/Ti-alloy neck–stem junction. *Arch. Orthop. Trauma Surg.* **2023**, *43*, 649–3657. [CrossRef]
3. Ellman, M.B.; Levine, B.R. Fracture of the Modular Femoral Neck Component in Total Hip Arthroplasty. *J. Arthroplast.* **2013**, *28*, 196.e1–196.e5. [CrossRef]
4. Wright, G.; Sporer, S.; Urban, R.; Jacobs, J. Fracture of a Modular Femoral Neck After Total Hip Arthroplasty, A Case Report. *J. Bone Joint Surg. Am.* **2010**, *92*, 1518–1521. [CrossRef]
5. McTighe, T.; Brazil, D. Modular Necks and Corrosion—Review of Five Cases. *Reconstr. Rev.* **2016**, *6*, 49–52. [CrossRef]
6. Park, C.V.; Lim, S.J.; Park, Y.S. Modular Stems: Advantages and Current Role in Primary Total Hip Arthroplasty. *Hip Pelvis* **2018**, *30*, 147–155. [CrossRef]
7. Solarino, G.; Vicenti, G.; Carrozzo, M.; Ottaviani, G.; Moretti, B.; Zagra, L. Modular neck stems in total hip arthroplasty: Current concepts. *EFORT Open Rev.* **2021**, *6*, 751–758. [CrossRef]
8. Maniscalco, P.; Quattrini, F.; Ciatti, C.; Ghidoni, L.; Ghidoni, G.; Burgio, V.; Pogliacomi, F.; Vaienti, E.; Ceccarelli, E. Neck modularity in total hip arthroplasty: A retrospective study of nine hundred twenty-eight titanium neck implants with a maximum follow-up of eighteen years. *Int. Orthop.* **2020**, *44*, 2261–2266. [CrossRef] [PubMed]
9. Castagnini, F.; Bordini, B.; Lucchini, S.; Cosentino, M.; Tassinari, E.; Traina, F. Mid-term outcomes of revision hip arthroplasty due to titanium modular neck failure. *Arch. Orthop. Trauma Surg.* **2023**, 1–10. [CrossRef]
10. Goffton, W.T.; Illical, E.M.; Feibel, R.J.; Kim, P.R.; Baulle, P.E. A Single-Center Experience with a Titanium Modular Neck Total hip Arthroplasty. *J. Arthroplast.* **2017**, *32*, 2450–2456. [CrossRef] [PubMed]
11. Fokter, S.K.; Levašič, V.; Kovač, S. The innovation trap: Modular neck in total hip arthroplasty. *Zdrav. Vestn.* **2017**, *86*, 1–12.
12. Dolinar, D.; Gorenšek, M.; Jenko, M.; Godec, M.; Šetina Batič, B.; Donik, Č.; Kocijan, A.; Debeljak, M.; Kocjančič, B. Biomaterials in endoprosthetics. *Mater. Tehnol.* **2018**, *52*, 89–98. [CrossRef]
13. Jenko, M.; Gorensek, M.; Godec, M.; Hodnik, M.; Setina Batic, B.; Dolinar, D. Surface chemistry and microstructure of metallic biomaterials for hip and knee endoprosthesis. *Appl. Surf. Sci.* **2018**, *427*, 584–593. [CrossRef]
14. Gorenšek, M.; Jenko, M. *Expert Opinion about the Relevant Proceedings of the District Court in Celje: Fracture of a Modular Prosthesis with a Mobile Neck, Manufactured by Wright Medical Technology/MICROPORT*; Profemur Z/Profemur Plus: Ljubljana, Slovenia, 2018; pp. 1–45.
15. *ASTM F75-23*; Standard Specification for Cobalt-28 Chromium-6 Molybdenum Alloy Castings and Casting Alloy for Surgical Implants (UNS R30075). ASTM International: West Conshohocken, PA, USA, 2012.
16. *ASTM F136-13*; Standard Specification for Wrought Titanium-6Aluminum-4Vanadium ELI (Extra Low Interstitial) Alloy for Surgical Implant Applications (UNS R56401). ASTM International: West Conshohocken, PA, USA, 2021.
17. Kovac, S.; Mavcic, B.; Kotnik, M.; Levašič, V.; Sirše, M.; Fokter, S.K. What Factors Are Associated with Neck Fractures in One Commonly Used Bi-modular THA Design? A Multicenter, Nationwide Study in Slovenia. *Clin. Orthop. Relat. Res.* **2019**, *466*, 1324–1332. [CrossRef] [PubMed]
18. Soteranos, N.G.; Sauber, T.J.; Todd, T.T.; Tupis, T. Modular Femoral Neck Fracture after primary total hip arthroplasty. *J. Arthroplast.* **2013**, *28*, 196–199. [CrossRef] [PubMed]
19. Viceconti, M.; Baleani, M.; Squarzoni, S.; Toni, A. Fretting wear in a modular neck hip prosthesis. *J. Biomed. Mater. Res.* **1997**, *35*, 207–216. [CrossRef]
20. Oladokun, A.; Pettersson, B.; Bryant, M.; Engqvist, H.; Persson, B.; Hall, R.; Neville, A. The Fretting of CoCrMo and Ti6Al4V Alloys in Modular Prostheses. *Tribol.-Mater. Surf. Interfaces* **2015**, *9*, 165–173. [CrossRef]
21. Gilbert, J.L.; Buckley, C.A.; Jacobs, J.J. In Vivo Corrosion of Modular Hip Prosthesis Components in Mixed and Similar Metal Combinations. The Effect of Crevice, Stress, Motion, and Alloy Coupling. *J. Biomed. Mater. Res.* **1993**, *27*, 1533–1544. [CrossRef]
22. Eliaz, N. (Ed.) *Degradation of Implant Materials*; Springer: New York, NY, USA, 2012. [CrossRef]
23. Eliaz, N. Corrosion of Metallic Biomaterials: A Review. *Materials* **2019**, *12*, 407. [CrossRef]
24. Virtanen, S. Degradation of Titanium and Its alloys. In *Degradation of Implant Materials*; Chapter 2; Eliaz, N., Ed.; Springer: New York, NY, USA, 2012. [CrossRef]

25. Murena, L.; Maritan, G.; Concina, C.; Scamacca, V.; Ratti, C.; Canton, G. Fracture of the cobalt-crome modular neck in total hip arthroplasty. *Acta Biomed.* **2019**, *90*, 187–191. [CrossRef]
26. Bellefontaine, G. The Corrosion of CoCrMo Alloys for Biomedical Applications. Master's Thesis, School of Metallurgy and Materials, University of Birmingham, Birmingham, UK, 2010.
27. Gilbert, J.L.; Mali, S.; Urban, R.M.; Silverton, C.D.; Jacobs, J. In vivo oxide-induced stress corrosion cracking of Ti-6Al-4V in a neck-stem modular taper: Emergent behavior in a new mechanism of in vivo corrosion. *J. Biomed. Mater. Res. Part B Appl. Biomater.* **2012**, *100*, 584–594. [CrossRef]
28. Fokter, S.K.; Noč, N.; Levašič, V.; Hanc, M.; Zajc, J. Dual-Modular Versus Single-Modular Stems for Primary Total Hip Arthroplasty: A Long-Term Survival Analysis. *Medicina* **2023**, *59*, 290. [CrossRef]
29. Aljenaei, F.; Catels, I.; Louati, H.; Beaul, P.E.; Nganbe, M. Effects of Hip Implant Modular Neck Material and Assembly Method on Fatigue Life and Distraction Force. *J. Orthop. Res.* **2017**, *9*, 2023–2030. [CrossRef] [PubMed]
30. Zajc, J.; Moličnik, A.; Fokter, K.S. Dual Modular Titanium Alloy Femoral Stem Failure Mechanisms and Suggested Clinical Approaches. *Materials* **2021**, *14*, 3078. [CrossRef] [PubMed]
31. Sukopp, M.; Taylor, D.; Forst, R.; Seehaus, F. Femoral stem fracture in Hip Revision Arthroplasty, A Systematic Literature Review of the Real-World Evidence. *Z. Orthop.* **2022**, *160*, 160–171. [CrossRef]
32. Silverton, C.D.; Jacobs, J.J.; Devitt, J.W.; Cooper, H.J. Midterm Results of a Femoral Stem with a Modular Neck Design: Clinical Outcomes and Metal Ion Analysis. *J. Arthroplast.* **2014**, *29*, 1768–1773. [CrossRef] [PubMed]
33. Colas, S.; Allalou, A.; Poichotte, A.; Piriou, P.; Dray-Spira, R.; Zureik, M. Exchangeable Femoral Neck (Dual-Modular) THA Prostheses Have Poorer Survivorship Than Other Designs: A Nationwide Cohort of 324,108 Patients. *Clin. Orthop. Relat. Res.* **2017**, *475*, 2046–2059. [CrossRef]

coatings

MDPI

Article

Ciprofloxacin-Loaded Composite Granules Enriched in Silver and Gallium Ions—Physicochemical Properties and Antimicrobial Activity

Kamil Pajor [1], Łukasz Pajchel [1], Anna Zgadzaj [2], Paulina Kowalska [1], Anna Kowalczuk [3] and Joanna Kolmas [1,*]

[1] Department of Analytical Chemistry, Faculty of Pharmacy, Medical University of Warsaw, ul. Banacha 1, 02-097 Warsaw, Poland
[2] Department of Environmental Health Sciences, Faculty of Pharmacy, Medical University of Warsaw, ul. Banacha 1, 02-097 Warsaw, Poland
[3] National Medicines Institute (NIL), Chelmska 30/34, 00-725 Warszawa, Poland
* Correspondence: joanna.kolmas@wum.edu.pl

Abstract: Various calcium phosphates (hydroxyapatite, α- and β-tricalcium phosphate, and brushite) containing silver or gallium ions were synthesized via standard methods and subjected to physicochemical analysis by Fourier transform infrared spectroscopy (FT-IR), powder X-ray diffractometry (PXRD), and atomic absorption spectrometry (AAS). In the next step, the obtained calcium phosphate powders, sodium alginate, and chondroitin were used to produce composite granules. Ciprofloxacin, a broad-spectrum antibiotic that can be used in local delivery systems targeting bone tissue, was loaded into the granules. The release of silver and gallium ions as well as ciprofloxacin was then examined by inductively coupled plasma mass spectrometry (ICP-MS) and high-performance liquid chromatography (HPLC), respectively. The cytotoxicity of the granules was studied using a neutral red uptake (NRU) test and mouse embryonic fibroblasts. Moreover, preliminary antibacterial activity against *Staphylococcus aureus* and *Escherichia coli* was measured. The study showed that the type of calcium phosphates enriched in silver or gallium significantly affects the release profile of these ions. Biphasic calcium phosphates also have an impact on the morphology of the granules. Most of the granules turned out to be non-toxic to mammalian cells. Microbiological tests showed high antibacterial activity against both strains of bacteria.

Keywords: calcium phosphates; silver; gallium; ciprofloxacin; drug release

Citation: Pajor, K.; Pajchel, Ł.; Zgadzaj, A.; Kowalska, P.; Kowalczuk, A.; Kolmas, J. Ciprofloxacin-Loaded Composite Granules Enriched in Silver and Gallium Ions—Physicochemical Properties and Antimicrobial Activity. *Coatings* **2023**, *13*, 494. https://doi.org/10.3390/coatings13030494

Academic Editors: Ajay Vikram Singh, Seungil Kim and Huirong Le

Received: 12 December 2022
Revised: 15 January 2023
Accepted: 20 February 2023
Published: 23 February 2023

1. Introduction

Surgical site infection (SSI) is still a huge problem and a major challenge in orthopedic surgery. Conventional orthopedic implants are prone to bacterial adhesion and biofilm formation, making antibiotics less effective [1–3]. Orthopaedic SSI, which leads to a bone infection known as osteomyelitis, may be caused by many different strains of bacteria. The most common of these, i.e., *Staphylococcus aureus*, *Pseudomonas aeruginosa*, *Escherichia coli*, and *Acinetobacter baumanii*, can occur as resistant strains (e.g., methicillin-resistant *S. aureus*, MRSA), which hinder and prolong the treatment process and require a careful selection of antibiotics [1,4–7].

Ciprofloxacin, which belongs to the fluoroquinolone family, is one of the antibacterial drugs with favorable bactericidal and penetration effects on most bone infection pathogens [8–10]. Nevertheless, consistent increases in hospital-acquired infections caused by resistant strains of bacteria often reduce its effectiveness. According to the literature, the use of other antibacterial agents, such as silver and gallium ions, can help solve this problem [11,12].

Silver is well known as an antibacterial agent, used in the treatment of open wounds, burns, chronic ulcers, and on surfaces in hospitals to decrease nosocomial infections [13,14]. Silver exhibits a broad antimicrobial spectrum, including against various resistant strains, which is connected with the poor ability of microorganisms to develop immunity against silver [13,15]. The mechanism of action is mainly based on the interaction of silver with thiolic groups of proteins, where hydrogen atoms are exchanged for silver atoms. As a result, Ag-S bonding is formed, which causes the inactivation of bacteria proteins and, finally, cell death [15]. It is also worth noting that silver can enhance the antibacterial activity of antibiotics [14]. Unfortunately, higher concentrations of silver ions exhibit toxicity towards human cells, necessitating restricted therapeutic concentrations of silver.

The antibacterial mechanism of gallium action is known as "the Trojan horse strategy", which is strictly connected to its similarities with iron (such as the atomic radius, electronic configuration, and coordination chemistry). This results in gallium being actively transported into bacteria, where it replaces iron in various metabolic pathways, blocking them and impairing the functioning of bacterial cells [15–17]. Although its antibacterial activity is weaker, gallium is not as toxic as silver, and because of its different mechanisms of action, it can complement silver as an antibacterial agent.

In the treatment of bone infections, special attention must be paid to the route of administration of antibacterial agents. Antibiotics are typically administered intravenously or orally. Unfortunately, due to the low vascularity of bone tissue, it may lead to an increased risk of systemic adverse effects, their intensification, and the destruction of human natural microbiota because of the need for higher doses of drugs in order to obtain a therapeutic concentration in an infected area [18]. Therefore, the best solution to the aforementioned problem can be the direct delivery of antibiotics to bone tissue, as well as other antibacterial agents, in an attempt to widen the antibacterial spectrum of the implemented material [19].

Among biomaterials used in orthopedic surgery, calcium phosphates (CaPs) seem to be the best choice as a delivery system for antibacterial substances. CaPs (hydroxyapatite, $Ca_{10}(PO_4)_6(OH)_2$; α- or β-tricalcium phosphate: α- or β-$Ca_3(PO_4)_2$; and brushite $CaHPO_4 \cdot 2H_2O$) have become increasingly important as inorganic biomaterials, especially in orthopedics and dentistry, where they are used in fracture or bone defect treatments, total bone augmentation, spinal surgery, craniomaxillofacial reconstruction, and as dental implants and coatings for bone implants [20,21]. The interest in these materials results from their specific properties, especially their similarity to the mineral fraction of human bones and teeth [20,22]. CaPs exhibit bioactive behavior towards bone tissue, such as osteoconductivity and osteointegration, allowing the adhesion, proliferation, migration, and differentiation of bone cells, making these materials an excellent active scaffold for remodeling implanted bone [20,23,24]. Another crucial feature of CaPs, strictly connected to their potential use in delivery systems, is the ease with which they can adsorb drug substances, enabling them to be used as carriers for antibiotics or other antibacterial agents. Hydroxyapatite (HA) exhibits the highest similarity with the mineral fraction of bone tissue. However, tricalcium phosphate (TCP) and brushite (DCPD) are more soluble and biodegradable than HA [20,25]. By combining different CaPs and changing their ratios, biphasic or even multiphasic materials can be obtained, with adjustable properties, e.g., biomaterials with modified solubility, which facilitates a gradual release of antibacterial agents and drugs to the local environment [22,26,27].

To the best of our knowledge, there are few studies that focus on the development of materials that simultaneously deliver an antibiotic and ions with antibacterial properties [28,29]. Nevertheless, according to reports of a significant increase in the therapeutic effectiveness of antibiotics, while reducing the dose, such a solution seems to have great potential. The work in Ref. [30] also indicates a synergistic effect of these antibacterial agents and a less frequent occurrence of the problem of resistance.

The study presented in this work focused on the synthesis of different CaPs (HA, α-TCP, β-TCP, and brushite) doped with gallium or silver ions and then on the fabrication of porous composite granules containing these CaPs and loaded with ciprofloxacin. Physicochemical characterization of the obtained materials was performed using infrared spectroscopy, powder X-ray diffractometry, transmission and scanning electron microscopy, and atomic absorption spectrometry. The release kinetics of ciprofloxacin and gallium and silver ions were then explored. Preliminary biological studies were carried out, along with in vitro antibacterial activity against *Staphylococcus aureus* and *Escherichia coli*.

2. Materials and Methods

2.1. Synthesis of Silver- and Gallium-Containing Calcium Phosphate Powders

In this work, seven samples of different calcium phosphates enriched in silver or gallium ions were synthesized using the well-established wet method, which was described in detail in our previous work [31]. The powder materials obtained are listed in Table 1.

Table 1. List of all synthesized calcium phosphate powders with the estimated number of doped ions.

Material	Comment	Nominal wt% of Doped Ion
Ag-HA	Silver-containing hydroxyapatite	0.22
Ag-aTCP	Silver-containing tricalcium phosphate α type	0.23
Ag-bTCP	Silver-containing tricalcium phosphate β type	0.23
Ag-DCPD	Silver-containing brushite	1.26
Ga-HA	Gallium-containing hydroxyapatite	3.35
Ga-aTCP	Gallium-containing tricalcium phosphate α type	3.61
Ga-bTCP	Gallium-containing tricalcium phosphate β type	3.61

The reagents used in the aforementioned procedure are presented below. Calcium nitrate tetrahydrate $Ca(NO_3)_2 \cdot 4H_2O$ (Sigma-Aldrich, Mumbai, India), ammonium dibasic phosphate $(NH_4)_2HPO_4$ (Chempur, Piekary Slaskie, Poland), gallium nitrate trihydrate $Ga(NO_3)_3 \cdot 3H_2O$ (Sigma-Aldrich, Burlington, MA, USA), and silver nitrate $AgNO_3$ (Avantor Performance Materials, Gliwice, Poland) were used as sources of calcium, phosphor, gallium, and silver, respectively. An adequate amount of $Ca(NO_3)_2 \cdot 4H_2O$ and $(NH_4)_2HPO_4$ was weighed out to obtain a specific molar ratio of (Ca + Ag)/P or (Ca + Ga)/P: 1.67 for hydroxyapatite, 1.5 for tricalcium phosphate, and 1.0 for brushite. An aqueous solution of ammonium dibasic phosphate was added dropwise into an aqueous solution of calcium nitrate tetrahydrate and one of the previously mentioned sources of gallium or silver, with gentle stirring. The mixture was then adjusted to a proper pH (10.0 for hydroxyapatite or tricalcium phosphate and 5.0 for brushite) and left under gentle stirring at a temperature of 60 °C for 2 h. Next, the precipitate was left aging for 24 h. Finally, the precipitates were washed, soaked several times with distilled water, and dried at 120 °C (HA and TCP) or 60 °C (DCPD) in air. In order to obtain TCPs from the synthesized powders, they were sintered at 700 °C for 8 h and then at 1050 °C for 8 h (β-TCP) or at 700 °C for 8 h and then at 1250 °C for 8 h (α-TCP).

2.2. Preparation of Biphasic Granules

The following reagents were used in order to fabricate biphasic granules: sodium alginate (Sigma Aldrich, Burlington, MA, USA), calcium chloride anhydrous $CaCl_2$ (Sigma-Aldrich, Shanghai, China), chondroitin sulfate sodium salt (TCI, Zwijndrecht, Belgium), and the previously synthesized powders: Ag-HA, Ag-aTCP, Ag-bTCP, Ag-DCPD, Ga-HA, Ga-aTCP, and Ga-bTCP.

Firstly, a 4% aqueous solution of sodium alginate was prepared at 40 °C, and an adequate amount of chondroitin sulfate sodium salt was added to obtain a 0.5% suspension. After this, seven types of granules were prepared by combining two different CaP powders: one doped with silver, and a second one doped with gallium ions; a total of 1.0 g of each

powder was added to 10 mL of the suspension and mixed thoroughly until dense, and a milky slurry was acquired. Approximately 0.2 g of ciprofloxacin hydrochloride (TCI, Tokyo, Japan) was then added to the slurry. At the same time, a cross-linking aqueous solution containing $CaCl_2$ (1.5%) was prepared. The slurry was added dropwise to the cross-linking solution with magnetic stirring, and granules were formed. These were left in the $CaCl_2$ solution for 20 min, then rinsed with distilled water several times, dried in air at room temperature, and lyophilized (see Figure 1). The obtained granules were covered with polycaprolactone (PCL) (Sigma-Aldrich, Gillingham, UK) by soaking them in a 7 % PCL chloroform solution. All the obtained granules are listed in Table 2.

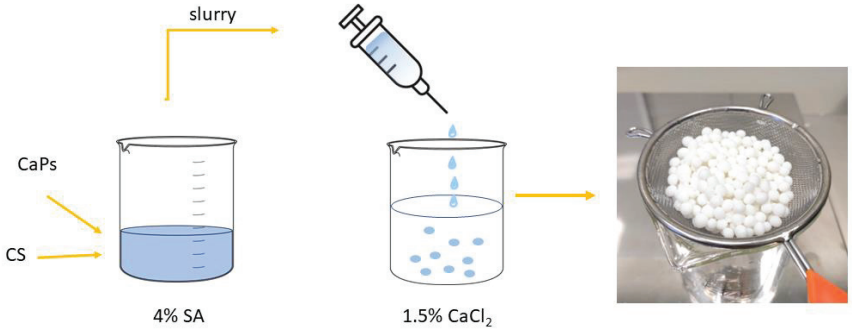

Figure 1. Scheme of composite granules preparation (CS—chondroitin sulfate, SA—sodium alginate, CaPs—different calcium phosphates).

Table 2. List of granules prepared of previously obtained CaP powders.

Standard Granules	Granules Layered with PCL	Silver Component	Gallium Component
G1	G1p	Ag-DCPD	Ga-HA
G2	G2p	Ag-DCPD	Ga-aTCP
G3	G3p	Ag-aTCP	Ga-bTCP
G4	G4p	Ag-HA	Ga-aTCP
G5	G5p	Ag-HA	Ga-bTCP
G6	G6p	Ag-bTCP	Ga-HA
G7	G7p	Ag-aTCP	Ga-HA

2.3. Physicochemical Analysis of CaP Powders

The chemical structure of all the obtained CaP powders was evaluated using Fourier transform infrared spectroscopy (FT-IR). The study was conducted using a Spectrum 1000 spectrometer (Perkin Elmer, Llantrisant, UK) using a standard KBr pellet technique. The measurements were performed with 30 scans and a 2 cm^{-1} resolution, over a range of 2000–400 cm^{-1}. Powder X-ray diffractometry (PXRD) was carried out to analyze the crystalline homogeneity. The study was performed using a PXRD diffractometer (Bruker D8 Advance, Bruker, Billerica, MA, USA) equipped with an LYNEXEYE position-sensitive detector and with Cu-Kα radiation (λ = 0.15418 nm). The data were collected using Bragg–Brentano (θ/θ) horizontal geometry in flat reflection mode (between 20° and 45°) (2θ) in a continuous scan, and 0.08° steps and 2 s/step were used, with a total time equal to 384 s/step. Phases for obtained diffractograms were determined by comparing them with adequate standard patterns (JCPDS 09-0077 for DCPD, JCPDS 09-0432 for HA, JCPDS 09-0169 for β-TCP, and JCPDS 09–0348 for α-TCP).

FT-IR spectra and PXRD diffractograms were then processed in GRAM/AI 8.0 software (Thermo Scientific, Burlington, ON, USA) and KaleidaGraph 3.5 Software (Synergy Software, Reading, PA, USA).

Atomic absorption spectrometry (AAS) was conducted to evaluate the content of Ag^{+} and Ga^{3+} in the synthesized CaP powders. The study was carried out on an AAS spectrometer (ANALYST 400, Perkin Elmer, Llantrisant, UK), with detection at a wavelength of λ = 287.42 nm and λ = 328.07 nm, for gallium and silver, respectively. The samples were prepared by dissolving the powder in super-pure 63% nitric acid and diluting the obtained solution with distilled water. The calibration curves were prepared by dissolving an adequate amount of calibration standard in distilled water—$AgNO_3$ (Avantor Performance Materials, Gliwice, Poland) and $Ga(NO_3)_3 \cdot 3H_2O$ (Sigma-Aldrich, Burlington, MA, USA), for silver and gallium, respectively—and then preparing the dilution series in distilled water.

2.4. Physicochemical Analysis of Granules

Scanning electron microscopy (SEM) using a JSM 6390 LV SEM microscope (JEOL, Tokyo, Japan) (at 20 or 30 kV accelerating voltage) was conducted to examine the morphology of the obtained granules. Before the experiments, the granules were covered with a gold layer in a vacuum chamber, and images were taken of the outer and inner surfaces (after the cross-section).

The release study was performed for all granules containing ciprofloxacin. Therefore, 0.5 g of granules was put into a conical tube, to which 50 mL of phosphate-buffered saline (PBS) (pH = 7.4) was added. The tubes were then placed in a water bath at 37 °C under continuous stirring. The release studies of ions (gallium and silver) and ciprofloxacin were carried out for four weeks. Sample aliquots were collected after 1 h, 2 h, 3 h, 6 h, 12 h, 24 h, 48 h, 5 days, 7 days, 14 days, and 28 days. After the collection of the samples, the tubes were replenished with PBS as per the initial volume.

In order to determine the amount of silver and gallium ions released from the granules, inductively coupled plasma mass spectrometry (ICP-MS, Agilent Technologies 7800, Santa Clara, CA, USA) was used. Samples and a dilution series for calibration curves were prepared in the same manner as previously, with a change of solvent from distilled water to PBS.

The amount of ciprofloxacin released was evaluated using a reverse-phase HPLC method. An HPLC instrument was used, consisting of a column (Varian RP-18, 250 × 4.6 mm), thermostat (Shimadzu CTO-10ASVP, Shimadzu, Tokyo, Japan), pump (Varian Prostar 210), injection loop (20 mL Rheodyne), and UV-Vis detector (Varian Prostar 325). The mobile phase was composed of acetonitrile and phosphate buffer (pH = 3.0; 20:80), with detection at a wavelength of λ = 278 nm.

2.5. In Vitro Cytotoxicity Study

The neutral red uptake assay was conducted in accordance with ISO 10993, Annex A [32,33], with BALB/c 3T3 mouse embryonic fibroblasts (American Type Culture Collection). Quantitative estimation of the cell viability was based on their neutral red uptake compared to the untreated culture. Cells were seeded in 96-well microplates (15,000 cells/100 µL) in Dulbecco's Modified Eagle Medium (Lonza), supplemented with 10% of calf bovine serum, 100 IU/mL penicillin, and 0.1 mg/mL streptomycin, and incubated for 24 h (5% CO_2, 37 °C, >90% humidity). After that, each well was examined to ensure that the cells formed a confluent monolayer. The culture medium was replaced by the extracts. Extracts were obtained by the preincubation of the materials in a culture medium (100 mg/mL) with a 5% serum concentration, at 37 °C for 24 h and sterilized by filtration. Cells were treated with a twofold dilution series of the extracts for 24 h at 540 nm. As the reference materials, polyethylene film and latex were used (non-cytotoxic and highly cytotoxic, respectively). The cell viability was calculated by comparing OD540 then the treatment medium was removed. The cultures were washed with PBS and treated with medium containing the dye for 2 h. The medium was discarded, and the cells were washed with PBS and treated with an ethanol and acetic acid water solution (desorbing fixative). The color of each well was evaluated colorimetrically, results were compared with

the untreated control. Samples were classified as cytotoxic if they reduced cell survival to below 70%. If the BALB/c 3T3 fibroblasts retained a viability of at least 70% across the full range of tested dilutions, they were considered to be non-cytotoxic.

2.6. Microbiological Activity Studies

The antibacterial activity of the synthesized granules was assessed against Gram-negative *E. coli* bacteria (ATCC 25922) and Gram-positive *S. aureus* bacteria (ATCC 6438), according to a methodology previously reported in [34], with 0.5 McFarland standard microbial cultures. Bacterial strains cultured on MacConkey and Columbia agar (Biocorp, Warsaw, Poland) were transported to Tryptic soy broth medium (Merck, Burlington, MA, USA) and incubated for 24 h at 37 °C, after which the density of the bacterial suspension was measured using a densitometer (Biomerieux, Marcy-l'Étoile, France) and then diluted to a density with an order of magnitude equal to 10^6 CFU/mL. Next, 50 mg of each type of granule produced was placed in 5 mL of Tryptic soy broth medium, and the bacterial suspensions prepared earlier were added. The mixture was incubated for 24 h at 37 °C, after which the bacterial colonies were counted using a Scan300 counter (Interscience, Saint Nom la Bretêche, France). As a positive control (C+), free microbial culture was assessed at the same time intervals. The measurements were repeated three times. The data are presented as mean ± SD.

3. Results

3.1. Characterization of Synthesized Powders

In the first step, the selected calcium phosphates containing silver or gallium ions were synthesized (see Table 1). For comparison, their unsubstituted counterparts—hydroxyapatite (HA), α- and β- tricalcium phosphates (aTCP and bTCP, respectively), and dicalcium phosphate dihydrate (DCPD)—were prepared using the same methods.

It should be noted that while there are many papers on substituted hydroxyapatite in the available literature, substitutions with silver and gallium ions in other calcium phosphates (brushite, α -TCP, and β -TCP) are described in only a few papers [28,31,34–37].

Figure 2A,B show the FT-IR spectra in the most informative range: 2000–400 cm^{-1}. The spectra of the Ag-HA and Ga-HA samples were similar and had a dominant band at approximately 1110–955 cm^{-1} and bands at approximately 603 and 565 cm^{-1}, corresponding to the vibrations of $\nu_1 + \nu_3$ and ν_4 of the apatite phosphates, respectively. Both spectra exhibited a band at approximately 630 cm^{-1}, originating from the liberational vibrations of the structural OH groups of HA [35,38].

The spectra of the Ag-aTCP and Ga-aTCP samples were characterized by very wide and poorly separated bands, similar to the spectra of unsubstituted α-TCP (as evidenced in the literature and Figure S1 in Supplementary Materials) [39–41]. It should be noted that the spectra were very complex and barely identifiable, which is consistent with theoretical data showing that the α-TCP spectrum can contain up to 216 phosphate bands (24 distinct bands in the case of ν_1; 48 distinct bands for ν_2; and 72 bands each for ν_3 and ν_4) [40]. In addition, it should be noted that the Ag-aTCP spectrum showed a narrow band at approximately 725 cm^{-1}, which is characteristic of pyrophosphates formed during the thermal treatment of calcium phosphates [41–43]. This band was also present in the spectra of samples synthesized at high temperatures: Ag-bTCP and Ga-bTCP.

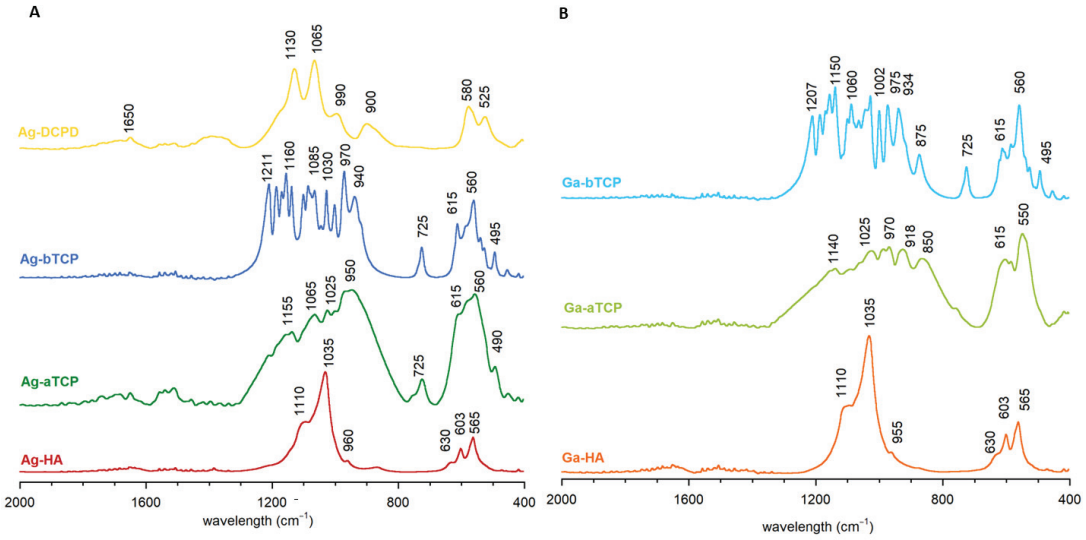

Figure 2. FT-IR spectra of the obtained calcium phosphates: (**A**) enriched with silver ion, (**B**) enriched with gallium ion.

As for the spectra of Ag-bTCP and Ga-bTCP samples (Figure 2), in the ν_1 and ν_3 vibration region, they contained narrow, well-separated bands, which is characteristic of β-TCP [39,44]. In turn, the ν_4 region contained two major bands (at approximately 615 and 550 cm^{-1}), confirming the β-TCP structure of these materials (see Figure S1).

The representative spectrum of brushite enriched with silver ions (Ag-DCPD) is presented in Figure 2A. The dominant features here are ν_3 phosphate bands at approximately 1130 and 1065 cm^{-1}, as well as ν_1 bands at approximately 990 cm^{-1}. The wide band at 900 cm^{-1} proves the presence of P-OH groups, characteristic of the structure of brushite (Figure S1 in Supplementary Materials). In the ν_4 region, two typical DCPD bands can be seen at 580 and 525 cm^{-1} [45,46].

The PXRD diffractograms of the obtained powders are shown in Figure 3A,B. For comparison, the patterns of the unsubstituted powders are summarized in Figure S2 in Supplementary Materials. All reflections on the Ag-HA and Ga-HA diffractograms were indexed to hydroxyapatite (JCPDS 09-432). The reflections were wide, especially for the Ga-HA sample, which is typical of nanocrystalline samples.

In turn, the PXRD pattern of the Ga-aTCP sample exhibited narrow, sharp reflections only from the α-TCP crystalline structure (JCPDS 09-348). The diffractogram of the Ag-aTCP sample contained additional reflections at approximately 27.0 and 27.9°, attributable to calcium pyrophosphate, in accordance with the presented FT-IR tests.

The Ag-bTCP and Ga-bTCP samples were not homogeneous and, like Ag-aTCP, contained calcium pyrophosphate. The diffractogram for the Ag-DCPD sample showed the presence of only one crystalline phase; all reflections originated from the brushite structure (JCPDS 09-077).

For all the obtained powders, the content of silver and gallium was examined by AAS spectrometry. It turned out that the ions were introduced with a fairly good yield from 66 to 97%. The concentration of silver decreased in the following order: Ag-DCPD (1.06 ± 0.03 wt.%); Ag-bTCP (0.20 ± 0.02 wt.%); Ag-aTCP (0.18 ± 0.03 wt.%); and Ag-HA (0.15 ± 0.02 wt.%).

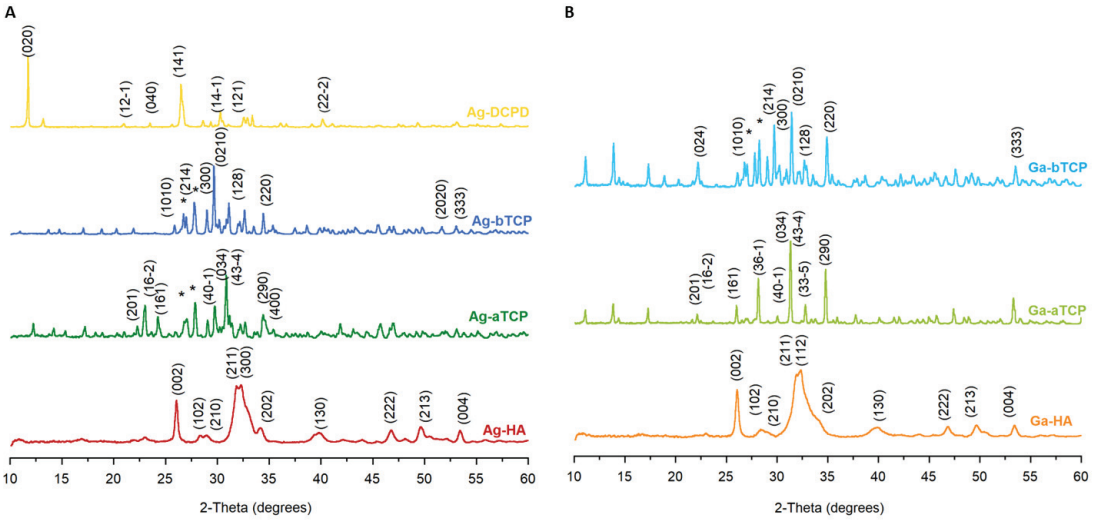

Figure 3. PXRD diffractograms of the obtained calcium phosphates: (**A**) enriched with silver ion, (**B**) enriched with gallium ion (*-calcium pyrophosphate).

Ga-aTCP and Ga-bTCP were synthesized at high temperatures. The amount of gallium was approximately 3.50 ± 0.02 and 3.52 ± 0.03 wt.%, and the substitution efficiency was the highest (97%). In turn, the gallium concentration in the Ga-HA sample amounted to 2.21 ± 0.02 wt.%, which was 66% of the nominal value.

The above physicochemical tests of the obtained CaPs powders allowed us to confirm their identity and the degree of substitution with foreign ions, i.e., silver and gallium.

3.2. Morphology of the Synthetic Granules

The next step was to obtain composite granules containing alginate, chondroitin sulfate, and two different calcium phosphates enriched with silver and gallium ions. In this way, seven types of granules were obtained (see Table 2).

According to literature reports, bone substitute materials are often prepared in the form of granules or microgranules [47,48]. This form is beneficial in the case of filling small bone defects. Moreover, by filling the 3D space, the materials form intra-granular pores between the granules, thus contributing to better vascularization and facilitated adhesion of bone cells.

Representative SEM photos of each granule type are shown in Figure 4.

Figure 4A shows a granule in its entirety. It can be seen that it has a regular, spherical shape, quite a rough surface, and an average diameter of 3–4 mm. The images that follow (Figure 4B–H) depict cross-sections of the granules. G1 and G2 granules are characterized by the most compact structure, with the least developed surface. In both of these, single clusters of crystals are visible, with elongated shapes, typical of brushite (DCPD). The cross-sections with the highest porosity and the least homogeneous structure belong to the G3, G4, and G7 samples. The G5 sample appears to be the most homogeneous, with regular microporosity.

All types of granules were also prepared by covering them with an additional layer of PCL. This treatment did not significantly affect the morphology of the surface or the interior of the granules (data not shown).

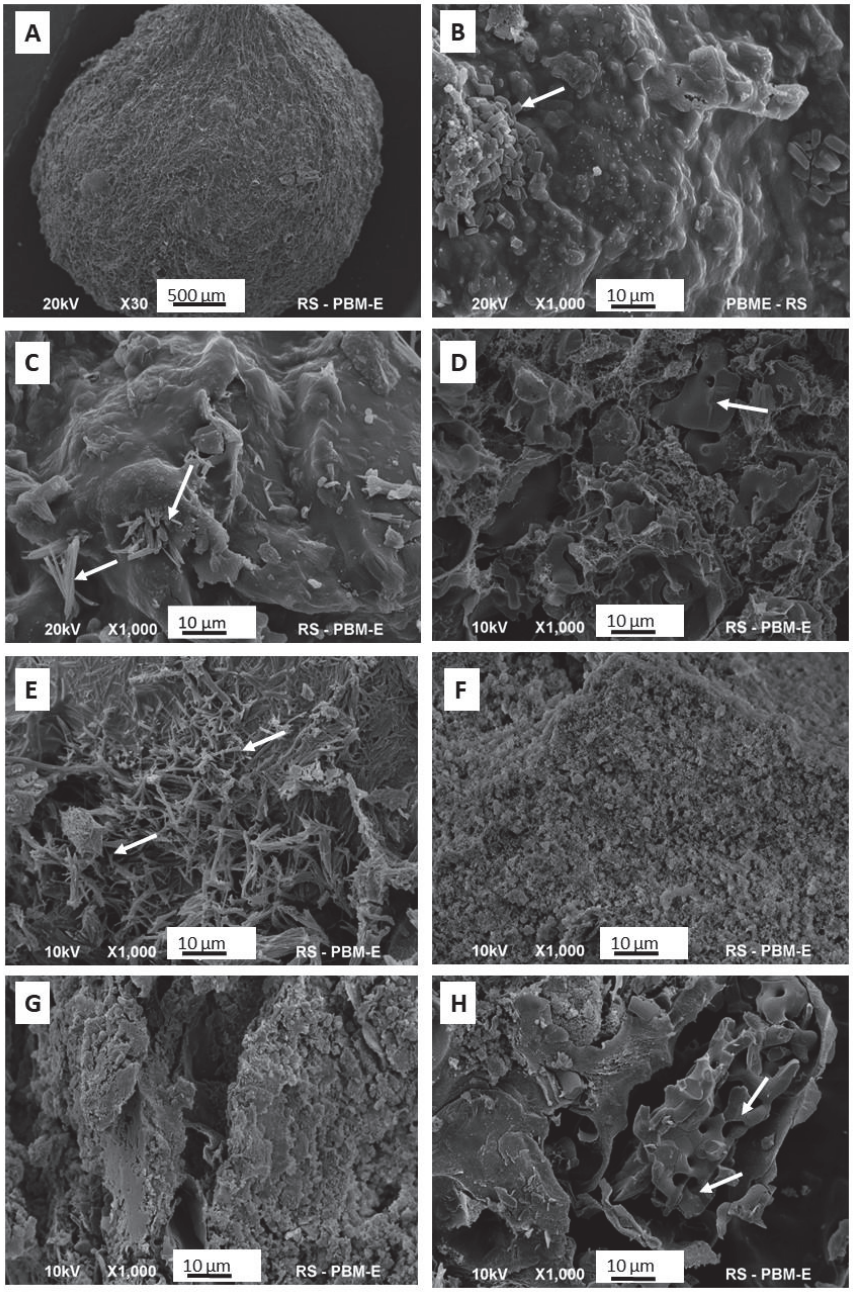

Figure 4. SEM representative images of the granules: (**A**) the outer surface of the granule; (**B**–**H**) internal cross-sections of granules G1–G7. The arrows indicate the crystals of calcium phosphates.

3.3. Ion Release Studies

The obtained composite granules were tested for the release of silver and gallium ions. Figure 5 shows the silver release curves for standard and polycaprolactone-coated granules (A and B, respectively). Figure 5A clearly shows that the greatest amount of released silver could be observed for samples containing Ag-DCPD powder (curves G1 and G2). In granules containing tricalcium phosphates (i.e., Ag-aTCP and Ag-bTCP), no silver release was observed throughout the entire study period (samples G3 and G6; results not shown), or the release of silver was significantly delayed. In the case of sample G7, the first concentration of released silver was recorded on the fifth day.

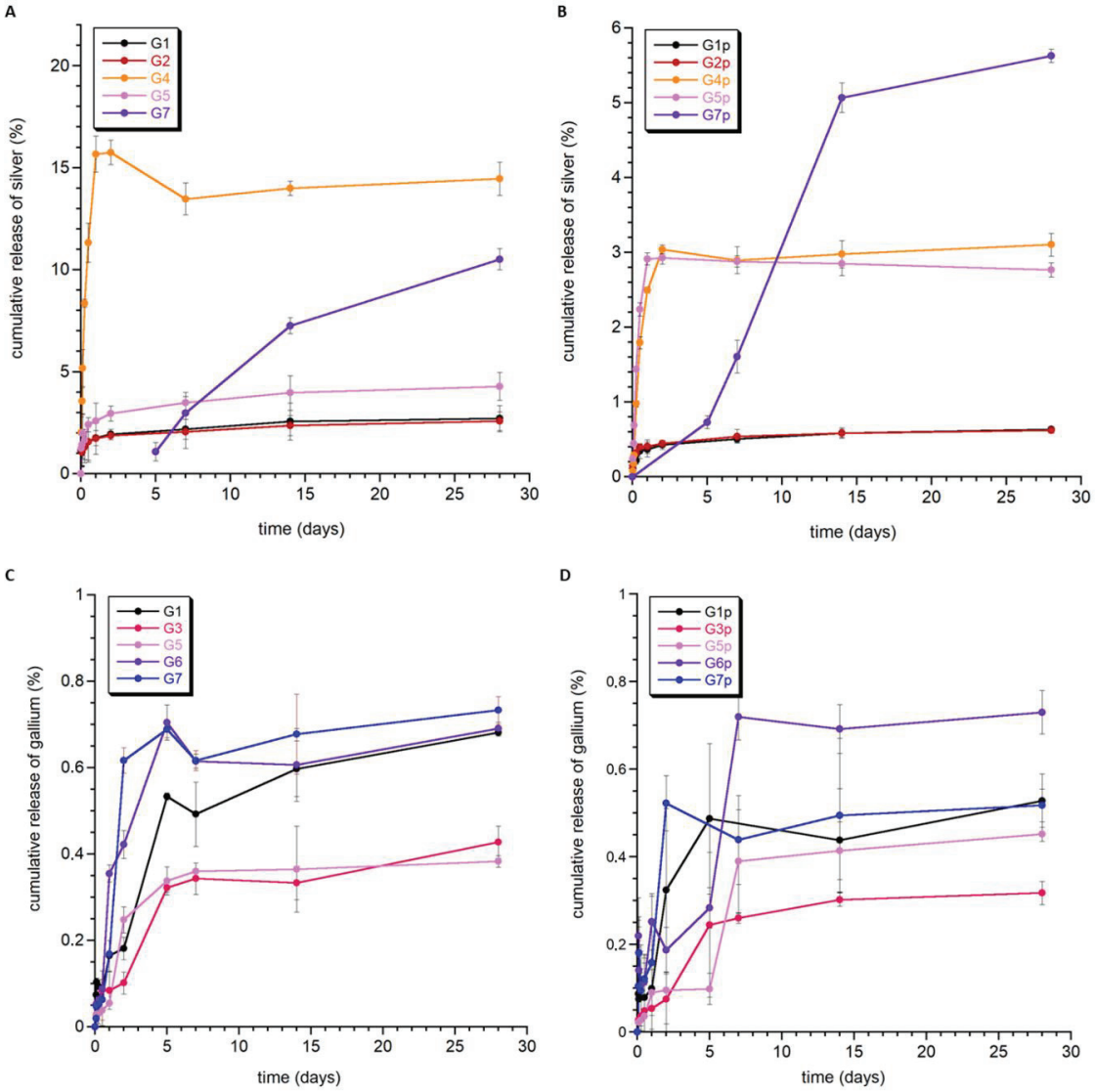

Figure 5. Release profiles of silver (**A**,**B**) and gallium ions (**C**,**D**) from the granules.

It is also worth noting that the amount of silver released from the G1 and G2 granules was similar, so it can be assumed that the composition of these granules and their morphology did not have a significant impact on the release of silver ions, and the main factor determining the kinetics of release was the type of CaP, to which silver ions were introduced.

The granules containing silver ions in hydroxyapatite (G4 and G5) were characterized by different kinetics of Ag^+ release to those of the G1 and G2 granules. Silver ions were released during the first 50 h, and then, a plateau could be observed in the curve. Considering the fact that hydroxyapatite is characterized by lower solubility than brushite, it can be assumed that the released silver ions mainly came from the surface of apatite crystals. This is also supported by the low degree of Ag^+ release (the remaining amount was not released during the experiment). It is also worth noting that sample G5 had the smallest amount of released silver, most likely due to the different morphology of the granule interior.

Covering the composite samples with an additional layer of PCL polymer (Figure 5B) did not cause any significant differences in the silver ion release profile. On the other hand, in all but one of the samples (i.e., not G5), the total amount of released ions decreased significantly (even almost five-fold). As with granules without PCL, no release or a delayed release was observed in samples containing Ag-TCP (sample G7—first measurements on the fifth day of the experiment).

Figure 5C,D show the gallium ion release profiles for granules with and without the cover of PCL. Of particular note is the fact that, despite the higher content of gallium than silver in the samples, a significantly lower degree of release was recorded. There was also a smaller difference between the release of gallium from the PCL and non-PCL samples. Samples G2 and G4 showed a trace release of gallium ions (data not shown). In both samples, the gallium ions were substituted into α-TCP crystals. The G1, G3, G5, G6, and G7 granules released a similar amount of gallium ions at a similar rate (see Figure 5C).

Summarizing the obtained results, it can be stated that the release of both silver and gallium ions is very slow. During the time under study (28 days), the percentage of released silver did not exceed 20%, and gallium was even lower and did not reach 1%. We can therefore assume that the obtained materials are stable during this time, and the release will proceed with the degradation of the obtained granules. It should be noted that we presented similar research on the release of silver and gallium ions from hydroxyapatite-containing granules in Ref. [49], and we also demonstrated a slow release of these ions there. The results of ion release from granules containing non-apatite silver and gallium sources are shown here for the first time.

3.4. Ciprofloxacin Release

Figure 6 shows the release profile of ciprofloxacin from granules G1–G7 (without PCL coating) and G1p–G7p (with PCL coating). Generally, the percentage of ciprofloxacin released in vitro at pH = 7.4 ranged between 38% and 55%. For each type of granule, the release profile of ciprofloxacin was characterized by a slight burst release in the first few hours (see Figure 6B,D). It can be assumed that the type of material does not have a significant impact on the drug release profile, although coverage of PCL granules seemed to weaken the release of the drug during the first few hours in some samples (G1p, G4p, G5p, and G7p). At the same time, it could also be seen that the total amount of released ciprofloxacin was slightly lower for the PCL-coated samples than for the standard granules.

In Figure 6, instead of a plateau, a slight tendency towards a downward curve can be observed (see Figure 5A,B, G5 and G7 curves). This may be related to the high affinity of calcium phosphates to the adsorption of drug molecules. It is worth noting that the ease of adsorption of molecules and ions depends on many factors, including the chemical properties of the adsorbed molecules and their size, but also the surface properties of calcium phosphate (including their surface area, porosity, and particle morphology). Each type of granule contained two different calcium phosphates; however, in each case, one of them was hydroxyapatite enriched with silver or gallium ions. Our research and

the available literature show that substitution with gallium and silver ions affects the morphology and size of crystals [31,50]. Significant reduction in the size of crystals and their strong tendency to form agglomerates occurs for apatite samples containing gallium ions. The powders consist of very fine plate-like crystals in the order of a few nanometers in size. This makes them characterized by a very large specific surface area and, thus, high susceptibility to adsorption. Therefore, it can be assumed that the downward slope of the curves is related to the re-adsorption of the drug on the surface of calcium phosphate, in particular, nanocrystalline hydroxyapatite.

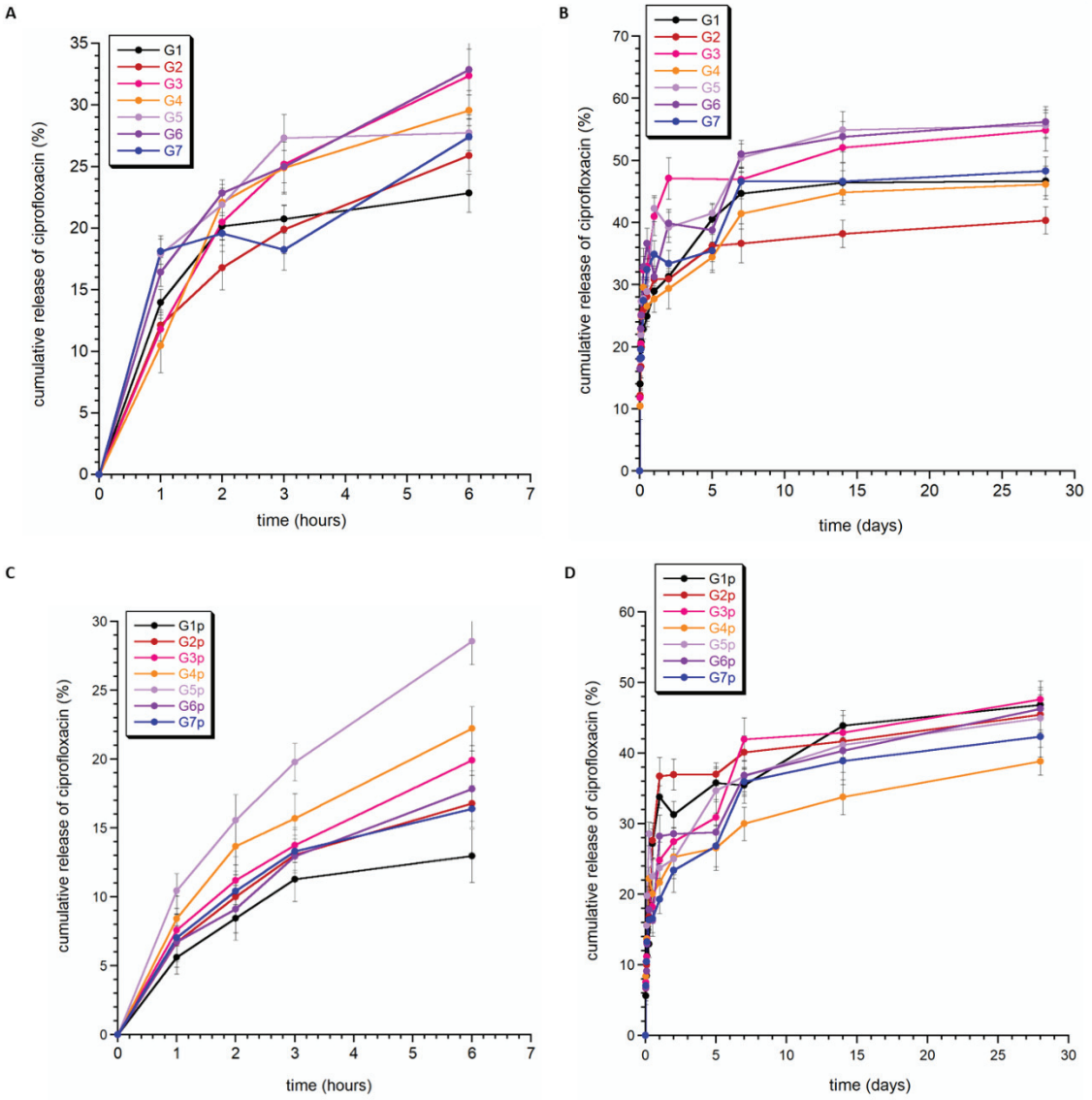

Figure 6. Release profiles of ciprofloxacin from the granules without PCL (**A**,**B**) and the granules with PCL (**C**,**D**).

The semi-empirical Korsmeyer–Peppas model was used to evaluate the mechanism of ciprofloxacin release from the obtained composites. This model was chosen because it is dedicated to the description of drug release from polymer systems and typical hydrogels. Moreover, the use of this model is possible when the amount of released drug substance does not exceed 80% [51,52].

The model is described by the following formula:

$$X\% = kt^n, \text{ where}$$

X% is the fraction (in %) of the dissolved drug at a given time t;

K is the constant describing the features of the structure and geometry of the matrix;

N is a parameter indicating the release mechanism [53].

Figure 6B,D show that the percentage of ciprofloxacin released did not exceed 60%. The fitting parameters are presented in Table 3. The correlation coefficient (R^2) in all fittings was quite high and ranged between 0.9239–0.9979. The n parameter describing the drug release mechanism, for all analyzed fittings, was in the range of 0–0.45. In the Korsmeyer–Peppas model, for $n \leq 0.43$, drug release kinetics occur according to Fickian diffusion from polydispersive systems (see Figure S4A,B in Supplementary Materials) [50]. Thus, we can conclude that the obtained materials release the drug similarly to typical hydrogels: quite quickly and with non-zero kinetics.

Table 3. Fitting parameters for ciprofloxacin release from granules (k—constant; n—parameter of release mechanism; R^2—correlation coefficient).

Sample	k/min^{-n}	n	R^2
G1	17.0 ± 1.1	0.17 ± 0.01	0.9791
G2	11.5 ± 2.1	0.23 ± 0.03	0.9351
G3	17.9 ± 1.4	0.13 ± 0.02	0.9979
G4	21.8 ± 2.4	0.15 ± 0.02	0.9238
G5	11.1 ± 1.2	0.16 ± 0.01	0.9331
G6	11.0 ± 1.1	0.23 ± 0.02	0.9791
G7	17.7 ± 1.8	0.15 ± 0.02	0.9324
G1p	12.7 ± 0.9	0.17 ± 0.02	0.9683
G2p	21.0 ± 1.5	0.16 ± 0.02	0.9655
G3p	14.9 ± 1.5	0.15 ± 0.02	0.9494
G4p	21.4 ± 1.7	0.15 ± 0.02	0.9555
G5p	10.6 ± 1.2	0.23 ± 0.02	0.9711
G6p	18.9 ± 1.8	0.15 ± 0.02	0.9384
G7p	9.4 ± 0.2	0.24 ± 0.02	0.9855

3.5. Cytotoxicity Studies

The viability of the BALB/c 3T3 cells did not fall below 70%, in comparison to the untreated control, in most samples. Therefore, all these materials were classified as non-cytotoxic in the neutral red uptake assay (see Table 4). Only G1, G2, and Ag-DCPD powder (all samples containing brushite doped with silver ions) decreased the viability of 3T3 cells to less than 70% after exposure to the undiluted extracts (100 mg/mL), and these were classified as cytotoxic. However, in the first dilutions of the twofold dilution series, none of the samples negatively affected the cell culture condition, i.e., the cell viability did not differ from the untreated control (see Figure 6).

Table 4. Results of the neutral red uptake test for the highest concentrations of tested extracts (100 mg/mL) in comparison to the untreated control.

Sample	Cell Viability ± SD [%]	IC50 [mg/mL]	Classification
Pure HA	101 ± 2	N	Non-cytotoxic
Ag-HA	102 ± 4	N	Non-cytotoxic
Ga-HA	94 ± 4	N	Non-cytotoxic
Pure β-TCP	105 ± 2	N	Non-cytotoxic
Ag-bTCP	98 ± 3	N	Non-cytotoxic
Ga-bTCP	114 ± 1	N	Non-cytotoxic
Pure α-TCP	101 ± 3	N	Non-cytotoxic
Ag-aTCP	106 ± 3	N	Non-cytotoxic
Ga-bTCP	99 ± 1	N	Non-cytotoxic
Pure DCPD	111 ± 6	N	Non-cytotoxic
Ag-DCPD	21 ± 10	83	Cytotoxic
G1	10 ± 7	76	Cytotoxic
G2	44 ± 4	94	Cytotoxic
G3	99 ± 3	N	Non-cytotoxic
G4	87 ± 4	N	Non-cytotoxic
G5	100 ± 4	N	Non-cytotoxic
G6	85 ± 4	N	Non-cytotoxic
G7	99 ± 3	N	Non-cytotoxic
LT	0 ± 0	<10	Cytotoxic
PE	102 ± 7	N	Non-cytotoxic

LT—latex, reference cytotoxic material. PE—polyethylene foil, reference non-cytotoxic material. N—calculation was not possible due to the lack of cytotoxicity in the whole range of tested concentrations. Results with cell viability decreased under 70% are underlined.

The obtained results are very promising. In the case of hydroxyapatite and tricalcium phosphate, they show that the amount of silver and gallium introduced did not cause a toxic effect on fibroblasts. Our previous studies on silver-containing hydroxyapatite [31] showed that a higher amount of silver in the HA powder obtained by the same method is cytotoxic, as is the gallium-containing hydroxyapatite obtained by the dry method (unpublished data). In turn, attention should be paid to the toxicity of the Ag-DCPD material and granules containing this material. Further research on the optimal concentration of silver is required in order to obtain a material that is non-toxic to mammalian cells.

3.6. Antibacterial Activity

The results for the test of antibacterial activity against *S. aureus* and *E. coli* for the synthesized granules are presented in Tables 5 and 6. It can be seen that biphasic granules containing ciprofloxacin (both without cover and covered with polycaprolactone) exhibited antibacterial activity against both strains of bacteria, reaching a 6-logarithmic reduction in bacterial growth in most samples. All types of granules reduced the growth of Gram-negative *E. coli* bacteria entirely. On the other hand, in the case of Gram-positive *S. aureus* bacteria, diminished antibacterial activity could be observed for G1 and G2 granules (with and without PCL), which were the only granules composed of brushite. The full impact of the aforementioned granules on the bacterial growth of *S. aureus* is shown in Table 6. It should be mentioned that the antibacterial activity of granules containing brushite decreased over time (with a similar observation recorded for *E. coli*).

Table 5. Bacterial growth of *S. aureus* and *E. coli* in medium containing examined samples after 24 h of incubation.

Type of Granules	Bacterial Growth [CFU/mL]	
	Staphylococcus aureus	*Escherichia coli*
G1	1.25×10^3	0
G2	1×10^2	0
G3	5×10^1	0
G4	5×10^1	0
G5	5×10^1	0
G6	5×10^1	0
G7	0	0
G1p	1.5×10^3	0
G2p	2.75×10^3	0
G3p	0	0
G4p	0	0
G5p	0	0
G6p	0	0
G7p	0	0

The average initial bacterial concentration for *S. aureus* was equal to 5×10^6 CFU/mL. The average initial bacterial concentration for *E. coli* was equal to 4.75×10^6 CFU/mL.

Table 6. Bacterial growth of *S. aureus* in a medium containing selected examined samples after 24 h of incubation in three repetitions with weekly intervals.

Type of Granules	Bacterial Growth—*Staphylococcus aureus* [CFU/mL]		
	1st Week	2nd Week	3rd Week
G1	1.25×10^3	2.61×10^4	1.55×10^5
G1p	1.5×10^3	1.65×10^3	4.96×10^5
G2	1×10^2	1.45×10^3	2.51×10^5
G2p	2.75×10^3	4.68×10^4	1.6×10^5

Average initial bacterial concentrations for *S. aureus* were equal to 5×10^6 CFU/mL (1st week), 4.65×10^6 CFU/mL (2nd week), and 6.58×10^6 CFU/mL (3rd week).

This is an interesting observation, especially in the context of fibroblast toxicity studies (see Section 3.5). It seems that the G1, G2, G1p, and G2p granules, which contain brushite as a source of silver, do not meet the conditions of bone substitute materials releasing antibacterial agents.

Moreover, when comparing the results for granules with and without PCL, it should be noted that, in the case of granules covered with PCL, there was less inhibition of the bacterial growth, which is associated with a slower release of active substances from these types of granules, as has been seen in release studies.

4. Conclusions

In the study presented here, ciprofloxacin was loaded into composite granules containing calcium phosphates substituted with silver and gallium ions. These formulations showed a sustained release of the antibiotic and ions with antibacterial activity. During the first five hours, a slight burst release was found, while in the hours that followed, a slower, diffusion-mediated, sustained release was observed. Moreover, most of the obtained granules were able to effectively inhibit the growth of *S. aureus* and *E. coli* bacterial strains. These granules were non-toxic toward mammalian BALB/c 3T3 cells. Accordingly, composite granules have promising potential as drug carriers and bone-filling materials. The exception is granules containing Ag-DCPD, which turned out to be toxic to mammalian cells, and at the same time, granules made of it had ineffective antibacterial activity.

However, further research is necessary, and should be primarily focused on selecting the optimal granule composition in order to obtain the highest antibacterial activity while ensuring there is no toxicity to mammalian cells. It is also worth conducting research in order to select the appropriate amount of ions with antibacterial activity in relation to the amount of introduced antibiotic. In addition, further analyses should aim to use vivo models.

Supplementary Materials: The following supporting information can be downloaded at: https://www.mdpi.com/article/10.3390/coatings13030494/s1. Figure S1: FT-IR spectra of the unsubstituted calcium phosphates; Figure S2: PXRD diffractograms of the unsubstituted calcium phosphates; Figure S3: The NRU test results obtained for samples Ag-DCPD (A), G1 (B), and G2 (C) in the whole range of tested concentrations. Black stars indicate a decrease in cell viability under 70%, which classified each of these samples as cytotoxic. The rest of the tested materials did not reveal cytotoxicity in the whole range of tested dilutions; Figure S4: Cumulative release of ciprofloxacin (%)—fitting curves. A—the composite without PCL; B the composite coated with PCL.

Author Contributions: Conceptualization, J.K. and K.P.; methodology, J.K., A.Z. and Ł.P.; investigation, K.P., A.Z., Ł.P., P.K. and A.K.; resources, K.P. and P.K.; data curation, Ł.P.; writing—original draft preparation, K.P. and J.K.; writing—review and editing, J.K.; visualization, K.P. and J.K.; supervision, J.K.; funding acquisition, J.K. All authors have read and agreed to the published version of the manuscript.

Funding: Studies were supported by the Ministry of Education and Science in Poland within the statutory activity of the Medical University of Warsaw (FW232/N/2022) and NCN Sonata Bis grant (Project NCN UMO2016/22/E/ST5/00564).

Institutional Review Board Statement: Not applicable.

Informed Consent Statement: Not applicable.

Data Availability Statement: The data that support the findings of this study are available from the corresponding author upon reasonable request.

Conflicts of Interest: The authors declare no conflict of interest.

References

1. Chen, A.F.; Wessel, C.B.; Rao, N. Staphylococcus aureus screening and decolonization in orthopedic surgery and reduction of surgical site infections. *Clin. Orthop. Relat. Res.* **2013**, *471*, 2383–2399. [CrossRef] [PubMed]
2. Cheng, L.; Li, R.; Liu, G.; Zhang, Y.; Tang, X.; Wang, J.; Liu, H.; Qin, Y. Potential antibacterial mechanism of silver nanoparticles and the optimization of orthopedic implants by advanced modification technologies. *Int. J. Nanomed.* **2018**, *13*, 3311.
3. Chae, K.; Jang, W.Y.; Park, K.; Lee, J.; Kim, H.; Lee, K.; Lee, C.K.; Lee, Y.; Lee, S.H.; Seo, J. Antibacterial infection and immune-evasive coating for orthopedic implants. *Sci. Adv.* **2020**, *6*, eabb0025. [CrossRef]
4. Jenks, P.; Laurent, M.; McQuarry, S.; Watkins, R. Clinical and economic burden of surgical site infection (SSI) and predicted financial consequences of elimination of SSI from an English hospital. *J. Hosp. Infect.* **2014**, *86*, 24–33. [CrossRef]
5. Greene, L.R. Guide to the elimination of orthopedic surgery surgical site infections: An executive summary of the Association for Professionals in Infection Control and Epidemiology elimination guide. *Am. J. Infect. Control.* **2012**, *40*, 384–386. [CrossRef] [PubMed]
6. Khalid, H.; Nafees, F.; Khaliq, M.A. Infective Organisms and their Changing Antibiotic Sensitivity Trends in Surgical Site Infection after Orthopedic Implant Surgeries. *Pak. J. Med. Health Sci.* **2018**, *12*, 1256–1258.
7. Li, B.; Webster, T.J. Bacteria antibiotic resistance: New challenges and opportunities for implant-associated orthopedic infections. *J. Orthop. Res.* **2018**, *36*, 22–32. [CrossRef] [PubMed]
8. Blondeau, J.M. Fluoroquinolones: Mechanism of action, classification, and development of resistance. *Surv. Ophthalmol.* **2004**, *49*, S73–S78. [CrossRef] [PubMed]
9. Manchon, A.; Prados-Frutos, J.C.; Rueda-Rodriguez, C.; Salinas-Goodier, C.; Alkhraisat, M.H.; Rojo, R.; Rodriguez-Gonzalez, A.; Berlanga, A.; Lopez-Cabarcos, E. Antibiotic release from calcium phosphate materials in oral and maxillofacial surgery. molecular, cellular, and pharmaceutical aspects. *Curr. Pharm. Biotechnol.* **2017**, *18*, 52–63. [CrossRef]
10. Rehman, A.; Patrick, W.M.; Lamont, I.L. Mechanisms of ciprofloxacin resistance in Pseudomonas aeruginosa: New approaches to an old problem. *J. Med. Microbiol.* **2019**, *68*, 1–10. [CrossRef]
11. Lu, M.; Liao, J.; Dong, J.; Wu, J.; Qiu, H.; Zhou, X.; Li, J.; Jiang, D.; He, T.-C.; Quan, Z. An effective treatment of experimental osteomyelitis using the antibacterial titanium/silver-containing nHP66 (nano-hydroxyapatite/polyamide-66) nanoscaffold biomaterials. *Sci. Rep.* **2016**, *6*, 39174. [CrossRef]

12. Sorinolu, A.J.; Godakhindi, V.; Siano, P.; Vivero-Escoto, J.L.; Munir, M. Influence of silver ion release on the inactivation of antibiotic-resistant bacteria using light-activated silver nanoparticles. *Mater. Adv.* **2022**, *3*, 9090–9102. [CrossRef]
13. McRee, A.E. Therapeutic review: Silver. *J. Exot. Pet Med.* **2015**, *2*, 240–244. [CrossRef]
14. Barras, F.; Aussel, L.; Ezraty, B. Silver and antibiotic, new facts to an old story. *Antibiotics* **2018**, *7*, 79. [CrossRef] [PubMed]
15. Kolmas, J.; Groszyk, E.; Kwiatkowska-Różycka, D. Substituted hydroxyapatites with antibacterial properties. *BioMed. Res. Int.* **2014**, *2014*, 178123. [CrossRef] [PubMed]
16. Best, M.G.; Cunha-Reis, C.; Ganin, A.Y.; Sousa, A.; Johnston, J.; Oliveira, A.L.; Smith, D.G.; Yiu, H.H.; Cooper, I.R. Antimicrobial properties of gallium (III)-and iron (III)-Loaded polysaccharides affecting the growth of Escherichia coli, Staphylococcus aureus, and Pseudomonas aeruginosa, in vitro. *ACS Appl. Biol. Mater.* **2020**, *3*, 7589–7597. [CrossRef]
17. Łapa, A.; Cresswell, M.; Campbell, I.; Jackson, P.; Goldmann, W.H.; Detsch, R.; Boccaccini, A.R. Gallium-and cerium-doped phosphate glasses with antibacterial properties for medical applications. *Adv. Eng. Mater.* **2020**, *22*, 1901577. [CrossRef]
18. Li, H.-K.; Rombach, I.; Zambellas, R.; Walker, A.S.; McNally, M.A.; Atkins, B.L.; Lipsky, B.A.; Hughes, H.C.; Bose, D.; Kümin, M. Oral versus intravenous antibiotics for bone and joint infection. *N. Engl. J. Med.* **2019**, *380*, 425–436. [CrossRef] [PubMed]
19. Romanò, C.L.; Scarponi, S.; Gallazzi, E.; Romanò, D.; Drago, L. Antibacterial coating of implants in orthopedics and trauma: A classification proposal in an evolving panorama. *J. Orthop. Surg. Res.* **2015**, *10*, 1–11. [CrossRef] [PubMed]
20. Dorozhkin, S.V. Bioceramics of calcium orthophosphates. *Biomaterials* **2010**, *31*, 1465–1485. [CrossRef]
21. Dorozhkin, S.V. Nanosized and nanocrystalline calcium orthophosphates. *Acta Biomater.* **2010**, *6*, 715–734. [CrossRef] [PubMed]
22. Bal, Z.; Kaito, T.; Korkusuz, F.; Yoshikawa, H. Bone regeneration with hydroxyapatite-based biomaterials. *Emergent Mater.* **2020**, *3*, 521–544. [CrossRef]
23. Bouler, J.-M.; Pilet, P.; Gauthier, O.; Verron, E. Biphasic calcium phosphate ceramics for bone reconstruction: A review of biological response. *Acta Biomater.* **2017**, *53*, 1–12. [CrossRef] [PubMed]
24. Owen, G.R.; Dard, M.; Larjava, H. Hydroxyapatite/beta-tricalcium phosphate biphasic ceramics as a regenerative material for the repair of complex bone defects. *J. Biomed. Mater. Res. Part B Appl. Biomater.* **2018**, *106*, 2493–2512. [CrossRef]
25. Schmitz, J.P.; Hollinger, J.O.; Milam, S.B. Reconstruction of bone using calcium phosphate bone cements: A critical review. *J. Oral Maxillofac. Surg.* **1999**, *57*, 1122–1126. [CrossRef]
26. Mofakhami, S.; Salahinejad, E. Biphasic calcium phosphate microspheres in biomedical applications. *J. Control. Release* **2021**, *338*, 527–536. [CrossRef]
27. Shao, R.; Quan, R.; Zhang, L.; Wei, X.; Yang, D.; Xie, S. Porous hydroxyapatite bioceramics in bone tissue engineering: Current uses and perspectives. *J. Ceram. Soc. Japan* **2015**, *123*, 17–20. [CrossRef]
28. Predoi, D.; Iconaru, S.L.; Predoi, M.H.; Buton, N. Development of novel tetracycline and ciprofloxacin loaded silver doped hydroxyapatite suspensions for biomedical applications. *Antibiotics* **2022**, *12*, 74. [CrossRef]
29. Jackson, J.; Lo, J.; Hsu, E.; Burt, H.M.; Shademani, A.; Lange, D. The combined use of gentamycin and silver nitrate in bone cement for a synergistic and extended antibiotic action against Gram-positive and Gram-negative bacteria. *Materials* **2021**, *14*, 3413. [CrossRef]
30. Wan, G.; Ruan, L.; Yin, Y.; Yang, T.; Ge, M.; Cheng, X. Effects of silver nanoparticles in combination with antibiotics on the resistant bacteria Acinetobacter baumannii. *Int. J. Nanomed.* **2016**, *11*, 3789–3800. [CrossRef]
31. Pajor, K.; Pajchel, Ł.; Zgadzaj, A.; Piotrowska, U.; Kolmas, J. Modifications of hydroxyapatite by gallium and silver ions—Physicochemical characterization, cytotoxicity, and antibacterial evaluation. *Int. J. Mol. Sci.* **2020**, *21*, 5006. [CrossRef] [PubMed]
32. *EN ISO 10993-5*; 2009 Biological Evaluation of Medical Devices—Part 5: Tests for in Vitro Cytotoxicity (ISO 10993-5:2009), Annex A Neutral Red Uptake (NRU) Cytotoxicity Test. International Organization for Standardization: Geneva, Switzerland, 2009.
33. *EN ISO 10993-12*; 2012 Biological Evaluation of Medical Devices—Part 12: Sample Preparation and Reference Materials (ISO 10993-12:2012). International Organization for Standardization: Geneva, Switzerland, 2012.
34. Sayahi, M.; Santos, J.; El-Feki, H.; Charvillat, C.; Bosc, F.; Karacan, I.; Milthorpe, B.; Drouet, C. Brushite (Ca,M)HPO_4, $2H_2O$ doping with bioactive ions (M = Mg^{2+}, Sr^{2+}, Zn^{2+}, Cu^{2+}, and Ag^{+}): A new path to functional biomaterials? *Mater. Today Chem.* **2020**, *16*, 10030. [CrossRef]
35. Fadeeva, I.V.; Gafurov, M.R.; Kiiaeva, I.A.; Orlinskii, S.B.; Kuznetsova, L.M.; Filippov, Y.Y.; Fomin, A.S.; Davydova, G.A.; Selezneva, I.I.; Barinov, S.M. Tricalcium phosphate ceramics doped with silver, copper, zinc and iron (III) ions in concentration of less than 0.5% for bone tissue regeneration. *BioNanoScience* **2017**, *7*, 434–438. [CrossRef]
36. Kolmas, J.; Groszyk, E.; Piotrowska, U. Nanocrystalline hydroxyapatite enriched in selenite and manganese ions: Physicochemical and antibacterial properties. *Nanoscale Res. Lett.* **2015**, *10*, 989. [CrossRef]
37. Gopi, D.; Shinyjoy, E.; Kavitha, L. Synthesis and spectral characterization of silver/magnesium co-substituted hydroxyapatite for biomedical applications. *Spectrochim. Acta Part A Mol. Biomol. Spectrosc.* **2014**, *127*, 286–291. [CrossRef]
38. Okada, M.; Furuzono, T. Hydroxylapatite nanoparticles: Fabrication methods and medical applications. *Sci. Technol. Adv. Mater.* **2012**, *13*, 064103. [CrossRef]
39. Jillavenkatesa, A.; Condrate Sr, R. The infrared and Raman spectra of β-and α-tricalcium phosphate ($Ca_3(PO_4)_2$). *Spectrosc. Lett.* **1998**, *31*, 1619–1634. [CrossRef]
40. Martínez, T.; Espanol, M.; Charvillat, C.; Marsan, O.; Ginebra, M.; Rey, C.; Sarda, S. α-tricalcium phosphate synthesis from amorphous calcium phosphate: Structural characterization and hydraulic reactivity. *J. Mater. Sci.* **2021**, *56*, 13509–13523. [CrossRef]

41. Kolmas, J.; Kaflak, A.; Zima, A.; Ślósarczyk, A. Alpha-tricalcium phosphate synthesized by two different routes: Structural and spectroscopic characterization. *Ceram. Int.* **2015**, *41*, 5727–5733. [CrossRef]
42. Boonchom, B.; Baitahe, R. Synthesis and characterization of nanocrystalline manganese pyrophosphate $Mn_2P_2O_7$. *Mater. Lett.* **2009**, *63*, 2218–2220. [CrossRef]
43. El Kady, A.M.; Mohamed, K.R.; El-Bassyouni, G.T. Fabrication, characterization and bioactivity evaluation of calcium pyrophosphate/polymeric biocomposites. *Ceram. Int.* **2009**, *35*, 2933–2942. [CrossRef]
44. dos Santos Tavares, D.; de Oliveira Castro, L.; de Almeida Soares, G.D.; Alves, G.G.; Granjeiro, J.M. Synthesis and cytotoxicity evaluation of granular magnesium substituted β-tricalcium phosphate. *J. Appl. Oral Sci.* **2013**, *21*, 37–42. [CrossRef] [PubMed]
45. Walczyk, D.; Malina, D.; Krol, M.; Pluta, K.; Sobczak-Kupiec, A. Physicochemical characterization of zinc-substituted calcium phosphates. *Bull. Mater. Sci.* **2016**, *39*, 525–535. [CrossRef]
46. Lee, D.; Kumta, P.N. Chemical synthesis and stabilization of magnesium substituted brushite. *Mater. Sci. Eng. C* **2010**, *30*, 934–943. [CrossRef]
47. Arbez, B.; Kun-Darbois, J.D.; Convert, T.; Guillaume, B.; Mercier, P.; Huber, L.; Chappard, D. Biomaterial granules used for filling bone defects constitute 3D scaffolds: Porosity, microarchitecture, and molecular composition analyzed by microCT and Raman microspectroscopy. *J. Biomed. Mater. Res. B* **2019**, *107*, 415–423. [CrossRef]
48. Szurkowska, K.; Zgadzaj, A.; Kuras, M.; Kolmas, J. Novel hybrid material based on Mg^{2+} and SiO_4^{4-} co-substituted nanohydroxyapatite, alginate and chondroitin sulfate for potential use in biomaterials engineering. *Ceram. Int.* **2018**, *44*, 18551–18559. [CrossRef]
49. Pajor, K.; Michalicha, A.; Belcarz, A.; Pajchel, L.; Zgadzaj, A.; Wojas, F.; Kolmas, J. Antibacterial and cytotoxicity evaluation of new hydroxyapatite-based granules containing silver or gallium ions with potential use as bone substitutes. *Int. J. Mol. Sci.* **2022**, *23*, 7102. [CrossRef]
50. Kurtjak, M.; Vucomanovic, M.; Krajnc, A.; Kramer, L.; Turk, B.; Suvorow, D. Designing Ga(III)-containing hydroxyapatite with antibacterial activity. *RSC Adv.* **2016**, *6*, 112839–112852. [CrossRef]
51. Cavallaro, G.; Lazzara, G.; Milioto, S.; Parisi, F.; Evtugyn, V.; Roshina, E.; Fakhrullin, R. Nanohydrogel formation within the halloysite lument for triggered and sustained release. *ACS Appl. Mater. Interface* **2018**, *10*, 8265–8273. [CrossRef]
52. Fosca, M.; Rau, J.V.; Uskokovic, V. Factors influencing the drug release from calcium phosphate cements. *Bioactive Mater.* **2022**, *7*, 341–363. [CrossRef]
53. Lisuzzo, L.; Cavallaro, G.; Milioto, S.; Lazzara, G. Halloysite nanotubes coated by chitosan for controlled release of khellin. *Polymers* **2020**, *12*, 1766. [CrossRef] [PubMed]

coatings

MDPI

Article

Studies of New Layer Formation on the Surface of Zinc Doped Hydroxyapatite/Chitosan Composite Coatings in Biological Medium

Mikael Motelica-Heino [1], Mihai Valentin Predoi [2], Steluta Carmen Ciobanu [3], Simona Liliana Iconaru [3,*] and Daniela Predoi [3,*]

[1] Department of Civil Engineering and Environment, Université d'Orléans, ISTO, UMR 7327 CNRS, 1A Rue de la Férollerie, 45071 Orléans, France
[2] Department of Mechanics, University Politehnica of Bucharest, BN 002, 313 Splaiul Independentei, Sector 6, 060042 Bucharest, Romania
[3] National Institute of Materials Physics, Atomistilor Street, No. 405A, P.O. Box MG 07, 077125 Magurele, Romania
* Correspondence: simonaiconaru@gmail.com (S.L.I.); dpredoi@gmail.com (D.P.)

Abstract: Usually, before being used in biomedical applications, a biomaterials' bioactivity is tested by *in vitro* methods that simulate similar conditions to those found in the human body. In this work, we report on the synthesis of zinc-doped hydroxyapatite–chitosan (ZnHApC) composite coatings by the vacuum deposition method. The surface microstructure and the chemical and molecular modification of the coatings before and after soaking in DMEM (Dulbecco's Modified Eagle's Medium) were studied. For this objective, techniques such as attenuated total reflection (ATR), Fourier transform infrared (FTIR) spectroscopy, metallographic microscopy (MM), and scanning electron microscopy (SEM) were applied used. Also, water contact angle measurements and swelling studies were made on ZnHApC composite coatings before and after soaking in a biological medium. The coatings' adherence to the substrate was also studied. The results of antifungal studies on ZnHApC composite coatings against the *Candida albicans* microbial strain reveal their good antifungal activity. The biocompatibility of the composite coatings was tested using a primary osteoblast cell line. Our results suggest that zinc-doped hydroxyapatite–chitosan samples could be used as a bioimplant material due to their enhanced bioactivity and biocompatibility.

Keywords: biological medium; zinc; surface changes; hydroxyapatite; osteoblast cell line

Citation: Motelica-Heino, M.; Predoi, M.V.; Ciobanu, S.C.; Iconaru, S.L.; Predoi, D. Studies of New Layer Formation on the Surface of Zinc Doped Hydroxyapatite/Chitosan Composite Coatings in Biological Medium. *Coatings* **2023**, *13*, 472. https://doi.org/10.3390/coatings13020472

Academic Editor: Seungil Kim

Received: 31 December 2022
Revised: 10 February 2023
Accepted: 17 February 2023
Published: 19 February 2023

1. Introduction

Usually, prior to being used in biomedical applications (e.g., coatings for medical devices, metallic implants, bone fillers, etc.), biomaterials are tested for their bioactivity through *in vitro* methods that simulate similar conditions to those found in the human body [1]. For this purpose, since the beginning of the 1990s, SBF (simulated body fluid) was proposed by Kokubo et al. as a medium that could predict the in vivo bone bioactivity of a biomaterial [2]. Normally, the SBF solution contains only the inorganic part of blood serum [3,4].

Recently, in the literature, it was proposed to use DMEM (Dulbecco's Modified Eagle's Medium) solution as a substitute for SBF solution in order to evaluate a material's bioactivity [1,4]. DMEM solution is frequently used as a culture medium for cell lines, and, unlike SBF, contains both the inorganic and the organic parts of blood serum [1,4]. In previous studies, it has been highlighted that by immersing samples in SBF or DMEM solution (between 1 and 21 days), the precipitation of an apatitic layer on the sample surface occurs [4–6]. It is well known that the formation of new bone tissue around the implant implies many biological processes that take place at the interface between the implant and

the bone tissue [6]. Hydroxyapatite (HAp) is one of the most often used biomaterials for covering metallic implants [6,7].

Among the most common causes that lead to implant failure are infections that occur immediately after the implant and the formation of an insufficient amount of new bone tissue around the implant [8]. Furthermore, previous studies have shown that the bioactivity of hydroxyapatite layers can be improved by ionic substitution [8,9]. For example, in the study conducted by Kazimierczak P. et al. [10] regarding the biocompatibility and osteoinductivity of chitosan–agarose–nanohydroxyapatite scaffolds, it was reported that the hydrophilic surface of the obtained nanocomposites confers on them a good biocompatibility with the osteoblast (hFOB 1.19) cell line. Furthermore, the presence of zinc ions in the zinc-doped nanohydroxyapatite-based bone scaffolds gives them excellent antimicrobial properties and a nontoxic effect against the osteoblast cell line [11].

On the other hand, *Candida* species are well known as an important nosocomial pathogen. Moreover, *Candida albicans* is frequently identified in the biofilm found on the surface of implanted biomedical devices (e.g., urinary catheters, joint replacements, etc.) [12–14]. Therefore, the attainment of biomaterials with good antifungal activity is of great interest to the medical community and could represent a viable alternative to the classic antimycotic treatment.

Currently, for the development of bioceramic layers, techniques such as electrophoretic deposition [15], pulsed laser deposition (PLD) [16], matrix-assisted pulsed laser deposition (MAPLE) [17], radio frequency magnetron sputtering (RFMS) [18], the sol-gel method [19], electrochemical deposition [20], vacuum deposition [21], etc., are used.

For example, Vranceanu D. M. et al. [6] have found, along with the growth of the immersion time (up to 21 days) of silver-doped hydroxyapatite (AgHAp) and hydroxyapatite (HAp) coatings in a DMEM solution, the formation of increased quantities of new apatite phases on their surface [6]. This behavior suggests that the studied samples have an improved biomineralization ability [6]. The results obtained on the AgHAp and HAp coatings after immersion in an SBF solution were discussed. Their results indicate that the DMEM solution may be used for preliminary evaluation of biomineralization efficiency [6].

Another study, conducted by Dumelie N. and collaborators [22] revealed that after the immersion of up to 21 days in a DMEM medium of calcium-deficient hydroxyapatite coatings on a Ti6Al4V substrate, the precipitation of a new crystalline apatite occurs. It was also noticed that there was an increase in the Ca/P atomic ratio value from 1.5 (before the immersion in the DMEM medium) to a Ca/P value of around 1.65 (after the immersion in the DMEM medium) [22]. Further, it was noticed that by immersing in a DMEM solution, the dissolution of calcium-deficient hydroxyapatite coatings occurs followed by the precipitation of a new apatite layer [22]. These results make such biomaterials suitable for use in orthopedic or dental applications since they favor the formation of new bone tissue [22].

It is known that Zinc (Zn) ions are one of the significant trace elements present in bone tissue [23]. Zinc ions participate in important bone processes such as bone development and biomineralization [23–25]. Therefore, the Zn incorporation in the hydroxyapatite structure can enhance their bioactivity [23–26].

The point of this study was to evaluate for the first time the new layer formation on the surface of zinc-doped hydroxyapatite–chitosan (ZnHApC) composite coatings after soaking in a biological medium (DMEM). For this purpose, we used techniques such as attenuated total reflection (ATR), Fourier transform infrared (FTIR) spectroscopy, metallographic microscopy (MM), and scanning electron microscopy (SEM). In addition, water contact angle measurements and swelling and adhesion studies were performed. The ZnHApC coatings were developed by vacuum deposition technique, and their physicochemical and biological features before and after soaking in a DMEM medium were presented. The biological assay conducted on ZnHApC was done with the aid of a primary osteoblast cell line. Moreover, antifungal activity against the *Candida albicans* fungal strain was evaluated.

2. Materials and Methods

2.1. Synthesis of Zinc-Doped Hydroxyapatite–Chitosan (ZnHApC) Powders

For the synthesis of zinc-doped hydroxyapatite–chitosan ($Ca_{10-x}Zn_x(PO_4)_6(OH)_2$; x_{Zn} = 0.07; ZnHApC) powders, the protocol described in our previous paper was used [21]. For this objective, during the synthesis, the [Ca + Zn]/P ratio was kept at 1.67 and the pH value was maintained at 11. The obtaining procedure was performed in air. The proper amounts of $Zn(NO_3)_2 \cdot 6H_2O$ (Alfa Aesar, Karlsruhe, Germany) and $Ca(NO_3)_2 \cdot 4H_2O$ (calcium nitrate tetrahydrate; Sigma Aldrich, St. Louis, MO, USA) were dissolved and the obtained solution was slowly added into a solution containing $(NH_4)_2 \cdot HPO_4$ (Alfa Aesar, Karlsruhe, Germany) and chitosan ($C_6H_{11}NO_4$; Sigma Aldrich, St. Louis, MO, USA). The obtained mixture was stirred at 100 °C for 4 h and then centrifugated. Then, the precipitate was redispersed in an aqueous solution under vigorous stirring at 100 °C. Last, the ZnHApC precipitate was dried at 100 °C and used for the vacuum deposition of the ZnHApC composite coatings.

2.2. Deposition of ZnHApC Coatings on Si Substrate

The ZnHApC thin films were deposited on Si substrates. Before the vacuum deposition, the substrate was cleaned several times with acetone and dried in the air at 40 °C. The parameters used for the coating's deposition were described in detail by Predoi et al. [16]. Further, the ZnHApC thin films were soaked in a DMEM medium (Sigma Aldrich, St. Louis, MO, USA) in an incubator (GFL 4010, GFL Gesellschaft für Labortechnik mbH, Burgwedel, Germany) at 37 °C ± 0.5 °C. Initially, 2 sample batches were soaked in DMEM (which was changed daily). The first sample batch was taken out after 7 days (ZnHApC-7D) and the second sample batch after 14 days (ZnHApC-7D). After being taken out from the biological environment, the samples were washed with double-distilled water and placed in a desiccator.

2.3. Physical, Chemical, and Morphological Characterizations

The attenuated total reflection-Fourier transform infrared (ATR-FTIR) spectra were obtained with the aid of a Jasco FTIR-6600 spectrometer (Easton, MD, USA). The spectra were acquired from 450 to 2000 cm^{-1} with a spectral resolution of 4 cm^{-1} averaging 128 scans.

The morphology and EDX compositional studies of ZnHApC powders and coatings were performed using a scanning electron microscope (Hitachi S4500, Hitachi, Tokyo, Japan).

Preliminary assessments of the ZnHApC coatings surface before and after the soaking in the biological medium were obtained using the 10× magnification objective of an inversed trinocular metallographic microscope OX.2153-PLM, (Euromex, Arnhem, The Netherlands). Image J software (Image J 1.51j8) [27] was used for the 3D representation of SEM and metallographic images.

The water contact angle studies were performed under ambient conditions using a contact angle goniometer (DSA30 Kruess GmbH, Hamburg, Germany). For these experiments, the sessile drop technique was used. The contact angle measurements were repeated 3 times for each composite coating. The values of the contact angle ± SD are presented.

Dried ZnHApC, ZnHApC-7D, and ZnHApC-14D coatings were weighted (W_D) before the swelling test. Then the dried coatings were immersed in deionized water. Finally, the samples were taken out of the water after 24 h. The water excess was removed with filter paper and then the samples were weighed again (W_W). The swelling test was repeated 3 times, and the results are presented as mean value ± SD. The swelling percentage was calculated with the following formula:

$$\text{Swelling } (\%) = \frac{W_{W-W_D}}{W_D} \times 100 \quad (1)$$

The adherence of the ZnHApC, ZnHApC-7D, and ZnHApC-14D coatings to the substrate was determined using the tape-pull test. The adhesion tests were performed using the 3M Performance Flatback Tape 2525, having a peel adhesion of 7.5 N/cm.

2.4. Cytotoxicity Assay

The biological properties of the ZnHApC, ZnHApC-7D, and ZnHApC-14D samples were investigated using primary human osteoblast cells, hFOB 1.19. The cells were procured from the upper part of a patient's femur following the protocol described by Gallagher et al. [28]. The *in vitro* biocompatibility study assays were performed as previously reported in detail in [29] and the cell viability of the hFOB 1.19 cells was determined after 24 and 72 h of incubation with the composite layers. The *in vitro* experiments were done in triplicate. The data were reported as mean ± standard deviation (SD). Furthermore, the statistical analysis was performed using the t-test and analysis of variance (ANOVA).

2.5. Antifungal In Vitro Assay

Studies regarding the antifungal activity of the ZnHApC, ZnHApC-7D, and ZnHApC-14D coatings were performed against the fungal strain *Candida albicans* ATCC 10231. The *in vitro* antifungal assays were done according to the experiments described in [30] and the activity of the samples was determined after 24, 48, and 72 h of incubation with the fungal suspensions. All the experiments were performed in triplicate and the data were graphically represented as mean ± SD.

3. Results

ATR-FTIR measurements were used to study the molecular changes that took place before and after the soaking of ZnHApC coatings in DMEM (Figure 1). In Figure 1, the presence of characteristic adsorption bands of HAp can be easily observed. The absorption bands were found at 480, 564, 606, 960, and 1090 cm^{-1} and are ascribed to PO_4^{3-} vibration, and their presence was observed for all studied coatings [21,31]. On the other hand, in the FTIR spectra of ZnHApC-14D (Figure 1c) coatings, the presence of the adsorption bands at 869, 1416, and 1484 cm^{-1}, ascribed to CO_3^{2-} groups, was noticed, which suggests the presence of a carbonated hydroxyapatite layer on the sample's surface [31]. Furthermore, in the region from 1300 until 1500 cm^{-1}, bands that are ascribed to the chitosan structure are present [21,31].

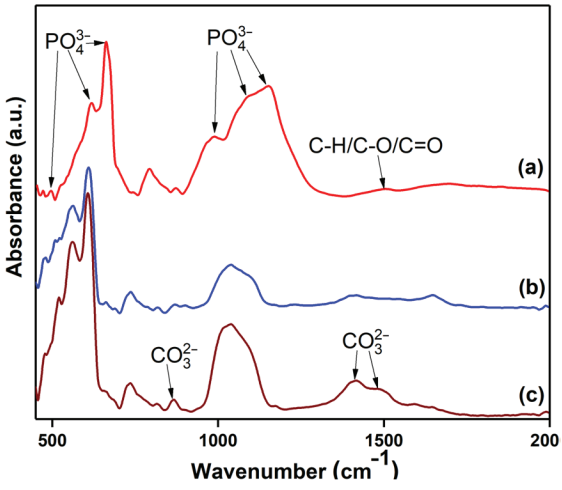

Figure 1. Absorbance ATR-FTIR spectra of ZnHApC (**a**), ZnHApC-7D (**b**), and ZnHApC-14D (**c**) coatings.

According to the studies made by Vladescu A. and collaborators, [32] the presence of carbonate bands in the FTIR spectra suggests the formation of an apatitic layer. Moreover, the presence of carbonate bands in the FTIR spectra underlines the replacement of PO_4^{3-} with CO_3^{2-} functional groups in the HAp structure [31,32].

After the coatings were soaked in DMEM for 7 and 14 days, the increase in adsorption band intensity can be observed. Also, the ZnHApC-14D exhibits more intense peaks ascribed to carbonate groups. The FTIR studies' results underline that samples soaking in DMEM induce some changes in the soaked coatings [31,32].

First, we have conducted SEM and EDX studies on ZnHApC powders and the results are depicted in Figure 2. Close observation of the SEM micrographs reveals that the ZnHApC powders consist mainly of spherical particles with dimensions in the nanometric range. In the collected SEM images, it can also be observed that the nanoparticles are agglomerated.

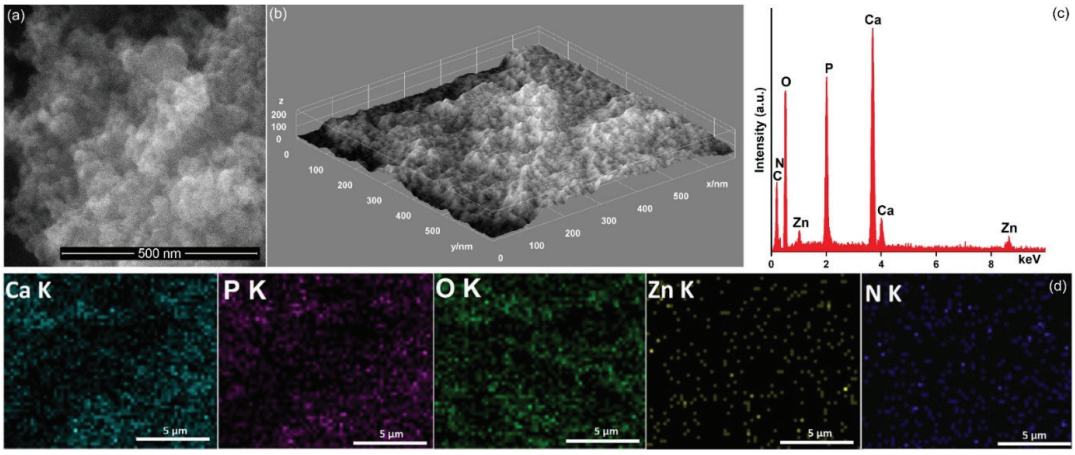

Figure 2. SEM micrographs in 2D and 3D obtained for ZnHApC powders (**a**,**b**). EDX spectra (**c**) and elemental distribution maps ZnHApC powders (**d**).

From the EDX spectra and elemental distribution maps, as depicted in Figure 2, the characteristic peaks of Ca, P, Zn, N, and O are present in the ZnHApC powders. The N line in the EDX spectra arises due to the presence of chitosan in the sample. Also, the surface homogeneity is underlined by the good distribution of the chemical elements in the studied powder. The results of the EDX chemical composition highlighted the purity of the samples.

Figure 3 shows the results of the SEM and EDX studies performed on the ZnHApC coatings before and after soaking (for 7 and 14 days) in DMEM. In the case of ZnHApC, the coatings were inspected before soaking in DMEM. There was the presence of a continuous and uniform layer on the Si substrate surface without the observation of any crack on the coating surface, as indicated by the SEM micrographs (Figure 3a,d).

The formation of a new layer based on calcium and phosphorus (probably a calcium-deficient hydroxyapatite) on the surface of the ZnHApC coatings after 7 and 14 days of exposure to DMEM was proven. The formation of the new layer probably took place by the biomimetic mineralization process as explained by Vranceanu, D.M. and coworkers [6] in their paper entitled: "*In vitro* evaluation of Ag doped hydroxyapatite coatings in acellular media".

Regarding the EDX chemical composition of the analyzed layers, our results indicate the presence of the following chemical elements: calcium, phosphorus, zinc, carbon, nitrogen, and oxygen, in all the samples (Figure 3g–i). Some variation of Ca and P line intensity was observed.

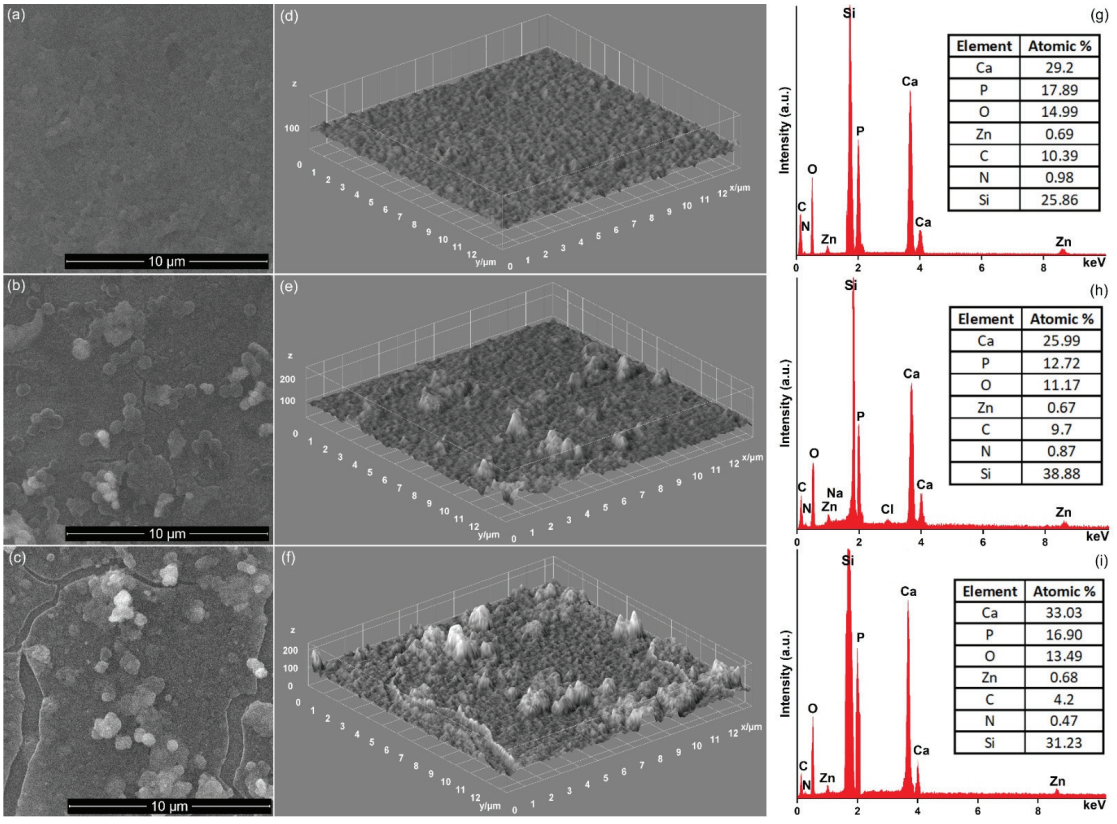

Figure 3. Scanning electron microscopy micrographs (2D and 3D representations) of ZnHApC (**a**,**d**), ZnHApC-7D (**b**,**e**), and ZnHApC-14D(**c**,**f**) coatings and their 3D representations. The energy dispersive X-ray analysis (EDX) spectrum of ZnHApC (**g**), ZnHApC-7D (**h**), and ZnHApC-14D (**i**) coatings.

The results of energy dispersive X-ray spectroscopy (EDS) quantitative analysis (inset of Figure 3g–i) suggest the presence of stoichiometric hydroxyapatite (Ca + Zn)/P = 1.67 in the chitosan matrix in the case of ZnHApC composite coatings. After the soaking in a DMEM medium, the value of the (Ca + Zn)/P ratio varies between 2.095 (for the ZnHApC-7D sample) and 1.99 (for the ZnHApC-14D sample). These values can indicate the formation of a new apatite layer. Our results are in good agreement with the EDX quantitative results previously reported by Vranceanu, D.M. et al. [6].

In the EDX elemental distribution obtained for the ZnHApC-14D coatings, it can be observed that the major constituent are Ca, P, and O. The minor components are represented by Zn, N, and C. Furthermore, the well spatial distribution of both minor and major elements on the ZnHApC-14D coatings surface was observed (Figure 4).

The complementary information regarding the surface characteristics of ZnHApC coatings were achieved by metallographic microscopy (MM) measurements. Figure 5 presents the metallographic image characteristics of the ZnHApC (a and d), ZnHApC-7D (b and e), and ZnHApC-14D (c and h) coatings. In Figure 5, the lack of fissures on the coatings' surface can be observed. The metallographic data sustain the results provided by the SEM studies regarding the formation of a new layer on the ZnHApC subsurface. This is supported by the change in surface morphology of the DMEM-immersed coatings

compared to that of the nonimmersed coating. The SEM features were in agreement with the findings previously reported in the literature [6,32–34].

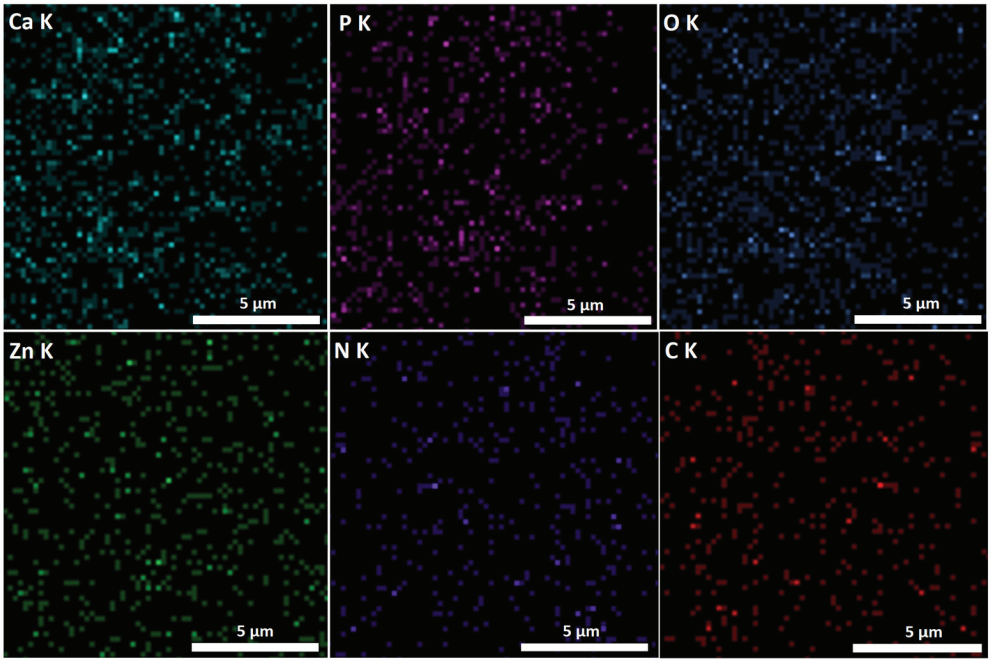

Figure 4. The EDX elemental distributions obtained for ZnHApC-14D coating.

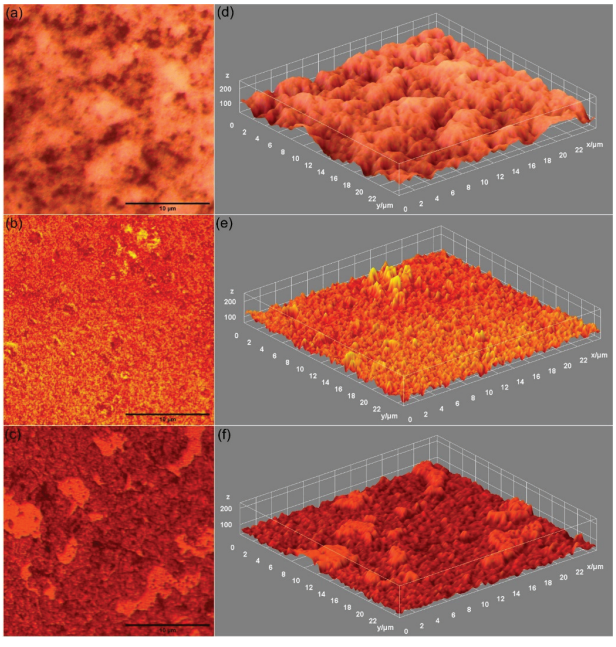

Figure 5. Images in 2D and 3D obtained by metallographic studies on ZnHApC (**a**,**d**), ZnHApC-7D (**b**,**e**), and ZnHApC-14D (**c**,**f**) coatings.

Furthermore, the adherence of ZnHApC, ZnHApC-7D, and ZnHApC-14D on the silicium substrate was investigated using the tape-pull test method. This test is widely known and used for the determination of a coatings' adherence being deemed one of the simplest and fastest-used methods to evaluate a coating's adhesion. In the case of ZnHApC, ZnHApC-7D, and ZnHApC-14D, the experiments highlighted that the scotch tape came off approximately clear, having an insignificant amount of material stuck to it. Therefore, the analysis performed on the coatings suggested that not much of the ZnHApC, ZnHApC-7D, and ZnHApC-14D coatings were actually removed from the substrate. These results emphasized that the ZnHApC, ZnHApC-7D, and ZnHApC-14D coatings presented a good adhesion to the substrate.

The surface properties of ZnHApC t"In 'ilms were evaluated by contact angle measurements and their results are revealed in Table 1. It is known that values higher than 90° indicate a hydrophobic nature of the material surface and values <90° suggest the hydrophilic nature of the sample surface [35].

Table 1. Water contact angle on ZnHApC composite coatings surfaces.

Sample	Contact Angle θ (°)
ZnHApC	57.86 ± 2.75
ZnHApC-7D	48.97 ± 2.3
ZnHApC-14D	42.05 ± 1.5

The obtained value for the contact angle varies between 57.86 ± 2.75° (for ZnHApC) and 42.05 ± 1.5° (for ZnHApC-14D). Therefore, a decrease in the contact angle value that could be attributed to the hydrophilic behavior of apatite could be noticed. More than that, in previous studies, it was shown that the hydrophilic surfaces allowed better cell proliferation and a good growth of apatite in the physiological environment, thus supporting bone growth [36]. In this context, the wettability features of ZnHApC, ZnHApC-7D, and ZnHApC-14D suggest that our samples are hydrophilic which makes them suitable for biomedical applications (orthopedics, dentistry, tissue engineering, etc.) with our results being in concordance with the results previously reported [37].

The water uptake abilities of ZnHApC thin films before and after their soaking in DMEM medium were evaluated by aqueous swelling studies. The results of aqueous swelling studies are presented in Figure 6. Our results suggest that the swelling percentage decreased with the increase in immersion time of the ZnHApC thin films in the DMEM medium.

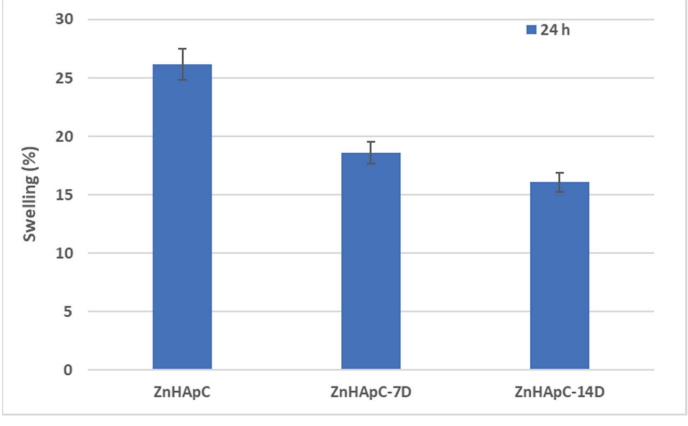

Figure 6. Aqueous swelling percentage of ZnHApC, ZnHApC-7D, and ZnHApC-14D coatings.

The higher swelling percentage was obtained for the ZnHApC thin films (26%), and the lowest value was obtained for the ZnHApC-14D sample (16%). In agreement with the results reported by Bhowmick, A. et al. [38], this behavior may be attributed to the fact that the presence of the apatitic layer on the ZnHApC thin films' surface induced a decrease in the water update capacity. Ponnusamy, S., and coworkers, showed that swelling properties facilitate the use of nutrients from the physiological environment and lead to better adherence [39].

The biocompatibility of the ZnHApC, ZnHApC-7D, and ZnHApC-14D coatings was assessed by *in vitro* experiments using human fetal osteoblast hFOB 1.19 cells. The coatings were incubated for 24 and 72 h with the hFOB 1.19 cell suspensions, and their viability was determined with the aid of the MTT assay. The results obtained from the in vitro MTT tests regarding the cell viability of the hFOB 1.19 incubated with ZnHApC, ZnHApC-7D, and ZnHApC-14D coatings are depicted in Figure 7.

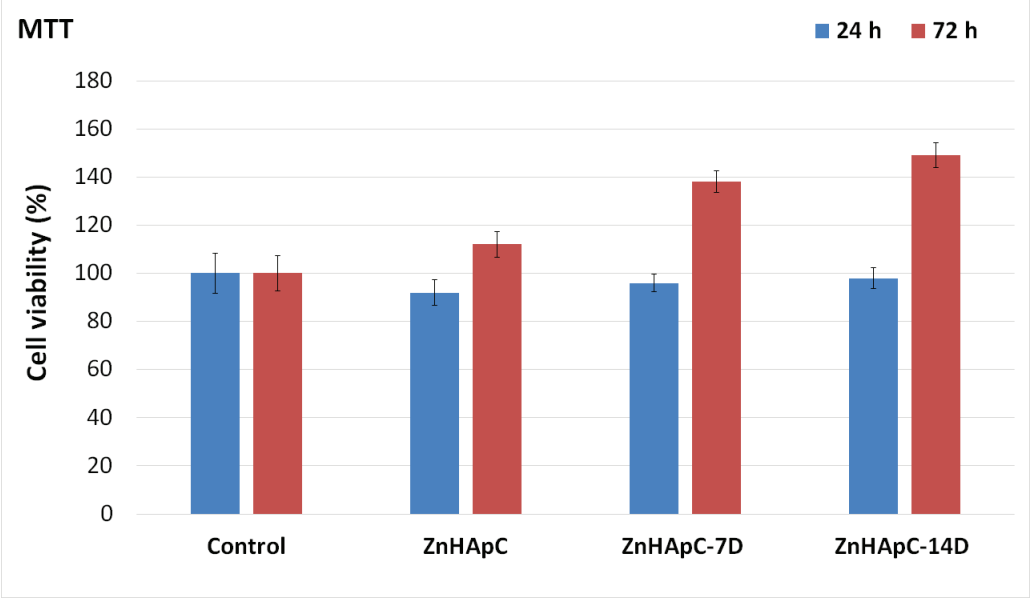

Figure 7. Cell viability of the hFOB 1.19 cells after 24 and 72 h of incubation in the presence of ZnHApC, ZnHApC-7D, and ZnHApC-14D. The results of the experiments are graphically represented as mean ± SD. The data were statistically analyzed using paired and two-sample t-tests for means, with $p \leq 0.05$ accepted as statistically significant.

The experiments were performed in triplicate and the presented data is mean ± SD. The results of the MTT assay determined that all the samples exhibited very good biocompatibility after 24 h of incubation with the hFOB 1.19 cells. However, an increase in cell viability was observed in the case of ZnHApC-7D and ZnHApC-14D compared to the ZnHApC sample. The data suggested that the cell viability increased for the ZnHApC coatings immersed in a DMEM medium. More than that, the results also suggested that the immersion period of the samples in the DMEM medium had an influence on cell viability. In addition, the results of the MTT assays highlighted that all the samples exhibited excellent biocompatibility, being above 92% compared to the control. The obtained results are in concordance with previously reported data regarding hydroxyapatite biocompatibility and its properties of promoting the adherence and proliferation of osteoblast cells [40–50]. Moreover, the cell viability of the hFOB 1.19 cells after 72 h of exposure to ZnHApC, ZnHApC-7D, and ZnHApC-14D coatings presented a significant increase compared to the

control cell culture. Furthermore, the results obtained from the MTT assays after 72 h of exposure of the hFOB 1.19 cells with the composite layers emphasized that all the composite layers presented strong biocompatibility activity and that also helped promote the hFOB 1.19 cells' proliferation and adhesion on the surfaces of the coatings. In addition, the studies demonstrated that the increase observed in the cell viability of hFOB 1.19 cells exposed to ZnHApC-7D and ZnHApC-14D for 72 h was higher than the increase observed in the case of the ZnHApC composite layers. These results could be attributed to the surface changes attained by the ZnHApC composite layers following their immersion in the DMEM medium for 7 and 14 days. More than that, the data also suggested that the increase in cell viability was also influenced by the period of time that the layers were immersed in the DMEM. Therefore, the results highlighted that the immersion in DMEM of the ZnHApC composite layers provided the layers with new surface properties that are responsible for a better proliferation and adhesion of the hFOB 1.19 cell.

Furthermore, the morphology of the hFOB 1.19 cells incubated for 24 and 72 h with the ZnHApC, ZnHApC-7D, and ZnHApC-14D coatings was investigated by microscopy. The results of the morphology investigation of the hFOB 1.19 cells incubated for 24 h with ZnHApC, ZnHApC-7D, and ZnHApC-14D coatings are depicted in Figure 8.

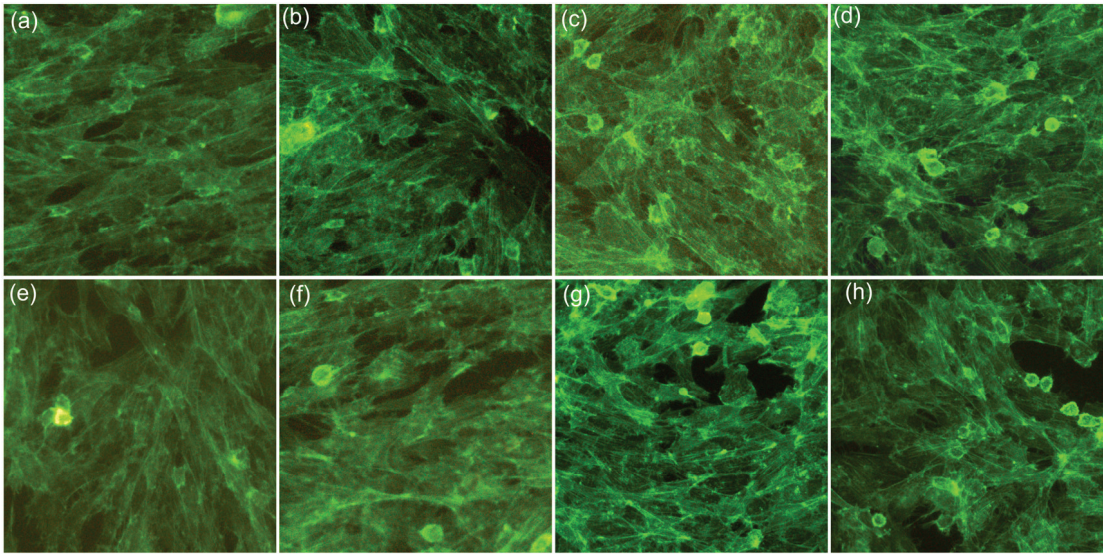

Figure 8. The morphology of hFOB 1.19 cells incubated with ZnHApC (**b**,**f**), ZnHApC-7D (**c**,**g**), and ZnHApC-14D (**d**,**h**) for 24 h (**a**–**d**) and 72 h (**e**–**h**) relative to an untreated hFOB 1.19 cell culture used as control (**a**,**e**).

The images of the hFOB 1.19 cells incubated with ZnHApC, ZnHApC-7D, and ZnHApC-14D coatings highlighted that the cells have adhered on the surface of the ZnHApC, ZnHApC-7D, and ZnHApC-14D coatings and also that the adhered cells exhibit the typical morphology of the hFOB 1.19 cells. Moreover, the visualization of the hFOB 1.19 cells incubated for 24 h with the ZnHApC, ZnHApC-7D, and ZnHApC-14D coatings revealed that coatings did not induce changes to the morphology of the hFOB 1.19 cells. Furthermore, the fluorescence micrographs highlighted that after 72 h of incubation with the ZnHApC composites, the hFOB 1.19 cells adhered and spread until covering almost the entire surface of the composite layers. In addition, the results of the visualization depicted that after 72 h of exposure to the composite layers, the osteoblast cells had the appearance of being organized in confluent layers spread out on the surface of the composite layers. More than that, the results also suggested that the composite layers immersed in a DMEM medium exhib-

ited better biological activity, conferring upon the cells the ability to proliferate and adhere to their surface. These results are in agreement with the MTT assay and emphasized that the immersion in the DMEM medium of the composite layers, as well as the immersion time period, influenced the physicochemical and biological activities of the composite surface, conferring on them enhanced biological properties that lead to better proliferation and adhesion of the cells. Therefore, the data obtained from both the MTT assay, as well as the optical visualization, suggested that the surface of the composite layers affected the metabolic activity of the cells by enhancing their growth. The increase in the hFOB 1.19 cell number was not significant after 24 h of incubation compared to the control cell culture, however, the results showed an abrupt and significant increase ($p < 0.05$) in the number of hFOB 1.19 cells after 72 h of incubation. These results are in good agreement with the results of the quantitative MTT *in vitro* assay and highlighted that ZnHApC, ZnHApC-7D, and ZnHApC-14D coatings have good biocompatibility and could be suitable for being used in biomedical applications.

The results are in good agreement with previously reported studies [51–53] regarding the biological properties of materials based on zinc ions and hydroxyapatite on human osteoblast cells MG-63 [50], mesenchymal stem cells derived from human adipose (MSCs) [44], and MRC-5 fibroblast cells [45]. More than that, in their study, Thian et al. [44] reported that the presence of zinc ions in the structure of hydroxyapatite influenced the bioactivity properties of HAp. In addition to the existing reported data, the results of this study also emphasize that immersion in DMEM of the ZnHApC for 7 and 14 days had an influence on the biological properties of the coatings. Therefore, in the case of ZnHApC-7D and ZnHApC-14D coatings, both the MTT *in vitro* assays, as well as the microscopic visualization, the results depicted that the cell viability, adherence, and proliferation are higher compared to the control cells and ZnHApC coatings. This phenomenon has been explained due to the effect and transformation that appear on the surface of the ZnHApC coatings after being immersed in a DMEM medium. Even though complex studies are still scarce, it has been reported that the increase of the surface charge could also lead to an increase in the wettability and surface energy of various HAp surfaces when using SBF and DMEM mediums [54,55]. Bodhak et al. [50] demonstrated that the increase in the surface energy of HAp obtained by immersion in SBF and DMEM mediums created a better hFOB cell attachment and more points of adhesion between the cells and the surface. On the other hand, Clupper et al. [54] demonstrated that S520 fibers immersed in SBF and DMEM showed promising preliminary results regarding the proliferation, and cell attachment, of osteoblast cells. These preliminary results are promising stepping stones for the future development of novel materials and coatings for biomedical applications that will possess higher bioactive properties and promote faster healing.

In addition, for a better understanding of the complex nature of the influence of the DMEM medium on the biological properties of ZnHApC composite layers, the antifungal properties of ZnHApC, ZnHApC-7D, and ZnHApC-14D coatings were also investigated. For this purpose, due to the fact *Candida albicans* is known as being one of the most opportunistic microorganisms and is also the prevailing cause of fungal infections in humans [56–59], the antifungal properties of the ZnHApC, ZnHApC-7D, and ZnHApC-14D coatings were evaluated against *C. albicans* ATTCC 10231. The composite layers were exposed to the fungal suspensions and their activity against the fungal cell's development was assessed at three different time intervals, 24, 48, and 72 h. The results of the antifungal studies were represented graphically and are depicted in Figure 9.

The results of the *in vitro* studies regarding the antifungal properties of the ZnHApC, ZnHApC-7D, and ZnHApC-14D composite layers depicted that all the investigated samples exhibited good inhibitory effects against the *C. albicans* fungal cells' development. More than that, the data also suggested that the antifungal activity was influenced by both the incubation time as well as the investigated samples. Therefore, the results showed that the antifungal activity of the samples increased with the increase in the incubation time. In addition, the data also suggested that the best inhibitory against the develop-

ment and adherence of *C. albicans* fungal cells on the surface of the composite layers was attributed to the ZnHApC-14D composite layers, therefore implying that the antifungal activity of the ZnHApC composite layers was also influenced by the DMEM immersion. The data obtained in this study is in agreement with previously reported data regarding the antimicrobial properties of materials based on zinc-doped hydroxyapatite in a polymer matrix [26,60–64]. The antifungal properties could be attributed both to the constituent elements of the materials used in the obtaining of the composite layers, as well as to the synergies that could take place between both the constituent elements found in the coatings and the substrate, as well as the synergies between the constituent elements of the composite layers [65,66]. In the case of ZnHApC, ZnHApC-7D, and ZnHApC-14D composite layers, the antifungal properties could be associated first with the presence of zinc ions as well as the presence of chitosan. Over the years, chitosan has been employed in different medical applications due to the fact that is a natural, biodegradable, linear polysaccharide that has been reported to possess both good biocompatibility as well as strong broad-spectrum antimicrobial activity [67–69]. Even though there are numerous papers regarding studies on the antibacterial activity of zinc-doped hydroxyapatite against gram-positive and gram-negative bacterial strains, different efficiencies have been reported [60,61,70–72]. The differences in antimicrobial activity amongst the materials might were reported to be attributed to both particles' physio-chemical characteristics and, especially, to the different surface properties, which can be strongly influenced by the type of material as well as their surface properties.

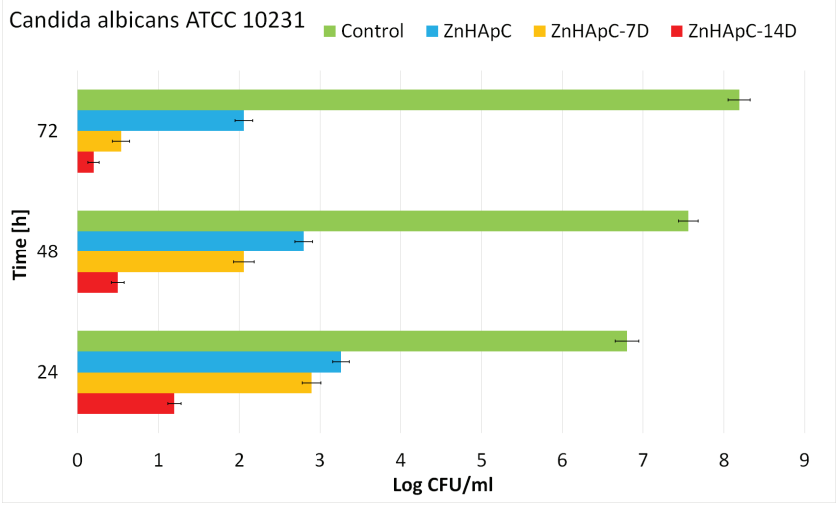

Figure 9. The graphical representation of the antifungal activity of ZnHApC, ZnHApC-7D, and ZnHApC-14D composite layers after 24, 48, and 72 h of exposure to *Candida albicans* ATCC 10231.

The results obtained by the biological assays emphasized that the Immersion in DMEM medium for 7 and 14 days of the ZnHApC composite layers determined changes in the layers' surfaces and granted the layers novel enhanced biological properties that helped promoted the adherence and proliferation of osteoblast cells on their surfaces while inhibiting the development of *C. albicans* fungal cells. In addition, the data also suggested that the immersion time helped improve the biological properties of the ZnHApC composite layers. The results of this study could contribute significantly as leading-edge knowledge for the future development of coatings with enhanced biological properties and antifungal properties for biomedical applications.

4. Conclusions

The main objective of this paper was to develop, by an adapted coprecipitation method, zinc-doped hydroxyapatite–chitosan (ZnHApC) powders. The ZnHApC nanopowders were used for fabrication by the vacuum deposition method of ZnHApC coatings. Then, on the obtained coatings, studies were performed in order to evaluate the formation of a new apatitic layer after their exposure to DMEM (a biological medium) for 7 and 14 days. Thus, FTIR, SEM, EDX, and metallographic studies were carried out. Our findings prove the development of a layer rich in Ca and P that underlines the good mineralization abilities of ZnHApC exposed to a biological medium. The good biocompatibility of ZnHApC, ZnHApC-7D, and ZnHApC-14D was pointed out with the aid of the hFOB 1.19 cell line. Furthermore, the antifungal activity of the ZnHApC, ZnHApC-7D, and ZnHApC-14D composite layers was also assessed against *C. albicans* fungal cells. The results of the biological assays demonstrated that all the samples exhibited good biocompatibility and strong inhibitory effects against the tested fungal cells. In addition, the results also suggested that the biological properties of the ZnHApC composite layers were considerably enhanced due to immersion in the DMEM medium. More than that, the data also emphasized that the biological properties of the layers were also influenced differently according to their immersion time in the DMEM medium. These first results are promising stepping stones for the future development of novel materials and coatings for biomedical applications that will possess higher bioactive properties, promote faster healing, and exhibit antifungal properties.

Author Contributions: Conceptualization, M.M.-H. and D.P.; methodology, D.P.; software, M.V.P.; validation, M.M.-H., D.P. and S.L.I.; formal analysis, M.M.-H.; investigation, M.M.-H., D.P., S.C.C., M.V.P. and S.L.I.; resources, M.M.-H., D.P. and M.V.P.; data curation, M.M.-H.; writing—original draft preparation, D.P., S.C.C., M.V.P. and S.L.I.; writing—review and editing, M.M.-H., D.P., S.C.C., M.V.P. and S.L.I.; visualization, M.M.-H., D.P., S.C.C., M.V.P. and S.L.I.; supervision, M.M.-H., S.L.I. and D.P.; project administration, D.P.; funding acquisition, D.P. All authors have read and agreed to the published version of the manuscript.

Funding: This work was supported by the Romanian Ministry of Research and Innovation through the PN-III-P2-2.1-PED-2019-1375, contract number 331PED/2020. Also, this research was supported by Contract No. T-IS 251801/04.05.2018 and Scientific Research Contract Nr.1/4.06.2020.

Institutional Review Board Statement: Not applicable.

Informed Consent Statement: Not applicable.

Data Availability Statement: Data available on demand from the corresponding author.

Acknowledgments: We would like to thank Rodica V. Ghita for her help with the vacuum deposition of coatings. Also, the authors would like to thank Monica Luminita Badea for assistance with the biological assays.

Conflicts of Interest: The authors declare no conflict of interest. The funders had no role in the design of the study; in the collection, analyses, or interpretation of data; in the writing of the manuscript; or in the decision to publish the results.

References

1. Rohanová, D.; Boccaccini, A.R.; Horkavcová, D.; Bozděchová, P.; Bezdička, P.; Častorálová, M. Is non-buffered DMEM solution a suitable medium for in vitro bioactivity tests? *J. Mater. Chem. B* **2014**, *2*, 5068–5076. [CrossRef]
2. Kokubo, T. Bioactive glass ceramics: Properties and applications. *Biomaterials* **1991**, *12*, 155–163. [CrossRef] [PubMed]
3. Kokubo, T.; Takadama, H. How useful is SBF in predicting in vivo bone bioactivity? *Biomaterials* **2006**, *27*, 2907–2915. [CrossRef] [PubMed]
4. Lee, J.T.; Leng, Y.; Chow, K.L.; Ren, F.; Ge, X.; Wang, K.; Lu, X. Cell culture medium as an alternative to conventional simulated body fluid. *Acta Biomater.* **2011**, *7*, 2615–2622. [CrossRef]
5. Um, S.H.; Chung, Y.W.; Seo, Y.; Seo, H.; Ok, M.R.; Kim, Y.C.; Han, H.S.; Chung, J.J.; Edwards, J.R.; Jeon, H. Robust Hydroxyapatite Coating by Laser-Induced Hydrothermal Synthesis. *Adv. Funct. Mater.* **2020**, *30*, 2005233. [CrossRef]
6. Vranceanu, D.M.; Parau, A.C.; Cotrut, C.M.; Kiss, A.E.; Constantin, L.R.; Braic, V.; Vladescu, A. In vitro evaluation of Ag doped hydroxyapatite coatings in acellular media. *Ceram. Int.* **2019**, *45*, 11050–11061. [CrossRef]

7. Faria, D.; Abreu, C.S.; Buciumeanu, M.; Dourado, N.; Carvalho, O.; Silva, F.S.; Miranda, G. Ti6Al4V laser surface preparation and functionalization using hydroxyapatite for biomedical applications. *J. Biomed. Mater. Res. Part B Appl. Biomater.* **2018**, *106*, 1534–1545. [CrossRef] [PubMed]
8. Arcos, D.; Vallet-Regí, M. Substituted hydroxyapatite coatings of bone implants. *J. Mater. Chem. B* **2020**, *8*, 1781–1800. [CrossRef] [PubMed]
9. Ratnayake, J.T.B.; Mucalo, M.; Dias, G.J. Substituted hydroxyapatites for bone regeneration: A review of current trends. *J. Biomed. Mater. Res. B Appl. Biomater.* **2017**, *105*, 1285–1299. [CrossRef] [PubMed]
10. Boccaccini, A.R.; Keim, S.; Ma, R.; Li, Y.; Zhitomirsky, I. Electrophoretic deposition of biomaterials. *J. R. Soc. Interface* **2010**, *7*, S581–S613. [CrossRef] [PubMed]
11. Kazimierczak, P.; Benko, A.; Nocun, M.; Przekora, A. Novel chitosan/agarose/hydroxyapatite nanocomposite scaffold for bone tissue engineering applications: Comprehensive evaluation of biocompatibility and osteoinductivity with the use of osteoblasts and mesenchymal stem cells. *Int. J. Nanomed.* **2019**, *14*, 6615–6630. [CrossRef] [PubMed]
12. Kazimierczak, P.; Golus, J.; Kolmas, J.; Wojcik, M.; Kolodynska, D.; Przekora, A. Noncytotoxic zinc-doped nanohydroxyapatite-based bone scaffolds with strong bactericidal, bacteriostatic, and antibiofilm activity. *Biomat. Adv.* **2022**, *139*, 213011. [CrossRef]
13. Douglas, L.J. Candida biofilms and their role in infection. *Trends Microbiol.* **2003**, *11*, 30–36. [CrossRef]
14. Ferreira, A.V.; Prado, C.G.; Carvalho, R.R.; Dias, K.S.T.; Dias, A.L.T. Candida albicans and non-C. albicans Candida species: Comparison of biofilm production and metabolic activity in biofilms, and putative virulence properties of isolates from hospital environments and infections. *Mycopathologia* **2013**, *175*, 265–272. [CrossRef] [PubMed]
15. Pierce, G.E. Pseudomonas aeruginosa, Candida albicans, and device-related nosocomial infections: Implications, trends, and potential approaches for control. *J. Ind. Microbiol. Biotechnol.* **2005**, *32*, 309–318. [CrossRef] [PubMed]
16. Rajesh, P.; Mohan, N.; Yokogawa, Y.; Varma, H. Pulsed laser deposition of hydroxyapatite on nanostructured titanium towards drug eluting implants. *Mater. Sci. Eng. C* **2013**, *33*, 2899–2904. [CrossRef] [PubMed]
17. Negroiu, G.; Piticescu, R.M.; Chitanu, G.C.; Mihailescu, I.N.; Zdrentu, L.; Miroiu, M. Biocompatibility evaluation of a novel hydroxyapatite-polymer coating for medical implants (in vitro tests). *J. Mater. Sci. Mater. Med.* **2008**, *19*, 1537–1544. [CrossRef] [PubMed]
18. Snyders, R.; Bousser, E.; Music, D.; Jensen, J.; Hocquet, S.; Schneider, J.M. Influence of the chemical composition on the phase constitution and the elastic properties of RF-sputtered hydroxyapatite coatings. *Plasma Process. Polym.* **2008**, *5*, 168–174. [CrossRef]
19. Hench, L.L.; West, J.K. The sol-gel process. *Chem. Rev.* **1990**, *90*, 33–72. [CrossRef]
20. Qiu, D.; Yang, L.; Yin, Y.; Wang, A. Preparation and characterization of hydroxyapatite/titania composite coating on NiTi alloy by electrochemical deposition. *Surf. Coat. Technol.* **2011**, *205*, 3280. [CrossRef]
21. Predoi, D.; Ciobanu, C.S.; Iconaru, S.L.; Raaen, S.; Badea, M.L.; Rokosz, K. Physicochemical and Biological Evaluation of Chitosan-Coated Magnesium-Doped Hydroxyapatite Composite Layers Obtained by Vacuum Deposition. *Coatings* **2022**, *12*, 702. [CrossRef]
22. Dumelie, N.; Benhayoune, H.; Richard, D.; Laurent-Maquin, D.; Balossier, G. In vitro precipitation of electrodeposited calcium-deficient hydroxyapatite coatings on Ti6Al4V substrate. *Mater. Charact.* **2008**, *59*, 129–133. [CrossRef]
23. Wu, S.; Ma, S.; Zhang, C.; Cao, G.; Wu, D.; Gao, C.; Lakshmanan, S. Cryogel biocomposite containing chitosan-gelatin/cerium–zinc doped hydroxyapatite for bone tissue engineering. *Saudi J. Biol. Sci.* **2020**, *27*, 2638–2644. [CrossRef]
24. Yamaguchi, M. Role of nutritional zinc in the prevention of osteoporosis. *Mol. Cell. Biochem.* **2010**, *338*, 241–254. [CrossRef] [PubMed]
25. Huang, Y.; Zhang, X.; Mao, H.; Li, T.; Zhao, R.; Yan, Y.; Pang, X. Osteoblastic cell responses and antibacterial efficacy of Cu/Zn co-substituted hydroxyapatite coatings on pure titanium using electrodeposition method. *RSC Adv.* **2015**, *5*, 17076–17086. [CrossRef]
26. Predoi, D.; Iconaru, S.L.; Predoi, M.V. Fabrication of Silver- and Zinc-Doped Hydroxyapatite Coatings for Enhancing Antimicrobial Effect. *Coatings* **2020**, *10*, 905. [CrossRef]
27. ImageJ. Available online: http://imagej.nih.gov/ij (accessed on 20 November 2022).
28. Gallagher, A.J.; Gundle, R.; Beresford, N.J. Isolation and culture of bone forming cells (osteoblasts) from human bone. *Hum. Cell Cult. Protoc.* **1996**, *2*, 233–263. [CrossRef]
29. Predoi, D.; Iconaru, S.L.; Predoi, M.V. Bioceramic Layers with Antifungal Properties. *Coatings* **2018**, *8*, 276. [CrossRef]
30. Chen, J.; Nan, K.; Yin, S.; Wang, Y.; Wu, T.; Zhang, Q. Characterization and biocompatibility of nanohybrid scaffold prepared via in situ crystallization of hydroxyapatite in chitosan matrix. *Colloids Surf. B.* **2010**, *81*, 640–647. [CrossRef]
31. Iconaru, S.L.; Ciobanu, C.S.; Predoi, G.; Rokosz, K.; Chifiriuc, M.C.; Bleotu, C.; Stanciu, G.; Hristu, R.; Raaen, S.; Raita, S.M.; et al. Biological and Physico-Chemical Properties of Composite Layers Based on Magnesium-Doped Hydroxyapatite in Chitosan Matrix. *Micromachines* **2022**, *13*, 1574. [CrossRef] [PubMed]
32. Vlădescu, A.; Pârâu, A.; Pană, I.; Cotruț, C.M.; Constantin, L.R.; Braic, V.; Vrânceanu, D.M. In Vitro Activity Assays of Sputtered HAp Coatings with SiC Addition in Various Simulated Biological Fluids. *Coatings* **2019**, *9*, 389. [CrossRef]
33. Stojanović, S.; Mitić, Ž.; Miljković, M.; Rajković, J.; Trajanović, M.; Najman, S. SEM-EDX analysis of BIO-OSS®granules after incubation in cell culture medium. In Proceedings of the III Advanced Ceramics and Applications Conference, 29 September 2014; Atlantis Press: Paris, France, 2016; pp. 259–264. [CrossRef]

34. John, Ł.; Bałtrukiewicz, M.; Sobota, P.; Brykner, R.; Cwynar-Zając, Ł.; Dzięgiel, P. Non-cytotoxic organic–inorganic hybrid bioscaffolds: An efficient bedding for rapid growth of bone-like apatite and cell proliferation. *Mater. Sci. Eng. C* **2012**, *32*, 1849–1858. [CrossRef] [PubMed]
35. Silverstein, R.M.; Webster, F.X.; Kiemle, D.; Bryce, D.L. *Spectrometric Identification of Organic Compounds*, 8th ed.; John Wiley & Sons: Hoboken, NJ, USA, 2014.
36. Law, K.Y. Definitions for Hydrophilicity, Hydrophobicity, and Superhydrophobicity: Getting the Basics Right. *J. Phys. Chem. Lett.* **2014**, *5*, 686–688. [CrossRef]
37. Ansari, Z.; Kalantar, M.; Soriente, A.; Fasolino, I.; Kharaziha, M.; Ambrosio, L.; Raucci, M.G. In-Situ Synthesis and Characterization of Chitosan/Hydroxyapatite Nanocomposite Coatings to Improve the Bioactive Properties of Ti6Al4V Substrates. *Materials* **2020**, *13*, 3772. [CrossRef] [PubMed]
38. Saleem, O.; Wahaj, M.; Akhtar, M.A.; Ur Rehman, M.A. Fabrication and Characterization of Ag-Sr-Substituted Hydroxyapatite/Chitosan Coatings Deposited via Electrophoretic Deposition: A Design of Experiment Study. *ACS Omega* **2020**, *5*, 22984–22992. [CrossRef] [PubMed]
39. Bhowmick, A.; Pramanik, N.; Mitra, T.; Gnanamani, A.; Das, M.; Kundu, P.P. Mechanical and biological investigations of chitosan–polyvinyl alcohol based ZrO_2 doped porous hybrid composites for bone tissue engineering applications. *New J. Chem.* **2017**, *41*, 7524–7530. [CrossRef]
40. Ponnusamy, S.; Subramani, R.; Elangomannan, S.; Louis, K.; Periasamy, M.; Dhanaraj, G. Novel Strategy for Gallium-Substituted Hydroxyapatite/Pergularia daemia Fiber Extract/Poly(N-vinylcarbazole) Biocomposite Coating on Titanium for Biomedical Applications. *ACS Omega* **2021**, *6*, 22537–22550. [CrossRef] [PubMed]
41. Thian, E.S.; Ahmad, Z.; Huang, J.; Edirisinghe, M.J.; Jayasinghe, S.N.; Ireland, D.C.; Brooks, R.A.; Rushton, N.; Bonfield, W.; Best, S.M. The role of surface wettability and surface charge of electrosprayed nanoapatites on the behaviour of osteoblasts. *Acta Biomater.* **2010**, *6*, 750–755. [CrossRef]
42. Predoi, D.; Iconaru, S.L.; Deniaud, A.; Chevallet, M.; Michaud-Soret, I.; Buton, N.; Prodan, A.M. Textural, Structural and Biological Evaluation of Hydroxyapatite Doped with Zinc at Low Concentrations. *Materials* **2017**, *10*, 229. [CrossRef] [PubMed]
43. Battistoni, C.; Casaletto, M.P.; Ingo, G.M.; Kaciulis, S.; Mattogno, G.; Pandolfi, L. Surface characterization of biocompatible hydroxyapatite coatings. *Surf. Interface Anal.* **2000**, *29*, 773–781. [CrossRef]
44. Thian, E.S.; Konishi, T.; Kawanobe, Y.; Lim, P.N.; Choong, C.; Ho, B.; Aizawa, M. Zinc-substituted hydroxyapatite: A biomaterial with enhanced bioactivity and antibacterial properties. *J. Mater. Sci. Mater. Med.* **2013**, *24*, 437–445. [CrossRef] [PubMed]
45. Radovanović, Ž.; Veljović, D.; Jokić, B.; Dimitrijević, S.; Bogdanović, G.; Kojić, V.; Petrović, R.; Janaćković, D. Biocompatibility and antimicrobial activity of zinc(II)-doped hydroxyapatite, synthesized by a hydrothermal method. *J. Serb. Chem. Soc.* **2012**, *77*, 1787–1798. [CrossRef]
46. Ren, F.; Xin, R.; Ge, X.; Leng, Y. Characterization and structural analysis of zinc-substituted hydroxyapatites. *Acta Biomater.* **2009**, *5*, 3141–3149. [CrossRef] [PubMed]
47. Ben-Nissan, B.; Choi, A.H. Sol–gel production of bioactive nano-coatings for medical applications. Part 1: An introduction. *Nanomedicine* **2006**, *1*, 311–319. [CrossRef] [PubMed]
48. Fahami, A.; Beall, G.W.; Betancourt, T. Synthesis, bioactivity and zeta potential investigations of chlorine and fluorine substituted hydroxyapatite. *Mater. Sci. Eng. C Mater. Biol. Appl.* **2016**, *59*, 78–85. [CrossRef]
49. Zhang, J. Biocompatibility and anti-bacterial activity of Zn-containing HA/TiO2 hybrid coatings on Ti substrate. *J. Hard. Tissue Biol.* **2013**, *22*, 311–318. [CrossRef]
50. Tank, K.P.; Chudasama, K.S.; Thaker, V.S.; Joshi, M.J. Pure and zinc doped nano-hydroxyapatite: Synthesis, characterization, antimicrobial and hemolytic studies. *J. Cryst. Growth* **2014**, *401*, 474–479. [CrossRef]
51. Bodhak, S.; Bose, S.; Bandyopadhyay, A. Role of surface charge and wettability on early stage mineralization and bone cell–materials interactions of polarized hydroxyapatite. *Acta Biomater.* **2009**, *5*, 2178–2188. [CrossRef]
52. Korbut, A.; Włodarczyk, M.; Rudnicka, K.; Szwed, A.; Płociński, P.; Biernat, M.; Tymowicz-Grzyb, P.; Michalska, M.; Karska, N.; Rodziewicz-Motowidło, S.; et al. Three Component Composite Scaffolds Based on PCL, Hydroxyapatite, and L-Lysine Obtained in TIPS-SL: Bioactive Material for Bone Tissue Engineering. *Int. J. Mol. Sci.* **2021**, *22*, 13589. [CrossRef]
53. du Pree, I.; Richter, W.; van Papendorp, D.; Joubert, A. hFOB 1.19 osteoblast cells grown on a biomimetic biphasic nanoscaffold: An in vitro evaluation for possible bone tissue engineering. *Biomed. Res.* **2018**, *29*, 2442–2448.
54. Kazimierczak, P.; Vivcharenko, V.; Truszkiewicz, W.; Wójcik, M.; Przekora, A. Osteoblasts response to Novel chitosan/agarose/hydroxyapatite bone scaffold—Studies on mc3t3-e1 and hfob 1.19 cellular models. *Eng. Biomater.* **2019**, *15*, 24–29.
55. Clupper, D.C.; Gough, J.E.; Hall, M.M.; Clare, A.G.; LaCourse, W.C.; Hench, L.L. In vitro bioactivity of S520 glass fibers and initial assessment of osteoblast attachment. *J. Biomed. Mater. Res. A* **2003**, *67*, 285–294. [CrossRef] [PubMed]
56. Bedi, R.S.; Chow, G.; Wang, J.; Zanello, L.; Yan, Y.S. Bioactive materials for regenerative medicine: Zeolite-hydroxyapatite bone mimetic coatings. *Adv. Eng. Mater.* **2012**, *14*, 200–206. [CrossRef]
57. Papon, N.; Courdavault, V.; Clastre, M.; Bennett, R.J. Emerging and emerged pathogenic Candida species: Beyond the Candida albicans paradigm. *PLoS Pathog* **2013**, *9*, e1003550. [CrossRef] [PubMed]
58. Martin, M.V. The use of fluconazole and itraconazole in the treatment of Candida albicans infections: A review. *J. Antimicrob. Chemoth.* **1999**, *44*, 429–437. [CrossRef]

59. Weiner, L.M.; Webb, A.K.; Limbago, B.; Dudeck, M.A.; Patel, J.; Kallen, A.J.; Edwards, J.R.; Sievert, D.M. Antimicrobial-resistant pathogens associated with health care associated infec-tions: Summary of data reported to the National Healthcare Safety Network at the Centers for Disease Control and Prevention, 2011–2014. *Infect. Cont. Hosp. Epidemol.* **2016**, *37*, 1288–1301. [CrossRef]
60. Kullberg, B.J.; Arendrup, M.C. Invasive candidiasis. *N. Engl. J. Med.* **2015**, *373*, 1445–1456. [CrossRef]
61. Predoi, D.; Iconaru, S.L.; Predoi, M.V. Dextran-Coated Zinc-Doped Hydroxyapatite for Biomedical Applications. *Polymers* **2019**, *11*, 886. [CrossRef]
62. Predoi, D.; Iconaru, S.L.; Predoi, M.V.; Buton, N.; Motelica-Heino, M. Zinc Doped Hydroxyapatite Thin Films Prepared by Sol–Gel Spin Coating Procedure. *Coatings* **2019**, *9*, 156. [CrossRef]
63. Maleki-Ghaleh, H.; Siadati, M.H.; Fallah, A.; Koc, B.; Kavanlouei, M.; Khademi-Azandehi, P.; Moradpur-Tari, E.; Omidi, Y.; Barar, J.; Beygi-Khosrowshahi, Y.; et al. Antibacterial and Cellular Behaviors of Novel Zinc-Doped Hydroxyapatite/Graphene Nanocomposite for Bone Tissue Engineering. *Int. J. Mol. Sci.* **2021**, *22*, 9564. [CrossRef]
64. Okada, M.; Oshita, M.; Kataoka, M.; Azuma, Y.; Furuzono, T. Shareability of antibacterial and osteoblastic-proliferation activities of zinc-doped hydroxyapatite nanoparticles in vitro. *J. Biomed. Mater. Res.* **2022**, *110*, 799–805. [CrossRef] [PubMed]
65. Phatai, P.; Prachumrak, N.; Kamonwannasit, S.; Kamcharoen, A.; Roschat, W.; Phewphong, S.; Futalan, C.M.; Khemthong, P.; Butburee, T.; Youngjan, S.; et al. Zinc-Silver Doped Mesoporous Hydroxyapatite Synthesized via Ultrasonic in Combination with Sol-Gel Method for Increased Antibacterial Activity. *Sustainability* **2022**, *14*, 11756. [CrossRef]
66. Iconaru, S.L.; Predoi, M.V.; Motelica-Heino, M.; Predoi, D.; Buton, N.; Megier, C.; Stan, G.E. Dextran-Thyme Magnesium-Doped Hydroxyapatite Composite Antimicrobial Coatings. *Coatings* **2020**, *10*, 57. [CrossRef]
67. Predoi, D.; Ciobanu, C.S.; Iconaru, S.L.; Predoi, S.A.; Chifiriuc, M.C.; Raaen, S.; Badea, M.L.; Rokosz, K. Impact of Gamma Irradiation on the Properties of Magnesium-Doped Hydroxyapatite in Chitosan Matrix. *Materials* **2022**, *15*, 5372. [CrossRef] [PubMed]
68. Cheung, R.C.; Ng, T.B.; Wong, J.H.; Chan, W.Y. Chitosan: An update on potential biomedical and pharmaceutical applica-tions. *Mar. Drugs* **2015**, *13*, 5156–5186. [CrossRef]
69. Pena, A.; Sanchez, N.S.; Calahorra, M. Effects of chitosan on Candida albicans: Conditions for its antifungal activity. *Biomed. Res. Int.* **2013**, *2013*, 527549. [CrossRef]
70. Sudarshan, N.R.; Hoover, D.G.; Knorr, D. Antibacterial action of chitosan. *Food Biotechnol.* **1992**, *6*, 257–272. [CrossRef]
71. Ofudje, E.A.; Adeogun, A.I.; Idowu, M.A.; Kareem, S.O. Synthesis and characterization of Zn-Doped hydroxyapatite: Scaffold application, antibacterial and bioactivity studies. *Heliyon* **2019**, *5*, e01716 31. [CrossRef]
72. de Lima, C.O.; de Oliveira, A.L.M.; Chantelle, L.; Silva Filho, E.C.; Jaber, M.; Fonseca, M.G. Zn-doped mesoporous hydroxyapatites and their antimicrobial properties. *Colloids Surf. B* **2021**, *198*, 111471. [CrossRef]

coatings

MDPI

Article

Study of Argon and Oxygen Mixtures in Low Temperature Plasma for Improving PLA Film Wettability

Joanna Izdebska-Podsiadły

Department of Printing Technology, Institute of Mechanics and Printing, Faculty of Mechanical and Industrial Engineering, Warsaw University of Technology, Konwiktorska 2, 00-217 Warsaw, Poland; joanna.podsiadly@pw.edu.pl; Tel.: +48-22-234-33-57

Abstract: Oxygen (O_2) and argon (Ar) plasma give a significant improvement in the wettability of PLA films. This study investigates the effectiveness of plasma activation with a mixture of these two gases. The study includes contact angle measurements with water and diiodomethane and calculation of surface free energy (SFE) together with its polar and dispersion components. In addition, a chemical analysis of the surface, surface roughness, weight loss and the change in tensile strength were examined. As a result of the study, it was found that the use of a mixture of oxygen and argon during the plasma activation of the polylactide film gives better improvement in wettability than the use of pure gases. Moreover, the use of a mixture of these gases in equal proportions turned out to be the most effective, providing the highest value of the SFE and its polar component, as well as the lowest value of the water contact angle. Furthermore, plasma activation with this gas mixture results in reduced surface etching compared to other gas compositions, which manifests itself in lower weight reduction and an insignificant change in tensile strength.

Keywords: biodegradable polymers; PLA films; plasma activation; argon plasma; oxygen plasma; hydrophilicity; wettability

Citation: Izdebska-Podsiadły, J. Study of Argon and Oxygen Mixtures in Low Temperature Plasma for Improving PLA Film Wettability. *Coatings* **2023**, *13*, 279. https://doi.org/10.3390/coatings13020279

Academic Editor: David Schaubroeck

Received: 18 December 2022
Revised: 20 January 2023
Accepted: 23 January 2023
Published: 26 January 2023

1. Introduction

Polylactide (PLA) is one of the most popular biodegradable plastics [1]. It is a good eco-friendly alternative to traditional plastics, which are currently the source of much debate regarding their use due to the problem of environmental pollution [2]. The question of the use of plastics is no longer just a matter of post-consumer waste or depleting oil resources, but also the threat of microplastics, which are found in the seas, oceans, soil, or in food products, cosmetics and even human blood [3,4]. Therefore, it seems important to replace plastics with biodegradable plastics, which are completely decomposed by microorganisms (bacteria and fungi) through aerobic or anaerobic processes into carbon dioxide or methane, respectively, and water and biomass. Furthermore, polylactide, besides being biodegradable, is produced from renewable raw materials [5]. PLA is mainly used in the production of disposable consumer goods in the packaging industry, e.g., loose-fill packaging, compost bags, food packaging and disposable tableware [6] and in the textile industry, e.g., disposable clothing. It also has biomedical applications such as surgical threads, in the production of implants [7], scaffolds for bone regeneration [8] or drug delivery microsphere [9]. At the same time, the properties of polylactide depend on the constituent isomers, molecular weight, processing temperature and annealing time [10].

Polylactide is a fairly hydrophobic material, as the water contact angle of unmodified PLA is 70–80° [11]. Moreover, PLA films, like all polymeric materials, are non-absorbent materials, which means that they require surface preparation before printing and finishing processes [12,13]. Both effective improvement of wettability and cleaning of the material's surface are possible through the use of plasma activation processes [14–16]. In addition, plasma activation also results in improved adhesion [17], as well as sterilization of the material [18]. Only low-temperature plasma, also called non-thermal, cold, or non-equilibrium

plasma, is applicable for modifying polymeric materials due to their thermal sensitivity. Low-temperature plasma activation, depending on the device, can be carried out as low-pressure plasma (pressures in the range of 10–75 Pa are the most commonly used) or atmospheric plasma [18,19]. With low pressures, it is easier to control the plasma reaction because the discharge is more stable [20].

A number of different gases are used for plasma activation of polymers, such as air, oxygen (O_2), helium (He), argon (Ar), nitrogen (N_2), ammonia (NH_3), carbon dioxide (CO_2), tetrafluoromethane (CF_4), etc. The type of gas used during plasma activation determines the physical and chemical properties of the surface being modified [14,16]. At the same time, the use of reactive gases, among which oxygen is the most commonly used, leads to chemical changes, while the use of inert gases, of which argon is a representative, leads mainly to crosslinking [11,12,21]. Previous research [22–25] demonstrated the beneficial effect of oxygen plasma on PLA films, while other reported works [11,26,27] described the effect of argon plasma on PLA. Considering good results that can be obtained with both gases and taking into account the significant differences in the changes occurring in the material during plasma activation, this scientific work studies the effects of their mixture on polylactide films. Gas mixtures including oxygen and argon have important applications in thermal plasma processes [28]. Moreover, the effect of gas mixtures has been studied for traditional plastics such as low-density polyethylene (LDPE) [29,30], polyethylene terephthalate (PET) [31] and polyethersulfone (PES) [32]. Due to the significant influence of the type of polymer [22] and the parameters of the activation process [33] on the activation efficiency and given the growing importance of PLA for environmental reasons, this study concentrates on cold plasma activation with a mixture of gases for PLA films, which, to the author's knowledge, has not been studied so far.

Plasma activation of polymers is mainly aimed at changing their wettability, achieving the required adhesion and cleaning the surface, which is achieved by changing the chemical structure through functionalization with oxygen-containing functional groups and changing the roughness through etching or ion bombardment [21,34–36]. The type of functional groups generated on the polymer surface depends on the gas used for plasma activation [20,37]). Evaluation of the chemical changes in the surface layer and identification of the types of functional groups that appear is commonly performed by Fourier transform infrared (FTIR) spectroscopy and X-ray photoelectron spectroscopy (XPS). Oxygen-containing functional groups are highly polar groups, and therefore oxygen-containing polymers will exhibit better wettability than oxygen-free polymers [38].

Wettability, or the ability of a surface to be wetted by various liquids, is one of the most important surface properties determining the ability to further coat, bond, print, laminate or otherwise refine polymeric materials. A common way to determine the wettability of a polymeric material is to measure the contact angle of the polymer using a drop of water planted on its surface [16,39,40].

An important parameter affecting the contact angle is the surface roughness [41], and it has a significant effect if $R_a \geq 100$ nm. Moreover, the influence depends on the magnitude of the contact angle, and for hydrophilic surfaces for which it is less than 60°, an increase in roughness will result in a decrease in the contact angle [42]. Atomic force microscopy (AFM) and confocal microscopy can be used to characterize surface topography and roughness.

A parameter closely related to the contact angle is the surface free energy (SFE). Various methods are available for determining SFE values, including Fowkes, Owens–Wendt, van Oss–Chauhury–Good, Neumann, Zisman, for which knowledge of the contact angles of the surface layer of the polymeric material with at least two measuring fluids is required. The Owens–Wendt method is chosen here as being the most applicable [43]. The calculation of SFE and its polar and dispersion components makes it possible to determine the polar or non-polar nature of interactions at the liquid/solid boundary and the hydrophilic or hydrophobic nature of the surface [44]. High values of SFE and its polar component are important for printing, coating, and bonding processes, for example, as proper wetting

of a substrate with ink, requires that the substrate's SFE be much higher than the surface tension of the liquid [45].

The purpose of this research is to determine the effect of a mixture of oxygen and argon on improving the wettability of plasma-activated PLA films and to determine how the gas proportions affect the effects of plasma activation. In addition, the chemical and physical changes occurring during the modification are identified and the optimum proportion of each gas for obtaining the highest hydrophilicity of plasma-activated PLA film is determined.

These studies supplement the state of knowledge in the field of low pressure plasma treated PLA. This work has particular significance due to the fact that PLA is a biodegradable material which is an attractive alternative to currently dominant plastic materials which are increasingly controversial for their environmental impact.

2. Materials and Methods

2.1. Materials

Commercially available, biodegradable and compostable EarthFirst PLA BCP film (Plastic Suppliers, Inc., EarthFirst, Ghent, Belgium) was used for the study. It is a high-gloss transparent film dedicated to packaging purposes with FDA certificates for food contact and compostability certificates in accordance with the EN 13432 standard. The material used was 50 µm thick with the following properties: surface free energy 38 mJ/m^2, gloss 125 G.U. (60°), haze 7%, oxygen transmission rate O_2TR = 29 $cc/100\ in^2/24$ h, moisture vapor transmission rate MVTR = 10 $g/100\ in^2/24$ h and ultimate tensile strength MD = TD = 55 MPa. The film was supplied by the manufacturer in the form of A4 sheets, which were cut to 105 mm × 148 mm format before the plasma activation process. The film samples were conditioned in a climatized laboratory room in standard ambient conditions: temp. 23.0 ± 0.5 °C, relative humidity (RH) 50.0 ± 1.5% (ISO 187:1990) before treatment, moreover, all test procedures were carried out under such conditions.

Two pure industrial gases were used in the study: oxygen O_2 (99.8%) and argon (99.998%). The gases were compressed in cylinders at 200 bar, stored and operated in standard ambient conditions.

2.2. Plasma Activation

PLA films were exposed to low-pressure plasma in a half-automated vacuum chamber with a Diener Nano low-pressure plasma system basic unit (Diener Electronic, Altensteig, Germany). Process parameters were as follows: radio frequency 40 kHz, power pressure 0.4 mbar (40 Pa), gas supply process pressure 0.3 mbar (30 Pa), pumping off pressure 0.2 mbar (20 Pa), control pressure via gas, venting time 1 min, gas supply time 2 min and plasma activation time 4 min. The process parameters were selected on the basis of previous studies [25,27,33]. The temperature in the chamber was close to that in a climatized laboratory room, as in this process the plasma temperature hardly rises compared to the non-excited gas. Two gases, oxygen and argon, were used for testing, with different proportions of these gases used during activation, namely: 100% Ar, 75% Ar + 25% O_2, 50% Ar + 50% O_2, 25% Ar + 75% O_2, 100% O_2.

2.3. Contact Angle Measurements and Calculation of Surface Free Energy

The contact angles (CA) were measured with Tangent method 2 [27], using a DSA 100 drop shape analysis system (Krüss, Hamburg, Germany). Two measuring fluids, distilled water and diiodomethane 99% CH_2I_2 (Sigma-Aldrich, Taufkirchen, Germany), were used for the measurements. Sessile drops of the liquids were deposited on the film with needles of 0.5 mm diameter and the drop shape analysis was done 15 s. after the drop deposition. All measurements were done in stable environmental conditions (temp. 23.0 ± 1.0 °C). Fifteen contact angle measurements were made for each sample both before activation and immediately after plasma activation. The surface free energy of PLA film

and its polar and dispersive components were calculated with the Owens–Wendt method. Formulas for calculating the SFE (1) and its components (2)–(3) are presented below [46,47].

$$\gamma_S = \gamma_S^d + \gamma_S^p \tag{1}$$

$$\left(\gamma_S^d\right)^{0.5} = \frac{\gamma_d(cos\Theta_d + 1) - \sqrt{\left(\gamma_d^p/\gamma_w^p\right)}\gamma_w(cos\Theta_w + 1)}{2\left(\sqrt{\gamma_d^d} - \sqrt{\gamma_d^p(\gamma_w^d/\gamma_w^p)}\right)} \tag{2}$$

$$\left(\gamma_S^p\right)^{0.5} = \frac{\gamma_w(cos\Theta_w + 1) - 2\sqrt{\gamma_S^d\gamma_w^d}}{2\sqrt{\gamma_w^p}} \tag{3}$$

where γ_S^d is the dispersive component of SFE of the examined films, γ_S^p is the polar component of SFE of the films, γ_d is the SFE of diiodomethane, γ_d^d is the dispersive component of diiodomethane SFE (= 48.5 mJ/m^2), γ_d^p is the polar component of diiodomethane SFE (= 2.3 mJ/m^2), γ_w is the SFE of water, γ_w^d is the dispersive component of water SFE (= 21.8 mJ/m^2), γ_w^p is the polar component of water SFE (= 51 mJ/m^2), Θ_d is the contact angle of diiodomethane and Θ_w is the water contact angle.

2.4. Chemical and Topographic Surface Analysis

Chemical analysis of the surface was carried out by X-ray photoelectron spectroscopy. XPS tests were performed on a 100 SSX ESCA Spectrometer (Surface Science Laboratories Inc., Mountain View, AB, Canada). A monochromatic Al K α radiation was used with energy 9 kV, 19 mA. Measuring spot sizes were appropriately 0.25 mm × 1.0 mm, 0.15 mm × 0.8 mm, 0.15 mm × 0.1 mm. Overview spectra parameters were as follows: passing energy 150 eV, resolution/channel: 0.16 eV, step size/measurement point 0.5 eV, neutralizer energy 0.5 eV. Meanwhile, the binding spectra settings were following: matching energy: 50 eV, resolution/channel: 0.054 eV, step size/measurement point: 0.1 eV, neutralizer energy: 0.5 eV. The decomposition of the carbon and oxygen peak into corresponding components was performed with CASA XPS software (version 2.3.15, Casa Software Ltd., Teignmouth, UK) [27,48].

Surface topographic analysis and roughness measurements were made using the Sensofar Plμ Neox microscope optical profiler (Sensofar-Tech, SL., Terrassa, Spain). Topographic images were taken at three different locations on the sample using the following microscope settings: lens 50 × 0.95 N, white light, measured area 768 × 576 pixels (254.64 × 190.90 μm^2), layer thickness 15.2 μm and threshold 15%. The roughness was determined using Sensofar software (Sensofar-Tech, SL., Terrassa, Spain).

2.5. Weight Loss and Change in Mechanical Properties

Weight loss was determined from weight measurements taken immediately before and after plasma activation of the samples using a semi-microbalance Sartorius LE 225D-OCE (Sartorius, Göttingen, Germany). Samples with dimensions of 50 mm × 50 mm were used for the analysis. The weight loss value was calculated from 4 measurements.

The tensile strength of the film was tested using a static testing machine Roell (Zwick-Roell GmbH & Co. KG, Ulm, Germany) and testXpert II software. The test was conducted in accordance with ISO 527-3. Measurements were performed on 5 samples per film, both for treated and untreated films.

2.6. Statistical Analysis

Statistical analysis was done using a data analysis toolkit in Excel (Office 365, Microsoft, Redmont, WA, USA). ANOVA test was used to analyze the data. In order to check which group averages differed significantly, a Tukey–Kramer post-hoc test was performed. In addition, as roughness and contact angle are a pair of parameters that can have a significant

impact on each other's values, their correlation was verified using the r-Pearson test. Significant differences were assumed with a significance level greater than 95% ($p < 0.05$).

3. Results and Discussion

3.1. Analysis of Changes in Water Contact Angle and Surface Roughness

The change in water contact angle (WCA) is the primary parameter used to analyze changes in wettability. As roughness may have a significant effect on WCA values, changes in these two parameters resulting from plasma activation of the PLA film are analyzed together in this chapter. The changes in contact angle and roughness are shown in Figures 1 and 2, respectively.

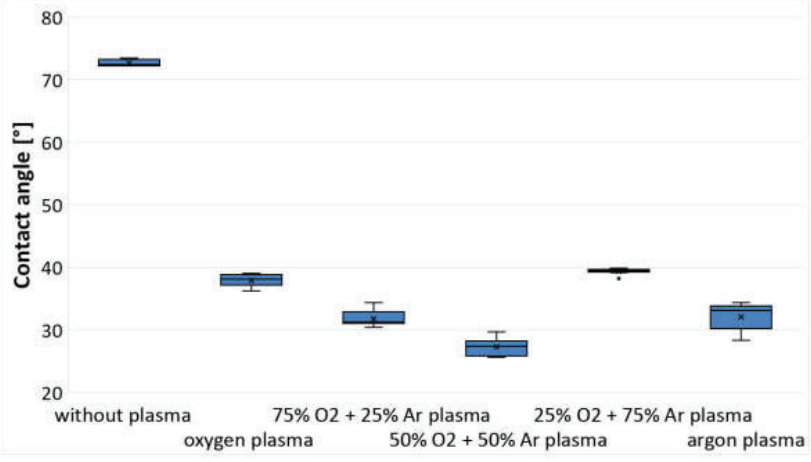

Figure 1. Values of water contact angle of PLA film, unmodified and plasma modified, using different gas compositions (box plot chart for 15 measurements, where: upper whisker—maximum, lower whisker—minimum, box height shows 1st and 3rd quartile and includes median).

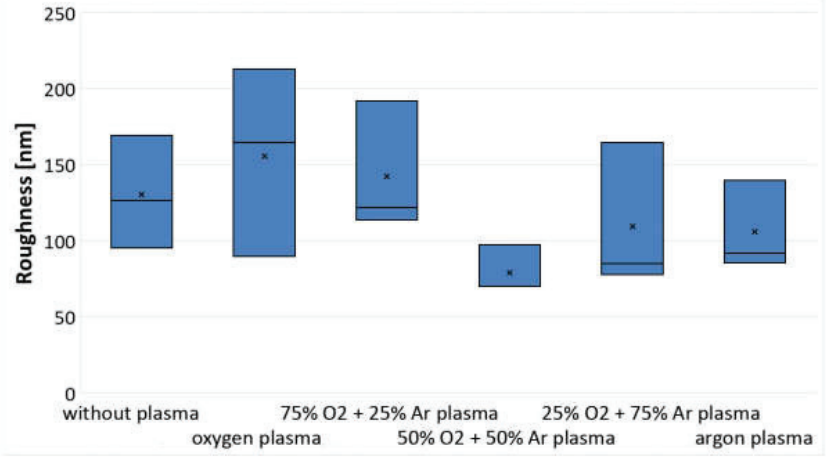

Figure 2. Values of roughness of PLA film, unmodified and plasma modified, using different gas compositions (box plot chart for 3 measurements, where box height shows maximum, minimum and median).

As a result of plasma activation, a change was observed from a nearly hydrophobic (the value of the contact angle before plasma activation was 72.6°) to a hydrophilic material (the values of the contact angle after plasma activation were in the range of 27.3–39.4°) (Figure 3). Using one-way analysis of variance (ANOVA), a significant effect of plasma activation on the obtained water contact angle values was confirmed. The result of the ANOVA test for contact angle measurements ($F(5,84) = 2.323$, $p = 9.4 \times 10^{-91}$) indicates significant differences between group averages. At the same time, the best wettability was obtained for the film modified with a mixture of gases, where their proportion was equal, as confirmed by an analysis of the absolute values of the mean differences. Furthermore, the Tukey–Kramer test confirmed statistically significant differences between the averages of all groups with the exception of the activation carried out with 75% O_2 + 25% Ar and 100% Ar plasma. Similar conclusions regarding the positive effect of argon in the gas mixture used for plasma activation were made by Kim et al. [29], Fang et al. [31] and Saxena et al. [32]. However, for other polymeric materials (LDPE film, PET film and PES membranes, respectively), they showed that different proportions of gases in the mixture give the best results (90%, 99.7%–99.8%, and 40% Ar, respectively).

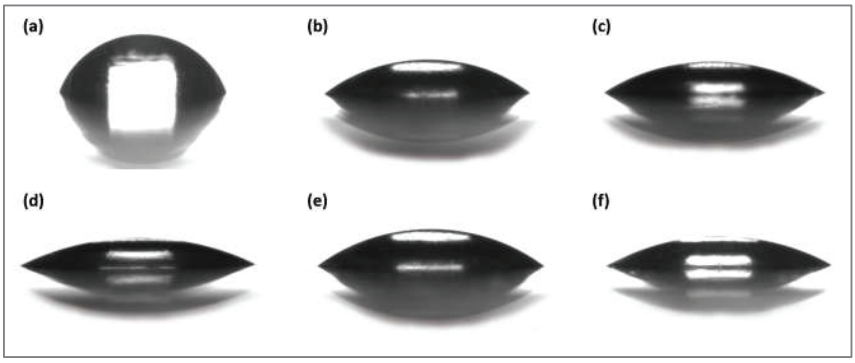

Figure 3. Water contact angle of (**a**) non-activated PLA film, (**b**) oxygen plasma-activated PLA film, (**c**) plasma-activated PLA film with a gas mixture of 25% Ar + 75% O_2, (**d**) plasma-activated PLA film with a gas mixture of 50% Ar + 50% O_2, (**e**) plasma-activated PLA film with a gas mixture of 75% Ar + 25% O_2, (**f**) argon plasma-activated PLA film.

One-way analysis of variance showed no statistically significant differences between group averages for roughness ($F(5,12) = 3.106$, $p = 0.318$). However, although the F-test result was not statistically significant, it is worth noting that the plasma-activated film with 50% Ar + 50% O_2 gas had the lowest surface roughness (Figure 2), indicating that the contact angle was indeed the lowest. The remaining samples, especially those modified by plasma with 100% and 75% oxygen, were characterized by high roughness, which theoretically could significantly affect the value of the contact angle by lowering it, but this was not confirmed by the statistical analysis carried out. Verification of whether there was a significant relationship between water contact angle and roughness was carried out using the r-Pearson test. The result obtained, with $p = 0.547$ ($p > 0.05$), does not support a statistically significant correlation between the two parameters. Therefore, roughness has no confirmed influence on the contact angle values obtained in the case studied.

Moreover, the topographical changes of the material's surface prove that plasma activation led not only to the functionalization of the surface and its etching, but also to the cleaning of the surface of impurities formed on the surface of the produced film [16]. Surface topography of the films is presented in Figure 4.

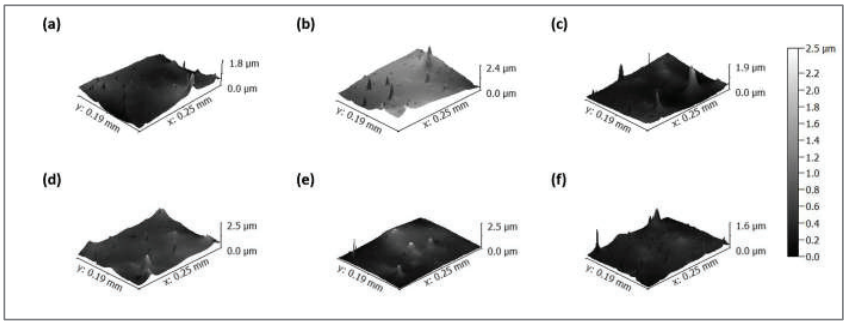

Figure 4. Surface topography of (**a**) non-activated PLA film, (**b**) oxygen plasma-activated PLA film, (**c**) plasma-activated PLA film with a gas mixture of 25% Ar + 75% O_2, (**d**) plasma-activated PLA film with a gas mixture of 50% Ar + 50% O_2, (**e**) plasma-activated PLA film with a gas mixture of 75% Ar + 25% O_2, (**f**) argon plasma-activated PLA film.

3.2. Analysis of Surface Free Energy and Its Components

Based on measurements of the contact angle with water and diiodomethane, the values of SFE and its components were determined using the Owens–Wendt equation. The results obtained are shown in Figure 5.

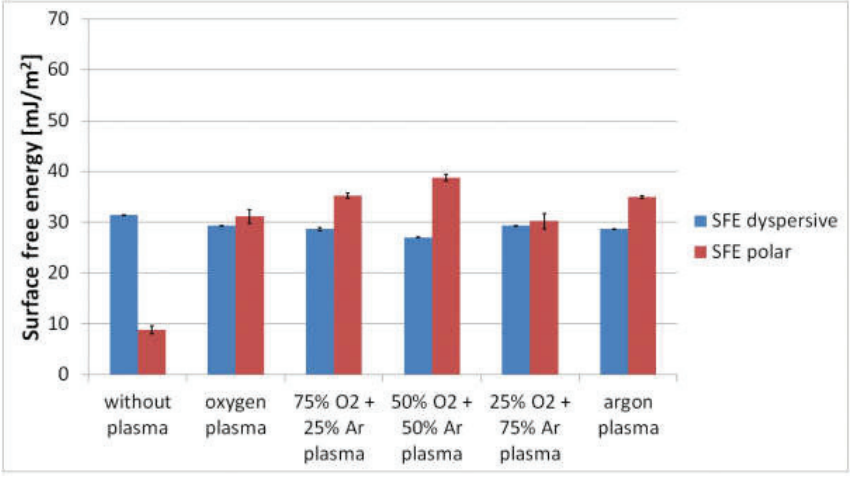

Figure 5. Values of surface free energy and its polar and dispersive components for unmodified and plasma-modified PLA film using different gas compositions.

Plasma activation resulted in a significant increase in the values of SFE (from 40.1 to a maximum of 65.8 mJ/m^2) and its polar component (from 8.8 to a maximum of 38.7 mJ/m^2) while slightly reducing its dispersive component (from 31.4 to a maximum of 27.0 mJ/m^2). The obtained values of SFE and its polar component confirm that the greatest improvement in hydrophilicity can be achieved using plasma activation with oxygen and argon in equal proportions. Moreover, the results obtained testify to the correct choice of activation process parameters and to high efficiency in improving the wettability of PLA films for both plasma with oxygen, argon and a mixture of these gases.

In comparison, Jordá-Vilaplana et al. [49] obtained similar but still lower SFE values (58.9 mJ/m^2) only for air atmospheric plasma activation of PLA film using the most aggressive parameters, while for other parameters the values were much lower. On the other hand, Moraczewski et al. [22] obtained an SFE value slightly higher than ours at over

70 mJ/m^2 for PLA film activated with pure oxygen, although using an activation time of as much as 30 min, but when the time was reduced to 3 min, the result was already much worse (SFE of about 53 mJ/m^2).

3.3. Surface Chemistry Analysis

Although the water contact angle, as mentioned earlier, depends on the surface roughness, it is primarily a function of surface chemistry [34].

XPS analysis was performed for unmodified film, modified with pure argon and pure oxygen, and a mixture of these two gases at 50% Ar and 50% O_2 (Figure 6). Samples activated with a mixture of gases in different proportions were omitted, as their wettability was lower than that of the 50% Ar + 50% O_2 samples. The composition of the surface layer of the samples was determined from the detailed analysis of the Cls and O1s peaks of the XPS spectra (Table 1).

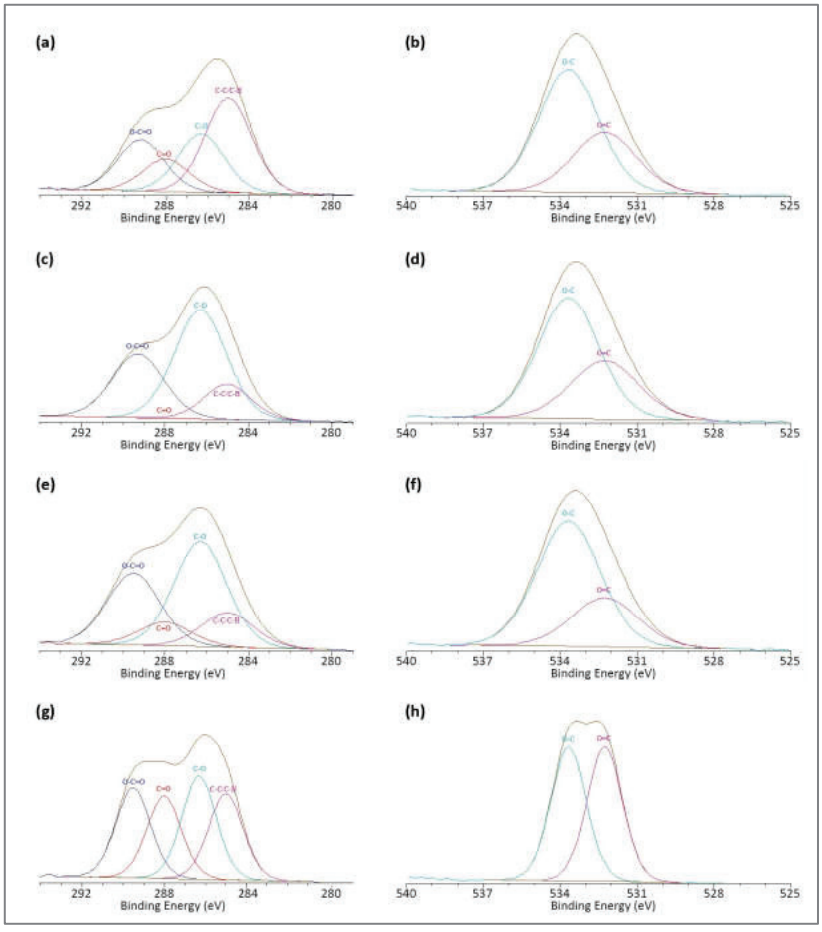

Figure 6. Carbon and oxygen XPS signals of PLA films: (**a**) Cls peaks of untreated film, (**b**) Ols peaks of untreated film, (**c**) Cls peaks of 50% O_2 + 50% Ar plasma treated film, (**d**) Ols peaks of 50% O_2 + 50% Ar plasma treated film, (**e**) Cls peaks of 100% Ar plasma treated film, (**f**) Ols peaks of 100% Ar plasma treated film, (**g**) Cls peaks of 100% O_2 plasma treated film, (**h**) Ols peaks of 100% O_2 plasma treated film.

Table 1. Various components (in area %) of Cls and Ols peaks of XPS spectra of PLA films untreated and plasma treated with different gas compositions.

PLA Films	C1s Components (%)				O1s Components (%)	
	C-C/C-H 285 eV	C-O 286.3 eV	C=O 288 eV	O-C=O 289.1 eV	O=C 532.25 eV	O-C 533.66 eV
Without plasma	39.9	24.6	13.8	21.7	34.1	65.9
50% O_2 + 50% Ar plasma	15.6	53.3	0	31.1	34.8	65.2
100% Ar plasma	14.6	44.8	9.9	30.7	29.2	70.8
100% O_2 plasma	23.8	28.5	22.8	25.0	50.1	49.9

The results confirm that plasma activation, regardless of the type of gas or gas mixture used, led to noticeable chemical changes on the sample surface. At the same time, the type of gas had a significant effect on the changes occurring in the surface layer of the polymer. The use of argon during activation led to the breaking of C-C and C-H bonds of the polymer chain and the formation of free radicals. Carbon radicals, as highly unstable elements, can react with one another leading to cross-linking of polymer chains and react with air when the sample is removed from the chamber after modification [11,16]. The results testify to significant oxidation of the sample after modification, both those modified with pure argon and with a mixture of oxygen and argon. Primarily hydroxyl and carboxyl groups were formed on the surface. In contrast, the use of oxygen during activation led to the formation of both hydroxyl, carboxyl and carbonyl groups. The hydroxyl group is polar, which makes it a suitable hydrogen bond donor. Not only does it improve water wettability, but the concentration of OH groups can also have a significant effect on the strength of adhesive bonds [50]. An example is the effect of hydroxyl groups from cellulose nanocrystals [51] on the adhesion properties of composite films [52]. In summary, the formation of polar compounds on the surface of a polymer has a significant impact on its functional properties and thus on its industrial applications, which can be adequately achieved by plasma activation and appropriately selected parameters. A higher number of oxygen-containing functional groups on the sample surface in the case of activation with a non-zero amount of argon is reflected in slightly lower water contact angle values and higher SFE values compared to those modified by pure oxygen plasma.

3.4. Analysis of Changes in Mass and Strength Properties

In addition to the changes in roughness indicative of the surface etching processes occurring during plasma activation, a removal of material from the surface can be identified by changes in mass [35]. Changes in sample mass and tensile strength are shown in Figures 7 and 8. In addition, Figure 9 shows an example of stress-strain carves obtained during PLA film strength tests.

Gas composition has a significant effect on the weight change of plasma-activated PLA film samples, as evidenced by the results of the ANOVA test ($(F(4,5) = 5.192$, $p = 0.016)$. Furthermore, the Tukey–Kramer test confirmed statistically significant differences between the means of all groups. Moreover, it was observed that the use of oxygen during plasma activation has a significant effect on mass loss (Figure 7). Increasing the proportion of oxygen in the gas mixture during the activation process led to greater mass loss. In the case of activation with pure argon, the mass loss was significantly lower. This is due to the fact that during plasma activation there is etching of the material, while with argon activation it is mainly just cleaning. Nevertheless, the values obtained do not indicate significant degradation of the material, although undoubtedly oxidation is accompanied more by chain scission than crosslinking [12,53]. Results by Kim et al. [29] confirm that cross-linking depends on the ratio of argon to oxygen and that pure argon plasma-treated samples showed the highest degree of cross-linking.

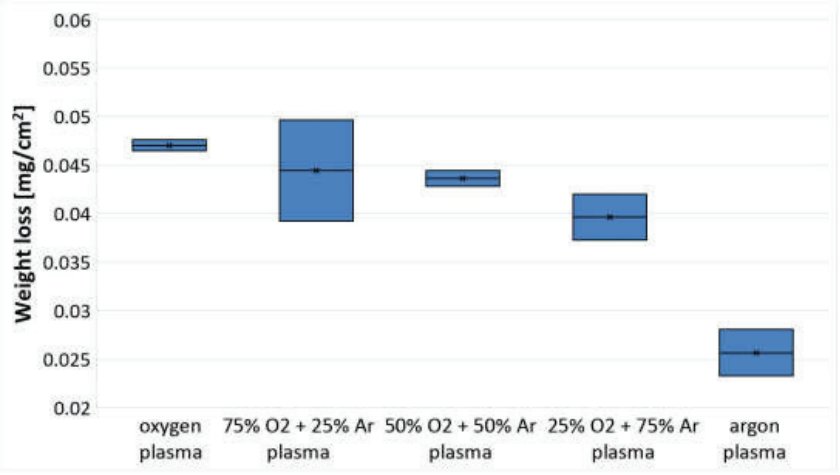

Figure 7. Changes in sample weight as a result of plasma modification of PLA with different gases and their mixtures (box plot chart for 2 measurements, where box height shows minimum, average and maximum).

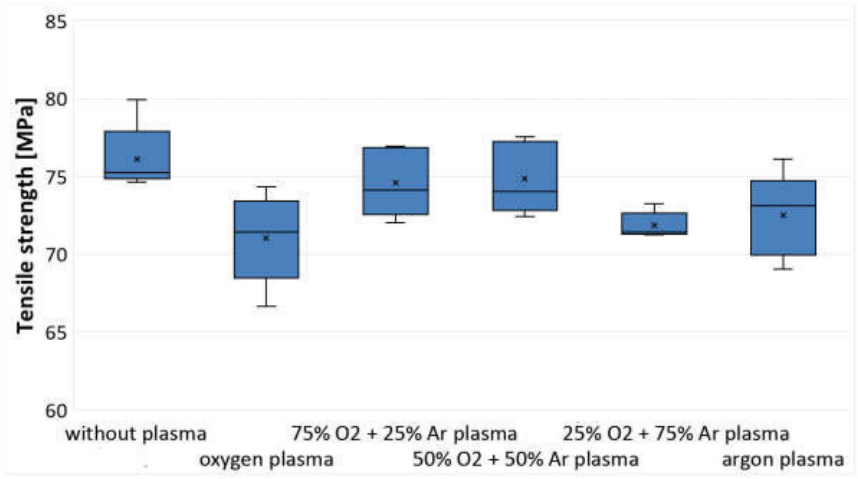

Figure 8. Changes in tensile strength as a result of plasma modification of PLA with different gases and their mixtures (box plot chart for 5 measurements, where: upper whisker—maximum, lower whisker—minimum, box height shows 1st and 3rd quartile and includes median).

The lack of significant degradation is also confirmed by the tensile strength results (Figure 8). It is true that activation regardless of the type of gas used led to a deterioration of the material's tensile properties, but these changes were not significant enough to affect the application aspects of the material. The results of the ANOVA test ((F(5,24) = 2.621, $p = 0.011$) confirm the significant differences in tensile strength values. Moreover, slightly worse resistance was obtained for plasma-activated materials using pure oxygen or mixtures of gases 25% O_2 + 75% Ar compared to pure argon or other mixtures of gases. This is evidenced by the results of the Tukey–Kramer test, which confirmed statistically significant differences only between, first, the averages of non-activated and plasma-activated films involving pure oxygen and, second, non-activated and plasma-activated films involving 25% O_2 + 75% Ar gases. Studies by other researchers [35] confirm the minor effect of cold

plasma on tensile strength, where both a slight decrease and a slight increase in tensile strength were recorded depending on the type of plasma and the type of polymer material.

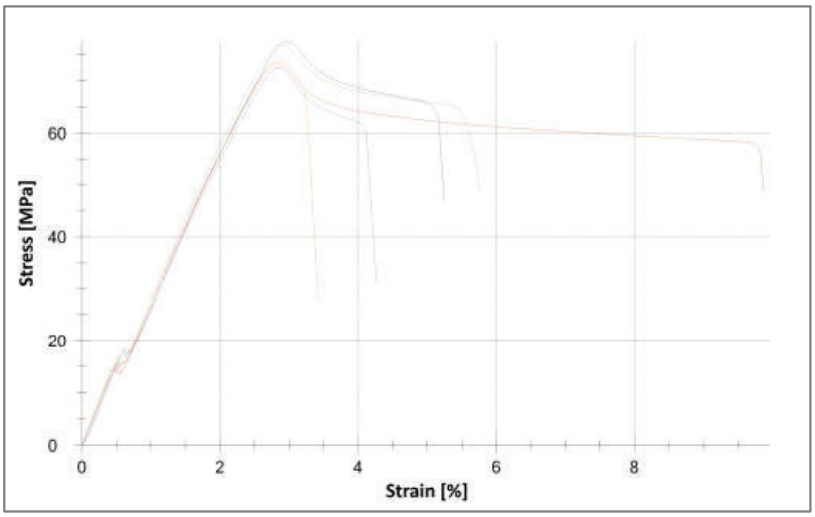

Figure 9. Stress-strain curves of plasma modified PLA with gases mixtures 50% Ar + 50% O_2 (lines correspond to 5 sample measurements).

Sample weight loss due to etching accompanying plasma activation of PLA film can be caused by chemical processes such as cleavage of chemical bonds, scission of polymer chains, or chemical degradation of film components by the influence of free radicals, or physical processes which include the removal or re-aggregation of low molecular weight components on the polymer surface [35]. The results obtained (Figure 7) suggest that the weight loss is related to physical processes. The higher weight loss of plasma-modified samples with a higher proportion of oxygen may indicate that during oxygen plasma activation, products poorly bound to the sample surface were formed on the modified PLA surface and were removed [22,25,49].

4. Conclusions and Future Perspectives

The results indicate that the use of a mixture of oxygen and argon during plasma activation of the polylactide film yields a superior improvement in hydrophilicity than the use of pure gases. The use of a 50% O_2 + 50% Ar gas mixture during plasma activation enables the best wettability of PLA films, as evidenced by the highest value of SFE and its polar component and the lowest value of water contact angle. Only slightly worse wettability results were obtained for the gas mixture of 75% O_2 + 50% Ar. Nevertheless, in this case there was a greater negative effect of plasma activation on surface roughness, weight loss and tensile strength.

Moreover, the use of a gas composition of 50% O_2 + 50% Ar during plasma activation results in the lowest surface roughness. In addition, the observed significant improvement in wettability is due to the significant number of highly polar groups, and the number of oxygen-containing functional groups is much higher than for activation with oxygen alone.

In addition, the proportion of oxygen during plasma modification led to increased weight loss compared to modification with argon or its higher proportion in the mixture. However, the use of a mixture of oxygen and argon leads to a reduction in weight loss, as well as a favorable effect on the strength properties of the modified film. Nevertheless, as a result of plasma activation, regardless of the type of gas, a slight reduction in tensile strength was observed, but it was too small to affect the applicability of PLA films.

Polylactide is not only important in medical applications, but it is also a major biodegradable plastic with industrial applications and could become the polymer of the XXI century, once its prices are further aligned with other plastics and when waste regulations are even further tightened. PLA helps reduce the problem of post-consumer waste due to its biodegradability and possibly even compostability in case of some PLA-based plastics. It is now widely used in 3D printing, where its market share is increasing year on year, and is finding growing use in packaging, both in flexible and rigid packaging applications. PLA is an alternative packaging material to PET, polystyrene (PS), polyvinyl chloride (PVC) and cellulosic polymers and has applications in multilayer compositions. In packaging applications, it can be used in the form of films and laminates as well as extruded and thermoformed packaging. Packaging generally requires printing, which involves appropriate wetting of the printing inks and their adhesion to the substrate, while lamination processes require appropriate adhesion as well—thus both printing and lamination require modification of the polylactide. As shown in this work, PLA modification can be efficiently achieved through a low-temperature plasma activation process, which is environmentally friendly—it does not generate chemical waste, allows the desired polymer surface properties to be obtained by adjusting the process parameters, and is useful for temperature-sensitive materials, both in the form of flat films and complex spatial details.

Funding: This research was funded by the European Union within the European Social Fund from WUT Development Program.

Institutional Review Board Statement: Not applicable.

Informed Consent Statement: Not applicable.

Data Availability Statement: Not applicable.

Acknowledgments: The author would like to thank Edgar Dörsam and IDD team from Institute of Printing Science and Technology, Darmstadt University of Technology, for providing access to the laboratory and equipment, and excellent work atmosphere. The author would also like to thank Dipl.-Ing. Karl Kopp from Darmstadt University of Technology, Eduard-Zintl-Institute of Inorganic and Physical Chemistry, Surface Chemistry of Nanomaterials Group for his great support with XPS Analysis.

Conflicts of Interest: The author declares no conflict of interest.

References

1. Kost, B.; Basko, M.; Bednarek, M.; Socka, M.; Kopka, B.; Łapienis, G.; Biela, T.; Kubisa, P.; Brzeziński, M. The influence of the functional end groups on the properties of polylactide-based materials. *Prog. Poly. Sci.* **2022**, *130*, 101556. [CrossRef]
2. Shlush, E.; Davidovich-Pinhas, M. Bioplastics for food packaging. *Trends Food Sci. Technol.* **2022**, *125*, 66–80. [CrossRef]
3. Khan, N.A.; Khan, A.H.; López-Maldonado, E.A.; Alam, S.S.; López López, J.R.; Méndez Herrera, P.F.; Mohamed, B.A.; Mahmoud, A.E.D.; Abutaleb, A.; Singh, L. Microplastics: Occurrences, treatment methods, regulations and foreseen environmental impacts. *Environ. Res.* **2022**, *215*, 114224. [CrossRef] [PubMed]
4. Leslie, H.A.; van Velzen, M.J.M.; Brandsma, S.H.; Vethaak, A.D.; Garcia-Vallejo, J.J.; Lamoree, M.H. Discovery and quantification of plastic particle pollution in human blood. *Environ. Int.* **2022**, *163*, 107199. [CrossRef] [PubMed]
5. Vroman, I.; Tighzert, L. Biodegradable Polymers. *Materials* **2009**, *2*, 307–344. [CrossRef]
6. Jasim Ahmed, J.; Mulla, M.Z.; Al-Zuwayed, S.A.; Joseph, A.; Auras, R. Morphological, barrier, thermal, and rheological properties of high-pressure treated co-extruded polylactide films and the suitability for food packaging. *Food Packag.* **2022**, *32*, 100812. [CrossRef]
7. Škrlová, K.; Rybková, Z.; Stachurová, T.; Zagora, J.; Malachová, K.; Měřinská, D.; Gabor, R.; Havlíček, M.; Muñoz-Bonilla, A.; Fernández-García, M.; et al. Long-term antimicrobial effect of polylactide-based composites suitable for biomedical use. *Polym. Test.* **2022**, *116*, 107760. [CrossRef]
8. Wang, M.; Favi, P.; Cheng, X.; Golshan, N.H.; Ziemer, K.S.; Keidar, M.; Webster, T.J. Cold atmospheric plasma (CAP) surface nanomodified 3D printed polylactic acid (PLA) scaffolds for bone regeneration. *Acta Biomater.* **2016**, *46*, 256–265. [CrossRef]
9. Chavan, Y.R.; Tambe, S.M.; Jain, D.D.; Khairnar, S.V.; Amin, P.D. Redefining the importance of polylactide-co-glycolide acid (PLGA) in drug delivery. *Ann. Pharm. Françaises* **2022**, *80*, 603–616. [CrossRef]
10. Nampoothiri, K.M.; Nair, N.R.; John, R.P. An overview of the recent developments in polylactide (PLA) research. *Bioresour. Technol.* **2010**, *101*, 8493–8501. [CrossRef]
11. Luque-Agudo, V.; Hierro-Oliva, M.; Gallardo-Moreno, A.M.; González-Martín, M.L. Effect of plasma treatment on the surface properties of polylactic acid films. *Polym. Test.* **2021**, *96*, 107097. [CrossRef]

12. Spyrides, S.M.M.; Alencastro, F.S.; Guimaraes, E.F.; Bastian, F.L.; Simao, R.A. Mechanism of oxygen and argon low pressure plasma etching on polyethylene (UHMWPE). *Surf. Coat. Technol.* **2019**, *378*, 124990. [CrossRef]
13. Izdebska, J. Chapter 1—Printing on Polymers: Theory and Practice. In *Printing on Polymers*, 1st ed.; Izdebska, J., Thomas, S., Eds.; William Andrew Publishing: Oxford, UK, 2016; pp. 1–20.
14. Izdebska-Podsiadły, J. Chapter 6—Application of Plasma in Printed Surfaces and Print Quality. In *Non-Thermal Plasma Technology for Polymeric Materials*; Thomas, S., Mozetič, M., Cvelbar, U., Špatenka, P., Praveen, K.M., Eds.; Elsevier: Oxford, UK, 2019; pp. 159–191.
15. Izdebska-Podsiadły, J. Effect of Plasma Surface Modification on Print Quality of Biodegradable PLA Films. *Appl. Sci.* **2021**, *11*, 8245. [CrossRef]
16. Ma, C.; Nikiforov, A.; Hegemann, D.; De Geyter, N.; Morent, R.; Ostrikov, K. Plasma-controlled surface wettability: Recent advances and future applications. *Int. Mater. Rev.* **2022**, *67*, 1–38. [CrossRef]
17. Tyczkowski, J.; Kierzkowska-Pawlak, H.; Sielski, J.; Krawczyk-Kłys, I. Low-Temperature Plasma Modification of Styrene–Butadiene Block Copolymer Surfaces for Improved Adhesion—A Kinetic Approach. *Polymers* **2020**, *12*, 935. [CrossRef]
18. Stepczyńska, M. Surface Modification by Low Temperature Plasma: Sterilization of Biodegradable Materials. *Plasma Process. Polym.* **2016**, *13*, 1080–1088. [CrossRef]
19. Vishnuvarthanan, M.; Rajeswari, N. Effect of mechanical, barrier and adhesion properties on oxygen plasma surface modified PP. *Innov. Food Sci. Emerg. Technol.* **2015**, *30*, 119–126. [CrossRef]
20. De Geyter, N.; Morent, R. Cold plasma surface modification of biodegradable polymer biomaterials. Ch.7. In *Biomaterials for Bone Regeneration*; Dubruel, P., Van Vlierberghe, S., Eds.; Elsevier: Oxford, UK, 2014.
21. Nageswaran, G.; Jothi, L.; Jagannathan, S. Chapter 4—Plasma Assisted Polymer Modifications. In *Non-Thermal Plasma Technology for Polymeric Materials*, 1st ed.; Thomas, S., Mozetič, M., Cvelbar, U., Špatenka, P., Praveen, K.M., Eds.; Elsevier: Oxford, UK, 2019; pp. 95–127. [CrossRef]
22. Moraczewski, K.; Stepczyńska, M.; Malinowski, R.; Rytlewski, P.; Jagodziński, B.; Żenkiewicz, M. Stability studies of plasma modification effects of polylactide and polycaprolactone surface layers. *Appl. Surf. Sci.* **2016**, *337*, 228–237. [CrossRef]
23. Hirotsu, T.; Nakayama, K.; Tsujisaka, T.; Mas, A.; Schue, F. Plasma surface treatments of melt-extruded sheets of poly(L-lactic acid). *Polym. Eng. Sci.* **2002**, *42*, 299–306. [CrossRef]
24. Song, A.Y.; Oh, Y.A.; Roh, S.H.; Kim, J.K.; Min, S.C. Cold Oxygen Plasma Treatments for the Improvement of the Physicochemical and Biodegradable Properties of Polylactic Acid Films for Food Packaging. *J. Food Sci.* **2016**, *81*, E86–E96. [CrossRef] [PubMed]
25. Izdebska-Podsiadły, J.; Dörsam, E. Storage stability of the oxygen plasma-modified PLA film. *Bull. Mater. Sci.* **2021**, *44*, 79. [CrossRef]
26. Inagaki, N.; Narushima, K.; Tsutsui, Y.; Ohyama, Y. Surface modification and degradation of poly(lactic acid) films by Ar-plasma. *J. Adhes. Sci. Technol.* **2002**, *16*, 1041–1054. [CrossRef]
27. Izdebska-Podsiadły, J.; Dörsam, E. Effects of argon low temperature plasma on PLA film surface and aging behaviors. *Vacuum* **2017**, *145*, 278–284. [CrossRef]
28. Murphy, A.B.; Arundell, C.J. Transport coefficients of argon, nitrogen, oxygen, argon-nitrogen, and argon-oxygen plasmas. *Plasma Chem. Plasma Process.* **1994**, *14*, 451–490. [CrossRef]
29. Kim, B.K.; Kim, K.S.; Park, C.E.; Ryu, C.M. Improvement of wettability and reduction of aging effect by plasma treatment of low-density polyethylene with argon and oxygen mixtures. *J. Adhes. Sci. Technol.* **2002**, *16*, 509–521. [CrossRef]
30. Karam, L.; Jama, C.; Nuns, N.; Mamede, A.-S.; Dhulster, P.; Chihib, N.-E. Nisin adsorption on hydrophilic and hydrophobic surfaces: Evidence of its interactions and antibacterial activity. *J. Pept. Sci.* **2013**, *19*, 1075–2617. [CrossRef]
31. Fang, Z.; Wang, X.; Shao, T.; Zhang, C. Influence of Oxygen Content on Argon/Oxygen Dielectric Barrier Discharge Plasma Treatment of Polyethylene Terephthalate Film. *IEEE Trans Plasma Sci.* **2017**, *45*, 310–317. [CrossRef]
32. Saxena, N.; Prabhavathy, C.; De, S.; DasGupta, S. Flux enhancement by argon–oxygen plasma treatment of polyethersulfone membranes. *Sep. Purif. Technol.* **2009**, *70*, 160–165. [CrossRef]
33. Izdebska-Podsiadły, J. Impact of low temperature plasma treatment parameters on wettability and printability of PLA film. *IC J.* **2020**, *12*, 1–7.
34. Mortazavi, M.; Nosonovsky, M. A model for diffusion-driven hydrophobic recovery in plasma treated polymers. *Appl. Surf. Sci.* **2012**, *258*, 6876–6883. [CrossRef]
35. Luna, P.; Mariño, A.; Lizarazo-Marriaga, J.; Beltrán, O. Dry etching plasma applied to fique fibers: Influence on their mechanical properties and surface appearance. *Procedia Eng.* **2017**, *200*, 141–147. [CrossRef]
36. Jiang, X.; Wu, L.; Yang, K.; Liu, T.; Liao, W.; Zhang, C.; Zhang, L.; Liu, Y.; Jiang, X. Kinetic etch front instability responsible for roughness formation in plasma etching. *Appl. Surf. Sci.* **2021**, *543*, 148862. [CrossRef]
37. Grace, J.M.; Gerenser, L.J. Plasma Treatment of Polymers. *J. Dispers. Sci. Technol.* **2003**, *24*, 305–341. [CrossRef]
38. Primc, G.; Mozetič, M. Hydrophobic Recovery of Plasma-Hydrophilized Polyethylene Terephthalate Polymers. *Polymers* **2022**, *14*, 2496. [CrossRef] [PubMed]
39. Hebbar, R.S.; Isloor, A.M.; Ismail, A.F. Chapter 12—Contact Angle Measurements. In *Membrane Characterization*; Hilal, N., Ismail, A.F., Matsuura, T., Oatley-Radcliffe, D., Eds.; Elsevier: Amsterdam, The Netherlands, 2017; pp. 219–255. [CrossRef]
40. Akbari, R.; Antonini, C. Contact angle measurements: From existing methods to an open-source tool. *Adv. Colloid Interface Sci.* **2021**, *294*, 102470. [CrossRef]
41. Kubiak, K.J.; Wilson, M.C.T.; Mathia, T.G.; Carval, P. Wettability versus roughness of engineering surfaces. *Wear* **2011**, *271*, 523–528. [CrossRef]

42. Busscher, H.J.; Weerkamp, A.H.; van Der Mei, H.C.; van Pelt, A.W.; de Jong, H.P.; Arends, J. Measurement of the Surface Free Energy of Bacterial Cell Surfaces and Its Relevance for Adhesion. *Appl. Environ. Microbiol.* **1984**, *48*, 980–983. [CrossRef]
43. Żenkiewicz, M. Analysis of the most important methods of investigations of polymeric materials' surface free energy. *Polimery* **2007**, *52*, 760–768. [CrossRef]
44. Liber-Kneć, A.; Łagan, S. Surface Testing of Dental Biomaterials—Determination of Contact Angle and Surface Free Energy. *Materials* **2021**, *14*, 2716. [CrossRef]
45. Żołek-Tryznowska, Z.; Prica, M.; Pavlović, Ž.; Cveticanin, L.; Annusik, T. The influence of aging on surface free energy of corona treated packaging films. *Polym. Test.* **2020**, *89*, 1–8. [CrossRef]
46. Owens, D.K.; Wendt, R.C. Estimation of the surface free energy of polymers. *J. Appl. Polym. Sci.* **1969**, *13*, 1741–1747. [CrossRef]
47. Rudawska, A.; Jacniacka, E. Analysis for determining surface free energy uncertainty by the Owen–Wendt method. *Int. J. Adhes. Adhes.* **2009**, *29*, 451–457. [CrossRef]
48. Kiss, É.; Bertóti, I.; Vargha-Butler, E.I. XPS and Wettability Characterization of Modified Poly(lactic acid) and Poly(lactic/glycolic acid) Films. *J. Colloid Interface Sci.* **2002**, *245*, 91–98. [CrossRef] [PubMed]
49. Jordá-Vilaplana, A.; Fombuena, V.; García-García, D.; Samper, M.D.; Sánchez-Nácher, L. Surface modification of polylactic acid (PLA) by air atmospheric plasma treatment. *Eur. Polym. J.* **2014**, *58*, 23–33. [CrossRef]
50. Rider, A.N.; Brack, N.; Andres, S.; Pigram, P.J. The influence of hydroxyl group concentration on epoxy–aluminium bond durability. *J. Adhes. Sci. Technol.* **2004**, *18*, 1123–1152. [CrossRef]
51. Marcuello, C.; Foulon, L.; Chabbert, B.; Molinari, M.; Aguié-Béghin, V. Langmuir-Blodgett Procedure to Precisely Control the Coverage of Functionalized AFM Cantilevers for SMFS Measurements: Application with Cellulose Nanocrystals. *Langmuir* **2018**, *34*, 9376–9386. [CrossRef] [PubMed]
52. Berzin, F.; Lemkhanter, L.; Marcuello, C.; Chabbert, B.; Aguié-Béghin, V.; Molinari, M.; Castellani, R.; Vergnes, B. Influence of the polarity of the matrix on the breakage mechanisms of lignocellulosic fibers during twin-screw extrusion. *Polym. Compos.* **2020**, *41*, 1106–1117. [CrossRef]
53. Yousifa, E.; Ahmedb, D.; Zainulabdeena, K.; Jawad, A. Photo-physical and Morphological Study of Polymers: A Review. *Phys. Chem. Res.* **2023**, *11*, 409–424. [CrossRef]

coatings

MDPI

Article

Activity of Colloidal Silver Solution against Microorganisms Implicated in Ocular Infections

Anna Rita Blanco [1], Andreana Marino [2], Manuela D'Arrigo [2] and Antonia Nostro [2,*]

[1] Alfa Intes Industria Terapeutica Splendore (ITS), 80026 Naples, Italy
[2] Department of Chemical, Biological, Pharmaceutical and Environmental Sciences, University of Messina, Via Ferdinando Stagno d'Alcontres 31, 98166 Messina, Italy
* Correspondence: anostro@unime.it; Tel.: +39-090-6766443

Abstract: Endophthalmitis most likely originates from both planktonic bacteria suspended in the tear film and bacteria adherent to the conjunctiva and the eyelid. This study aimed to expand the research on the effectiveness of a colloidal silver solution (Silverix®) against ocular microorganisms. The activity of Silverix® was evaluated against methicillin-resistant *Staphylococcus aureus*, *S. epidermidis*, ofloxacin-resistant *Pseudomonas aeruginosa,* and *Candida albicans* strains, previously characterized for their antibiotic resistance and biofilm-forming capabilities. The microbial killing was estimated at various times in the presence and absence of colloidal silver solution against planktonic and biofilm-embedded cells. The results documented the efficacy of Silverix® on planktonic cells of *S. aureus* and *S. epidermidis* (2.49–2.87 Log CFU/mL reduction) and *P. aeruginosa* strains (3–4.35 Log CFU/mL reduction). On the contrary, *C. albicans* showed mild susceptibility. Regarding early biofilm, the ocular isolates were harder to kill (2–2.6 Log CFU/mL reduction) than the reference strains, whereas a similar decrease (3.1 Log CFU/mL reduction) was estimated for *P. aeruginosa* strains. The light microscope images of biofilms treated with colloidal solution confirmed the ability of Silverix® to destroy the biofilm.

Keywords: colloidal silver; antimicrobial activity; antibiofilm activity; ocular infections

Citation: Blanco, A.R.; Marino, A.; D'Arrigo, M.; Nostro, A. Activity of Colloidal Silver Solution against Microorganisms Implicated in Ocular Infections. *Coatings* **2023**, *13*, 265. https://doi.org/10.3390/coatings13020265

Academic Editor: Seungil Kim

Received: 11 December 2022
Revised: 12 January 2023
Accepted: 18 January 2023
Published: 23 January 2023

1. Introduction

Endophthalmitis is an inflammatory condition of the intraocular cavities, usually caused by infection. It most likely originates from both planktonic bacteria suspended in the tear film and bacteria adherent to the conjunctiva and the eyelid [1,2]. The margin of the eyelid can be colonized by microorganisms with a sessile-growth lifestyle able to build biofilm communities with a key role in the development of chronic infections. One of the most common eye infections that usually affects both eyes along the edges of the eyelids is represented by blepharitis. Blepharitis is often a condition difficult to treat, characterized by edema, redness and inflammation of the ciliary edge which affects the lid and its dermis, eyelashes, conjunctiva and the meibomian glands. The etiology is complex, including chronic bacterial infections, infestations with certain parasites such as *Demodex*, and inflammatory skin conditions such as seborrheic dermatitis. Among various bacterial pathogens that impact blepharitis, emerge *Staphylococcus aureus*, *S. epidermidis*, *Propionibacterium acnes* and *Corynebacteria* sp.. Recently, microbial biofilms have been implicated in a wide array of ocular diseases, including recurrent or chronic blepharitis leading to dry eye, a pathology particularly widespread and often underestimated [3]. The microbial biofilms are cause of a worsening of the pathological picture with lowered vision and chronic inflammation of connective tissue. Today, blepharitis and dry eye disease are considered a single disease referred to as "Dry Eye Blepharitis Syndrome" (DEBS) [3]. Biofilms have become a clinical and therapeutic problem, as microorganisms embedded in a self-produced polymeric matrix constitute impenetrable microbial communities, plugging the meibomian glands or

blocking the lash follicles, less susceptible to conventional treatment than their planktonic counterparts [4]. Furthermore, a biofilm extracellular polymeric substance is composed of DNA, proteins, and polysaccharides; it can also constitute a nutrient source for the growth of *Demodex* mites. These eyelash mites are parasites that live in or around human hair follicles, in symbiosis with many bacterial species, and are involved in blepharitis with cylindrical dandruff [3]. In light of the above, together with the serious concern raised by the increasing phenomenon of antibiotic resistance, it is necessary to shift toward alternative therapies to achieve better success in infection treatment.

Renewed attention has been focused on silver (Ag) because of its broad-spectrum antimicrobial activity against Gram-positive [5] and Gram-negative [6] organisms, fungi [7], protozoa [8], and some viruses [9]. It is known that Ag interacts with multiple target sites, such as cell membranes and microbial proteins, affecting permeability and respiration and causing cell death [5–11]. Current studies on the experimental biofilm models suggest that it also interferes with bacterial adhesion, destabilizes the biofilm matrix, and kills the bacteria embedded in the biofilm [12–14]. However, silver ions (Ag^+) or salts have only limited usefulness as antimicrobial agents. As provided from current literature available on silver, there is still a lot to know about the clinical potential of this element. It is pivotal to take in consideration possible side effects for human health. Today, one of the most common forms of Ag is represented by colloidal silver (CS) in nanoparticles (NPs), as the Ag in nanoform is far better and more biocompatible agent. Nanoparticles have higher antibacterial activity than free Ag^+ due to both the physical properties of nanoparticles and the elution of Ag^+ [15]. AgNPs have multiple modes of action that lead to cell killing, cause structural and physiological alterations in microbial cell membranes, such as changes in permeability and membrane potential, as well as penetrate into the cell, resulting in binding interactions with proteins and DNA. The AgNPs have a surface/volume ratio much greater than the corresponding bulk material; therefore, interactions with microbial surfaces are facilitated, allowing a better ability to release/produce Ag^+/reactive oxygen species [16–18]. It should be emphasized that, due to the non-specific nature of these mechanisms, AgNPs do not exert selective pressure on bacteria and have a much lower risk of developing resistance than conventional antibiotics. Silver nanoparticles have been also incorporated into different matrices and formulations, such as gels, coatings, composites, membranes, and thin films, to use in biomedical applications, food production, cosmetics, and numerous household products [15,19–21]. A form of gelatin-capped AgNPs has been studied as a promising antimicrobial and antiangiogenic nanotherapeutic for preclinical treatment of bacterial keratitis and eye-related microbial infections [22]. Specifically, the stabilized AgNPs showed efficient dispersion in aqueous media and interaction with *S. aureus*, improving antibacterial properties [22].

Starting from the preliminary data presented as a poster at the EVER Annual Congress [23], the current study expands the research on the activity of a colloidal silver solution (CST), providing new results on its efficacy against ocular isolates of *S. aureus*, *S. epidermidis*, *Pseudomonas aeruginosa,* and *Candida albicans*, chosen as representative microorganisms implicated in eye infections. Furthermore, microscopic biofilm analysis were also performed.

2. Materials and Methods

2.1. Materials

CST is used to soak gauzes for periocular hygiene (Silverix®, Alfa Intes already on the Italian market; Ocusilver® available on other markets, Italy) containing the following active ingredients: CS of 20–30 nm (0.001%) as an antimicrobial agent, sodium hyaluronate (0.05%) as a hydrating agent, and glycol extracts of *Matricaria chamomilla* L. (0.22%) and *Euphrasia officinalis* L. (0.22%) as soothing and emollient agents. Specifically, the CS used as a raw material has an Ag content of 70% to 80% of Ag dried substance, as required in accordance with the European Pharmacopoeia (EU) for CS for external use. As per chemical and physical properties, it is soluble in water and insoluble in ethanol (96%) and methylene chloride. The appearance of the CST is liquid, with a limpid yellowish color.

The pH range is 6.30–8.30, with a characteristic floral scent due to the presence of natural extracts of *Matricaria chamomilla* and *Euphrasia officinalis*.

2.2. Microorganisms and Inoculum Preparation

The microbial strains, belonging to the private collection of the Microbiology Section, Department of Chemical, Biological, Pharmaceutical, and Environmental Sciences, University of Messina, and previously characterized for antibiotic resistance [24–27] and biofilm-forming ability [28–31], were used. Methicillin-resistant *Staphylococcus aureus* 815 and *S. epidermidis* 813 have been selected for their well-characterized biofilm-related properties such as the presence of the *icaA/icaD* genes evaluated by PCR analysis, slime production evaluated by the Congo red agar assay and ability of forming biofilm on polystyrene surface [24]. Moreover, *S. aureus* 815 was also characterized for its haemolytic activity and agr system by PCR analysis, properties correlated with a background of biofilm producers [28]. Ofloxacin-resistant *P. aeruginosa* 1 and *C. albicans* 4 strains have been selected for their biofilm formation on polystyrene surface [29–31]. The following international reference strains from American Type Culture Collection (ATCC) were also included: *S. aureus* ATCC 6538, *S. epidermidis* ATCC 35984, *P. aeruginosa* ATCC 9027, and *C. albicans* ATCC 10231.

Bacteria were cultured in Muller Hinton broth (MHB) at 37 °C for 24 h, while *C. albicans* was grown on RPMI-1640 at 37 °C for 48 h. For microbial inocula, the centrifuged cells were standardized in phosphate-buffered saline (PBS), pH 7.4, using turbidimetry absorbance to a concentration of 1×10^6 CFU/mL, approximatively.

2.3. Killing Activity

Aliquots of colloidal solution (1 mL) were dispensed into tubes containing the standardized microbial strain and incubated at 37 °C. After 0, 5, 10, and 15 min, the samples were serially diluted in PBS and seeded on Tryptic Soy Agar (TSA) or Sabouraud agar. All plates were then incubated at 37 °C for 18–24 h up to 48–72 h. CFU was counted [31]. All determinations were performed in triplicate, including the growth controls.

2.4. Effectiveness on Biofilm-Embedded Cells

As reported previously, microbial cultures were grown as biofilms on polystyrene flat-bottomed microtiter plates (Costar; Corning) [32]. Briefly, overnight culture in Tryptic Soy Broth (TSB, *P. aeruginosa* and *C. albicans*) or TSB + 1% glucose (TSBG, *S. aureus* and *S. epidermidis*) was adjusted to 10^5 CFU/mL and dispensed individually to 96-well cell culture polystyrene microtiter plates. The plates were incubated at 37 °C for 6 h (early biofilms) and 24 h (late biofilms). After incubation, the planktonic phase was gently removed, and the biofilm was carefully washed twice with sterile PBS. Biofilms were then treated with CST or PBS (control). The effect of CST on cell viability was evaluated after different exposure times of 5, 15, 30, and 120 min. The colloidal solution was removed, the remaining biofilm was resuspended in PBS and the wells were scraped with sterile pipette tips as previously reported [32]. The microbial counts were assessed by plating serial dilutions onto TSA. After an incubation period of 48 h at 37 °C, the CFU were detected. All determinations were performed in triplicate.

2.5. Light Microscopy

Microbial early (6 h) biofilms of *S. aureus* ATCC 6538, *S. epidermidis* ATCC 35984, *P. aeruginosa* ATCC 9027 and *C. albicans* ATCC 10231 formed on polystyrene flat-bottomed microtiter plates (Costar; Corning), as described above, were washed three times with sterile PBS and treated with CST. Sequentially, PBS was added, serving as the control. After an exposure time of 15 min, the CST was removed; the plates were washed with PBS and stained using 0.4% crystal violet for 10 min [33]. The biofilms were observed with a light microscope X 200 (Leica DMLB).

2.6. Statistical Analysis

ANOVA was employed to evaluate any significant differences between the values obtained with and without the solution. A p-value < 0.05 was considered significant.

3. Results

3.1. Killing Activity

The antimicrobial activity of CST was tested on Gram-positive and Gram-negative bacteria and yeasts. The Log CFU/mL of planktonic microbial cells following the exposure to CST is presented in Table 1. It can be observed that the microbial load decreased as the time exposure increased. After 5 min of exposure, a mild decrease in the bacterial count was observed for both ATCC and ocular isolates of *S. aureus* and *S. epidermidis* (1.65–1.92 Log reduction) and *P. aeruginosa* (1.5–1.95 Log reduction) strains.

Table 1. Effectiveness of colloidal solution against microbial strains in planktonic phase. Data are the means of Log CFU/mL ± SD of three independent experiments carried out in triplicate.

Strains	Time (min)			
	0	5	10	15
	Log CFU/mL			
S. aureus 815 (MRSA)	6.17 ± 0.31	4.25 ± 0.33	4.17 ± 0.35	3.30 ± 0.12
S. aureus ATCC 6538	5.28 ± 0.24	3.48 ± 0.22	3.08 ± 0.15	2.52 ± 0.08
S. epidermidis 813	6.06 ± 0.22	4.3 ± 0.18	4.0 ± 0.14	3.50 ± 0.10
S. epidermidis ATCC 35984	5.05 ± 0.25	3.4 ± 0.15	2.9 ± 0.10	2.56 ± 0.12
P. aeruginosa 1 (ofloxacin-resistant)	8.0 ± 0.41	6.5 ± 0.40	5.5 ± 0.26	5.0 ± 0.30
P. aeruginosa ATCC 9027	7.05 ± 0.35	5.1 ± 0.19	3.8 ± 0.08	2.70 ± 0.05
C. albicans 4	4.25 ± 0.20	4.14 ± 0.25	4.0 ± 0.22	3.6 ± 0.15
C. albicans ATCC 10231	4.0 ± 0.23	2.6 ± 0.23	2.42 ± 0.14	2.0 ± 0.11

Interestingly, after 15 min contact, the CST has proved to be more effective achieving a significant (p < 0.05) load decrease ranging from 2.49 to 2.87 Log CFU/mL (about 99.7%–99.8%) for *S. aureus* and *S. epidermidis* strains (both ATCC and ocular isolates) and equal to 3–4.35 Log CFU/mL (99.9%–99.99%) for *P. aeruginosa* strains ATCC and ocular isolate, respectively. Except for *C. albicans* ATCC 10231, which showed a decrease of 1.4–2 Log units, the *C. albicans* ocular isolate was the least susceptible strain.

3.2. Effectiveness on Preformed Biofilm

The effect of the colloidal solution on the viability of the cells embedded in early (6 h) and late (24 h)-established biofilms is reported in Figures 1–4. The results demonstrated that the inhibitory activity of the solution was more pronounced on early biofilm (Figures 1–4) than on late biofilm (Figures 1–4). Furthermore, different levels of susceptibility were found between the biofilm formed by ocular isolates and ATCC strains of *S. aureus* and *S. epidermidis*. Specifically, after 15 min of contact, a reduction of 2.63 Log for *S. aureus* and 2.4 Log for *S. epidermidis* ocular isolates and a reduction of 3.7 Log and 4 Log for *S. aureus* and *S. epidermidis* ATCC strains were detected (Figures 1 and 2). Regarding the effect of the colloidal solution on *P. aeruginosa* biofilm, a reduction of 3.1 Log was displayed for both the ocular isolate and ATCC strain at 15 min of exposure (Figure 3). For *C. albicans*, the biofilm cell count decreased at a much slower rate. After 120 min, a 3.7 Log reduction was achieved for *C. albicans* ATCC, while a 1.5 Log reduction was observed for the *C. albicans* ocular isolate (Figure 4).

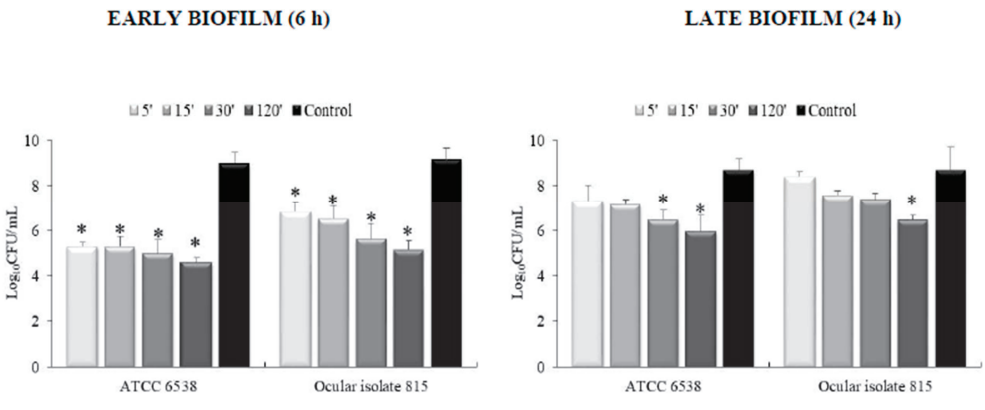

Strains	Log reduction 5'	15'	30'	120'
ATCC 6538	3.7	3.7	4	4.4
Ocular isolate 815	2.3	2.63	3.5	4

Strains	Log reduction 5'	15'	30'	120'
ATCC 6538	1.35	1.49	2.14	2.69
Ocular isolate 815	0.26	1.1	1.3	2.2

Figure 1. Quantitative measurement of *S. aureus* biofilm-embedded cells after treatment with CST. Data are expressed as means ± SD of three independent experiments carried out in triplicate and relative Log reduction. *, *p*-value < 0.05 shows the statistical difference between treated groups and control groups.

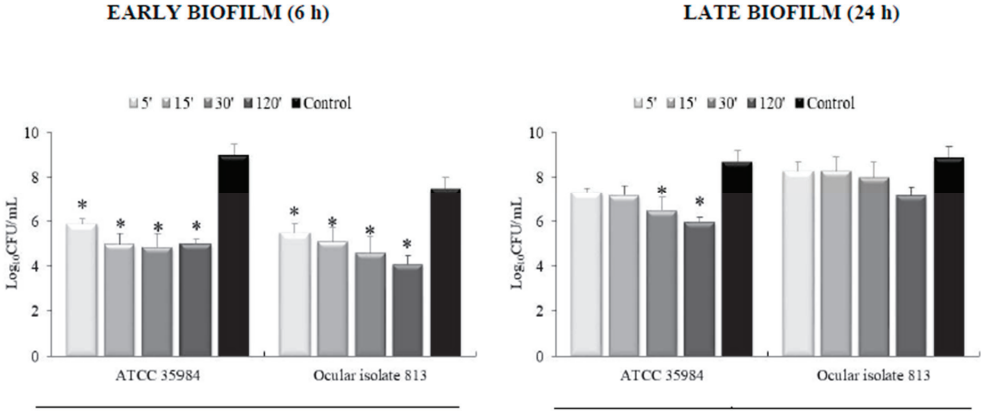

Strains	Log reduction 5'	15'	30'	120'
ATCC 35984	3.1	4	4.15	4
Ocular isolate 813	2	2.4	2.9	3.4

Strains	Log reduction 5'	15'	30'	120'
ATCC 35984	1.35	1.49	2.19	2.69
Ocular isolate 813	0.59	0.59	0.89	1.75

Figure 2. Quantitative measurement of *S. epidermidis* biofilm-embedded cells after treatment with CST. Data are expressed as means ± SD of three independent experiments carried out in triplicate and relative Log reduction. *, *p*-value < 0.05 shows the statistical difference between treated groups and control groups.

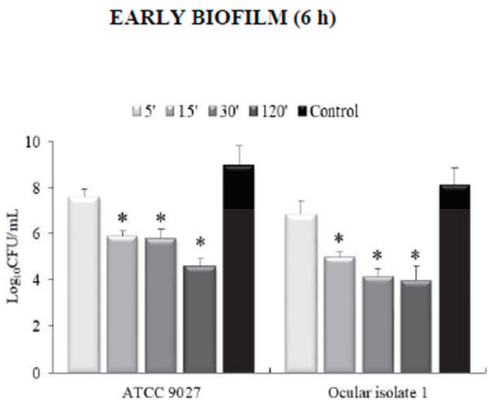

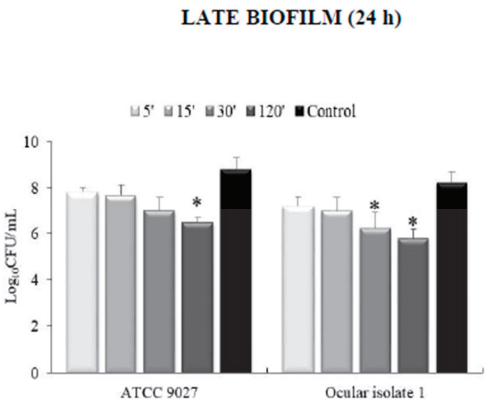

	Log reduction			
Strains	**5'**	**15'**	**30'**	**120'**
ATCC 9027	1.35	3.1	3.2	4.4
Ocular isolate 1	1.33	3.1	3.3	4.17

	Log reduction			
Strains	**5'**	**15'**	**30'**	**120'**
ATCC 9027	0.96	1.1	1.8	2.3
Ocular isolate 1	1	1.2	2	2.5

Figure 3. Quantitative measurement of *P. aeruginosa* biofilm-embedded cells after treatment with CST. Data are expressed as means ± SD of three independent experiments carried out in triplicate and relative Log reduction. *, *p*-value < 0.05 shows the statistical difference between treated groups and control groups.

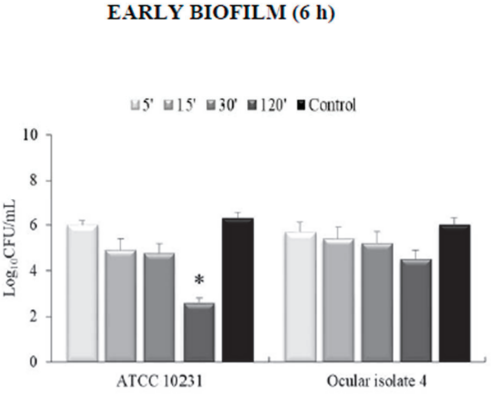

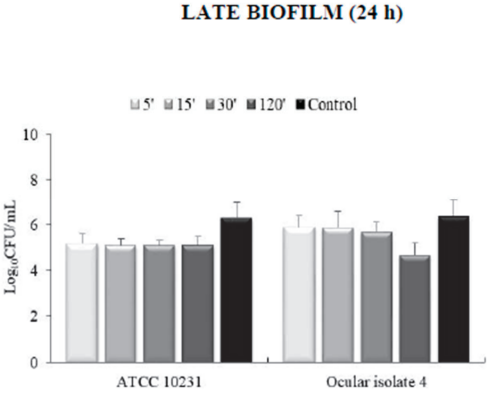

	Log reduction			
Strains	**5'**	**15'**	**30'**	**120'**
ATCC 10231	0.3	1.4	1.5	3.7
Ocular isolate 4	0.3	0.6	0.8	1.5

	Log reduction			
Strains	**5'**	**15'**	**30'**	**120'**
ATCC 10231	1.1	1.2	1.2	1.2
Ocular isolate 4	0.49	0.6	0.7	1.7

Figure 4. Quantitative measurement of *C. albicans* biofilm-embedded cells after treatment with the solution. Data are expressed as means ± SD of three independent experiments carried out in triplicate and relative Log reduction. *, *p*-value < 0.05 shows the statistical difference between treated groups and control groups.

In contrast, the late-established biofilms were less susceptible to the colloidal solution than the early biofilms. Discrete inhibition was achieved only after prolonged exposure times (30–120 min) for all microorganisms (Figures 1–4).

3.3. Light Microscopy

The results were substantiated by observing early biofilms under a light microscope (Figure 5). The images showed the ability of a colloidal solution to reduce the biofilm of *S. aureus*, *S. epidermidis*, and *P. aeruginosa*. After treatment for 15 min, the biofilm observed in controls (Figure 5a–c) became partially destroyed, and the bottom of the well was only covered by a few cells (Figure 5e–g). The effect was less evident for *C. albicans* (Figure 5d,h).

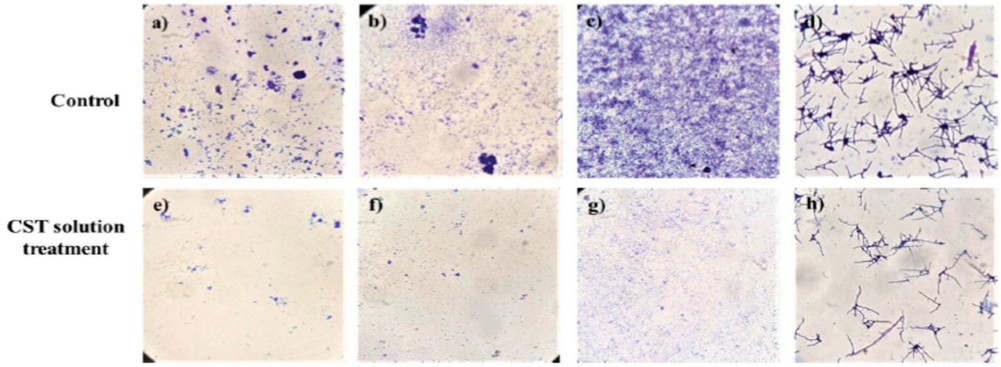

Figure 5. Light microscope images of early biofilms. Biofilm control and biofilm after treatment with CST for 15 min of (**a**,**e**) *S. aureus* ATCC 6538, (**b**,**f**) *S. epidermidis* ATCC 35984, (**c**,**g**) *P. aeruginosa* ATCC 9027, (**d**,**h**) *C. albicans* ATCC 10231.

4. Discussion

Bacteria are frequently associated with various ocular infections such as conjunctivitis, keratitis, blepharitis and endophthalmitis [34]. Conjunctivitis is the most common ocular infection and if became chronic can also affect the eye lid with potential risk for extra or intraocular infections [34]. Keratitis is a serious eye infection and can also progress to endophthalmitis. Both keratitis and endophthalmitis are potentially devastating ocular infections if not diagnosed and treated early. Effective antimicrobial therapy is the most important approach that should be promptly initiated for treatment of patients afflicted with these eye infections. However, the continue emergence of antimicrobial resistance and the close correlation between biofilm and antibiotic tolerance represent alarming concerns. The identification of alternative strategies effective alone or as adjuvants to common antimicrobials is highly desirable. In recent years, the introduction of AgNPs profoundly impacted clinical settings including the treatment of ocular infections, even those caused by resistant bacterial strains. Nanoparticles are effective in increasing the retention time of active compounds on the ocular surface, protecting them from enzymatic degradation and improving their corneal permeability. Colloidal silver nanoparticles have been demonstrated to be relatively safe when administered to oral mucosa, eye and skin of the animal models for short periods of time [35].

In this study, the CST solution (Silverix®) has been developed according to EU pharmacopoeia for the topical use of silver and it is used to soak gauzes for periocular hygiene. Silverix® is indicated for periocular hygiene of adults and children with ongoing infections such as blepharitis, meibomitis and in patients in treatment with ophthalmic ointments to provide a delicate cleaning while efficiently removing ointments' residues. Thanks to its unique composition, it can be used also by contact lenses users without any side effects reported to date. Silverix® is also recommended before and after ocular surgery for a cleaning of delicate periocular region. The findings of this study provide the scientific

basis for the efficacy of CST against planktonic and sessile microorganisms. The results documented that the activity against planktonic growth was more pronounced against *P. aeruginosa* than against *S. aureus* and *S. epidermidis*. Accordingly, higher activity of AgNPs on *E. coli* than on *S. aureus* has been reported [16]. It is known that the antimicrobial activity of AgNPs is influenced by differences in the structure, thickness, and composition of the cell walls of Gram-negative and Gram-positive bacteria. Notably, Gram-negative bacteria possess an inner layer of peptidoglycan less thick than Gram-positive bacteria, and their outer membrane consists of phospholipids, lipopolysaccharides (LPS), lipoproteins, and surface proteins [36]. Therefore, the thinner peptidoglycan layer and the negative charge of LPS that promotes the adhesion of AgNPs may explain the increased susceptibility of Gram-negative bacteria [37]. As exposed above, the activity of AgNPs is also influenced by the dimensions. By decreasing the particle size to nanometer range (between 1 and 100 nm), antibacterial activity of silver can be increased due to a larger surface area-to-mass ratio [38]. The dimensions of the nanoparticles of the colloidal silver solution (Silverix ®) ranged from 20 to 30 nm.

However, it is noteworthy that other components of the colloidal silver solution, such as *Matricaria chamomilla* L. and *Euphrasia officinalis chamomilla* extracts, have been studied for their antimicrobial activity [39,40]. Specifically, *M. chamomilla*-extract-mediated AgNPs exhibited highly effective antimicrobial activity against *S. aureus*, *E. coli*, and *C. albicans* [41]. Theoretically, the components present in the formulation act in combination, causing considerable effects on the cell structural and functional properties.

Interestingly, the colloidal silver solution showed antimicrobial activity against MRSA and ofloxacin-resistant *P. aeruginosa* 1. These strains are generally less susceptible to topical prophylaxis regimens. Specifically, MRSA is a major public health problem all over the world, frequently associated to serious ocular multi-resistant infections [42]. In accordance, Panáček et al. [43] demonstrated the significant bactericidal potential of colloidal AgNPs against MRSA and Gram-negative bacteria.

The colloidal silver solution showed minimum efficiency against *C. albicans* compared with bacteria, and this probably stems from the differences between the bacterial and yeast cells. On the other hand, it has been reported that the fungicidal activity of AgNPs is lower than the bactericidal effects [44].

Although growing antibiotic resistance is one of the major causes of treatment failure, the spread of biofilm-forming microorganisms contributes to serious public health threats, including ocular infections [45–48]. Here, we reported the inhibitory activity of a colloidal solution on preformed microbial biofilms, with a more pronounced effect on early biofilms than late biofilms. Indeed, a significant reduction in the viability of cells embedded in the early biofilm matrix and a disaggregation effect documented in microscopic images were observed. Kalishwaralal et al. [14] described the action of AgNPs on microorganisms organized in biofilms with a detachment of biofilms formed by pathogens causing keratitis, such as *P. aeruginosa* and *S. epidermidis*. The Authors suggested that the inhibitory effect of AgNPs on the mature biofilm may be due to the presence of water channels (useful for nutrient transport) which would allow the direct diffusion of AgNPs through the glycocalyx matrix layer, imparting the antimicrobial effect.

Silver nanoparticles have also been assayed for the effect on biofilm formation produced by the *P. aeruginosa*, *P. putida*, *Shigella flexneri*, *S. aureus* and *Streptococcus pneumonia* [49,50]. The inhibitory effect of AgNPs was analyzed alone or in combination with antibiotics [50]. Interestingly, AgNPs in combination with antibiotics increased the cell death and increased ROS generation than antibiotics or AgNPs alone. The enhancing effects for ampicillin and vancomycin against Gram-negative and Gram-positive bacteria, respectively suggest that AgNPs can be used as an adjuvant for the treatment of infectious diseases [50]. Although the mechanism of action is not yet known, it is plausible to hypothesize that the components of the colloidal solution may destroy the polar polymeric matrix and predispose the cells to specific interactions with the CST, thus having considerable effects on the structural properties of the biofilm. It is also speculated that the differ-

ent mechanisms employed by methicillin-susceptible *Staphylococcus aureus* (MSSA) and MRSA strains for biofilm formation may be involved in the reduced biofilm susceptibility of MRSA ocular isolates. MSSA strains predominantly form biofilms dependent on the polysaccharide intercellular adhesin type, whereas MRSA strains promote the formation of proteinaceous-type biofilms [51].

Effective antimicrobial strategies are needed in many preventive efforts in ophthalmology. The results of this study documented that the colloidal solution is active against microorganisms in both planktonic and biofilm phases and, therefore, could be used to assist in treating periocular surface infections.

Author Contributions: Conceptualization, A.N. and A.R.B.; methodology, A.N., A.R.B., A.M. and M.D.; software, M.D.; validation, A.N.; formal analysis, A.N., A.M. and M.D.; investigation, A.N. and A.M.; data curation, A.N.; writing—original draft preparation, A.N.; writing—review and editing, A.N. and A.R.B.; supervision, A.N. and A.R.B. All authors have read and agreed to the published version of the manuscript.

Funding: This research was supported by Alfa Intes Medical Division ITS (Casoria, Napoli, Italy) with a liberal donation to the University of Messina.

Institutional Review Board Statement: Not applicable.

Informed Consent Statement: Not applicable.

Data Availability Statement: Not applicable.

Acknowledgments: Editorial assistance was provided by Valentina Attanasio (Polistudium SRL, Milan, Italy).

Conflicts of Interest: Author A. Nostro received a liberal donation from Alfa Intes Medical Division ITS (Casoria, Napoli, Italy) for this research. Authors declare that they have no potential conflicts of interest regarding this work. In particular, the author A.R. Blanco declares to be employed in Alfa Intes Medical Division without any personal financial interest. Alfa Intes Medical Division had no role in the design of the study; in the collection, analysis, or interpretation of data; or the writing of the manuscript. Alfa Intes Medical Division approved the design and was allowed to review the manuscript prior to journal submission.

References

1. Durand, M.L. Bacterial and fungal endophthalmitis. *Clin. Microbiol. Rev.* **2017**, *30*, 597–613. [CrossRef] [PubMed]
2. Grzybowski, A.; Brona, P.; Kim, S.J. Microbial flora and resistance in ophthalmology: A review. *Graefes Arch. Clin. Exp. Ophthalmol.* **2017**, *255*, 851–862. [CrossRef] [PubMed]
3. Rynerson, J.M.; Perry, H.D. DEBS—A unification theory for dry eye and blepharitis. *Clin. Ophthalmol.* **2016**, *10*, 2455–2467. [CrossRef] [PubMed]
4. Olsen, I. Biofilm-specific antibiotic tolerance and resistance. *Eur. J. Clin. Microbiol. Infect. Dis.* **2015**, *34*, 77–86. [CrossRef] [PubMed]
5. Jung, W.K.; Koo, H.C.; Kim, K.W.; Shin, S.; Kim, S.H.; Park, Y.H. Antibacterial activity and mechanism of action of the silver ion in *Staphylococcus aureus* and *Escherichia coli*. *Appl. Environ. Microbiol.* **2008**, *74*, 2171–2178. [CrossRef]
6. Sondi, I.; Salopek-Sondi, B. Silver nanoparticles as antimicrobial agent: A case study on *E. coli* as a model for Gram-negative bacteria. *J. Colloid Interface Sci.* **2004**, *275*, 177–182. [CrossRef]
7. Gajbhiye, M.; Kesharwani, J.; Ingle, A.; Gade, A.; Rai, M. Fungus-mediated synthesis of silver nanoparticles and their activity against pathogenic fungi in combination with fluconazole. *Nanomedicine* **2009**, *5*, 382–386. [CrossRef]
8. Hendiger, E.B.; Padzik, M.; Sifaoui, I.; Reyes-Batlle, M.; López-Arencibia, A.; Rizo-Liendo, A.; Bethencourt-Estrella, C.J.; Nicolás-Hernández, D.S.; Chiboub, O.; Rodríguez-Expósito, R.L.; et al. Silver nanoparticles as a novel potential preventive agent against Acanthamoeba keratitis. *Pathogens* **2020**, *9*, 350. [CrossRef]
9. Gaikwad, S.; Ingle, A.; Gade, A.; Rai, M.; Falanga, A.; Incoronato, N.; Russo, L.; Galdiero, S.; Galdiero, M. Antiviral activity of mycosynthesized silver nano-particles against herpes simplex virus and human parainfluenza virus type 3. *Int. J. Nanomed.* **2013**, *8*, 4303–4314.
10. Maillard, J.Y.; Denyer, S.P. Focus on silver. In *European Wound Management Association (EWMA) Position Document: The Role of Topical Antimicrobials in Managing Wound Infection*; MEP Ltd.: London, UK, 2006.
11. Russell, A.D.; Hugo, W.B. Antimicrobial activity and action of silver. *Prog. Med. Chem.* **1994**, *31*, 351–370.
12. Feng, Q.L.; Wu, J.; Chen, G.Q.; Cui, F.Z.; Kim, T.N.; Kim, J.O. A mechanistic study of the antibacterial effect of silver ions on *Escherichia coli* and *Staphylococcus aureus*. *J. Biomed. Mater. Res.* **2000**, *52*, 662–668. [CrossRef]

13. Chaw, K.C.; Manimaran, M.; Tay, F.E. Role of silver ions in destabilization of intermolecular adhesion forces measured by atomic force microscopy in *Staphylococcus epidermidis* biofilms. *Antimicrob. Agents Chemother.* **2005**, *49*, 4853–4859. [CrossRef]
14. Kalishwaralal, K.; BarathManiKanth, S.; Pandian, S.R.; Deepak, V.; Gurunathan, S. Silver nanoparticles impede the biofilm formation by *Pseudomonas aeruginosa* and *Staphylococcus epidermidis*. *Colloids Surf. B Biointerfaces* **2010**, *79*, 340–344. [CrossRef]
15. Richter, K.; Facal, P.; Thomas, N.; Vandecandelaere, I.; Ramezanpour, M.; Cooksley, C.; Prestidge, C.A.; Coenye, T.; Wormald, P.J.; Vreugde, S. Taking the silver bullet colloidal silver particles for the topical treatment of biofilm-related infections. *ACS Appl. Mater. Interfaces* **2017**, *9*, 21631–21638. [CrossRef]
16. Marambio-Jones, C.; Hoek, E.M.V. A review of the antibacterial effects of silver nanomaterials and potential implications for human health and the environment. *J. Nanopart. Res.* **2010**, *12*, 1531–1551. [CrossRef]
17. Kim, J.S.; Kuk, E.; Yu, K.N.; Kim, J.H.; Park, S.J.; Lee, H.J.; Kim, S.H.; Park, Y.K.; Park, Y.H.; Hwang, C.Y.; et al. Antimicrobial effects of silver nanoparticles. *Nanomedicine* **2007**, *3*, 95–101. [CrossRef]
18. Lara, H.H.; Garza-Treviño, E.N.; Ixtepan-Turrent, L.; Singh, D.K. Silver nanoparticles are broad-spectrum bactericidal and virucidal compounds. *J. Nanobiotechnol.* **2011**, *9*, 30. [CrossRef]
19. Franci, G.; Falanga, A.; Galdiero, S.; Palomba, L.; Rai, M.; Morelli, G.; Galdiero, M. Silver nanoparticles as potential antibacterial agents. *Molecules* **2015**, *20*, 8856–8874. [CrossRef]
20. Porel, S.; Ramakrishna, D.; Hariprasad, E.; Gupta Dutta, A.; Radhakrishnan, T. Polymer thin film with in situ synthesized silver nanoparticles as a potent reusable bactericide. *Curr. Sci.* **2011**, *101*, 927–934.
21. Tran, Q.H.; Nguyen, V.Q.; Le, A.T. Silver nanoparticles: Synthesis, properties, toxicology, applications and perspectives. *Adv. Nat. Sci. Nanosci. Nanotechnol.* **2018**, *9*, 049501. [CrossRef]
22. Luo, L.J.; Lin, T.Y.; Yao, C.H.; Kuo, P.Y.; Matsusaki, M.; Harroun, S.G.; Huang, C.C.; Lai, J.Y. Dual-functional gelatin-capped silver nanoparticles for antibacterial and antiangiogenic treatment of bacterial keratitis. *J. Colloid Interfaces Sci.* **2019**, *536*, 112–126. [CrossRef] [PubMed]
23. Blanco, A.R.; Marino, A.; D'Arrigo, M.; Nostro, A. Efficacy of a colloidal silver-based topical solution on microbial biofilms. In *Acta Ophthalmologica*; Wiley: Hoboken, NJ, USA, 2018; Volume 96, p. 14.
24. Blanco, A.R.; Sudano-Roccaro, A.; Spoto, G.C.; Nostro, A.; Rusciano, D. Epigallocatechin gallate inhibits biofilm formation by ocular staphylococcal isolates. *Antimicrob. Agents Chemother.* **2005**, *49*, 4339–4343. [CrossRef] [PubMed]
25. Marino, A.; Blanco, A.R.; Ginestra, G.; Nostro, A.; Bisignano, G. Ex vivo efficacy of gemifloxacin in experimental keratitis induced by methicillin-resistant *Staphylococcus aureus*. *Int. J. Antimicrob. Agents* **2016**, *48*, 395–400. [CrossRef] [PubMed]
26. Consoli, G.M.L.; Granata, G.; Picciotto, R.; Blanco, A.R.; Geraci, C.; Marino, A.; Nostro, A. Design, synthesis and antibacterial evaluation of a polycationic calix [4]arene derivative alone and in combination with antibiotics. *MedChemComm* **2017**, *9*, 160–164. [CrossRef]
27. Blanco, A.R.; Nostro, A.; D'Angelo, V.; D'Arrigo, M.; Mazzone, M.G.; Marino, A. Efficacy of a fixed combination of tetracycline, chloramphenicol, and colistimethate sodium for treatment of *Candida albicans* keratitis. *Investig. Ophthalmol. Vis. Sci.* **2017**, *58*, 4292–4298. [CrossRef]
28. Di Stefano, A.; D'Aurizio, E.; Trubiani, O.; Grande, R.; Di Campli, E.; Di Giulio, M.; Di Bartolomeo, S.; Sozio, P.; Iannitelli, A.; Nostro, A.; et al. Viscoelastic properties of *Staphylococcus aureus* and *Staphylococcus epidermidis* mono-microbial biofilms. *Microb. Biotechnol.* **2009**, *2*, 634–641. [CrossRef]
29. Nostro, A.; Guerrini, A.; Marino, A.; Tacchini, M.; Di Giulio, M.; Grandini, A.; Akin, M.; Cellini, L.; Bisignano, G.; Saraçoğlu, H.T. In vitro activity of plant extracts against biofilm-producing food-related bacteria. *Int. J. Food Microbiol.* **2016**, *238*, 33–39. [CrossRef]
30. Nostro, A.; Marino, A.; Ginestra, G.; Cellini, L.; Di Giulio, M.; Bisignano, G. Effects of adaptation to carvacrol on *Staphylococcus aureus* in the planktonic and biofilm phases. *Biofouling* **2017**, *33*, 470–480. [CrossRef]
31. Scaffaro, R.; Lopresti, F.; D'Arrigo, M.; Marino, A.; Nostro, A. Efficacy of poly(lactic acid)/carvacrol electrospun membranes against *Staphylococcus aureus* and *Candida albicans* in single and mixed cultures. *Appl. Microbiol. Biotechnol.* **2018**, *102*, 4171–4181. [CrossRef]
32. Nostro, A.; Marino, A.; Blanco, A.R.; Cellini, L.; Di Giulio, M.; Pizzimenti, F.; Roccaro, A.S.; Bisignano, G. In vitro activity of carvacrol against staphylococcal preformed biofilm by liquid and vapour contact. *J. Med. Microbiol.* **2009**, *58*, 791–797. [CrossRef]
33. Azeredo, J.; Azevedo, N.F.; Briandet, R.; Cerca, N.; Coenye, T.; Costa, A.R.; Desvaux, M.; Di Bonaventura, G.; Hébraud, M.; Jaglic, Z.; et al. Critical review on biofilm methods. *Crit. Rev. Microbiol.* **2017**, *43*, 313–351. [CrossRef]
34. Teweldemedhin, M.; Gebreyesus, H.; Atsbaha, A.H.; Asgedom, S.W.; Saravanan, M. Bacterial profile of ocular infections: A systematic review. *BMC Ophthalmol.* **2017**, *17*, 212. [CrossRef]
35. Maneewattanapinyo, P.; Banlunara, W.; Thammacharoen, C.; Ekgasit, S.; Kaewamatawong, T. An evaluation of acute toxicity of colloidal silver nanoparticles. *J. Vet. Med. Sci.* **2011**, *73*, 1417–1423. [CrossRef]
36. Nikaido, H.; Vaara, M. Molecular basis of bacterial outer membrane permeability. *Microbiol. Rev.* **1985**, *1*, 1–32. [CrossRef]
37. Rai, M.K.; Deshmukh, S.D.; Ingle, A.P.; Gade, A.K. Silver nanoparticles: The powerful nanoweapon against multidrug-resistant bacteria. *J. Appl. Microbiol.* **2012**, *112*, 841–852. [CrossRef]
38. Rai, M.; Yadav, A.; Gade, A. Silver nanoparticles as a new generation of antimicrobials. *Biotechnol. Adv.* **2009**, *27*, 76–83. [CrossRef]

39. Sharifi-Rad, M.; Nazaruk, J.; Polito, L.; Morais-Braga, M.F.B.; Rocha, J.E.; Coutinho, H.D.M.; Salehi, B.; Tabanelli, G.; Montanari, C.; Del Mar Contreras, M.; et al. *Matricaria* genus as a source of antimicrobial agents: From farm to pharmacy and food applications. *Microbiol. Res.* **2018**, *215*, 76–88. [CrossRef]
40. Singh, H.; Du, J.; Singh, P.; Yi, T.H. Ecofriendly synthesis of silver and gold nanoparticles by *Euphrasia officinalis* leaf extract and its biomedical applications. *Artif. Cells Nanomed. Biotechnol.* **2018**, *46*, 1163–1170. [CrossRef]
41. Dogru, E.; Demirbas, A.; Altinsoy, B.; Duman, F.; Ocsoy, I. Formation of *Matricaria chamomilla* extract-incorporated Ag nanoparticles and size-dependent enhanced antimicrobial property. *J. Photochem. Photobiol. B.* **2017**, *174*, 78–83. [CrossRef]
42. Deguchi, H.; Kitazawa, K.; Kayukawa, K.; Kondoh, E.; Fukumoto, A.; Yamasaki, T.; Kinoshita, S.; Sotozono, C. The trend of resistance to antibiotics for ocular infection of *Staphylococcus aureus*, coagulase-negative staphylococci, and *Corynebacterium* compared with 10-years previous: A retrospective observational study. *PLoS ONE* **2018**, *13*, e0203705. [CrossRef]
43. Panáček, A.; Libor Kvítek, L.; Prucek, R.; Kolar, M.; Vecerova, R.; Pizúrova, N.; Sharma, V.K.; Nevecna, T.; Zboril, R. Silver colloid nanoparticles: Synthesis, characterization, and their antibacterial activity. *J. Phys. Chem.* **2006**, *110*, 16248–16253. [CrossRef] [PubMed]
44. Shehabeldine, A.M.; Salem, S.S.; Ali, O.M.; Abd-Elsalam, K.A.; Elkady, F.M.; Hashem, A.H. Multifunctional silver nanoparticles based on chitosan: Antibacterial, antibiofilm, antifungal, antioxidant, and wound-healing activities. *J. Fungi* **2022**, *8*, 612. [CrossRef] [PubMed]
45. Bispo, P.J.; Haas, W.; Gilmore, M.S. Biofilms in infections of the eye. *Pathogens* **2015**, *4*, 111–136. [CrossRef] [PubMed]
46. Aslam, B.; Wang, W.; Arshad, M.I.; Khurshid, M.; Muzammil, S.; Rasool, M.H.; Nisar, M.A.; Alvi, R.F.; Aslam, M.A.; Qamar, M.U.; et al. Antibiotic resistance: A rundown of a global crisis. *Infect. Drug Resist.* **2018**, *11*, 1645–1658. [CrossRef] [PubMed]
47. Brahma, U.; Sharma, P.; Murthy, S.; Sharma, S.; Chakraborty, S.; Sundarapu Naga Appalaraju, S.N.; Vasundhra Bhandari, V. Decreased expression of *femXAB* genes and *fnbp* mediated biofilm pathways in OS-MRSA clinical isolates. *Sci. Rep.* **2019**, *9*, 16028. [CrossRef]
48. Heidari, H.; Hadadi, M.; Sedigh Ebrahim-Saraie, H.; Mirzaei, A.; Taji, A.; Hosseini, S.R.; Motamedifar, M. Characterization of virulence factors, antimicrobial resistance patterns and biofilm formation of *Pseudomonas aeruginosa* and *Staphylococcus* spp. strains isolated from corneal infection. *J. Fr. Ophthalmol.* **2018**, *41*, 823–829. [CrossRef]
49. Fabrega, J.; Renshaw, J.C.; Lead, J.R. Interactions of silver nanoparticles with *Pseudomonas putida* biofilms. *Environ. Sci. Technol.* **2009**, *43*, 9004–9009. [CrossRef]
50. Gurunathan, S.; Han, J.W.; Kwon, D.N.; Kim, J.H. Enhanced antibacterial and anti-biofilm activities of silver nanoparticles against Gram-negative and Gram-positive bacteria. *Nanoscale Res. Lett.* **2014**, *9*, 373. [CrossRef]
51. McCarthy, H.; Rudkin, J.K.; Black, N.S.; Gallagher, L.; O'Neill, E.; O'Gara, J.P. Methicillin resistance and the biofilm phenotype in *Staphylococcus aureus*. *Front. Cell Infect. Microbiol.* **2015**, *5*, 1. [CrossRef]

coatings

MDPI

Article

A Novel Low-Profile Self-Expanding Biodegradable Percutaneous Heart Valve Frame That Grows with a Child

Mohamed Ibrahim [1], Kara X. Nghiem [2], Kaitlin Chung [2], Moataz Elsisy [3], Uma J. Gosai [4], Seungil Kim [5,6], Sangho Ye [5,6], William R. Wagner [2,5,6,7] and Youngjae Chun [1,2,5,*]

1 Department of Industrial Engineering, University of Pittsburgh, Pittsburgh, PA 15261, USA
2 Department of Bioengineering, University of Pittsburgh, Pittsburgh, PA 15261, USA
3 Department of Mechanical Design, Cairo University, Giza 12613, Egypt
4 Department of Biological Sciences, University of Pittsburgh, Pittsburgh, PA 15260, USA
5 McGowan Institute for Regenerative Medicine, University of Pittsburgh, Pittsburgh, PA 15219, USA
6 Department of Surgery, University of Pittsburgh, Pittsburgh, PA 15213, USA
7 Department of Chemical and Petroleum Engineering, University of Pittsburgh, Pittsburgh, PA 15261, USA
* Correspondence: yjchun@pitt.edu

Abstract: According to rough estimates, one in every 125 newborns born in the United States has a congenital cardiac abnormality that must be repaired. With the recent development of new biomaterials and innovative treatment methods, percutaneous cardiac valve replacement has been considered as an alternative to surgical procedures. While percutaneous heart valve replacement is a relatively new procedure with a few commercially available devices, the devices are not sufficiently low-profile, and do not grow with the child. To address this issue, a novel low-profile growing percutaneous pediatric heart valve frame made of two types of unique metallic biomaterials (supere lastic nitinol and biodegradable iron) has been developed through this study. The developed pediatric heart valve frame has an innovative mechanism that will expand its diameter by disconnecting biodegradable metals, enabling the growth of the device with the surrounding tissue in the cardiac space. The thermally treated iron wires show stable and gradual degradation characteristics, showing approximately 7.66% for both wires treated under 350 and 450 °C. Polymer-coated wires show a degradation range of 4.96 to 5.55% depending on the type of coating. Degradation test results show the predicted 9–23 months of degradation depending on the type of surface treatment (e.g., thermal treatment, polymer coating), which is a suitable range when compared with the theoretical arterial vessel remodeling process period in the human vascular system. Radial forces calculated by finite element analysis and measured by mechanical testing matched well, showing 5–6 N with a 20% diameter reduction considering the deployed valve frame in the heart. Biocompatibility study results demonstrated superior cell viability in thermally treated iron wires after 3 days of cell culture and showed rarely found platelets on the surface after 3-h blood exposure tests. Prototype devices were successfully fabricated using optimized advanced joining processes for dissimilar metallic materials such as nitinol and iron. This study represents the first demonstration of self-expanding and biodegradable percutaneous heart valve frames for pediatric patients that grow with a child.

Keywords: superelastic nitinol; biodegradable iron; percutaneous; pediatric heart valve

Citation: Ibrahim, M.; Nghiem, K.X.; Chung, K.; Elsisy, M.; Gosai, U.J.; Kim, S.; Ye, S.; Wagner, W.R.; Chun, Y. A Novel Low-Profile Self-Expanding Biodegradable Percutaneous Heart Valve Frame That Grows with a Child. *Coatings* **2023**, *13*, 184. https://doi.org/10.3390/coatings13010184

Academic Editor: Ajay Vikram Singh

Received: 21 December 2022
Revised: 10 January 2023
Accepted: 12 January 2023
Published: 14 January 2023

1. Introduction

Heart valve disease is a condition in which the valve between the main pumping chamber of the heart (left ventricle) and the main artery to the body (aorta) malfunctions. Heart valve disease sometimes may be a congenital condition. Defects in heart valves and associated structures for infants account for 25 to 30 percent of all cardiovascular malformations [1]. In adults, over 182,000 heart valve replacements are performed annually for the treatment of valvular heart disease, but it remains as a major cause of morbidity

and mortality, with approximately 91,000 transcatheter valve replacements performed in the USA every year [2–4].

There are typically two types of prosthetic heart valves used for replacement—mechanical and bioprosthetic. Mechanical heart valves are made entirely of synthetic materials such as metals and polymers, while bioprosthetic heart valves are made of tissue from animals (e.g., bovine or porcine) or humans [5,6]. Mechanical heart valves are durable, lasting at least 20 to 30 years [7,8]. However, these valves have limited central flow due to their design, such as bileaflets, the ball in a cage, or a tilting disc [6,9]. In addition, a major drawback is that mechanical heart valves require daily anticoagulant treatment because of the increased risk of artificial material-induced thrombosis and thromboembolism [10–13]. On the contrary, bioprosthetic heart valves have improved central blood flow due to their bio-mimicking trileaflet design and do not require anticoagulant therapy. However, these bioprosthetic heart valves also have some drawbacks, including limited durability due to leaflet calcification, leaflet tearing, fatigue damage, and tissue failure [14–17]. Therefore, 10 to 20 percent of homograft bioprostheses and 30 percent of heterograft bioprostheses fail within 10 to 15 years of implantation and require replacement [18–20].

Furthermore, both mechanical and bioprosthetic heart valves are large and bulky and require open heart surgery, which has a severe risk factor for infants and young children who are too weak or ill to undergo major open surgery [5]. Recently, a less invasive therapy, percutaneous heart valve replacement, has drastically improved with the development of novel biomaterials and suggests innovative treatment strategies. While percutaneous heart valve replacement is an emerging technology with a few commercially available devices, the devices are still relatively bulky for infants or children and will not grow with the child, which may not be suitable for pediatric patients with congenital heart disease.

To address this issue, this study has demonstrated a novel concept of a pediatric heart valve frame that utilizes two types of metallic biomaterials, i.e., superelastic nitinol and biodegradable metals such as iron, as depicted in Figure 1. Biodegradation of surface-modified iron will enable the pediatric device to grow with the child, while superelastic nitinol can play an important role in the self-expanding mechanism. Both thermal treatment and polymer coating strategies were adapted to extend the degradation period for the purpose of the desired length of mechanical integrity. With the outcomes produced from the degradation study, prototypes have been designed and fabricated to demonstrate the growing pediatric valve frame. In addition, both the blood and cytocompatibility of the degradable metallic devices have been studied.

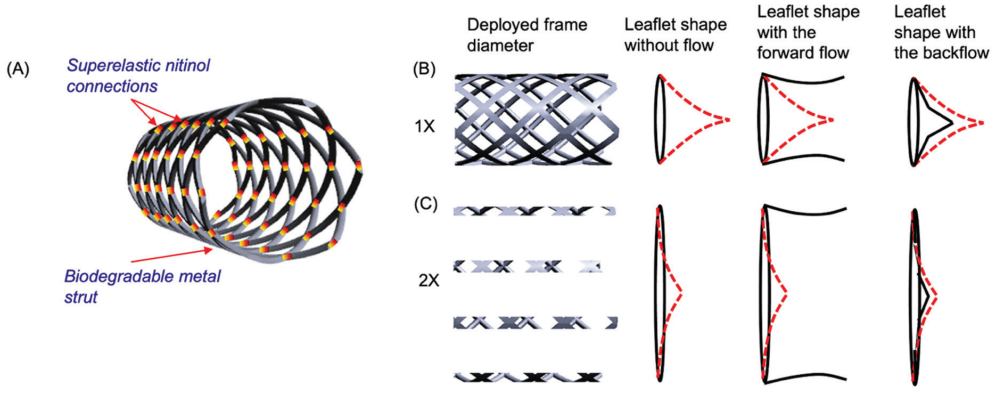

Figure 1. Schematic illustration of a growing pediatric percutaneous heart valve frame concept: (**A**) en face view of the frame that contains both superelastic nitinol and biodegradable metal, (**B**) original dimension of the device, showing the angle of leaflet, and (**C**) 200% increased dimension of the device with the leaflet angle change assuming the growth of the child.

2. Materials and Methods

2.1. Materials

Nitinol (Ni + Ti + Naval Ordinance Lab) was discovered in 1963 and has been used in a wide range of transcatheter devices due to its shape memory property [21]. The shape memory response is defined as mechanical deformation in a low-temperature state (i.e., martensite), with deformations fully recovered when the material is heated to body temperature (i.e., austenite). This shape memory behavior is critical for transcatheter devices because nitinol can easily be collapsed into a small-diameter catheter in its martensite phase. Upon exposure to blood temperature, it deploys spontaneously to its original shape (the austenite phase). Because the magnitude of its recoverable deformation is much greater than the elastic deformation of metals such as surgical steel, nitinol-based devices can be placed into remarkably smaller-diameter catheters for a wide range of catheter-based procedures [22–24].

An iron stent was first implanted in the rabbit model in 2001 [25]. Iron is one of the important biodegradable metallic biomaterials, with high radial strength compared with other biodegradable metals, e.g., magnesium. This attribute enables the iron-based stent to have thinner struts, permitting an endovascular low-profile device. There were no significant adverse events (e.g., thrombosis and excessive neointima hyperplasia) during a 6-18 month follow-up period with in vivo animal tests [25,26].

2.2. Surface Treatments

2.2.1. Thermal Treatments

A biodegradable material's mechanical performance and biodegradation behavior are crucial for biodegradable implant applications. Thermal treatment, or annealing, has been proven to have a substantial impact on the mechanical performance of pure iron (99.85%, outer diameter of 250 μm, GoodFellow, Pittsburgh, PA, USA) [27]. However, only a few research articles have addressed the influence of thermal annealing on the biodegradation behavior of pure iron [28]. When pure iron samples are thermally treated, a newly formed iron oxide layer starts to cover the outer surface of the iron, which may affect the sample's degradation rate. Furthermore, various treatment parameters, such as treatment temperatures and times, can significantly affect the growth of the iron oxide layer and its thickness [29]. At different treatment temperatures, Simmons et al. investigated the formation of iron oxide and its microstructure, showing that a distinct microstructure, a mixture of nonstoichiometric and stoichiometric magnetite and hematite, at 350 °C, was observed, while, at 450 °C, stoichiometric magnetite was the only oxide observed [30].

In this light, pure iron wire samples were prepared and subjected to multiple combinations of thermal treatments at different times to investigate the influence of these treatment parameters on the sample's degradation. Iron wires were thermally treated at both 350 °C and 450 °C for 0.5, 1.5, and 4 h. Additional wires were prepared at 550 degrees but were deemed inappropriate for experimental use due to flaking of the outer oxide layer.

2.2.2. Ultra-Thin Polymer Coating

Iron (Fe) wires (length: 70 mm, outer diameter: 250 μm, GoodFellow, Pittsburgh, PA, USA) underwent phytic acid–metal conversion coating [31] and coating with poly(carbonate urethane) urea (PCUU, inherent viscosity: 0.80 ± 0.1) [32,33], in which each coating step was separately investigated using scanning electron microscopy (SEM), as illustrated in Figure 2. For the phytic acid–metal conversion coating, phytic acid (PA) solution in deionized (DI) water (10 μg/L) was mixed with the same volume of $Zn(NO_3)_2$ solution in DI water (5 mmol/L) and then the pH was adjusted to 6.0 by adding 1N NaOH solution. Iron wires were washed with DI water and then immersed in the mixed PA-$Zn(NO_3)_2$ solution for 10 min with gentle shaking. After the PA-Zn^{2+} coating, the wires were washed with DI water three times and dried under a vacuum. In addition, PCUU was coated onto the PA-Zn^{2+} coated wires by dip coating using 2% (*w*/*v*) PCUU solution in hexafluoro-2-propanol (HFIP). The dip coating was repeated ten times for each wire. For the spray-coated wires,

10 mL of 2% PCUU solution was sprayed onto each PA-Zn^{2+} and PCUU-dip-coated wire at a 15 cm distance using a customized airbrush.

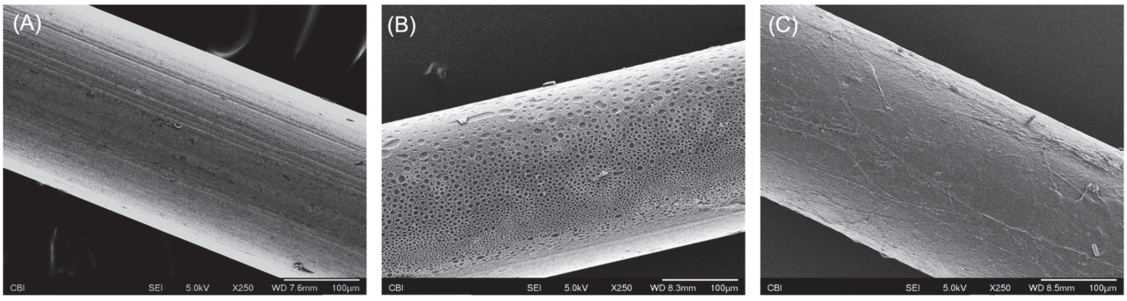

Figure 2. Iron wire samples treated with (**A**) phytic acid–Zn, (**B**) phytic acid–Zn + PCUU dip coating, and (**C**) phytic acid–Zn + PCUU dip and spray coating.

2.3. Degradation Test

Directly after the surface treatments of the iron wires, the degradation performance is assessed by immersion testing in phosphate-buffered solution (PBS, Fisher Scientific, Waltham, MA, USA). PBS is a physiologic aqueous solution that imitates the ionic concentration, osmolarity, and pH value of human blood but does not contain larger particles such as proteins, lipids, or blood cells. The iron samples were placed at the middle of a 0.5-inch-diameter silicone elastomer tube (Thermo Scientific, Waltham, MA, USA) by fixing these wire samples at the inner walls of the tubes, as shown in Figure 3A. The PBS was designed to flow in the tubes with the help of a peristaltic pump (Harvard Apparatus, Holliston, MA, USA) at a flow rate of 147.961 mL/min, flowing with a 100 mm Hg flow pressure, to mimic the blood flow parameters inside the aortic artery of the human body. The samples were fully immersed in the flow of PBS to ensure constant solution circumstances, and the immersion testing setup was kept at a constant temperature of 37 °C.

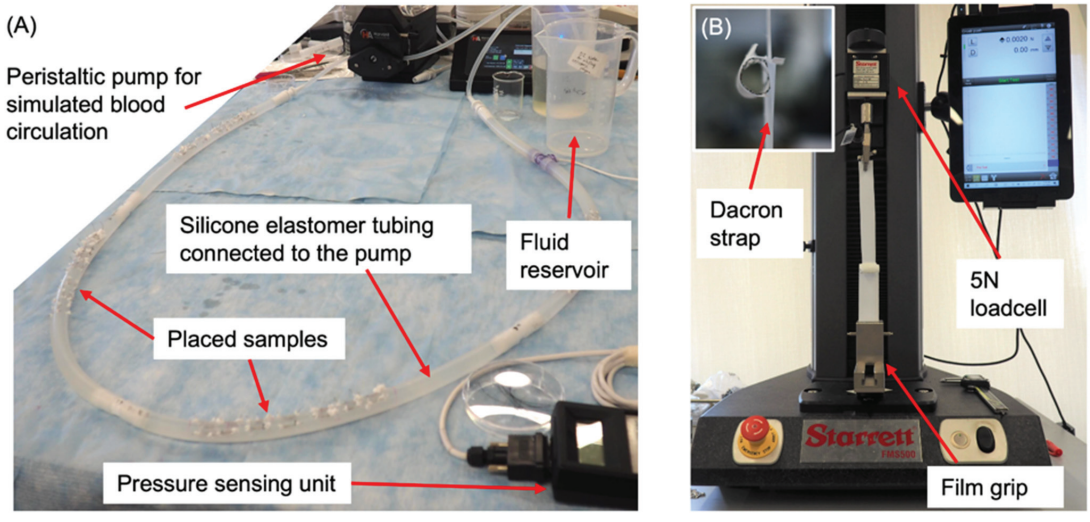

Figure 3. In vitro test device performance test setups: (**A**) degradation test setup, and (**B**) radial force measurement test setup.

After weighing and before immersion testing, four wire samples with the same treatment parameter combination were prepared to be submerged in PBS for four weeks. During

immersion testing, iron wires were formed into 0.25-mm-diameter and 10-mm-tall, exposed wires. In addition, wire samples were then regularly removed each week to check the effect of the immersion time on the degradation of the wires. Before weighing, all the prepared samples were cleaned in order with alcohol, acetone, and DI water and carefully dried. After sample removal, they were cleaned in acetone using an ultrasonic bath after immersion, and the leftover corrosion products were then removed with a small brush. Finally, the samples were washed with acetone once more before being weighed for the second time after the test.

2.4. Mechanical Testing

Radial force tests were performed using a force measurement system (FMS-500, Starrett, Athol, MA, USA) clipped to a Dacron strip, which was looped and tightened around the heart valve frame, as depicted in Figure 3B, to measure the required forces with the reduction of the diameter from 10 to 20% of its original diameter. To measure radial force, external circumferential pressure was applied on the outer surface of the valve while constraining the displacement of the lower surface of the valve. The pressure was multiplied by the surface area to calculate the radial force, and the change in diameter was used to calculate the diameter reduction %. The model was utilized to show the relationship between the valve diameter and the radial force. In addition, the model was used to predict the stress levels for the reduction ratio.

2.5. Computational Modeling

Finite element analysis (FEA) was utilized to predict the mechanical performance of the pediatric heart valve. The valve model was constructed as longitudinally repeated circumferential iron struts that were connected with nitinol connections. The 3D model of the valve was built using computer-aided design (SolidWorks, Waltham, MA, USA) and then imported into the Ansys software (Ansys, Canonsburg, PA, USA) for further computational analysis. A static structure module was employed to model and calculate the radial forces, stresses, and strains of the pediatric valve. The diameter of the valve was examined using 10, 12.5, and 15 mm while fixing the valve thickness to 0.2 mm. Figure 4A shows the structure of the pediatric valve, where the two materials were appropriately defined for the valve structure. In Figure 4B,C, the differences between connections made of nitinol and iron-based struts are, respectively, illustrated. The modeling of the nitinol behavior was conducted using the superelasticity built-in module in Ansys, where the material's pseudoelasticity properties were adopted from Wu et al. The iron material model from the Ansys material library was exploited to model the struts [34].

2.6. Prototype Fabrication

Nitinol wires with different diameters were joined by a precision micro laser-welding system (LZR-100; Sunstone Engineering, Payson, UT, USA). Welding parameters were optimized to acquire the best material and mechanical properties of the structure for nitinol wires with various thicknesses. The laser process parameters were 1.4 KW power, 0.7 mm spot size, 1.2 ms time duration, 3Hz frequency, and rectangular wave. A machined aluminum mandrel based on the anatomy of the animal model was used to create the nitinol backbone with the desired cylindrical geometry, where the external diameter of the mandrel corresponded to the deployed device's diameter. The mandrel diameter was oversized by 20% to produce the oversized stent backbone to achieve sufficient radial force for the device. The mandrel with the frame was heated up to 350–600 °C with a tube furnace (Lindberg/Blue M Moldatherm, Fisher Scientific, Pittsburgh, PA) for 30–40 min; then, the frame was rapidly cooled in water to 20 °C in 10 s (quenching). Thermal treatment was performed to set the final shape of the nitinol wires with the required superelastic properties, eliminating any potential local stress concentration caused by welding.

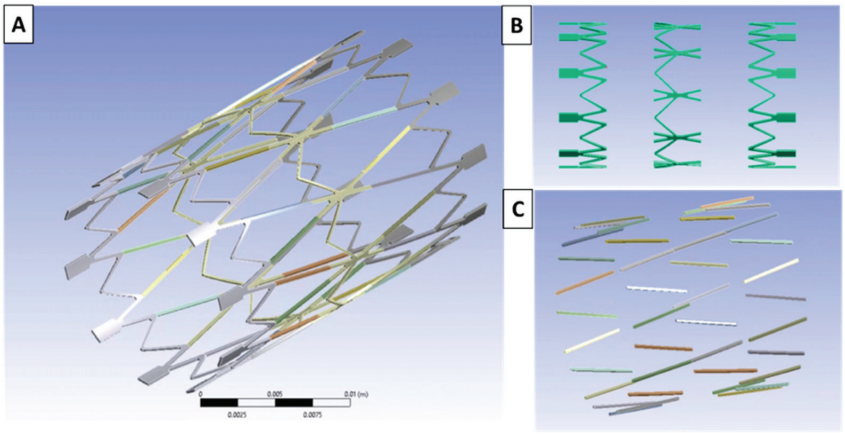

Figure 4. The 3D modeling of the pediatric heart valve: (**A**) valve's struts linked with connections, (**B**) nitinol connections, and (**C**) iron-based struts.

2.7. Biocompatibility Studies

In vitro cell viability studies were designed and conducted using a typical cell culture method and MTS assay. Rat vascular smooth muscle cells (rSMCs) were cultured in Dulbecco's modified Eagle medium (DMEM) with 10% heat-inactivated fetal bovine serum (HI-FBS) and 1% penicillin/streptomycin at 37 °C and 5% CO_2 [35]. Both the untreated and thermally treated iron wire samples were cultured for 3 days. Negative controls were also compared to determine the differences using the data normalization to the negative control including cultured cells in the medium. For the hemocompatibility studies, whole fresh ovine blood was collected and used under the approval of the Institutional Animal Care and Use Committee at the University of Pittsburgh. The collected blood was stored in a vacutainer tube (BD Vacutainer) and sterilized, and then incubated for 3 h at 37 °C in a hematology mixer (Fisher Scientific, Waltham, MA, USA) [36]. After 3 h, the samples were thoroughly rinsed with PBS solution 10 times, and then the deposited platelets on wires were qualitatively analyzed via scanning electron microscopy (SEM, JSM 6335F, JEOL, Tokyo, Japan).

3. Results

3.1. Degradation

Multiple wire samples were thermally treated at various combinations of treatment times and temperatures to investigate the effect of the iron oxide layer formation on the iron wires' degradation. In addition, these samples were treated for three time periods to check the influence of the iron oxide layer thickness on the degradation rate of pure iron wires. All treated wires were typically compared with the original wire (i.e., with no treatment) with respect to the final diameter over several weeks of testing in PBS. When the samples were thermally treated at a temperature of 350 °C, as depicted in Figure 5A, the wire's diameters increased with the increase in the treatment time before immersion testing due to the formation of an iron oxide layer. In this figure, at week zero, the wire diameter increased from 254 ± 1.23 µm for the untreated sample to 261 ± 0.89 µm after 4 h of heat treatment. The slope of the diameter reduction resulted in that of the 4 h treated samples being lower than that of the original one and the samples with a shorter treatment time, achieving a reasonable overall diameter of 241 ± 1.14 µm after 4 weeks of degradation testing.

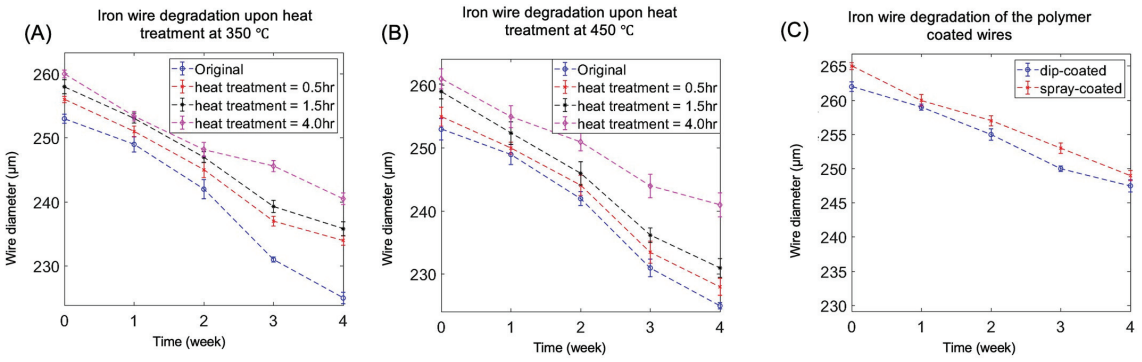

Figure 5. Iron wire diameter (μm) vs. the testing time (week): (**A**) heat-treated at 350 °C, (**B**) heat-treated at 450 °C, and (**C**) polymer-coated wire.

As in Figure 5B, the heat treatment temperature was increased to 450 °C, attaining a greater iron oxide layer thickness with a total wire diameter of 262 ± 1.04 μm for the 4 h heat-treated sample than the corresponding one under 350 °C heat treatment. The slope of the diameter reduction resulted in that of the 4 h treated sample being lower than that of the original one and the samples with a shorter treatment time, achieving a reasonable overall diameter of 242 ± 0.72 μm after 4 weeks of degradation testing. The lower slope of the diameter reduction indicates the superiority of heat treatment at different temperatures. Regarding the coated samples represented in Figure 5C, both dip and spray-dip-coated wires exhibited almost the same corrosion rate in terms of diameter reduction, but their slope of degradation was lower than the slope of thermally treated wires. In the fourth week, both coated samples showed a lower diameter reduction (diameter >250 μm), while all thermally treated wires were higher in corrosion with diameter (<250 μm).

As seen in Figure 6, when the wire samples were investigated using SEM, the diameter along the wire varied due to the non-regularity of the iron oxide layer along the wire length. As depicted in Figure 6A, the iron oxide layer with a bright glow only covers the right side of the wire, with a total diameter of 259.7 μm, while the dark iron wire with no oxide layer appears with a lower diameter of 253 μm on the left side of the image. Consistently, after two weeks of immersion testing, as shown in Figure 6B, the diameter over the wire's length varied from 224.7 μm on the left to 249.6 μm on the right of the figure. Hence, the wire's diameters collected from the SEM analysis were averaged for each sample due to the non-uniformity of the oxide layer over the length of the iron wires.

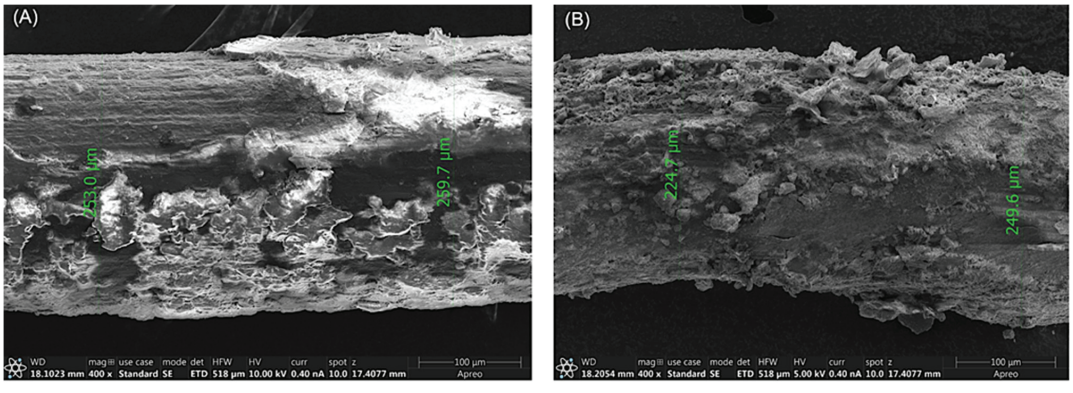

Figure 6. SEM imaging for the iron wire upon heat treatment at 450 °C: (**A**) for 4 h after the first week, and (**B**) for 3 h after the second week.

Since the wires were weighed before and after the immersion tests, another measure of degradation of body mass reduction was tracked and plotted, as in Figure 7. Both thermally treated samples at different temperatures showed the same corrosion trend as shown in Figure 7A,B. In both figures, the wire's masses were increasing with the increase in the treatment time before the immersion test due to the formation of an iron oxide layer with no loss in corrosion products. Before testing, as in Figure 7A, the wire mass increased from 0.0161 ± 0.0075 g for untreated samples to 0.0186 ± 0.0037 g after 4 h of 350 °C heat treatment. The slope of the mass reduction resulted in that of the 4 h treated samples being lower than that of the original one and the samples with a shorter treatment time, achieving a final wire mass of 0.0136 ± 0.0054 g after 4 weeks of degradation testing. As seen in Figure 7B, the heat treatment temperature was increased to 450 °C, and the wires' masses slightly increased compared to the values corresponding to the 350 °C heat treatment due to the greater iron oxide layer thickness. The wire mass increased to 0.0192 ± 0.0063 g for the 4 h heat-treated sample compared to the corresponding one under 350 °C heat treatment. The slope of the mass reduction resulted in that of the 4 h 450 °C thermally treated samples being lower than that of the original one and the samples with a shorter treatment time, achieving a reasonable overall mass of 0.0138 ± 0.0047 g after 4 weeks of degradation testing. The lower slope of the mass reduction indicates the superiority of heat treatment at different temperatures. Regarding the polymer-coated samples represented in Figure 7C, both dip and spray-dip-coated wires also exhibited very similar corrosion rates in terms of mass reduction to that in diameter reduction, but their slope of degradation was lower than the slope of thermally treated wires.

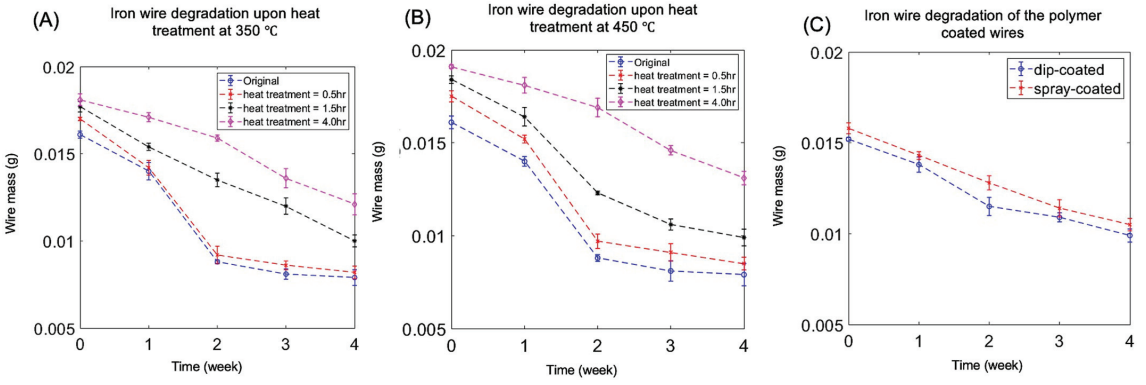

Figure 7. The relationship between the iron wire mass (g) and the types of surface treatment over time (week): (**A**) heat-treated at 350 °C, (**B**) heat-treated at 450 °C, and (**C**) polymer-coated wire.

3.2. Biocompatibility Study Results

Figure 8 shows the biocompatibility study results on both the cytotoxicity (i.e., cell viability) and hemocompatibility of the thermally treated iron wires to assess basic biological interactions. The cell viability study was analyzed via methyltransferase (MTS) assays, as shown in Figure 8A, which demonstrated higher cell viability in the thermally treated iron wire compared to the untreated wire after 3 days of incubation in vitro. The thermally treated wires showed approximately 21% higher cell viability than the untreated wire samples. The representative SEM image shown in Figure 8B shows uniformly distributed cells on the surface of the iron wire. Another biocompatibility study to evaluate the implantable device focused on hemocompatibility. In this study, only a qualitative assessment was conducted to evaluate the surface to observe the thrombosis formation using SEM analysis.

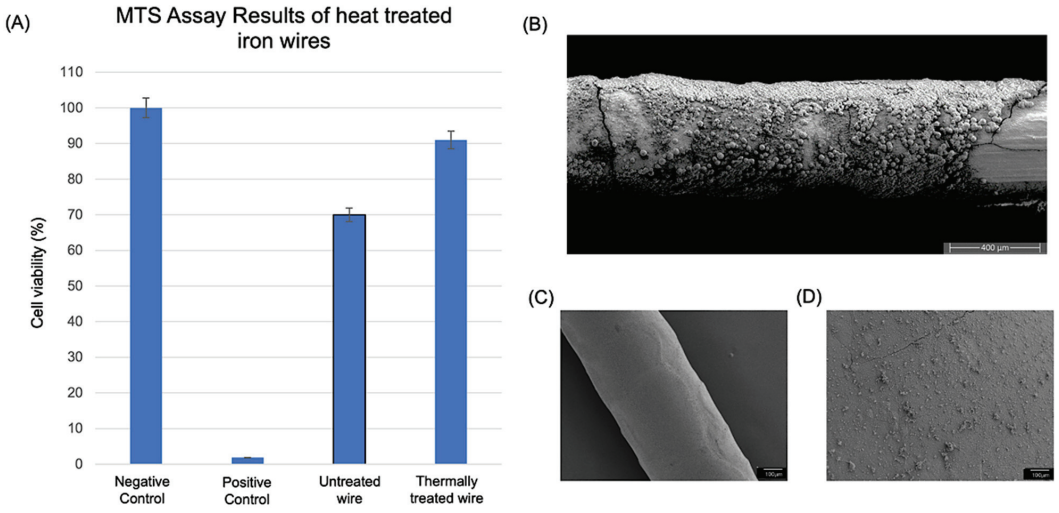

Figure 8. Cytotoxicity and hemocompatibility study results: (**A**) cell viability comparison study results of the thermally treated iron wires using MTS assay, (**B**) a representative scanning electron microscopy (SEM) image of the thermally treated wire after the cell viability test, (**C**) qualitative study results with SEM (low-magnification), and (**D**) high-magnification SEM image.

3.3. Prototype Fabrication

Figure 9A shows that the prototype pediatric valve frame consists of superelastic nitinol and biodegradable iron wires. The diameter is 15 mm and the length is 25 mm. Figure 1B shows three different segments of the nitinol–iron valve frame, which are the nitinol tube, iron wire, and "X"-shaped nitinol strut. This structure has been manufactured by (1) precision trimming of the "X"-shaped nitinol strut from a Neuroform stent (Stryker Corp., Fremont, CA, USA); (2) a superelastic thin-wall nitinol tube (0.006" inner diameter, Confluent Medical, Fremont, CA, USA) for joining two materials, and mechanical strengthening without creating severe deformation of the iron wire (125 µm thick, GoodFellow, Pittsburgh, PA, USA). A small amount of biocompatible polymer adhesive (Loctite 4902, Henkel Corp) was applied inside the nitinol tubes to tightly join both the nitinol strut and iron wire during the collapse and deployment procedure. An ultra-precision micro laser welding process was applied to create a solid joined structure via a localized metal melting process. Figure 9C shows the end section of the valve frame that required a "V"-shaped nitinol strut for the joining. A subsequential thermal annealing process was conducted under 350–600 °C for 30–40 min to release any potential stress concentration issue and to recover the superelasticity of the nitinol material. The fabricated frame was tested for radial strength exertion under varied diameter changes, which were compared with the computational modeling results to validate the device design.

3.4. Radial Strength Analysis and Experimental Validation

3.4.1. Computational Modeling Results of the Stress vs. Strain of the Valve Frame

The finite element model for the pediatric heart valve was built and utilized to estimate the stress caused at different sections of the valve. It was typically anticipated that the maximum stress in the proposed valve design would take place at the nitinol connections due to this being the location of the main deformation of the valve. As depicted in Figure 10A,B, the undeformed and the deformed shapes of the valve frames were observed, showing both the amount and shape of deformation that took place in the valve upon applying an external radial force. These figures show uniform valve deformation through the full length of the valve. The stresses caused in the structure of the valve after deformation were also calculated and are represented in Figure 10C, while the stresses inside the nitinol

connections only are shown in Figure 10E. Figure 10D depicts that the maximum Von Mises stress occurred on the stent connections, with a maximum stress value equal to 552 MPa. In terms of strain values in the pediatric heart valve, Figure 10D,F show the Von Mises strain of the valve, whereas Figure 9E depicts the Von Mises strain in the whole valve, while Figure 10F depicts only the strain inside the nitinol connections. The maximum Von Mises strain inside the valve was 1.1%; however, the maximum Von Mises strain in nitinol was 0.9%.

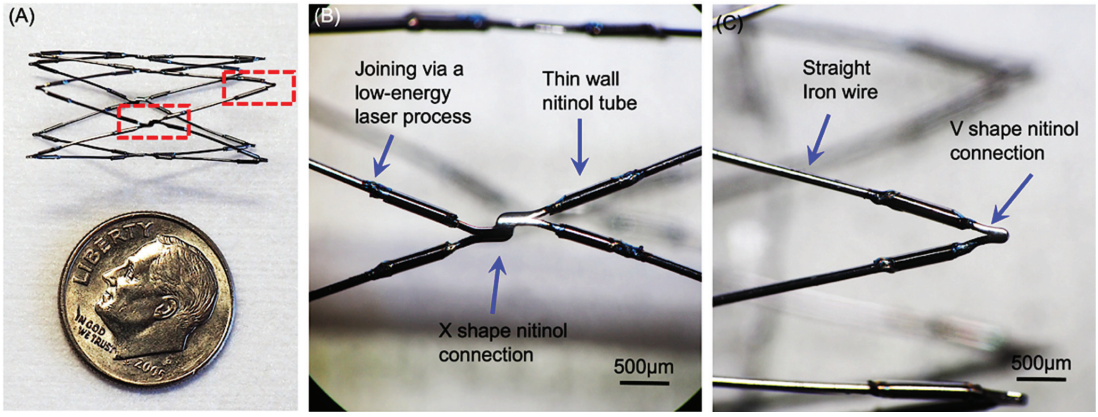

Figure 9. Prototype valve frame and details: (**A**) entire valve frame, (**B**) the nitinol and iron wire integration using a thin-wall nitinol tube for the middle connection, and (**C**) the end section device details with "V"-shaped nitinol connection.

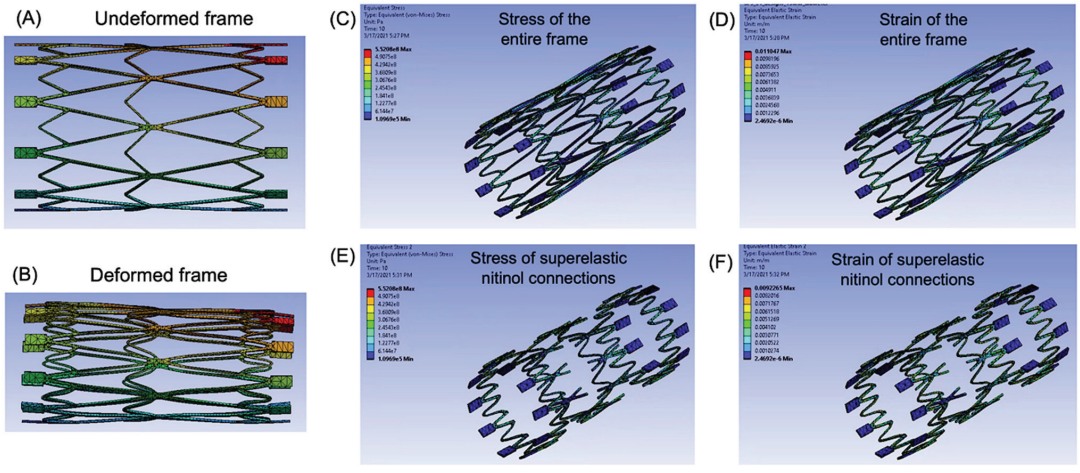

Figure 10. Stress and strain computational analysis of the pediatric valve: (**A**) undeformed valve shape, (**B**) deformed valve shape, (**C**) stress of the entire frame after deformation, (**D**) Von Mises strain in the frame after deformation, (**E**) stress of nitinol connection regions, and (**F**) Von Mises strain of nitinol connection regions.

3.4.2. Comparison of Computational Modeling and Experimental Results on Radial Strength

Upon solving the structural model of the heart valve, the radial forces were then computed with the advantage of the stress and strain results. The radial forces at multiple valve diameters of 10, 12.5, and 15 mm were solved to predict the effect of the designed

diameter on the radial force needed to deform the full structure. As shown in Figure 10A, the relationship between the radial force and diameter reduction % is composed of two segments: linear and non-linear segments. The first linear segment shows the reversible elastic deformation of the valve until it reaches a 10% diameter reduction, while the irreversible non-linear segment shows steady plastic deformation starting from 10% up to a +20% diameter reduction. In addition, the higher the valve diameter, the lower the radial forces that are required to crimp the valve to smaller diameters, and Figure 10A also depicts the radial force up to 30% diameter reduction. The maximum radial force for a 10 mm diameter is 6 N.

An experimental investigation was also performed to validate the computational simulation results for the radial forces required to collapse the valve up to various diameter reduction values (Figure 10B). Vertical forces were first collected at a sampling rate of 10 Hz, and then converted to circumferential averaged forces to plot the radial forces applied at various diameter reduction percentages. These depicted radial forces in Figure 11B also demonstrate the two successive linear and non-linear force–deformation segments, where the forces can be elastically reversible in the linear part and continue plastically after a 10% diameter reduction. The experimental test was performed up to a 20% diameter reduction to avoid the massive plastic deformation of the pediatric heart valve prototype, achieving 5 N as the maximum applied radial force.

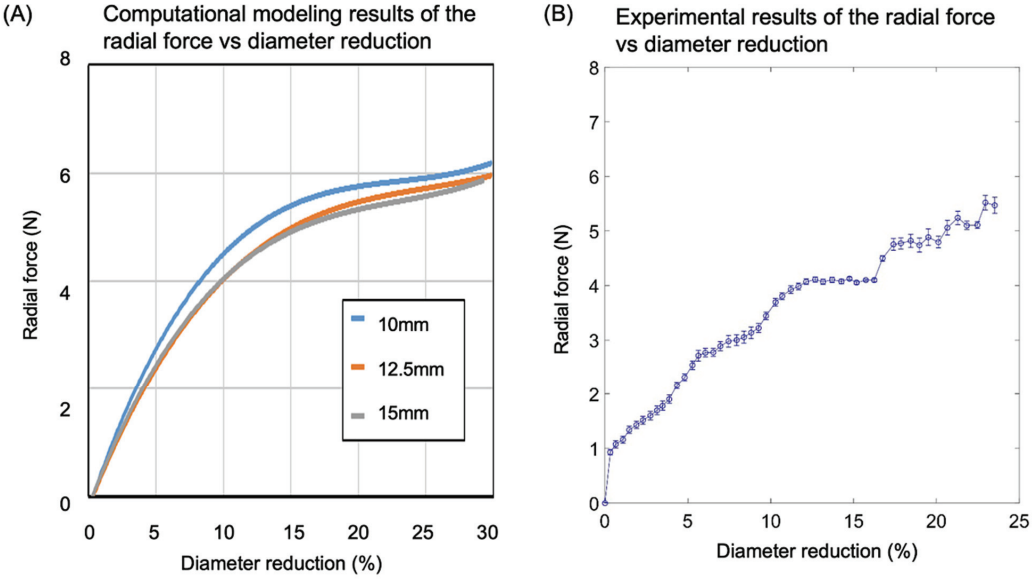

Figure 11. Computational (**A**) and experimental (**B**) results of the radial force (N) vs. diameter reduction (%) for the varied valve diameters.

4. Discussion

Despite the technological advancement in the area of endovascular devices, there are no appropriate heart valve devices available for pediatric patients who have congenital heart valve defects [37]. As the child grows, the implanted devices must be replaced often during growth. As a result, any percutaneous heart valve device technology that can avoid or eliminate repeated open surgery would provide a new therapeutic option for infants or children who have heart valve defects.

Vascular stents or percutaneous heart valves have offered an alternative to open surgical procedures including patients who are too weak or very young, who would be unsuitable for open operation [38]. In addition, a child will grow over time, so the endovascular device used in children must change its dimensions to accommodate the

anatomical size changes. A novel percutaneous heart valve frame studied here for pediatric patients allows partial biodegradation (>90%) for the device to change with the growth of the child. This new approach utilizes two novel metallic biomaterials, namely superelastic nitinol and biodegradable iron.

Iron degradation with surface treatments is one of the most important functions in the device. The iron materials used in our valve frame show an approximately 7%–10% diameter reduction per 4-week period in both thermally treated iron wires under two different temperature conditions, i.e., 350 and 450 °C (Figures 5–7). The polymer-coated iron wires showed slower degradation, with approximately 4% diameter reduction per 4 weeks. Therefore, 9–23 months are needed for the complete degradation of the wires. Considering a theoretical arterial vessel remodeling process period in the human vascular system of 6–12 months, the surface treatments shown in this study are valid and suitable for the required degradation period after the device's implantation [39,40].

In addition to the iron degradation study, an in vitro biocompatibility study was conducted to assess the materials' biological interaction, both quantitatively and qualitatively, using cell viability and hemocompatibility analyses. The thermally treated iron wire showed higher cell viability up to 21% compared to untreated samples, as shown Figure 8. This sample also shows qualitatively excellent hemocompatibility under an in vitro platelet adhesion study. There are limitations to the biocompatibility studies since only thermally treated wires were compared with untreated wire samples to assess cell viability, and only qualitative SEM-based analysis was used in the hemocompatibility evaluation. Although these study results show that the thermally treated iron wires are superior to untreated wires, a more detailed study including polymer-coated iron wires would be needed for diverse comparison studies in the future. In this work, the acute in vitro biocompatibility evaluation is important because any issues that may develop should be addressed prior to entering animal studies in the future.

The third fundamental study to develop a novel heart valve device is the design via computational modeling and subsequent mechanical testing [41,42]. Radial strength is one of the most important force values needed for self-expanding endovascular devices that contain superelastic nitinol [43]. Computational modeling and experimental test data, shown in Figures 9 and 10, have clearly demonstrated the optimized design and its validation through mechanical testing. The radial force exerted with 20% diameter reduction shows approximately 5 N both from computational and experimental results (Figure 10). It is challenging to compare the radial force of the newly developed nitinol–iron valve frame with commercial products, since there are no such devices available for pediatric patients. As a reference, commercial adult heart valve frames made of nitinol can be compared for validating the radial force produced in the experiment. Typical values of adult nitinol heart valve frames' radial force are in a range between 9 and 54 N [44]. The Acurate neo S (ANS; Symetis, Switzerland) shows the smallest radial force, lower than 9N, but two other CoreValve devices (CV 23, CV26, Medtronic, Minneapolis, MN, USA) show higher forces with an increased deployed diameter [44]. This comparison study's results show the relationship between the deployed diameter and radial force. The radial force is also dependent on the mesh geometry.

Once necessary fundamental studies were successfully conducted, a functional prototype was fabricated using various advanced manufacturing technologies, including a micro laser joining process [45–47]. As shown in Figure 9, a new joining process for constructing a heart valve frame was developed and optimized. Three typical endovascular device fabrication methods are (1) laser cutting of thin-wall metal tubes, (2) braiding thin metal wires, or (3) bending metal wires to the desired shape [48,49]. Since three different components were used to develop the new heart valve frame, none of these technologies could be used. Thus, a micro laser welding-based joining technique utilizing a thin-wall nitinol tube was selected as the best fabrication technique for the growing valve frame, minimizing the stress concentration and achieving durable connections for the three different materials.

5. Conclusions

In the present work, the development of a novel self-expanding biodegradable percutaneous heart valve frame for pediatric patients was conducted, which shows clinical significance. The new design of the heart valve frame employs two forms of metallic biomaterials, namely superelastic nitinol and biodegradable iron. The biodegradation of iron wires with varied surface treatment showed a gradual and stable diameter reduction of 7%–10% for 4-week blood-mimicking circulation tests. Polymer-coated wires show relatively slower degradation, showing approximately 4.69%–5.66% compared to the original wire diameter. The biodegradation of surface-modified iron struts allows the pediatric device to grow with the child with gradual degradation, and the superelastic nitinol connections offer a firm structure during delivery, deployment, and for the future tissue growth process. The device design was optimized both through computational modeling and experimental studies. The prototype valve frame has been successfully developed based on computational modeling, radial strength analysis, biodegradation, and acute in vitro biocompatibility studies. The radial force exerted with a 20% diameter reduction shows approximately 5 N both from computational and experimental results. The thermally treated iron wire showed higher cell viability up to 21% compared to untreated samples. This work has demonstrated the viability of employing nitinol–iron valve frames in children in vitro, showing potential as a new therapeutic option in children with congenital heart diseases.

Author Contributions: Conceptualization, Y.C. and W.R.W.; methodology, M.I. and Y.C.; software, M.E. and M.I.; validation, M.I. and K.X.N.; formal analysis, M.I., Y.C., S.K. and S.Y.; investigation, M.I., Y.C., K.C., S.K., U.J.G. and S.Y.; resources, Y.C. and W.R.W.; data curation, M.I. and M.E.; writing—original draft preparation, M.I., M.E., K.X.N., S.K. and S.Y.; writing—review and editing, Y.C.; visualization, M.I. and Y.C.; supervision, Y.C.; project administration, Y.C.; funding acquisition, Y.C. All authors have read and agreed to the published version of the manuscript.

Funding: This research was funded by the Independent Research Award funded by the Liam Ward Fund under the Children's Heart Foundation and the Pitt Central Research Development Fund.

Institutional Review Board Statement: Not applicable.

Informed Consent Statement: Not applicable.

Data Availability Statement: Not applicable.

Conflicts of Interest: The authors declare no conflict of interest.

References

1. Loffredo, C.A. Epidemiology of cardiovascular malformations: Prevalence and risk factors. *Am. J. Med. Genet.* **2000**, *97*, 319–325. [CrossRef] [PubMed]
2. Friedewald, V.E.; Bonow, R.O.; Borer, J.S.; Carabello, B.A.; Kleine, P.P.; Akins, C.W.; Roberts, W.C. The editor's roundtable: Cardiac valve surgery. *Am. J. Cardiol.* **2007**, *99*, 1269–1278. [CrossRef] [PubMed]
3. Association, A.H. *Heart Disease and Stroke Statistics—2004 Update*; American Heart Association: Dallas, TX, USA, 2004.
4. iData Research. *Cardiac Surgery Market Size, Share, and COVID-19 Impact Analysis*; iData Research: Burnaby, BC, Canada, 2020.
5. Kidane, A.G.; Burriesci, G.; Cornejo, P.; Dooley, A.; Sarkar, S.; Bonhoeffer, P.; Edirisinghe, M.; Seifalian, A.M. Current developments and future prospects for heart valve replacement therapy. *J. Biomed. Mater. Res. Part B Appl. Biomater.* **2009**, *88*, 290–303. [CrossRef] [PubMed]
6. Vongpatanasin, W.; Hillis, L.D.; Lange, R.A. Prosthetic heart valves. *N. Engl. J. Med.* **1996**, *335*, 407–416. [CrossRef] [PubMed]
7. Cobanoglu, A.; Fessler, C.L.; Guvendik, L.; Grunkemeier, G.; Starr, A. Aortic valve replacement with the Starr-Edwards prosthesis: A comparison of the first and second decades of follow-up. *Ann. Thorac. Surg.* **1988**, *45*, 248–252. [CrossRef]
8. Schoevaerdts, J.C.; Buche, M.; El Gariani, A.; Lichtsteiner, M.; Jaumin, P.; Ponlot, R.; Chalant, C. Twenty years' experience with the Model 6120 Starr-Edwards valve in the mitral position. *J. Thorac. Cardiovasc. Surg.* **1987**, *94*, 375. [CrossRef]
9. Head, S.J.; Çelik, M.; Kappetein, A.P. Mechanical versus bioprosthetic aortic valve replacement. *Eur. Heart J.* **2017**, *38*, 2183–2191. [CrossRef]
10. Gallegos, R.P.; Rivard, A.L.; Suwan, P.T.; Black, S.; Bertog, S.; Steinseifer, U.; Armien, A.; Lahti, M.; Bianco, R.W. In-vivo experience with the Triflo trileaflet mechanical heart valve. *J. Heart Valve Dis.* **2006**, *15*, 791.
11. Wu, Y.X.; Gregorio, R.; Renzulli, A.; Onorati, F.; De Feo, M.; Grunkemeier, G.; Cotrufo, M. Mechanical heart valves: Are two leaflets better than one? *J. Thorac. Cardiovasc. Surg.* **2004**, *127*, 1171–1179. [CrossRef]

12. Lim, K.H.H.; Caputo, M.; Ascione, R.; Wild, J.; West, R.; Angelini, G.D.; Bryan, A.J.; Calafiore, S.; Maria, A. Prospective randomized comparison of CarboMedics and St Jude Medical bileaflet mechanical heart valve prostheses: An interim report. *J. Thorac. Cardiovasc. Surg.* **2002**, *123*, 21–32. [CrossRef]
13. Gregoric, I.D.; Eya, K.; Tamez, D.; Cervera, R.; Byler, D.; Conger, J.; Tuzun, E.; Chee, H.K.; Clubb, F.J.; Kadipasaoglu, K. Preclinical hemodynamic assessment of a new trileaflet mechanical valve in the aortic position in a bovine model. *J. Heart Valve Dis.* **2004**, *13*, 254.
14. Schoen, F.J.; Levy, R.J. Tissue heart valves: Current challenges and future research perspectives. *J. Biomed. Mater. Res.* **1999**, *47*, 439–465. [CrossRef]
15. Wells, S.M.; Sellaro, T.; Sacks, M.S. Cyclic loading response of bioprosthetic heart valves: Effects of fixation stress state on the collagen fiber architecture. *Biomaterials* **2005**, *26*, 2611–2619. [CrossRef]
16. Sacks, M.S.; Schoen, F.J. Collagen fiber disruption occurs independent of calcification in clinically explanted bioprosthetic heart valves. *J. Biomed. Mater. Res.* **2002**, *62*, 359–371. [CrossRef]
17. Schoen, F.J.; Levy, R.J. Calcification of tissue heart valve substitutes: Progress toward understanding and prevention. *Ann. Thorac. Surg.* **2005**, *79*, 1072–1080. [CrossRef]
18. Yacoub, M.; Rasmi, N.R.H.; Sundt, T.M.; Lund, O.; Boyland, E.; Radley-Smith, R.; Khaghani, A.; Mitchell, A. Fourteen-year experience with homovital homografts for aortic valve replacement. *J. Thorac. Cardiovasc. Surg.* **1995**, *110*, 186–194. [CrossRef]
19. O'Brien, M.F.; Gregory Stafford, E.; Gardner, M.A.H.; Pohlner, P.G.; Tesar, P.J.; Cochrane, A.D.; Mau, T.K.; Gall, K.L.; Smith, S.E. Allograft aortic valve replacement: Long-term follow-up. *Ann. Thorac. Surg.* **1995**, *60*, S65–S70. [CrossRef]
20. Bloomfield, P.; Wheatley, D.J.; Prescott, R.J.; Miller, H.C. Twelve-year comparison of a Bjork–Shiley mechanical heart valve with porcine bioprostheses. *N. Engl. J. Med.* **1991**, *324*, 573–579. [CrossRef]
21. Busch, J.; Johnson, A.; Lee, C.; Stevenson, D. Shape-memory properties in Ni-Ti sputter-deposited film. *J. Appl. Phys.* **1990**, *68*, 6224–6228. [CrossRef]
22. Szold, A. Nitinol: Shape-memory and super-elastic materials in surgery. *Surg. Endosc.* **2006**, *20*, 1493–1496. [CrossRef]
23. Machado, L.; Savi, M. Medical applications of shape memory alloys. *Braz. J. Med. Biol. Res.* **2003**, *36*, 683–691. [CrossRef] [PubMed]
24. Shabalovskaya, S.A. Surface, corrosion and biocompatibility aspects of Nitinol as an implant material. *Bio-Med. Mater. Eng.* **2002**, *12*, 69–109.
25. Moravej, M.; Mantovani, D. Biodegradable metals for cardiovascular stent application: Interests and new opportunities. *Int. J. Mol. Sci.* **2011**, *12*, 4250–4270. [CrossRef] [PubMed]
26. Peuster, M.; Hesse, C.; Schloo, T.; Fink, C.; Beerbaum, P.; von Schnakenburg, C. Long-term biocompatibility of a corrodible peripheral iron stent in the porcine descending aorta. *Biomaterials* **2006**, *27*, 4955–4962. [CrossRef]
27. Batista, B.A.; Soares, R.B.; Lins, V.d.F.C.; Figueiredo, R.B.; Hohenwarter, A.; Matencio, T. Corrosion in hank's solution and mechanical strength of ultrafine-grained pure iron. *Adv. Eng. Mater.* **2020**, *22*, 2000183. [CrossRef]
28. Obayi, C.S.; Tolouei, R.; Mostavan, A.; Paternoster, C.; Turgeon, S.; Okorie, B.A.; Obikwelu, D.O.; Mantovani, D. Effect of grain sizes on mechanical properties and biodegradation behavior of pure iron for cardiovascular stent application. *Biomatter* **2016**, *6*, e959874. [CrossRef]
29. Marciuš, M.; Ristić, M.; Ivanda, M.; Musić, S. Formation of iron oxides by surface oxidation of iron plate. *Croat. Chem. Acta* **2012**, *85*, 117–124. [CrossRef]
30. Simmons, G.; Kellerman, E.; Leidheiser, H., Jr. The oxidation of iron as studied by conversion electron Mössbauer spectroscopy. *Corrosion* **1973**, *29*, 227. [CrossRef]
31. Yan, R.; Gao, X.; He, W.; Guo, R.; Wu, R.; Zhao, Z.; Ma, H. A simple and convenient method to fabricate new types of phytic acid–metal conversion coatings with excellent anti-corrosion performance on the iron substrate. *RSC Adv.* **2017**, *7*, 41152–41162. [CrossRef]
32. Gu, X.; Mao, Z.; Ye, S.-H.; Koo, Y.; Yun, Y.; Tiasha, T.R.; Shanov, V.; Wagner, W.R. Biodegradable, elastomeric coatings with controlled anti-proliferative agent release for magnesium-based cardiovascular stents. *Colloids Surf. B Biointerfaces* **2016**, *144*, 170–179. [CrossRef]
33. Liu, L.; Ye, S.-H.; Gu, X.; Russell, T.; Xu, Z.; Sankar, J.; Wagner, W.R.; Lee, Y.-C.; Yun, Y. Comparison of endothelial cell attachment on surfaces of biodegradable polymer-coated magnesium alloys in a microfluidic environment. *PLoS ONE* **2018**, *13*, e0205611. [CrossRef]
34. Wu, W.; Qi, M.; Liu, X.-P.; Yang, D.-Z.; Wang, W.-Q. Delivery and release of nitinol stent in carotid artery and their interactions: A finite element analysis. *J. Biomech.* **2007**, *40*, 3034–3040. [CrossRef]
35. Kim, S.; Nowicki, K.W.; Ye, S.; Jang, K.; Elsisy, M.; Ibrahim, M.; Chun, Y.; Gross, B.A.; Friedlander, R.M.; Wagner, W.R. Bioabsorbable, elastomer-coated magnesium alloy coils for treating saccular cerebrovascular aneurysms. *Biomaterials* **2022**, *290*, 121857. [CrossRef]
36. Ye, S.-H.; Arazawa, D.T.; Zhu, Y.; Shankarraman, V.; Malkin, A.D.; Kimmel, J.D.; Gamble, L.J.; Ishihara, K.; Federspiel, W.J.; Wagner, W.R. Hollow fiber membrane modification with functional zwitterionic macromolecules for improved thromboresistance in artificial lungs. *Langmuir* **2015**, *31*, 2463–2471. [CrossRef]
37. Lutter, G.; Ardehali, R.; Cremer, J.; Bonhoeffer, P. Percutaneous valve replacement: Current state and future prospects. *Ann. Thorac. Surg.* **2004**, *78*, 2199–2206. [CrossRef]

38. El-Omar, M.M.; Dangas, G.; Iakovou, I.; Mehran, R. Update on in-stent restenosis. *Curr. Interv. Cardiol. Rep.* **2001**, *3*, 296–305.
39. Schömig, A.; Kastrati, A.; Mudra, H.; Blasini, R.; Schühlen, H.; Klauss, V.; Richardt, G.; Neumann, F.J. Four-year experience with Palmaz-Schatz stenting in coronary angioplasty complicated by dissection with threatened or present vessel closure. *Circulation* **1994**, *90*, 2716–2724. [CrossRef]
40. Finotello, A.; Gorla, R.; Brambilla, N.; Bedogni, F.; Auricchio, F.; Morganti, S. Finite element analysis of transcatheter aortic valve implantation: Insights on the modelling of self-expandable devices. *J. Mech. Behav. Biomed. Mater.* **2021**, *123*, 104772. [CrossRef]
41. Salemizadeh Parizi, F.; Mehrabi, R.; Karamooz-Ravari, M.R. Finite element analysis of NiTi self-expandable heart valve stent. *Proc. Inst. Mech. Eng. Part H J. Eng. Med.* **2019**, *233*, 1042–1050. [CrossRef]
42. Elsisy, M.; Tillman, B.W.; Go, C.; Kuhn, J.; Cho, S.K.; Clark, W.W.; Park, J.; Chun, Y. Comprehensive assessment of mechanical behavior of an extremely long stent graft to control hemorrhage in torso. *J. Biomed. Mater. Res. Part B Appl. Biomater.* **2020**, *108*, 2192–2203. [CrossRef]
43. Egron, S.; Fujita, B.; Gullón, L.; Pott, D.; Schmitz-Rode, T.; Ensminger, S.; Steinseifer, U. Radial force: An underestimated parameter in oversizing transcatheter aortic valve replacement prostheses: In vitro analysis with five commercialized valves. *ASAIO J.* **2018**, *64*, 536–543. [CrossRef]
44. Elsisy, M.; Shayan, M.; Chen, Y.; Tillman, B.W.; Go, C.; Chun, Y. Assessment of mechanical and biocompatible performance of ultra-large nitinol endovascular devices fabricated via a low-energy laser joining process. *J. Biomater. Appl.* **2021**, *36*, 332–345. [CrossRef] [PubMed]
45. MI, K.; Zhou, Y. Effects of welding parameters on the mechanical performance of laser welded nitinol. *Mater. Trans.* **2008**, *49*, 2702–2708.
46. Deepan Bharathi Kannan, T.; Ramesh, T.; Sathiya, P. A review of similar and dissimilar micro-joining of nitinol. *JOM* **2016**, *68*, 1227–1245. [CrossRef]
47. Moeri, L.; Lichtenberg, M.; Gnanapiragasam, S.; Barco, S.; Sebastian, T. Braided or laser-cut self-expanding nitinol stents for the common femoral vein in patients with post-thrombotic syndrome. *J. Vasc. Surg. Venous Lymphat. Disord.* **2021**, *9*, 760–769. [CrossRef]
48. van Veenendaal, P.; Maingard, J.; Kok, H.K.; Ranatunga, D.; Buckenham, T.; Chandra, R.V.; Lee, M.J.; Brooks, D.M.; Asadi, H. Endovascular flow-diversion of visceral and renal artery aneurysms using dual-layer braided nitinol carotid stents. *CVIR Endovasc.* **2020**, *3*, 33. [CrossRef]
49. Zheng, Q.; Mozafari, H.; Li, Z.; Gu, L.; An, M.; Han, X.; You, Z. Mechanical characterization of braided self-expanding stents: Impact of design parameters. *J. Mech. Med. Biol.* **2019**, *19*, 1950038. [CrossRef]

MDPI
St. Alban-Anlage 66
4052 Basel
Switzerland
www.mdpi.com

Coatings Editorial Office
E-mail: coatings@mdpi.com
www.mdpi.com/journal/coatings

Academic Open
Access Publishing

mdpi.com

ISBN 978-3-0365-9339-5